Title
Search for a Light Pseudoscalar Higgs Boson and CMS Pixel Tracker Commissioning and Operation for Run 3

Author
Haza, Grace

Publication Date
2023

Search for a Light Pseudoscalar Higgs Boson and CMS Pixel Tracker Commissioning and Operation for Run 3

By

GRACE MARIE HAZA

DISSERTATION

Submitted in partial satisfaction of the requirements for the degree of

DOCTOR OF PHILOSOPHY

in

Physics

in the

OFFICE OF GRADUATE STUDIES

of the

UNIVERSITY OF CALIFORNIA

DAVIS

Approved:

Maxwell Chertok, Chair

John Conway

Michael Mulhearn

Committee in Charge

2023

"Things don't have purposes, as if the universe were a machine, where every part has a useful function. What's the function of a galaxy? I don't know if our life has a purpose and I don't see that it matters. What does matter is that we're a part. Like a thread in a cloth or a grass-blade in a field. It is and we are. What we do is like wind blowing on the grass."

- Ursula K. Le Guin, *The Lathe of Heaven*

Contents

LIST OF FIGURES

List of Tables

ABSTRACT

Search for a Light Pseudoscalar Higgs Boson and CMS Pixel Tracker Commissioning and Operation for Run 3

This dissertation presents a search for a light pseudoscalar Higgs boson in the $\mathrm{H} \to \mathrm{aa} \to \mu\mu\tau\tau$ decay channel using the full Run 2 dataset collected by the CMS detector at CERN. Due to the mass difference between the Higgs boson and the pseudoscalar Higgs boson, the final state particles have a boosted topology that includes overlapping τ decays. The search is performed for the fully hadronic, semi leptonic, and fully leptonic decays of the τ leptons. DeepDiTau, a tagger trained through machine learning, is used to identify $\tau_h\tau_h$ decays that are reconstructed as jets. The expected limits on $\sigma_H\mathcal{B}(\mathrm{H} \to \mathrm{aa} \to \mu\mu\tau\tau)/\sigma_{SM}$ for all channels in this search are presented.

The CMS pixel tracker was prepared for Run 3 with refurbishment, installation, and commissioning periods. This dissertation presents this process along with further calibrations and the beginning of Run 3 operation. Additionally, a dedicated radiation damage study on the innermost layer of the Barrel Pixels is presented.

ACKNOWLEDGMENTS

I thank Maxwell Chertok, my mentor since 2017 who guided me through all the steps of this thesis, encouraged me throughout my time as a PhD student, and demonstrated how to be a thoughtful physicist.

I thank my thesis committee members John Conway and Mike Mulhearn for their feedback on this document, and I am grateful to the entire UC Davis CMS group for their support and expertise.

I thank Feng for welcoming me to CERN, helping me debug code, and being my friend. I extend my thanks to the other members of our splendid analysis team including Rachel, Jingyu, and Redwan. Without their contributions, it simply would not be possible to tackle such an ambitious project.

I thank the tireless pixel experts and operations team, past and present: Atanu, Jory, and Klaas for introducing me to the group and igniting my interest, Danek for his willingness to explain all imaginable details of the pixels and to investigate any curiosity, Erik for his guidance as I took on leadership roles and for his detailed comments on sections of this thesis, and Giulia and Abbas for always being alongside me at Point 5 as we prepared for Run 3 and began operations.

I thank Liese van Zee, who encouraged my involvement in research when I was starting as an undergraduate at Indiana University - which somehow seems so long ago now!

I thank the wonderful cast of characters in the lunch gang at CERN for their advice, insights, rants, jokes, friendship, and stubborn dedication to having a meal together come hell or high water (or a global pandemic that relegates lunch to Zoom).

I dedicate my thesis to Lauren, Lia, Lily, and Violet. Finally, I especially thank both of my parents, who instilled in me the confidence to live a fulfilling life.

Chapter 1

Theoretical Motivation

The Standard Model is the theoretical structure supporting our current understanding of particle physics. The world as we typically experience it is mostly through atoms made of electrons, neutrons, and protons. However, as we probe to higher energies and different interactions, we see a richer array of fundamental particles that interact through fundamental forces.

The discovery of the Higgs boson is a testament to the ongoing success of the Standard Model. However, there are physics questions unanswered by the Standard Model, such as dark matter or a quantum theory of gravity. Supersymmetry and other beyond the Standard Model theories offer some possible explanations, and evidence for these theories can be searched for in collider experiments. In this chapter, the Standard Model is presented, including elementary particles, their interactions via fundamental forces, and the Higgs mechanism. Shortcomings of the Standard Model are presented as well as possible theoretical solutions, building from supersymmetry to the NMSSM and 2 Higgs doublet + singlet models. Lastly, the H → aa → $\mu\mu\tau\tau$ search is introduced, where a is an exotic pseudoscalar Higgs boson.

1.1 The Standard Model

Protons and neutrons are not indivisible particles but instead bound states of up quarks and down quarks. The electron and its associated neutrino are leptons. This structure is repeated at higher masses for a total of three generations. The middle generation is composed of the strange quark, charm quark, muon, and muon neutrino; the third generation contains the bottom quark, top quark, tau, and tau neutrino. The quarks and leptons have their own antiparticles with opposite charge. It is still to be determined whether neutrinos are their own antiparticles.

Particles interact through forces, which are mediated by gauge bosons. The electromagnetic force is transmitted through photons, the weak force is mediated by the Z boson and the $W^{\pm}$ boson, and the strong force is mediated by gluons. These particles are excitations of their respective fields - for example, the photon is an excitation of the electromagnetic field. The Higgs boson is an excitation of the Higgs field, which instead of transmitting a force, gives all particles their mass, with the possible exception of neutrinos. The particles of the Standard Model are shown in Figure 1.1.

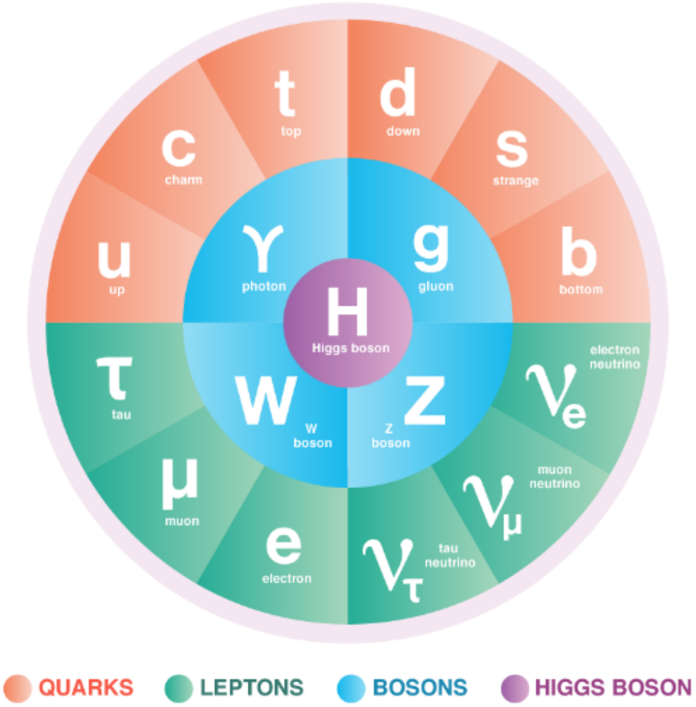

Figure 1.1: Particles of the Standard Model. Fermions are the fundamental building blocks of matter, and gauge bosons transmit the fundamental forces. The Higgs boson gives particles their mass [1].

Fermions are particles with half integer spin, and they follow Fermi-Dirac statistics and the Pauli exclusion principle. Bosons are particles with integer value spin and follow Bose-Einstein statistics. Hadrons are particles made of quarks, which are then categorized into mesons if they contain a quark and antiquark and baryons if they contain three quarks.

Due to varying coupling strengths, the lifetime of particles is greatly influenced by the force through which they decay. If a particle can decay multiple ways, it is likelier to decay via the strong interaction, then the electromagnetic interaction, then the weak interaction. Using the tau as an example, weak interactions mediated by the W boson are the only available decays, as depicted in Figure 1.2. Its lifetime is 2.9×10^{-13} s, or within a millimeter when traveling near the speed of light, so experimentalists using data from the CMS detector observe the decay products of the tau, not the particle itself. There are more examples of particles and their lifetimes in Figure 1.3.

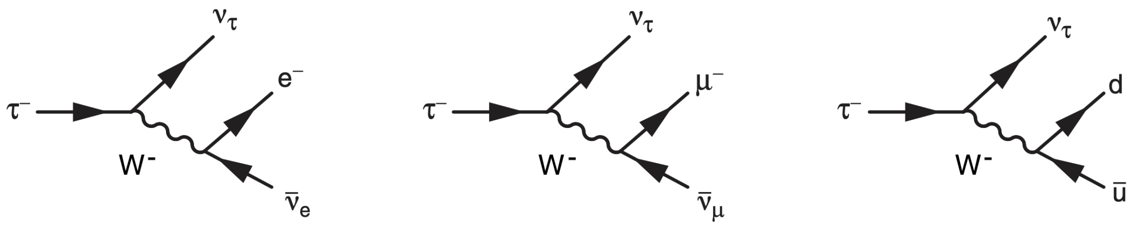

Figure 1.2: Taus can decay to electrons and muons as seen in the left and middle diagrams. The tau is massive enough to allow decays to quarks as well, as seen in the right diagram. The up and down quark form a charged pion. Note there is a neutrino present even in the hadronic decay to conserve lepton number.

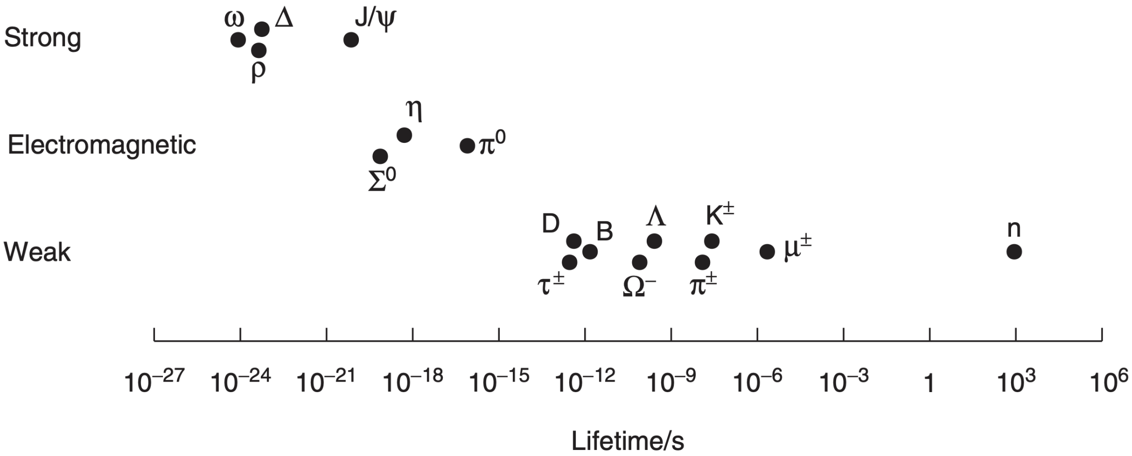

Figure 1.3: The variation of lifetimes of particles, which can be grouped by the type of interaction through which they decay. Note the range of the weak force, with taus decaying within collider detectors and muons traveling through the detector material[2].

Leptons of different generations could have different coupling strengths to the gauge bosons, which would also affect their lifetimes and decay behavior. Experimental evidence so far points to lepton universality, that is, that the couplings to the $W^{\pm}$ boson, Z boson, and photon are the same for electrons, muons, and taus, modulo small differences due to their masses.

Measuring the width of the Z boson allows the number of light neutrino flavors to be determined using Equation 1.1:

$$\Gamma_Z = 3\Gamma_{ll} + \Gamma_{hadrons} + N_\nu \Gamma_{\nu\nu} \tag{1.1}$$

where Γ_Z is the total decay width, Γ_{ll} is the width from the decays to leptons - due to lepton universality, they are the same for all generations, $\Gamma_{\mathrm{hadrons}}$ is the contribution from hadronic decays, and $N_{\nu\nu}$ is the number of flavors of light ($\nu_{\mathrm{mass}} < 1/2\ Z_{\mathrm{mass}}$) neutrinos. Experiments at LEP measured $\Gamma_{\nu\nu}$ to determine $N_{\nu\nu}$ and rule out the 2 or 4 family case, as shown in Figure 1.4.

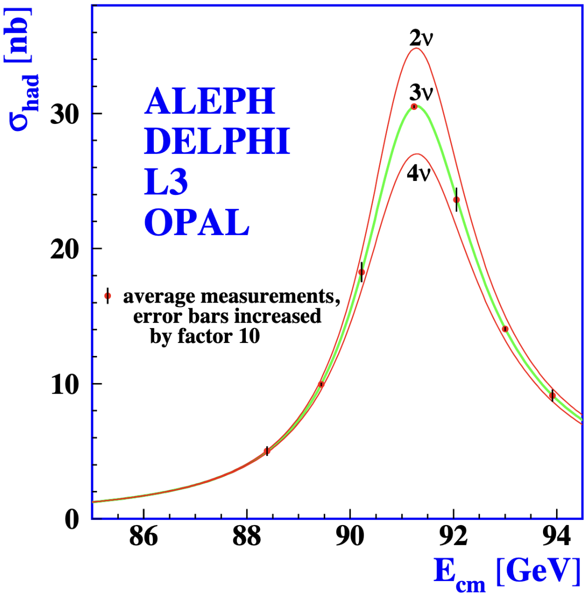

Figure 1.4: Measured hadronic cross section (data points) as a function of center-of-mass energy from the LEP detectors, ALEPH, DELPHI, L3, and OPAL, overlaid on the expected curves for different numbers of light neutrino flavors. [3].

1.1.1 Theoretical framework

We describe relativistic elementary particles using a theoretical framework based on systems of fields. From classical field theory is the concept of the Lagrangian L, the difference between the kinetic and potential energy of a system, which allows one to find the equations of motion describing that system. This classical concept can be extended to quantum field theory, where instead the Lagrangian density $\mathcal{L}$ is used. Here ϕ is a field and $\partial_\mu \phi$ is the corresponding derivative [32]:

$$\int L \, dt = \int \mathcal{L}(\phi, \partial_\mu \phi) \, d^4x \tag{1.2}$$

With the behavior of fields described by Lagrangian dynamics, another important ingredient of quantum mechanics is the wavefunction that contains information about measureable quantities of particles. The Klein-Gordon equation is a wave equation motivated by the need for a Lorentz-invariant relativistic formula of quantum mechanics:

$$(\partial^\mu \partial_\mu + m^2)\psi = 0 \tag{1.3}$$

Here, ψ is the wavefunction of the particle being acted on by the Lorentz-invariant scalar product, $\partial^\mu \partial_\mu$, and m is a mass term that satisfies the Einstein energy-momentum relationship [2]. However, the Klein-Gordon equation includes solutions with negative probability densities, a physical impossibility. The Dirac equation is a wave equation for spin-1/2 particles that solves this problem:

$$(i\gamma^\mu \partial_\mu - m)\psi = 0 \tag{1.4}$$

where the γ^μ refers to the four 4x4 matrices:

$$\gamma^0 = \begin{pmatrix} 1 & 0 & 0 & 0 \\ 0 & 1 & 0 & 0 \\ 0 & 0 & -1 & 0 \\ 0 & 0 & 0 & -1 \end{pmatrix}, \gamma^1 = \begin{pmatrix} 0 & 0 & 0 & 1 \\ 0 & 0 & 1 & 0 \\ 0 & -1 & 0 & 0 \\ -1 & 0 & 0 & 0 \end{pmatrix},$$

$$\gamma^2 = \begin{pmatrix} 0 & 0 & 0 & -i \\ 0 & 0 & i & 0 \\ 0 & i & 0 & 0 \\ -i & 0 & 0 & 0 \end{pmatrix}, \gamma^3 = \begin{pmatrix} 0 & 0 & 1 & 0 \\ 0 & 0 & 0 & -1 \\ -1 & 0 & 0 & 0 \\ 0 & 1 & 0 & 0 \end{pmatrix} \tag{1.5}$$

It is also useful to define γ^5:

$$\gamma^5 = i\gamma^0\gamma^1\gamma^2\gamma^3 \tag{1.6}$$

The wavefunction ψ that the Dirac equation acts on must have four degrees of freedom and is known as a Dirac spinor. Although it eliminates the negative probability densities, there are still solutions with negative energy. This can be interpreted as negative energy particles propagating backwards in time or antiparticle states with opposite charge that have positive energy and propagate forward in time. The existence of antiparticles was experimentally confirmed with the discovery of the positron, a positively-charged electron, by Anderson in 1933 [2].

1.1.2 Quantum electrodynamics

The photon is the propagator of the electromagnetic interaction. This interaction is described by quantum electrodynamics, the first quantum field theory. It is based on the idea of a photon being exchanged between charged particles. This is depicted by Feynman diagrams, with each vertex representing a factor of the fine structure constant $\sqrt{\alpha}$:

$$\alpha = \frac{e^2}{4\pi} \approx \frac{1}{137} \tag{1.7}$$

To evaluate the cross section of a process using perturbative expansion, all contributing Feynman diagrams containing up to a certain number of vertices are summed. In QED, as more vertices are present, their contributions diminish by factors of α, a small number, leading to a quick convergence of the perturbation series.

QED corresponds to a U(1) symmetry with the following Lagrangian:

$$\mathcal{L} = \bar{\psi}(i\gamma^\mu \partial_\mu - m_e)\psi - j^\mu A_\mu - \frac{1}{4}F_{\mu\nu}F^{\mu\nu} \tag{1.8}$$

where $j^\mu = -e\bar{\psi}\gamma^\mu\psi$ is the four-vector current, A_μ is the photon field, $F^{\mu\nu}$ is the field strength tensor, and $F^{\mu\nu}F_{\mu\nu}$ is the kinetic term for a massless spin-1 field. This describes the interaction among photons and electrons [2].

1.1.3 Quantum chromodynamics

Quantum chromodynamics (QCD) is the quantum field theory of the strong force. Quarks have quantum numbers corresponding to "color" of either red, green, or blue. Stable bound states of quarks are neutral in color - that is, equal mixes of red, green, and blue, equal mixes of antired, antigreen, and antiblue, or equal mixes of red and antired, blue and antiblue, and green and antigreen. This is represented by an $SU(3)$ color symmetry that is based on color confinement and asymptotic freedom [33].

Gluons themselves also carry color charge (unlike the analogous force carrier photon for QED, which has no electric charge). The strong force is unique because as the distance between the strongly interacting particles grows, the force increases as well. Because of this, in high energy processes like collisions at the Large Hadron Collider where particles are moving apart at high momenta, it is energetically favorable for more quarks to be created in an iterative process until the energies of the produced quarks and gluons form colorless bound bound states, hadrons. This process is known as hadronization. The spray of particles originating from quarks and gluons and coalescing into hadrons that form a collimated shower in particle detectors are reconstructed as jets. At the Large Hadron Collider, quarks, antiquarks, and gluons are produced in hard scatters and can initiate jets, or proton remnants from the colliding particles can also produce jets in the forward direction.

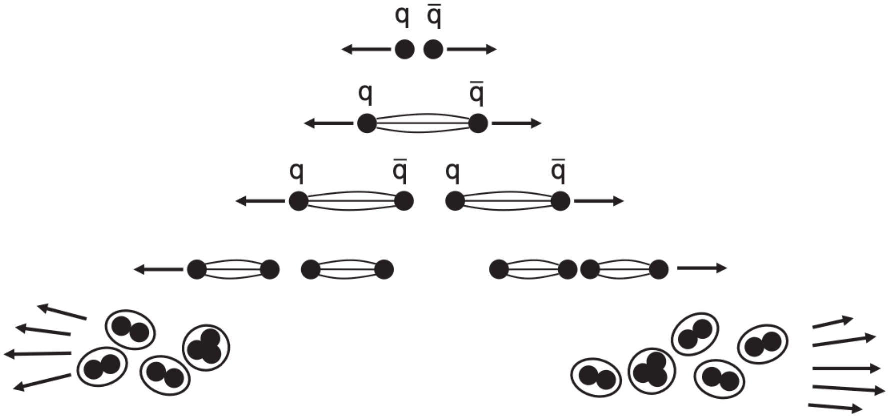

Figure 1.5: The process of hadronization. As quarks and gluons separate, more quarks and gluons are created until they group together to form colorless hadrons. This occurs on the scale of $\mathcal{O}$(fm).

1.1.4 The weak interaction and electroweak unification

The weak interaction is propagated by the weak gauge bosons: W^+, W^-, and Z. Spin-half particles have parity opposite to spin-half antiparticles, and vector bosons have negative parity. Parity is conserved in both QED and QCD interactions, but it is not conserved in weak interactions. This is a result of only left-handed chiral particle states and right-handed chiral antiparticle states interacting through the weak charged current, where chirality is the eigenvalue of the γ^5 operator. Weak interactions mediated by the the W^+ and W^- allow flavor changes and couple fermions of different charge [2].

The charged-current weak interaction is associated with an $SU(2)$ symmetry, a group whose generators can be written in terms of the 2x2 Pauli spin matrices. The associated wave function must have two components that differ by one unit of charge since they are connected through an interaction mediated by the W^+ and W^-. Because the charged-current weak interaction only couples to left-handed particles and right-handed antiparticles, right-handed particles and left-handed antiparticles are in weak isospin singlets with $I_W = 0$. This symmetry is denoted by $SU(2)_L$ [2].

There are three gauge fields W^1_μ, W^2_μ, W^3_μ, as required by $SU(2)$. The W^+ and W^- are linear combinations of these:

$$W_\mu^\pm = \frac{1}{\sqrt{2}}(W_\mu^1 \mp iW_\mu^2) \tag{1.9}$$

Meanwhile there is a neutral current W_μ^3 which does not couple to right-handed particles and left-handed antiparticles. The Z boson, which mediates the neutral current, couples to both right-handed and left-handed chiral states and mixes with the photon. It is feasible to represent the field corresponding to the photon, A_μ, and the field corresponding to the Z boson, Z_μ, as linear combinations of W_μ^3 and another gauge field, B_μ, which couples to weak hypercharge Y.

$$A_\mu = +B_\mu \cos\theta_W + W_\mu^{(3)} \sin\theta_W \tag{1.10}$$

$$Z_\mu = -B_\mu \sin\theta_W + W_\mu^{(3)} \cos\theta_W \tag{1.11}$$

The weak hypercharge has the same form as QED's U(1) symmetry. The weak mixing angle, θ_W, scales the relationship between the weak and electromagnetic couplings. This shows how the electromagnetic and weak forces can be unified [2]. After the value of the weak mixing angle was constrained by experiments with evidence of an interaction mediated by the Z boson, the $W^\pm$ and Z boson masses could be predicted to be in the ranges of 60 to 80 GeV and 75 to 92 GeV, respectively. Motivated by this, CERN's Super Proton Synchrotron was changed from a proton accelerator to a proton-antiproton collider. In 1982, W → eν was observed and in 1983, Z → ee and Z → $\mu\mu$ were observed. This allowed the first measurement of these bosons' masses to be made, which were indeed within the predicted range [34].

1.1.5 The Higgs mechanism

A real value scalar field ϕ has the Lagrangian density:

$$\mathcal{L} = \frac{1}{2}\partial_\mu\phi\partial^\mu\phi - V(\phi) \text{ with } V(\phi) = \frac{1}{2}\mu^2\phi^2 + \frac{1}{4}\lambda\phi^4 \tag{1.12}$$

The self-coupling λ must be positive to ensure the potential is bound from below. The μ^2 corresponds to the mass term. In the case where $\mu^2 > 0$, the minimum of the potential is when $\phi_0 = 0$. This corresponds to a spin-zero particle with a mass of μ. In the case where $\mu^2 < 0$, there are multiple values of ϕ that minimize the potential, $-v$ or $+v$, as shown in Figure 1.6. We call v the vacuum expectation value. This is a simple example of a symmetry being spontaneously broken [4].

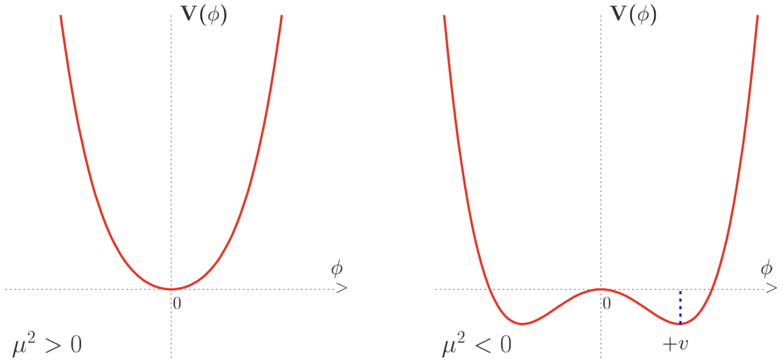

Figure 1.6: A potential with one minimum at $\phi = 0$ (left) and a potential with multiple minimia at $\phi \pm v$ (right) [4].

For a complex scalar field $\phi = \frac{1}{\sqrt{2}}(\phi_1 + i\phi_2)$, the Lagrangian density becomes:

$$\mathcal{L} = (\partial_\mu \phi)^*(\partial^\mu \phi) - \mu^2 \phi^* \phi - \lambda(\phi^* \phi)^2 \text{ with } \phi = \frac{1}{\sqrt{2}}(\phi_1 + i\phi_2) \tag{1.13}$$

This has the U(1) symmetry of QED. In the case of $\mu^2 < 0$, the minimum potential now has solutions

$$\phi_1^2 + \phi_2^2 = \frac{-\mu^2}{\lambda} = v^2 \tag{1.14}$$

The "choice" of v will break the global U(1) symmetry. This corresponds to a Lagrangian which describes a scalar particle with a mass of $m_H = \sqrt{2\lambda v}$ and massless Goldstone boson. Selecting the unitary gauge allows one to eliminate the unphysical mixing terms in the Lagrangian and the term corresponding to the massless Goldstone boson. Instead, that degree of freedom is absorbed by a longitudinal polarization state of a massive boson [4, 35].

The Higgs mechanism takes place within the Standard Model, which has a $SU(2)_\mathrm{L} \times U(1)_Y$ (where Y denotes hypercharge) local gauge symmetry from the electroweak interaction. In this case, the $U(1)$ local gauge invariance implies the existence of a new gauge field that can be labeled B_μ and spin-1 fields $W_\mu^{1,2,3}$ to match the electroweak theory presented in the previous section. One can then also derive the masses of the physical gauge bosons: $m_A = 0$, $m_W = \frac{1}{2} g_W v$, and $m_Z = \frac{1}{2} v \sqrt{g_W^2 + g'^2}$. Since the masses of the Z boson and $W^\pm$ boson depend on the vacuum expectation value of the Higgs field, we can say they acquire their mass through the electroweak symmetry breaking [2].

The success of this theory was confirmed with experimental evidence when the ATLAS and CMS experiments jointly announced the discovery of a Higgs boson-like particle with a mass of around 125 GeV, with the CMS result for H $\rightarrow \gamma\gamma$ shown in Figure 1.7 [5, 36].

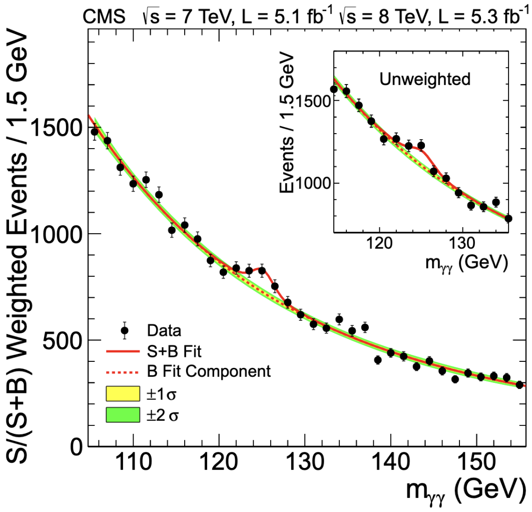

Figure 1.7: Diphoton invariant mass distribution showing an excess from the Higgs boson. This was combined with searches for the Higgs boson via other decay modes to find a combined significance of 5σ for a Higgs boson with a mass of 125.5 GeV [5].

1.2 Issues with the Standard Model

Although the Standard Model as outlined in the preceding sections has been experimentally confirmed with great precision, this mathematical framework to describe our physical world is not complete. There are several observed phenomena for which the Standard Model offers no explanation: the absence of a quantum theory of gravity, the existence of dark matter and dark energy in the cosmos, massive neutrinos, and the Higgs hierarchy problem.

Gravity is conspicuously absent from the Standard Model, though it is one of the four fundamental forces. Since the strength of gravity is incredibly weak compared to the other forces, it is difficult to test theories of gravity on microscopic scales. Without an explanation of how it fits into our understanding of particle physics, a major piece is missing from the Standard Model.

Measurements from astronomy and other particle physics experiments reveal gaps in our understanding of the particle content of the universe. The data from rotation curves of galaxies do not follow the predictions of massive galaxy dynamics according to the current understanding of gravity, if the observed luminous matter in galaxies is all that is present. This is one piece of evidence for dark matter, a non-luminous and significant contributor to galaxies' masses. The Standard Model does not offer a dark matter particle candidate [2].

Neutrinos are massless in the Standard Model, yet we know at least two flavors have (a very small) mass based on the observation of neutrino oscillations by the Super-Kamiokande Observatory. The neutrino oscillations do not set the absolute scale for neutrino masses but instead the difference in masses between neutrinos of different flavors [37].

The Higgs hierarchy problem refers to the apparent necessity of terms in the Lagrangian that cancel quantum corrections to the Higgs boson mass, Δm_H^2, and conspire to produce a Higgs boson at the electroweak scale.

$$\Delta m_H^2 = -\frac{|\lambda_f|^2}{8\pi^2}\Lambda_{UV}^2 + ... \tag{1.15}$$

The mass of the Higgs boson has corrections due to interactions with fermions, scalars, and gauge bosons, which are diagrammed in Figure 1.8. These contributions are proportional to Λ_{UV}, which sets the scale where new physics would cut off the Standard Model behavior. Without evidence of new physics at the electroweak scale that would introduce a relatively small Λ_{UV}, it seems there is some arbitrary tuning to cancel large contributions to the Higgs boson mass. Since boson masses are generated via the Higgs mechanism, the entire electroweak arena of the Standard Model is sensitive to this [6].

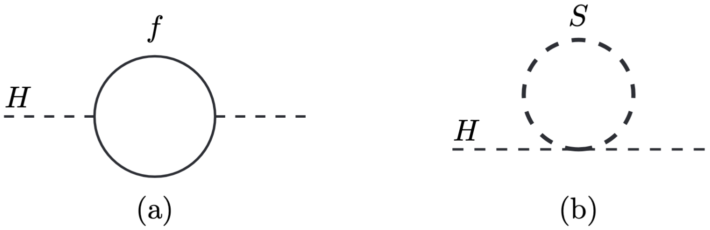

Figure 1.8: Diagrams for quantum corrections to the Higgs boson mass from fermions and scalars[6].

1.3 Supersymmetry and the Exotic Higgs sector

1.3.1 Minimal supersymmetry

Supersymmetry is an appealing solution to the hierarchy problem as it predicts a boson and fermion symmetry to cancel these loop correction terms [38]. It posits that every fundamental particle has a superpartner in a chiral or gauge supermultiplet. The fermions' supersymmetric partners are spin-0 particles known as sfermions (squarks and sleptons), and the bosons' supersymmetric partners are spin-1/2 particles known as gauginos (wino, bino, zino, photino, higgsino) [6]. If the symmetry was exact, superpartners would have the same mass as their standard counterparts. So why have we not discovered these superpartners? If supersymmetry exists, it must be a broken symmetry - this would give rise to supersymmetric partners of different (higher) masses [38].

Two Higgs doublets are necessary to preserve gauge anomaly cancellation and because only a Higgs doublet with hypercharge $Y = 1/2$ can have the Yukawa couplings necessary to give mass to charge $+2/3$ quarks and only a Higgs doublet with hypercharge $Y = -1/2$ can give mass to charge $-1/3$ quarks and leptons [6, 39]. Two Higgs doublet models (2HDM) including supersymmetric models are classified into four types based on the doublets' couplings to up-type quarks, down-type quarks, and leptons. The ratio of the vacuum expectation values of the two doublet fields is called $\tan\beta$. For Type I, the branching ratios of fermions are independent of $\tan\beta$. In Type II, decays to down type fermions are enhanced when $\tan\beta > 1$ and suppressed when $\tan\beta < 1$. Type III has branching ratios where decays to leptons are favored over decays to quarks when $\tan\beta > 1$ and quark decays favored over leptonic decays when $\tan\beta < 1$. Type IV can enhance decays to up-type quarks and leptons when tan $\beta > 1$ [40]. The types and their couplings are shown in Table 1.1.

	Type 1	Type 2	Type 3 (lepton-specific)	Type 4 (flipped)
Up-type quarks	Φ_2	Φ_2	Φ_2	Φ_2
Down-type quarks	Φ_2	Φ_1	Φ_2	Φ_1
Charged leptons	Φ_2	Φ_1	Φ_1	Φ_2

Table 1.1: Couplings of fermions to doublets in different types of 2HDM [26].

The superpotential of the minimal supersymmetric standard model (MSSM) is:

$$W_{\text{MSSM}} = \tilde{u}_R^* y_u (\tilde{Q}_\epsilon^T H_u) - \tilde{d}_R^* y_d (\tilde{Q}_\epsilon^T H_d) - \tilde{e}_R^* y_e (\tilde{L}_\epsilon^T H_d) + \mu (H_u^T \epsilon H_d) \tag{1.16}$$

where $\tilde{Q}$ is the squark supermultiplet, H_u and H_d are the Higgs doublets that give mass to up and down type fermions, $\tilde{e_R}$ and $\tilde{e_L}$ are the superpartners of the right handed and left handed parts of the electron Dirac field, $\tilde{u_R}$ and $\tilde{d_R}$ are the superpartners of up and down type quarks, and y_u, y_d, and y_e are dimensionless couplings. Some fine-tuning is necessary for canceling between the mass parameters and the μ parameters with $v \approx 246$ GeV with $\langle H_d^0 \rangle = v_d/\sqrt{2}$, $\langle H_u^0 \rangle = v_u/\sqrt{2}$, and $v^2 = v_u^2 + v_d^2$. This is a major shortcoming of the MSSM [27].

1.3.2 Next to minimal supersymmetric model

The next-to-minimal supersymmetric model (NMSSM) introduces an additional singlet to the Higgs sector and has the superpotential:

$$W_{\text{NMSSM}} = \hat{u} y_u (\tilde{Q}_\epsilon^T \hat{H}_u) - \tilde{d} y_d (\tilde{Q}_\epsilon^T \hat{H}_d) - \hat{e} y_e (\hat{L}_\epsilon^T \hat{H}_d) + \lambda \hat{S} (\hat{H}_u^T \epsilon \hat{H}_d) + \frac{1}{3} \kappa \hat{S}^3 \tag{1.17}$$

where λ and κ are dimensionless couplings, and the Higgs singlet is $\hat{S}$ which is composed of a complex spin-0 singlet S and a spin-1/2 singlino $\tilde{S}$ [27]. The full particle content is listed in Table 1.2. The Higgs doublet plus singlet models (2HDM+S) that correspond to the NMSSM fit into the Type II classification of 2HDM models.

Overall, the NMSSM has three CP-even scalars, denoted $H_{1,2,3}$, two CP-odd scalars, (pseudo)scalars, denoted $a_{1,2}$, and two charged scalars, denoted H^+ and H^-, to the Higgs

Table 1.2: NMSSM particle content. The Higgs supermultiplet $\hat{S}$ is not present in the MSSM but is in the NMSSM[27].

chiral supermultiplets		spin-0	spin-1/2	$SU_C(3)$	$SU_L(2)$	$U_Y(1)$
quark–squark	$\hat{Q}$	$\tilde{Q} = (\tilde{u}_L,\ \tilde{d}_L)^{\mathrm{T}}$	$Q = (u_L,\ d_L)^{\mathrm{T}}$	**3**	**2**	1/6
	$\hat{u}$	$\tilde{u}^*_R$	$u^\dagger_R$	**3**	**1**	−2/3
	$\hat{d}$	$\tilde{d}^*_R$	$d^\dagger_R$	**3**	**1**	1/3
lepton–slepton	$\hat{L}$	$\tilde{L} = (\tilde{\nu}_e,\ \tilde{e}_L)^{\mathrm{T}}$	$L = (\nu_e,\ e_L)^{\mathrm{T}}$	**1**	**2**	−1/2
	$\hat{e}$	$\tilde{e}^*_R$	$e^\dagger_R$	**1**	**1**	1
Higgs–Higgsino	$\hat{H}_u$	$H_u = (H^+_u,\ H^0_u)^{\mathrm{T}}$	$\tilde{H}_u = (\tilde{H}^+_u,\ \tilde{H}^0_u)^{\mathrm{T}}$	**1**	**2**	1/2
	$\hat{H}_d$	$H_d = (H^0_d,\ H^-_d)^{\mathrm{T}}$	$\tilde{H}_d = (\tilde{H}^0_d,\ \tilde{H}^-_d)^{\mathrm{T}}$	**1**	**2**	−1/2
	$\hat{S}$	S	$\tilde{S}$	**1**	**1**	0
gauge supermultiplets		spin-1/2	spin-1	$SU_C(3)$	$SU_L(2)$	$U_Y(1)$
gluon–gluino		$\tilde{g}$	g	**8**	**1**	0
W-boson–wino		$\tilde{W}^{\pm}, \tilde{W}^0$	$W^{\pm}, W^0$	**1**	**3**	0
B-boson–bino		$\tilde{B}^0$	B^0	**1**	**1**	0

sector. The lightest scalar, H_1, can have Standard Model-like behavior and correspond to the discovered Higgs boson. One of the CP-odd scalars is a superposition of two pseudoscalars, one from the MSSM doublet and one from the NMSSM singlet. This is what we will refer to as the light pseudoscalar Higgs boson, a. [41]. Two Higgs doublet models and the NMSSM can provide a pseudoscalar with an appreciable H→ aa branching fraction. In the general case of a 2HDM, which could contain only one pseudoscalar, this mass constraint requires some fine tuning - but in the context of the specific case of the NMSSM, which must contain two pseudoscalars, the branching fraction of H→aa can be small enough to fit with current observations without fine tuning and with $m_a < m_H/2$ [26].

1.3.3 Status on searches for exotic Higgs boson decays

For these models to be plausible, there must be some possibility of exotic decays in the Higgs boson's measured branching ratios. A meta-analysis of CMS results was performed on measured rates of H→ $\gamma\gamma$, H→ ZZ, H →WW, H → $\tau\tau$, H→ bb, and H→ $\mu\mu$. The couplings κ can be compared to what is expected from the Standard Model and fit the amount of invisible and so far undetected decays of the Higgs boson, as shown in Figure 1.9 [7]. Limits placed on the branching fractions still allow for exotic decays as shown in Figure

1.10, with up to a 47% branching ratio available to non-Standard Model decays at the 95% confidence level [7].

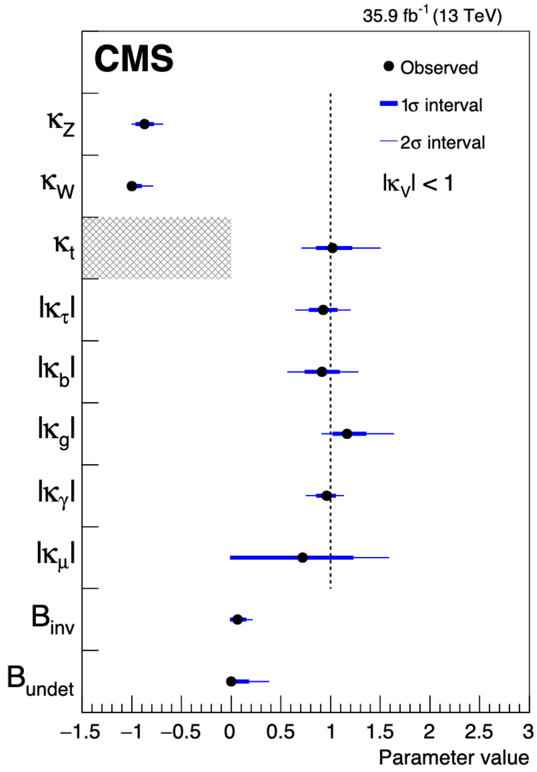

Figure 1.9: Fit where the B_{undet} and B_{inv} are free parameters with the constraint they must be positive. The κ values are the effective coupling modifiers to the Higgs boson [7].

Searches for phenomena predicted by the 2HDM+S and NMSSM models have been carried out at the LHC for the last several years. A previous iteration of the search presented in this dissertation was performed on 2016 data collected by the CMS detector, probing the H→ aa $\rightarrow \mu\mu\tau\tau$ channel, specifically with tau final states $\tau_\mu\tau_{had}$. The muons give a clean measurement of the light pseudoscalar Higgs boson mass, and the taus in the final state have a high branching ratio since it depends on lepton mass [26].

$$\frac{\Gamma(a \rightarrow \mu^+\mu^-)}{\Gamma(a \rightarrow \tau^+\tau^-)} = \frac{m_\mu^2\sqrt{1-(2m_\mu/m_a)^2}}{m_\tau^2\sqrt{1-(2m_\tau/m_a)^2}} \tag{1.18}$$

The null results were used to place limits in the context of 2HDM+S models using data collected by the CMS detector in 2016, as shown in Figure 1.11. Limits for a range of tan β values are shown in Figure 1.12.

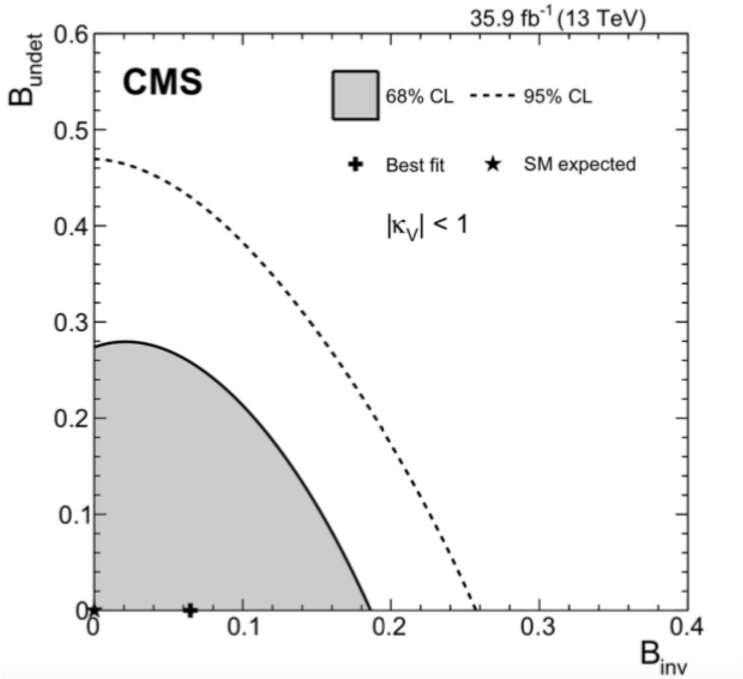

Figure 1.10: Constraints on the branching fractions of the Higgs boson in terms of undetected (non Standard Model) decay modes and invisible decay modes. The Standard Model predicts these branching fractions should be 0. $\mathcal{B}_{inv}$ and $\mathcal{B}_{undet}$ are free parameters with the constraint that they must be positive [7].

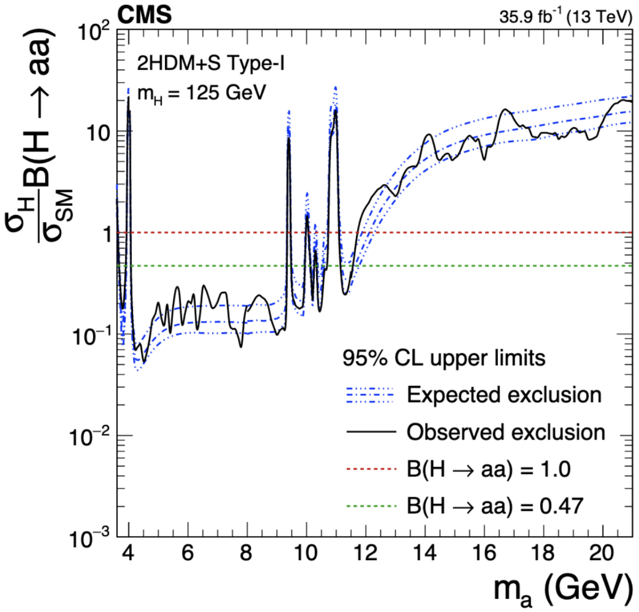

Figure 1.11: Observed and expected 95% CL limits on $\sigma_H\mathcal{B}(\mathrm{H}\to aa)$ using tan$\beta = 1.5$ for m$_H = 125$ GeV [8].

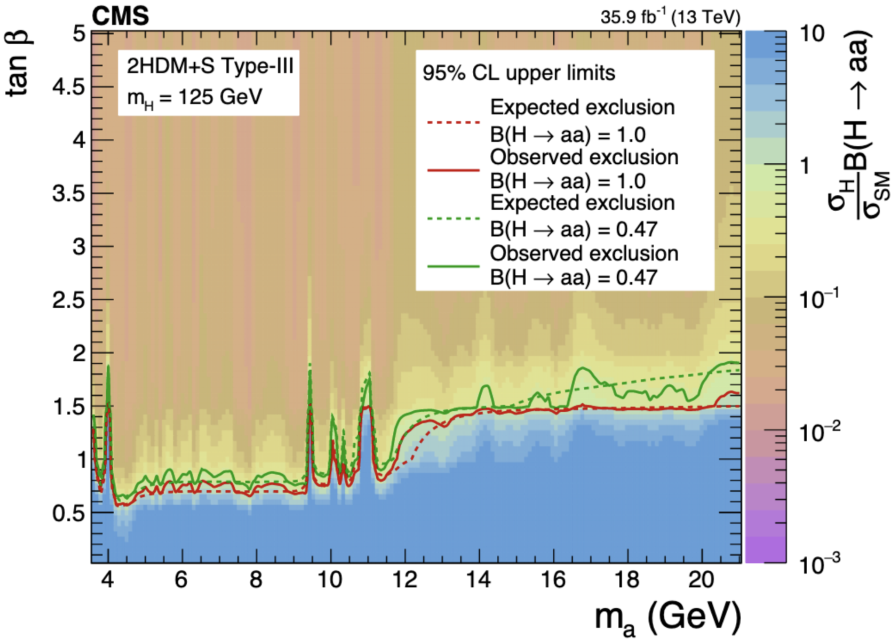

Figure 1.12: Observed and expected 95% CL limits n $\sigma_H \mathcal{B}$(H→ aa) for a range of tanβ and m$_a$ values [8].

Chapter 2

The Large Hadron Collider and the CMS Experiment

This chapter briefly introduces the Large Hadron Collider (LHC) and describes one of the general purpose physics detectors on the LHC beamline, the Compact Muon Solenoid (CMS). It describes the physics and operation of the different subdetectors of CMS: silicon tracker, calorimeters, muon system, magnet, trigger, data acquisition (DAQ), and event reconstruction methods.

2.1 The Large Hadron Collider

The Large Hadron Collider is a synchrotron and particle collider with a circumference of 26.7 km built underground in France and Switzerland. It was built in the tunnel that the LEP collider had been in. It uses a "two-in-one" super-conducting magnet design that was necessary due to space constraints in the tunnel and the need to have two separate rings with beams of particles with equal charge circulating in opposite directions. ATLAS and CMS are the two experiments probing general particle physics questions with the intent to collect as much luminosity as possible, ALICE is specialized for heavy ion collisions, and LHCb is designed for B hadron physics. The experiments are located at different points around the LHC ring with control rooms above ground near the detectors. The beams are crossed at interaction points in the center of each detector [10]. The LHC is part of the large accelerator complex at CERN, depicted in Figure 2.1.

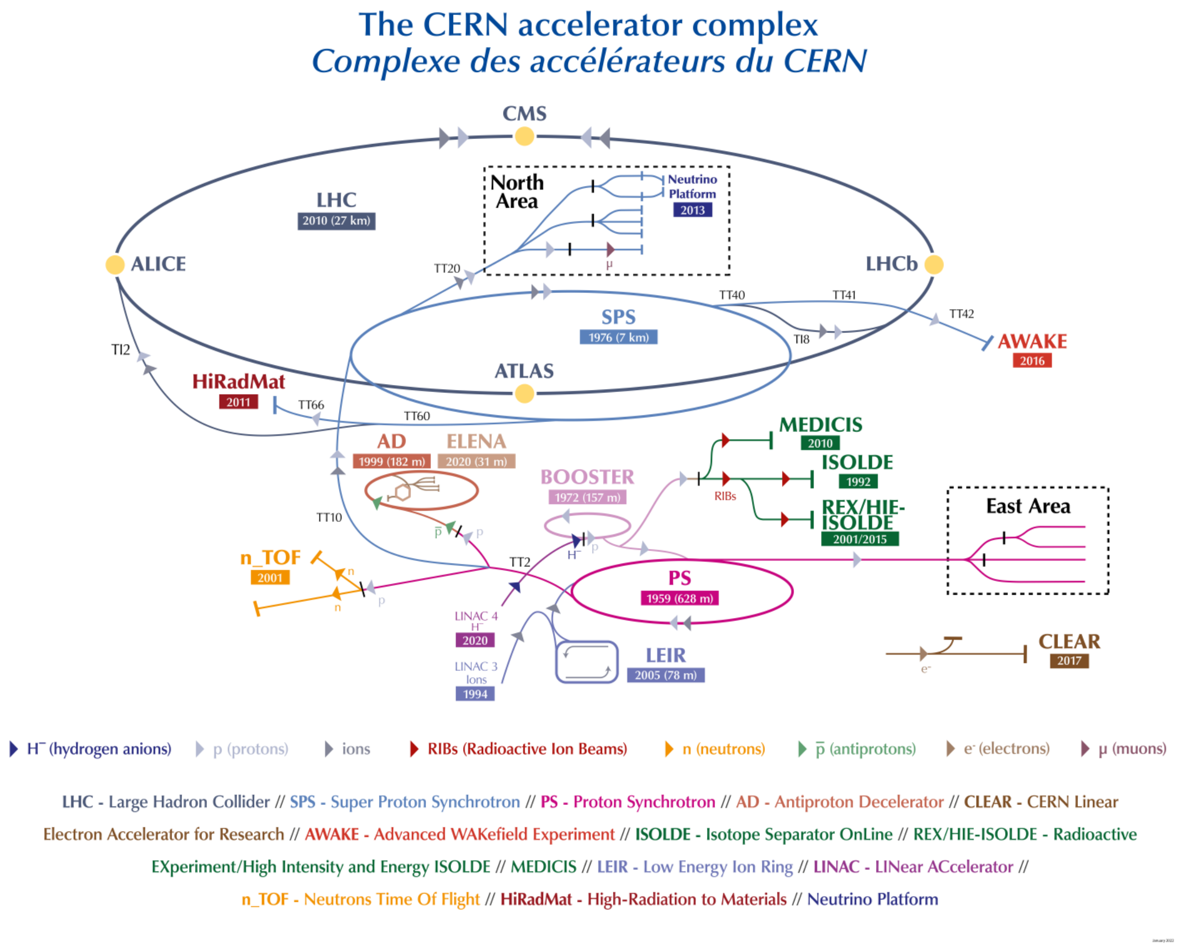

Figure 2.1: The CERN accelerator complex [9].

The LHC is a ring split into octants. ATLAS is located in Octant 1 with CMS directly across the ring in Octant 5. The other crossing points of the beams are in Octant 2 with the ALICE experiment and Octant 8 with the LHCb experiment. Beam 1 is injected in Octant 2, beam 2 is injected in Octant 8. Octants 3 and 7 have beam cleaning mechanisms, the radio frequency (RF) cavities are in Octant 4, and the beam dump is in Octant 6.

The LHC uses superconducting magnets cooled to temperatures below 2 K with superfluid helium and operate at fields above 8 T. There are 1232 main dipoles in the LHC ring. Within a cryodipole and moving radially outward from the beampipe, there is a beam screen, superconducting coils, non-magnetic collars, and iron yoke in the cold mass enclosed within superinsulation that also contains heat exchanging pipes. There are three separate vacuum systems in the LHC corresponding to the cryomagnets, insulation vacuum for helium distribution, and the beam vacuum. The beam vacuum system sections kept at room temperature have pressures in the range of 10^{-10} to 10^{-11} mbar. Pressures at cryogenic temperatures are quoted as gas densities normalized to hydrogen. For the specified 100 hour beam lifetime, interaction regions are in vacuum with densities below 10^{13} H_2 m^{-3} [10].

Once the beam quality has degraded over a fill, the beam is dumped. The beam dump mechanism also triggers in case of potential safety issues with the beam. Fast-pulsed kicker extraction magnets kick the beam horizontally, then DC septum magnets deflect the beam vertically. The beam is directed into 35 blocks of carbon in an "e" shape as shown in Figure 2.2. Carbon was selected selected for its high melting temperature and thermal shock resistance, and the carbon cores are surrounded by stainless steel with cooling water [10].

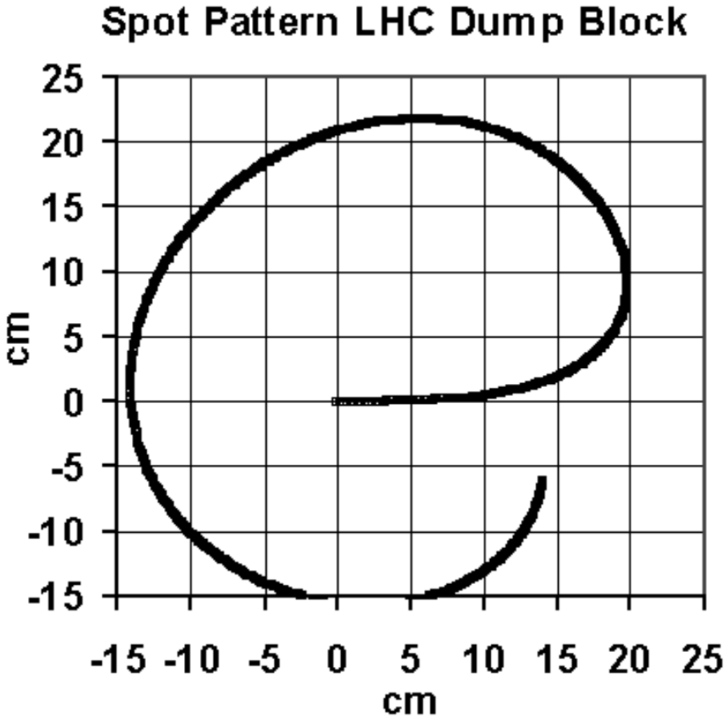

Figure 2.2: The beam spot shape on the absorber block [10].

2.2 CMS Experiment and Coordinate System

The CMS detector is located 100 m underground in Cessy, France. It is split into subdetectors tailored for different purposes - pixel and strip trackers, electromagnetic and hadronic calorimeters, and a system of muon detectors as shown in Figure 2.3. The CMS detector has a superconducting solenoid magnet creating a field of up to 3.8 T that bends the trajectories of charged particles. Because it is not feasible to store information from every collision, the triggering system of CMS determines which events have their information saved. A Level 1 Accept (L1Accept) signal prompts all subdetectors to read out the relevant data through the data acquisition (DAQ) system. The High Level Trigger then further discriminates among events. To analyze data from a collision event, a technique called Particle Flow is used for reconstruction. Run 2 refers to the luminosity delivered by the LHC over 2016, 2017, and 2018. The analysis in this dissertation uses Run 2 data, which refers to the data collected by CMS in the corresponding time period.

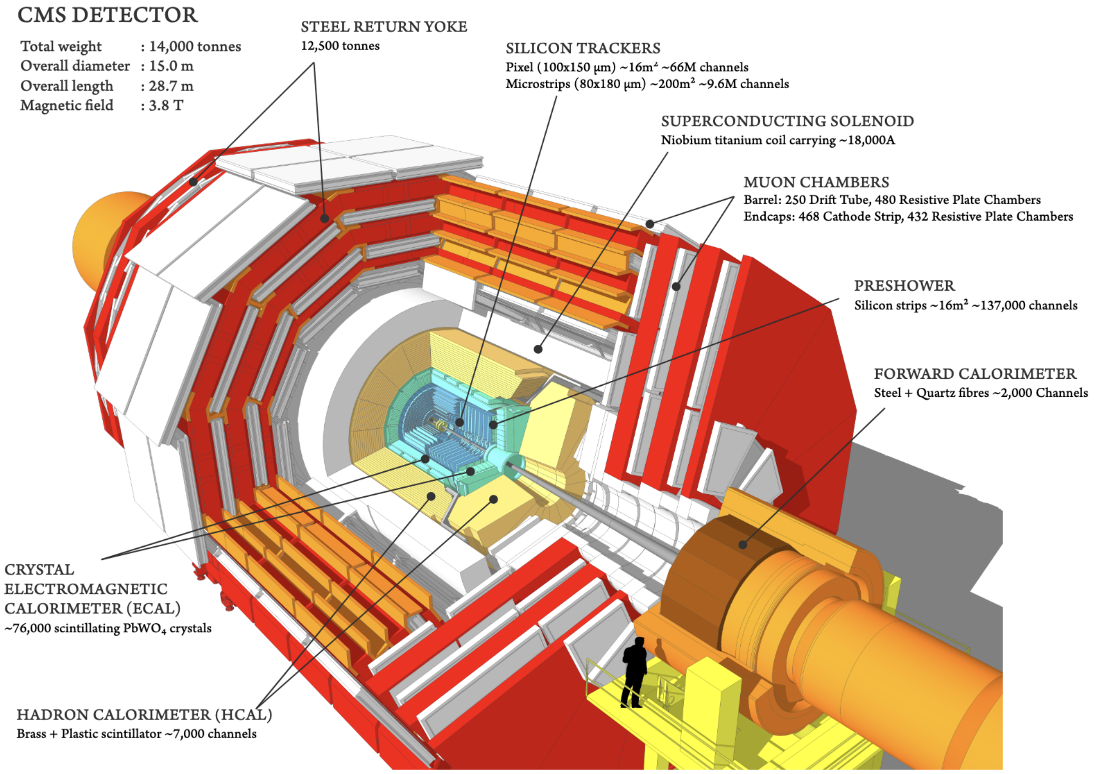

Figure 2.3: The CMS detector with its subdetectors [11].

The coordinate system of CMS is defined with positive y pointing vertically upwards, the positive x pointing radially inwards towards the center of the LHC ring, and with positive z pointing toward the Jura mountains parallel to the beam axis. The half of CMS with a positive x coordinate is sometimes referred to as the inner side of CMS and the half with a negative x coordinate as the outer side of CMS. Analogously, the positive z half of CMS is sometimes called the positive end and the negative z half the negative end. The azimuthal angle ϕ is in the x-y plane and the polar angle θ is measured from the z-axis. However, instead of θ, typically the polar angle is denoted with pseudorapidity $\eta = -\ln\tan(\theta/2)$ [19]. A common definition used in analyses for the angular separation of particles is $\Delta R = \sqrt{\Delta\eta^2 + \Delta\phi^2}$ with ϕ measured in radians. A diagram of CMS with the coordinate system overlaid is shown in Figure 2.4.

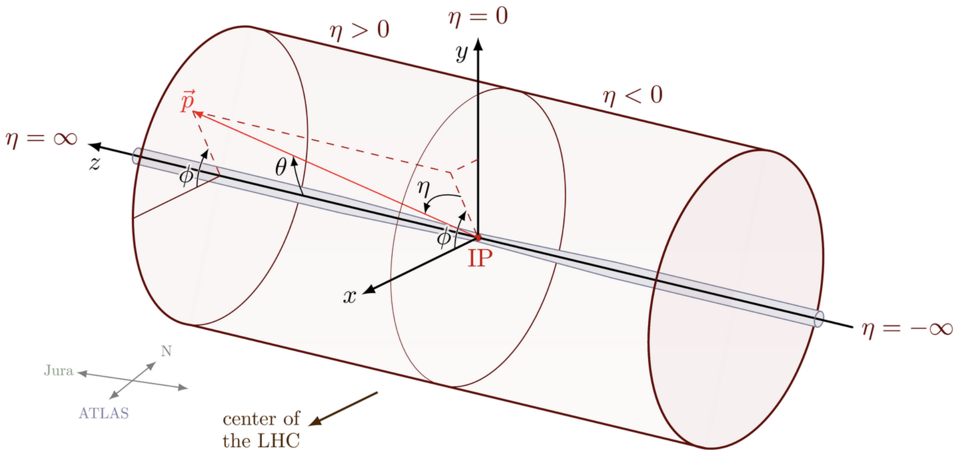

Figure 2.4: The coordinate system of CMS. IP stands for interaction point, denoting the center of the compact region where the beams collide. [12].

2.3 Silicon Tracking Detectors

All charged particles lose energy through ionization as they move through a material. For muons with energies below 100 GeV, ionization is the primary energy loss process, and for very low energy electrons, ionization is the primary energy loss before the critical energy is reached at which bremsstrahlung begins to dominate. The Bethe-Bloch equation characterizes ionization losses. Figure 2.5 shows the average energy loss of a charged particle moving through a medium as a function of momentum. There is a minimum around $\beta\gamma = 3$, which corresponds to the minimum ionizing particles (MIPs). The Landau distribution 2.6 show the relative probability as a function of the ratio of the signal charge to noise in silicon from muons [14].

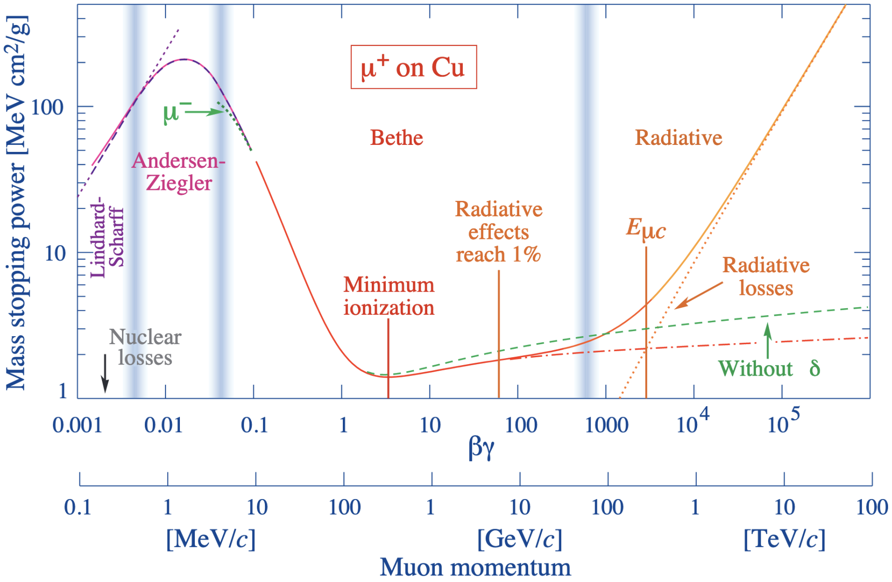

Figure 2.5: Different processes for energy loss from a muon traveling through a medium. This includes ionization and radiative losses [13].

As the ionizing particle moves through a medium, it transfers energy via photons to electrons in the material. Silicon is commonly chosen for as the material for tracking detectors due to its small band gap, high specific density, high carrier mobility, purity, rigidity, and popularity in industry which results in relatively low prices [42]. Silicon with a certain amount of doping with selected impurities has a useful level of semiconduction for use in charged particle tracking. When sufficient energy is transferred to electrons in the silicon's valence band, they overcome the bandgap to move into the conduction band. This results in a valence band hole and and an additional electron in the conduction band.

The number of electrons generated by an ionizing particle is five orders of magnitude smaller than the number of free charge carriers in a standard silicon sensor. To create a useful detector sensor, a reverse-biased pn-junction is created in the silicon by applying a

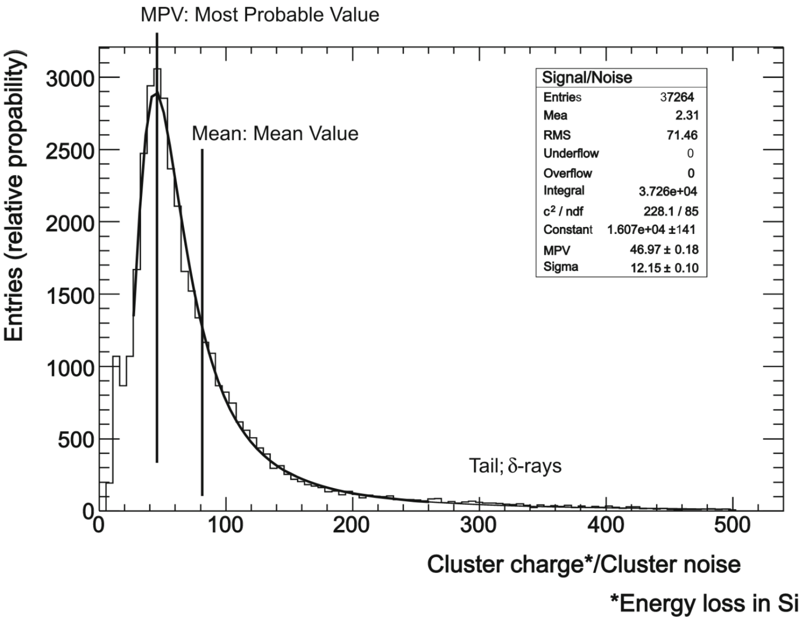

Figure 2.6: The Landau distribution showing signal/noise in 500 μm silicon in 3.8T field[14].

reverse bias voltage. This depletes the material, meaning there are no free charge carriers for recombination with these electrons. The electrons and the holes drift according to the electric field lines. There are different types of semiconductors: n-type has excess negative charges (electrons), while p-type has excess positive charges (holes).

The CMS silicon tracking system consists of the pixel tracker and the strip tracker. These subdetectors have the same operating principle, but a hit in the pixel detector provides precise position information in two dimensions, whereas a hit in the strip tracker provides precise position information in one dimension. In the pixel detector, a signal hit is created after an ionizing particle moves through the sensor and the generated electrons are collected by n^+ electrodes [16]. The induced charges are coupled to aluminum readout strips, which connect to a preamplifier, which in turn connects to an application specific integrated circuit (ASIC). Figure 2.7 shows an ionizing particle moving through a microstrip detector and examples of the signal shape are shown in Figure 2.8.

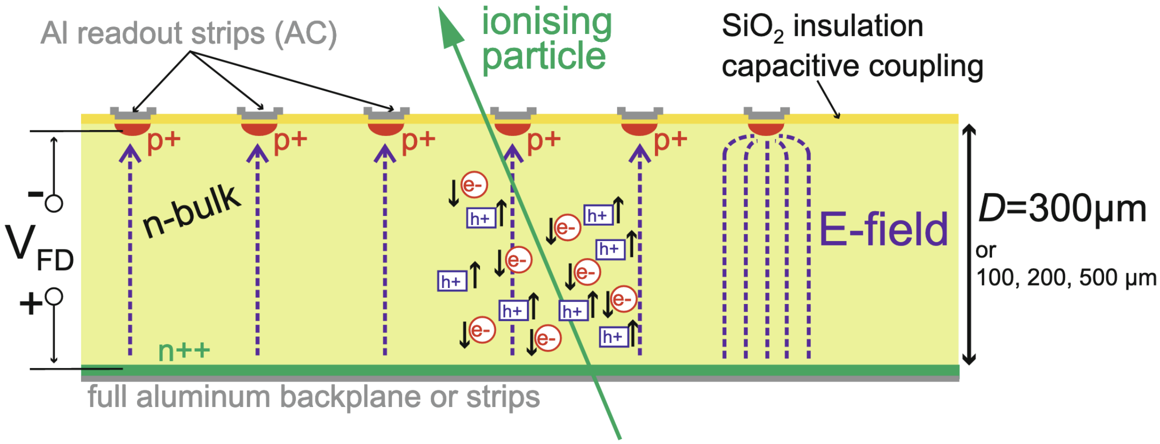

Figure 2.7: An ionizing particle moving through silicon leaves electrons and holes in its wake. They drift according to the electric field to readout strips that collect their charge [14].

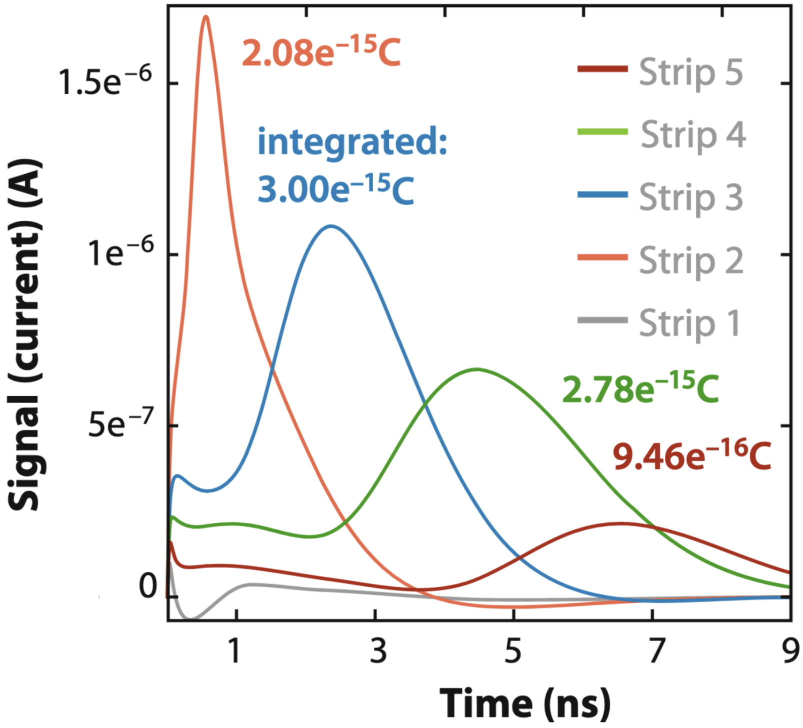

Figure 2.8: Signal development at different strips versus time for a charged particle[14].

2.4 Pixel Tracker

The pixel tracker is the innermost subdetector of the CMS detector. Along with the strip tracker, it traces out the path of charged particles bending under the influence of the magnet of CMS. It is made of the 1184 modules in Barrel Pixels (BPix) and 672 modules in Forward Pixels (FPix). Each module contains 66,560 silicon pixel sensors and 16 readout chips (ROCs). The individual pixels have an area of $100\mu m \times 150\mu m$ and sensor thickness of $285\mu m$. The modules are arranged into four cylindrical layers in BPix and three endcap disks on each end of CMS with inner and outer rings in FPix. Both BPix and FPix are split into quadrants called half cylinders with the names BmI, BmO, BpI, BpO based on whether they are the plus (p) or minus (m) end of CMS and whether they are on the inner (I) or outer side (O). The geometry of the detector is shown in Figure 2.9 and details about the positions and number of modules in each component are displayed in Table 2.1.

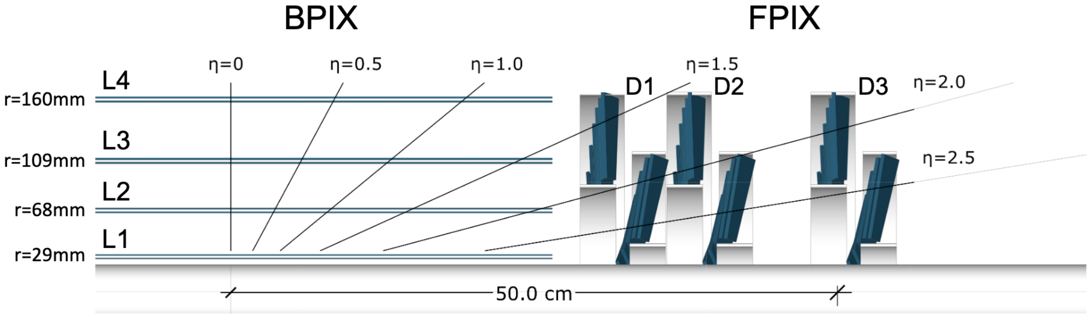

Figure 2.9: One quadrant in the r-z plane of the pixel detector. BPix has four layers that wrap around the beam axis and FPix has three disks that are perpendicular to the beam axis [15].

2.4.1 Effects of radiation

Radiation damage manifests in three main ways: increase of leakage current, increase of depletion voltage, and decrease of charge collection efficiency. The leakage current refers to the amount of current registered without any ionizing particles moving through the sensor. It increases as impurities introduce energy levels in the mid-gap region between the valence energy and conduction energy. The depletion voltage is the voltage necessary to apply across the silicon sensor to get rid of any free charge carriers. This quantity is changed as a result of the creation of charge defects in the sensor, creating new donors or acceptors and altering the effective charge. For n-type silicon, the aggregate effects first cause the depletion voltage to decrease, then subsequently increase. Electrons and

BPIX			
Layer	Radius [mm]	z position [mm]	Number of modules
L1	29	−270 to +270	96
L2	68	−270 to +270	224
L3	109	−270 to +270	352
L4	160	−270 to +270	512
FPIX			
Disk	Radius [mm]	z position [mm]	Number of modules
D1 inner ring	45–110	±338	88
D1 outer ring	96–161	±309	136
D2 inner ring	45–110	±413	88
D2 outer ring	96–161	±384	136
D3 inner ring	45–110	±508	88
D3 outer ring	96–161	±479	136

Table 2.1: Average radial and longitudinal positions of BPix layers and FPix rings [15].

holes that generate the current registered as a signal may become trapped in the material which leads to a decreased charge collection efficiency.

Each of these three effects dominates at different regimes - the leakage current is the main issue at $10^{14}\mathrm{n_{eq}/cm^2}$, the depletion voltage at $10^{15}\mathrm{n_{eq}/cm^2}$, and the charge collection efficiency due to trapping at $10^{16}\mathrm{n_{eq}/cm^2}$ [14]. At 3 cm from the interaction point, $\Phi = 3.0 \times 10^{15}\ \mathrm{n_{eq}/cm^2}$ is expected for an integrated luminosity of 500 $\mathrm{fb^{-1}}$, making leakage current and increasing depletion voltage the most relevant effects for the pixel tracker in CMS [16]. Sensors and readout chips were tested with radioactive sources and at beam tests to ensure their performance in terms of signal charge while still operating within the system's maximum bias voltage of 800 V. The hits rates for an instantaneous luminosity of $2.0 \times 10^{34}\mathrm{cm^{-2}s^{-1}}$ and fluence and radiation dose for 300 $\mathrm{fb^{-1}}$ for BPix layer 1 and 500 $\mathrm{fb^{-1}}$ for the rest of the detector are shown in Table 2.2.

2.4.2 Sensors

Sensors of $\mathrm{n^+}$-in-n type have free electrons as the dominant propagators of the current. This was chosen due to electrons' high mobility compared to holes. They also have a larger

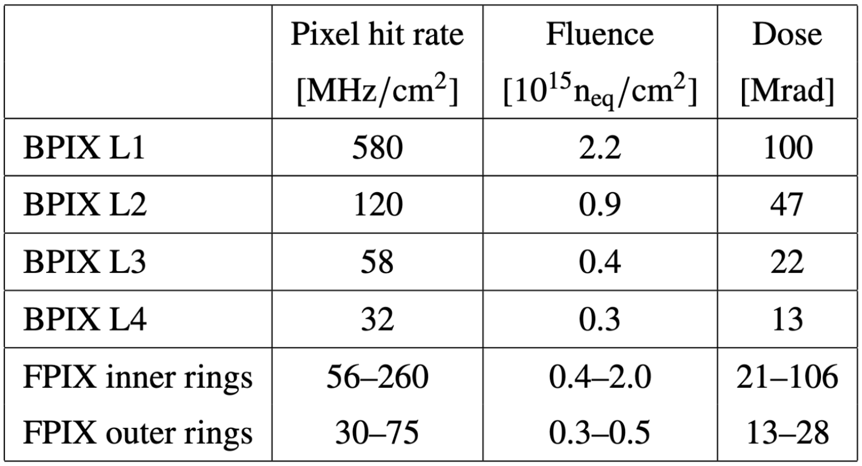

	Pixel hit rate [MHz/cm^2]	Fluence [10^{15}n$_{eq}$/cm^2]	Dose [Mrad]
BPIX L1	580	2.2	100
BPIX L2	120	0.9	47
BPIX L3	58	0.4	22
BPIX L4	32	0.3	13
FPIX inner rings	56–260	0.4–2.0	21–106
FPIX outer rings	30–75	0.3–0.5	13–28

Table 2.2: Expected hit rates, fluence, and radiation dose for BPix layers and FPix rings [15].

Lorentz drift in the magnetic field of CMS than holes, which improves spatial resolution because there is a higher chance the charges will be shared between multiple pixels. This design also has the benefit of allowing underdepleted operation because the electric field will be strongest near the DC-coupled electrodes used for charge collection. These sensors are created with double-sided processing with both sides of the sensors having photolithographic steps. Guard rings allow sensor edges to kept at ground potential, which means there is no need for HV protection for the ROCs [16].

2.4.3 ASICs

Readout chips are bump bonded to the silicon sensors and glued to the base strips of the modules. They are connected to the printed circuit board high density interconnect (HDI) with wirebonds. The ROCs used in BPix layer 1 are PROC600, which were designed to handle rates up to 600MHz/cm^2, and BPix layers 2, 3, 4, and FPix use PSI46dig, which can tolerate rates up to 150MHz/cm^2. These ROCs have pulse-height readout, and the 52 by 80 pixels are organized into 26 “double columns” of 2 by 80 pixels. The chip has an analog-to-digital converter (ADC) to output digital data. The external LHC clock is used by a Phase Locked Loop (PLL) circuit to distribute 80 and 160 MHz clocks to the ROCs. There is a trigger latency of 4.15 μs, during which pixel data must be stored until an L1Accept is received or not. The PROC600 allows the acquisition of hits into the buffer during readout induced by an L1Accept. Improvements to combat time walk effects have lowered the minimum needed operation threshold of the ROC from the previous version with 3400 electrons to 1700 electrons [17].

The readout of the ROCs is controlled by an ASIC called the Token Bit Manager (TBM). The TBM receives clock, L1Accept, fast commands, and configuration data from the Pixel FECs. When an L1Accept is received by the TBM, it passes a token to its ROCs and waits for it to return, adding a header and trailer to the data. The actual data packet received by the backend consists of a TBM header, ROC header, pixel level information like column and row address of hits and hit amplitudes, and a TBM trailer that may include error codes [17].

2.4.4 Modules

Each module has sensors bump-bonded to 16 ROCs and has a total active area of 16.2 mm by 64.8 mm. The HDI distributes power to the ROCs and has the decoupling capacitors, and TBMs are glued and wire-bonded to the HDIs. Layer 1 modules have two TBMs and other modules and a single TBM. Figure 2.10 shows the different components of a module.

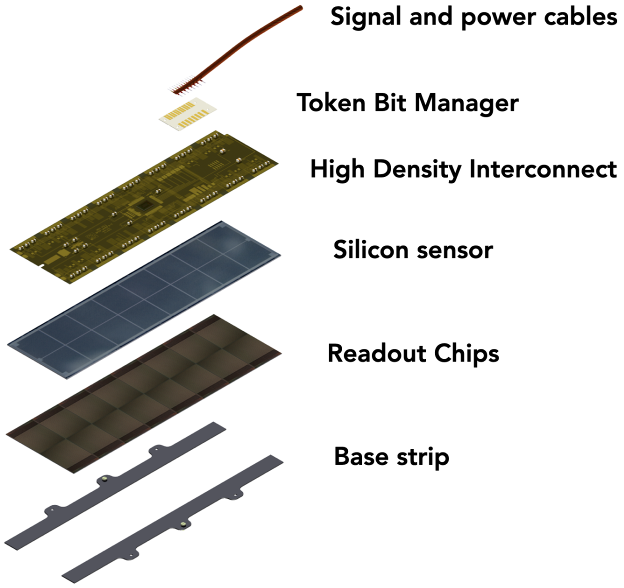

Figure 2.10: An exploded view of a pixel module [16].

2.4.5 Optical components

The data from the pixel detector is transmitted through optical signals to the Front End Drivers located in the counting room outside the experimental cavern. The electronics located within the service cylinder are referred to as portcards and come in two types: Pixel Opto Hybrid (POH) and Digital Opto Hybrid (DOH). The POHs receive electrical signals from the TBMs and send them to the Front End Drivers as optical signals, and the DOHs communicate between Pixel Front End Controllers and Tracker Front End Controllers and the detector [17].

2.4.6 Backend electronics

The pixel tracker's data acquisition system is a set of μTCA crates, each with a different purpose. It includes Tracker Front End Controllers, Pixel Front End Controllers, Front End Drivers, and Advanced Mezzanine Card 13s. There are a total of 1696 optical read out links for BPix and 672 for FPix. The Tracker Front End Controllers (TkFECs) program direct current to direct current (DCDC) converters, which are part of the pixel tracker's powering system. TkFECs each use a central control unit (CCU) with Inter-Integrated Circuit protocol and a Parallel Interface adapter to communicate with DCDC converters and Delay25 chips. There are 8 TkFECs, one for each half cylinder of BPix and one for each half cylinder of FPix [17].

The Pixel Front End Controllers (PxFECs) distribute the clock, trigger, and fast commands to detector modules. They also program DAC registers of ROCs and TBMs. A Trigger Timing and Control (TTC) clock is produced from the 40MHz LHC input clock sent to a Phase Lock Loop. TTC information including the clock and L1Accept and pixel-specific information like ROC and TBM reset commands are then encoded in the TTC clock. Each PxFEC is connected to eight DOHs. There are 16 PxFECs, 8 for BPix and 8 for FPix.

The Front End Drivers (FEDs) are used in all subdetectors as the gatekeeper between detector data and central CMS DAQ. They have firmware with two functions - to decode the incoming data from the detector and to build the events to conform to a universal CMS format. During the decode step, the FED firmware detects the presence of TBM headers and ROC headers and checks that the expected number of ROC headers arrived. The FEDs have their own error counters as well. The build and readout step merges the data from the decode step and transmits it to CMS Central DAQ via a Front End Readout Optical Link-40 (FEROL). It also communicates the Trigger Throttling System (TTS) state of each FED, which can be ready, busy, or out-of-sync. This corresponds to the status of the FIFOs and whether or not that FED is available to receive any new L1Accepts. A resynchronization command can be issued from the Trigger and Timing Control and Distribution System (TCDS) system to empty FIFOs of all FEDs.

The FED also receives the clock, triggers, and fast commands (TTC) from the CMS Trigger control and Distribution System (TCDS). This is mediated by the advanced mezzanine card in slot 13, the AMC13. The AMC13 takes the signal from the FEDs and passes them to the TCDS. The TTS signal determines whether FEDs can accept triggers or not and if event counters are synchronized - whether the FEDs are accepting or blocking L1Accepts from CMS. There are 108 FEDs for the pixel tracker.

The Advanced Mezzanine Card 13s (AMC13s) propagate signals to FECs which distributed them to sensor modules via portcards. They are converted from optical to electric signals by DOH, then decoded by Tracker Phase Locked Loop and Quartz Phase Locked Loop chips. Signals delivered via Delay25 chips have a granularity of 0.5 ns. There are 8 AMC13s for BPix and 4 AMC13s for FPix. Figure 2.11 depicts the complex chain of communication from sensor module to readout to central CMS DAQ [17].

2.4.7 Software

Pixel online software is a software collection written in C++ and used to control and communicate with the detector. So-called supervisors provide a graphical user interface on a webserver and perform state transitions to control pixel DAQ. There are different supervisors: PixelSupervisor, PixelDCSFSMInterface, PixelAMC13Supervisor, PixelFEDSupervisor, PixelFECSupervisor, PixelTKFECSupervisor, and PixelTCDSSupervisor that control hardware or establish connection to other services [17]. Parameters in the code can be changed, such as how many attempts a FED makes to recover a module during datataking before "blacklisting" the module and temporarily removing it from the list

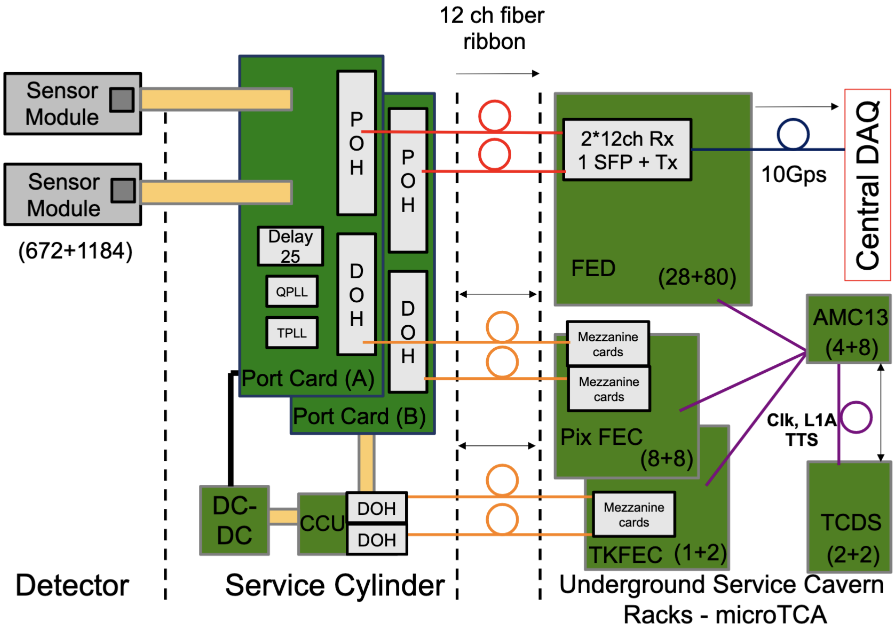

Figure 2.11: Pixel DAQ system [17].

to be read out. There is also an adjustable threshold for number of blacklisted modules before triggering a Soft Error Recovery. Soft Error Recoveries cost stable beam time but also can regain the function of modules that needed to be reprogrammed, so this threshold may be adjusted every few days, weeks, or months depending on the detector performance stability.

2.4.8 Powering

The pixel detector requires low voltages for the readout electronics, bias voltages for the silicon sensors, and an additional low voltage for electronics on the supply tube. The PSI46 chip ROC needs 1.6 V for the analog component and 2.2 V for the digital component (shared with TBM), and the supply tube needs 2.5 V for the CCU ASICs, POHs, and PLL chips. There are two power racks in the experimental cavern that have 32 A4603 CAEN power supplies for BPix and 24 A4603 CAEN power supplies for FPix. The direct current to direct current (DCDC) converters take an input voltage of 9-10 V and step it down to an output voltage of 2.4-2.5 V or 3.0-3.3 V. The powering scheme is shown in Figure 2.12.

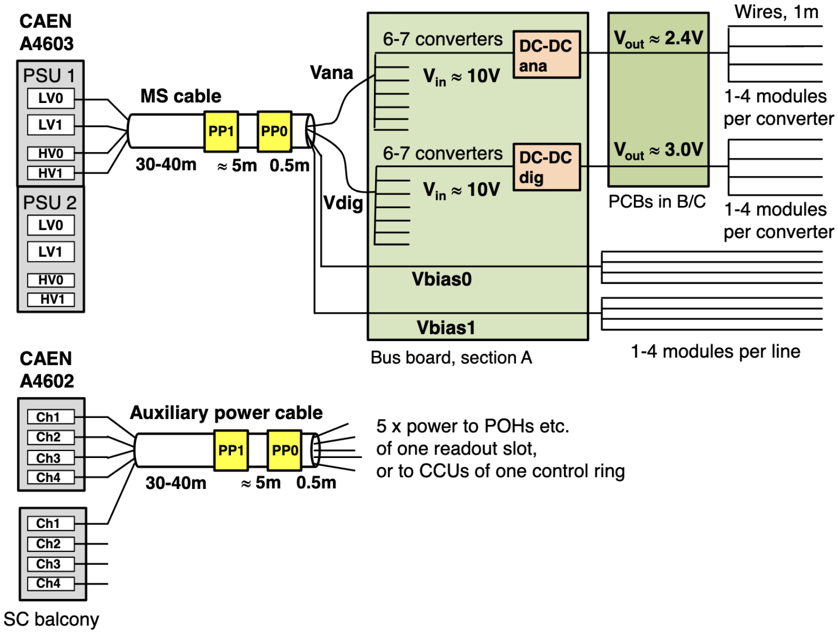

Figure 2.12: The powering scheme of the pixel tracker[16] .

2.4.9 Contribution to tracking

The hits from pixels are used as track seeds that are used by tracking algorithms to reconstruct the trajectories of charged particles through the detector. The tracks are used for reconstruction offline as well as the fast tracking online for HLT for primary vertex reconstruction, electron and photon identification, tau identification, and b-tagging. The pixel detector has four-hit coverage, meaning the track seeds come from four hits, which has a lower fake rate than track reconstruction requiring a fewer number of seeds. Tracking efficiency and track fake rate are important values for tracking performance and are quoted below, taken from [16]:

$$\text{Tracking efficiency} = \frac{\text{Num. of truth tracks matched to reconstructed tracks}}{\text{Num. of truth tracks}} \tag{2.1}$$

$$\text{Track fake rate} = \frac{\text{Num. of reconstructed tracks not matched to reconstructed tracks}}{\text{Num. of reconstructed tracks}} \tag{2.2}$$

The efficiency and fake rates are plotted in Figure 2.13. The fourth layer of BPix helps offset the negative impact of pile up on fake rates and also compensates for some of the degradation of the innermost layer of the strip tracker [16].

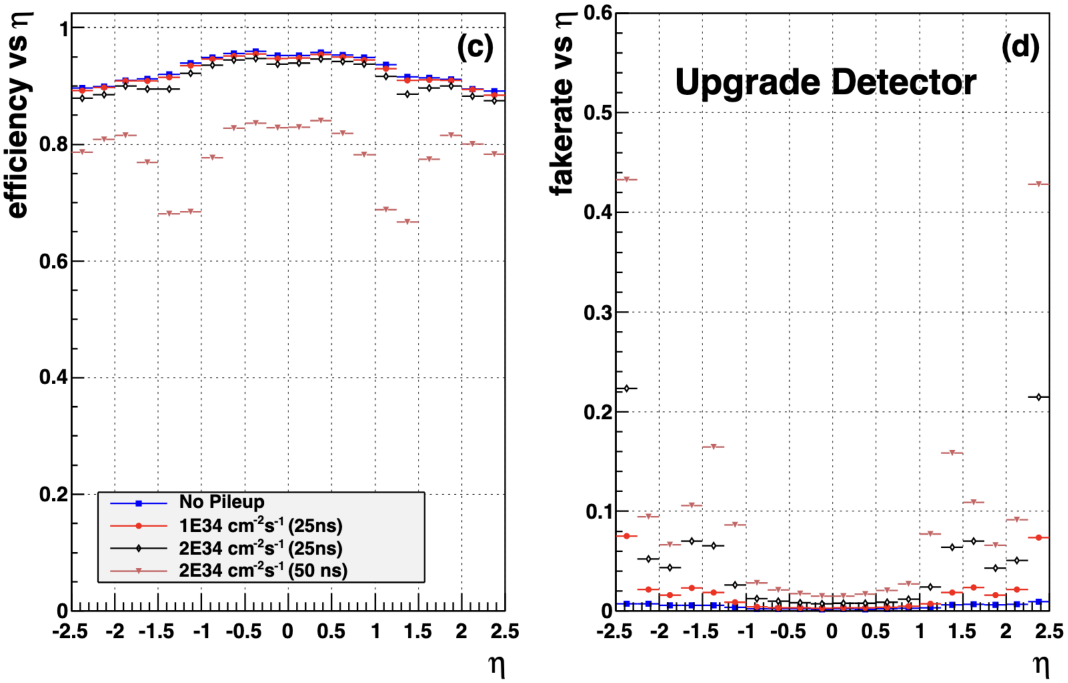

Figure 2.13: Efficiency and fake rate as a function of η based on $t\bar{t}$ samples requiring $p_T > 0.9$ GeV for both reconstructed and truth tracks. Here "Upgrade Detector" refers to the pixel detector used in 2017 and 2018 [16].

2.5 Strip tracker

Located at radii beyond the the pixel tracker, the silicon strip tracker contains 9.3 million silicon strips with a total of 198 m^2 of active detector area. A quadrant of the strip tracker is depicted in Figure 2.14. There are two cylindrical sections wrapping around the beam axis, the first of which is Tracker Inner Barrel (TIB), with four layers. The TIB provides single point resolution of 24 μm from its two inner layers and a resolution of 35 μm in its outer two layers, and is shown in Figure 2.15. The Tracker Inner Disk (TID) consists of three disks on both the plus and minus ends of CMS. Together TID and TIB can provide four hits with r-ϕ information. The second cylindrical section is Tracker Outer Barrel (TOB), with six layers that have single point resolution of 53 μm. Finally, there are the large endcaps, Tracker Endcap (TEC), with nine disks on both plus and minus ends of CMS and that provide ϕ measurements. The thickness of the silicon sensors in these strips is 320 μm for TIB, TID, and the inner four rings of TEC, and 500 μm in TOB and the outer three rings of TEC [43]. Information about the geometry of the strip tracker is summarized in Table 2.3.

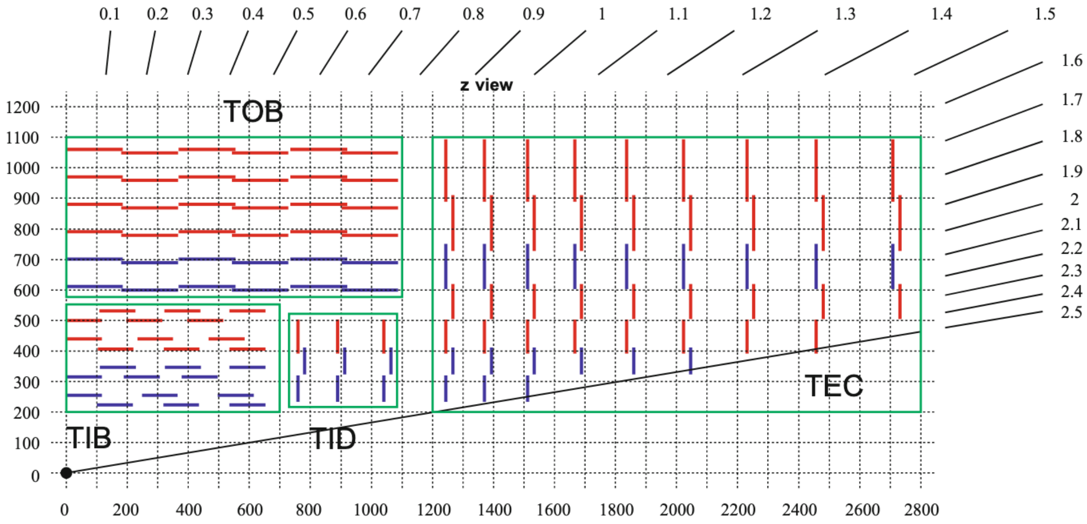

Figure 2.14: Geometry of the strip tracker with subsections labeled. Double-sided modules are shown in blue, and single-sided modules are shown in red. Dimensions in the r-z plane are in mm and η values are shown around the periphery of the figure [14].

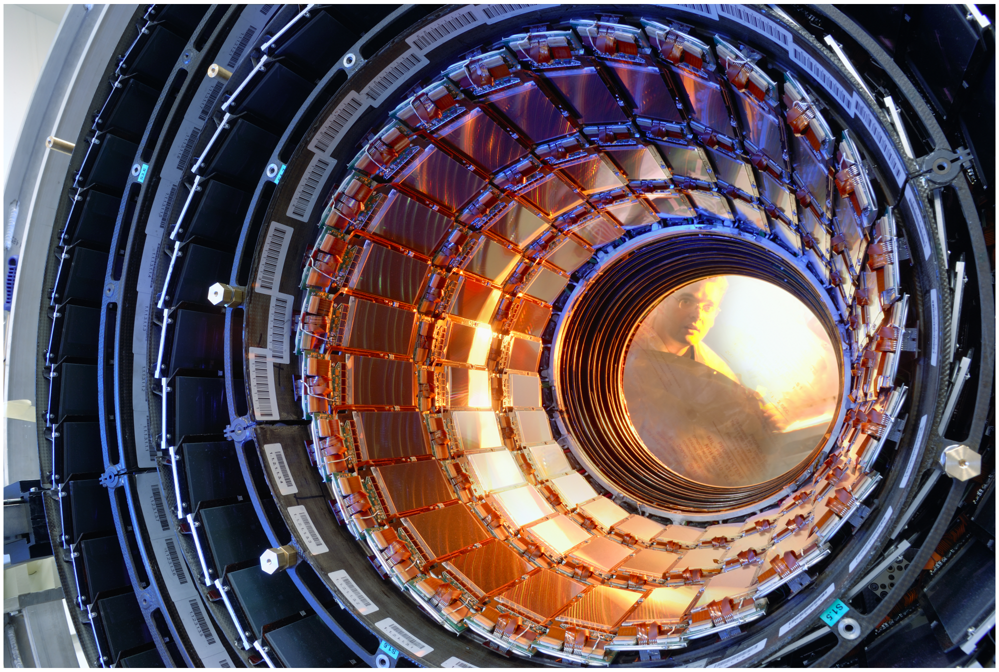

Figure 2.15: Tracker Inner Barrel [18].

Component	Form	Extent (cm)	Pitch (μm)
Tracker Inner Barrel (TIB)	4 layers	$25.5 < \|r\| < 49.8$	80: layers 1, 2 120: layers 3, 4
Tracker Inner Disk (TID)	3 disks	$70 < \|z\| < 105$	113 to 205
Tracker Outer Barrel (TOB)	6 layers	$60.8 < \|r\| < 108.0$	183: layers 1-4 122: layers 5,6
Tracker Endcap Disk (TEC)	9 disks	$22.5 < \|r\| < 113.5$, $124 < \|z\| < 282$	113 to 205

Table 2.3: Information about strip tracker components. The pitch refers to the distance between individual strips.

The TOB and TIB's inner two layers have double sided modules with an offset angle of 100 mrads. The second measurement allows determination of the second coordinate, z. The double-sided modules are also present in the first two rings of TID and rings 1, 2, and 5 of TED, which allow determination of radius. Altogether, the strip tracker covers $|\eta| < 2.4$ with at least nine hits, and four of those hits have two-dimensional information.

Tracker strips utilize p-on-n type silicon micro-strip sensors. In total there are 24,244 sensors in the strip tracker system, organized into 15,148 modules that have either one 320 μm or two 500 μm thick silicon sensors that are electrically connected with wire bonds. The APV25 is an ASIC used to read out the hits in the tracker strips when a L1Accept from central DAQ is received. Each APV25 has 128 readout channels with an preamplifier, shaper, and pipeline that can store the data in its buffer for up to 4 μs. Two APV25 chips signals are multiplexed into a single optical channel by an APVMUX chip. This stream is then sent on through optical links as the analog opto hybrid (AOH) converts the electrical signal to an optical one and transmits data to the FED. There are 96 optical fibers connected to each of the 450 FEDs in the strip tracker system. FPGAs are used to apply pedestal corrections and find clusters before the data is transmitted to central DAQ.

FECs are used to program the detector and distribute clock and trigger signals coming from the global Timing, Trigger, and Command system of CMS via Phase Locked Loop

(PLL) chips of the Communication and Control Units (CCUs). In total there are 356 CCUs. Because these need to transmit data both to and from the detector, digital opto-hybrids (DOH) can convert optical signal to electrical signals and also the reverse process [19]. Hybrids are used to power the chips, connect the lines among chips, and aid in cooling the system. Hybrids each contain 4 or 6 APV25 chips, an APVMUX chip, a PLL chip, and a Detector Control Unit (DCU) chip. Hybrid low voltages, sensor leakage current, and temperatures are monitored by DCUs. The connections are depicted in Figure 2.16.

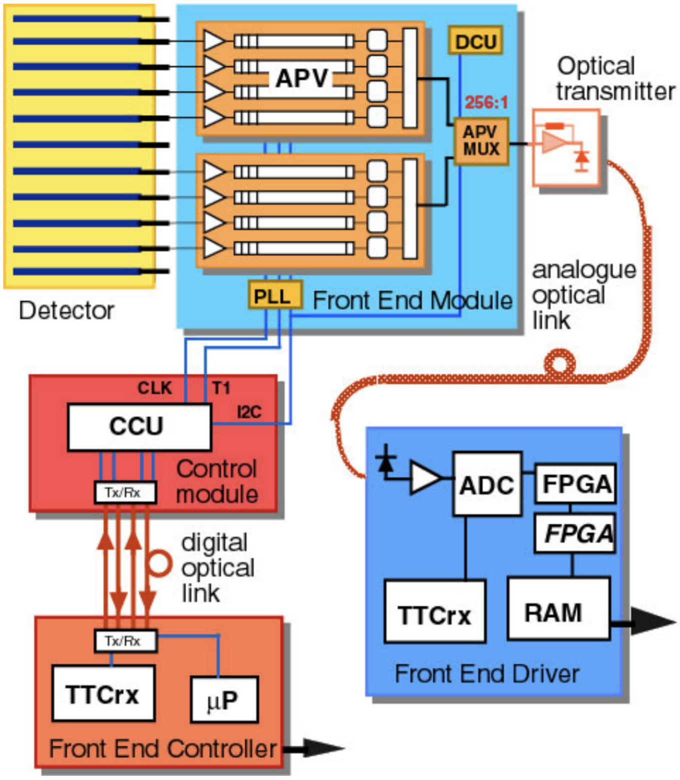

Figure 2.16: Strip tracker DAQ and readout [19].

The strip tracker is powered by 964 A4601H CAEN power supply modules that send 1.25V and 2.5V low voltages to the APV25 chips and two high voltage lines for the bias voltage of the silicon sensor. The CCUs have a 2.5 V power from 110 A4602 units. The A4601H and A4602 are in turn supplied by MAO CAEN A3486 modules, which provide a 48 V power source for the regulators and secondly a source for the service electronics[19].

2.6 Tracking performance

The pixels cover $|\eta| < 2.5$. With a 25 ns spacing between bunches and an instantaneous luminosity of $10^{34}\mathrm{cm}^{-2}\mathrm{s}^{-1}$, an average pile up (the number of total interactions at each bunch crossing) of 25 is expected. The pixels were upgraded for Run 2 to handle this. The spatial resolution is typically in the range of 13-20 μm, with the worst spatial resolution at the central part of detector at $\eta = 0$ because the magnetic field is parallel to beam axis; near the beam axis the resolution is 40 μm [16].

Good performance from the pixel tracker can be quantified with high efficiencies, low fake rates, low dead time or data loss, good position resolution, and a long lifetime of the detector. Figure 2.17 shows the cluster hit efficiency of the layers of BPix and disks of FPix using collisions in 2018. Figure 2.18 shows the hit residuals from BPix Layer 3. The hit efficiency of the strip tracker using 2018 data is shown in Figure 2.19 and the hit resolution is shown in Figure 2.20.

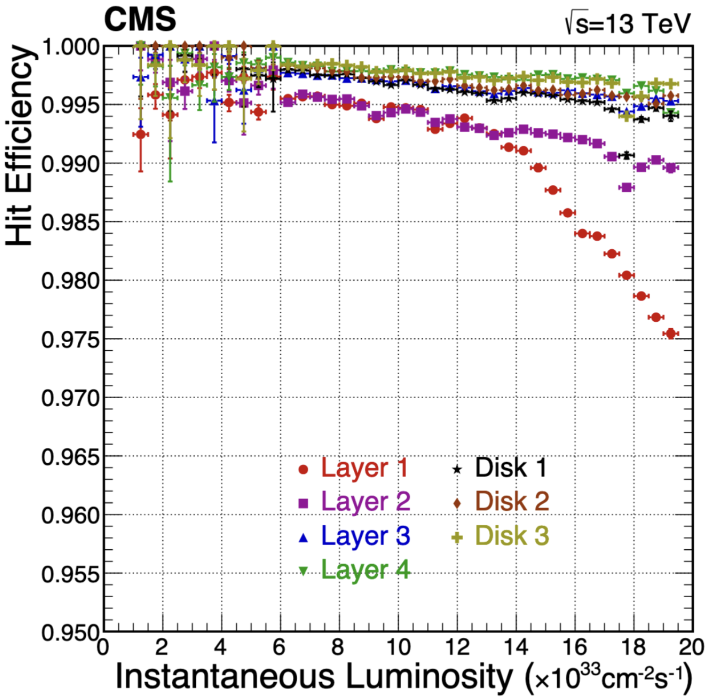

Figure 2.17: The cluster hit efficiency is above 0.975 for luminosities up to $10^{34}\mathrm{cm}^{-2}\mathrm{s}^{-1}$ in all pixel detector components [15].

There are five steps for track reconstruction in the tracking detector with information

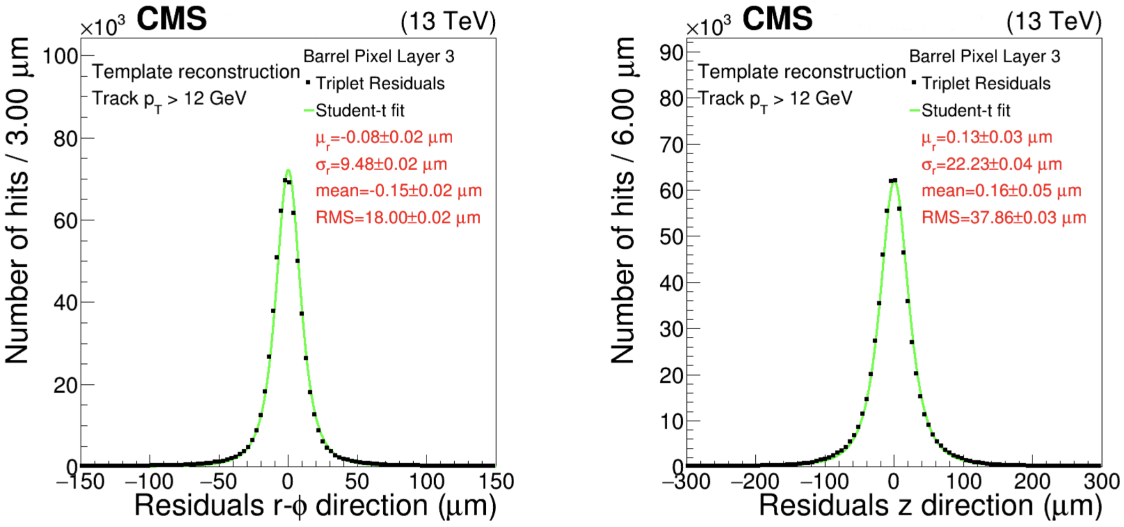

Figure 2.18: The hit residuals of BPix Layer 3 in the r-ϕ direction (left) and z-direction (right). The r-ϕ direction has a fitted width of 9.5 μm, and the z-direction has a fitted width of 22.2 μm. These values agree with simulation and confirm the modeling of position resolution, which is monitored over time [15].

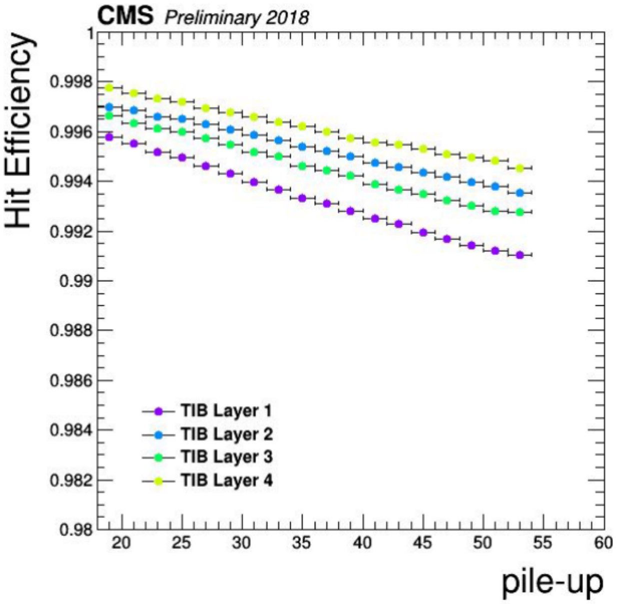

Figure 2.19: The hit efficiency of layers of TIB as a function of luminosity. The efficiency calculation requires high purity tracks and is the fraction of traversing tracks with a hit within a range of 15 strips.[20].

from both the pixel tracker and the strip tracker. First, hits are reconstructed by building clusters. Signals from pixels are kept for read out if above certain thresholds, specific

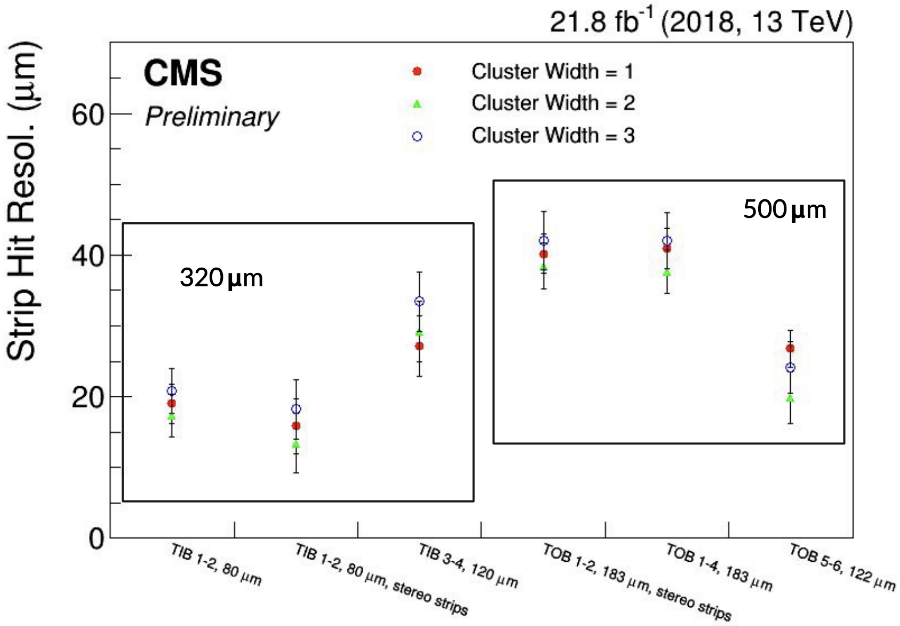

Figure 2.20: The hit resolution for different components of the strip tracker with different thicknesses of the silicon noted [20].

for each readout chip. Hits are then grouped with others from adjacent pixels to form clusters. In the pixel tracker, clusters are formed by requiring a signal to noise ratio of six. Hits from the strip tracker are accepted if the charge on a strip is greater than five times the expected noise or if a strip and its neighbor have a charge greater than twice the noise. The position of the cluster is determined by comparing the signal pulse heights. The reconstruction inefficiency (fraction of simulated hits that have no associated reconstructed hit) is below 0.5% for pixels, and the ghost hit rate is less than 0.01% [44].

The second step is seed generation, which defines the initial trajectory of a track by requiring at least 3 hits or 2 hits and a beam constraint. Seed generation occurs at a rate of 0.3 ms/seed. The third step is pattern recognition and trajectory building. After the initial seed, the track is built by moving through the layers of the tracker to build an actual track with a Kalman fitter and calculating the χ^2 to measure the quality of the track. The relative charges of the pixels at the edges of the cluster, the angle of the associated track, and Lorentz angle effects are used to determine the initial track seed. Next, ambiguity resolution selects among track candidates to prevent double counting.

If too many hits are shared among multiple track candidates, the track with the least overall number of hits is discarded. If the tracks have the same number of hits, the track with the highest χ^2 is thrown away. Lastly, the final track fit is performed as the layers are iterated through and then run backward toward the beam axis.

2.7 Electromagnetic Calorimeter

At very low energies, the energy loss of electrons dominated by ionization. The electron energies in CMS are in the GeV range, so the energy loss is dominated by bremsstrahlung, which is electromagnetic radiation produced by a charged particle when it is deflected by another charged particle and decelerated. Low energy photon energy loss is dominated by the photoelectric effect, which is when a photon is absorbed by an atomic electron and then ejected. In low Z materials, photons with energies up to 1 MeV predominately undergo Compton scattering, where a photon is scattered off a charged particle with a decrease in energy. Starting around 10 MeV, photons interacting via e^+e^- pair production in the field of the material's atomic nuclei becomes a dominant effect [13].

The radiation length X_0 is the average distance over which the energy of an electron is reduced through bremsstrahlung by a factor of $1/e$. Electromagnetic cascades (showers) are started by an electron/positron or photon. In an electromagnetic shower, the number of particles approximately doubles after each radiation length, so the number of particles in a shower is maximized right before the average energy of the particles drops below the energy threshold necessary for the bremsstrahlung process. The Molière radius R_M sets the scale for the lateral extent of a shower. Within one R_M, 90% of the energy from an electromagnetic cascade is contained[13]. Lead tungstate has a X_0 of 0.89 cm and R_M of 2.2 cm[44]. Overall, electromagnetic showers lead to most energy being deposited in a small region that is similar for particles of the same energy [2].

The CMS detector's electromagnetic calorimeter (ECAL) shown in its position in CMS in Figure 2.3 contains 80,000 lead tungstate ($PbWO_4$) crystals with an emission peak at a wavelength around 420 nm and a decay time of 10 ns. The light signals propagate to silicon avalanche photodiodes (APDs) in the barrel region, which measure the scintillation light produced in ECAL crystals. They are used because they are inexpensive, compact, have a fast rise time to manage the rates associated with LHC collisions, a relatively high quantum efficiency of 70-80%, and are not sensitive to magnetic fields. In the forward region, $1.479 < |\eta| < 3.0$, the ECAL endcap requires something more radiation hard than APDs, so vacuum phototriodes are used. The vacuum phototriodes are photomultipliers with a single gain stage. The drawback is they are more sensitive to magnetic field than APDs, but they nevertheless have acceptable performance in the 3.8 T field of CMS [28]. When the scintillation light reaches the photodiode or phototriode, it is amplified and digitized to be sent through the readout system. The information used as input for the trigger system is read out every 25 ns, and the more detailed information is buffered to account for the global trigger latency of 3 μs [28].

The barrel calorimeter (EB) extends from a radius of 1.29 m to 1.75 m radius from the beamline and covers $|\eta| < 1.479$. The crystal length corresponds to 25.8 X_0 and 10.4 R_M, and they are grouped together to form supermodules[19]. Figure 2.21 shows an EB supermodule. The electromagnetic endcap (EE) starts 3.154 m from the interaction point and covers $1.48 < |\eta| < 3.0$. These crystals are grouped together in groups of 5 by 5 to form "supercrystals", 146 of which are combined to form half of one endcap. The high temperature dependence of the light emission necessitates tight temperature control, and the system is cooled with 18°C water [19]. The ECAL covers up to $|\eta| < 3$ with the best energy measurement up to $|\eta| < 2.6$ [19].

The preshower's purpose is to distinguish between γ and π^0 particles. As H$\rightarrow \gamma\gamma$ was expected to be an important decay channel for the discovery of the Higgs boson, and about half of these decays were expected to have a photon in the zone covered by the endcap regions, $1.65 < |\eta| < 2.6$, the measurement of photons was a high priority in the design of CMS [28]. There are two layers of converters that initiate showers made of aluminum layers around lead followed by silicon detector modules that measure the shower. The first layer measures the shower in the vertical direction and the second layer in the horizontal direction. The preshower is required to operated at -5°C to keep leakage currents low and keep the noise low enough not to interfere with DC-coupled electronics.

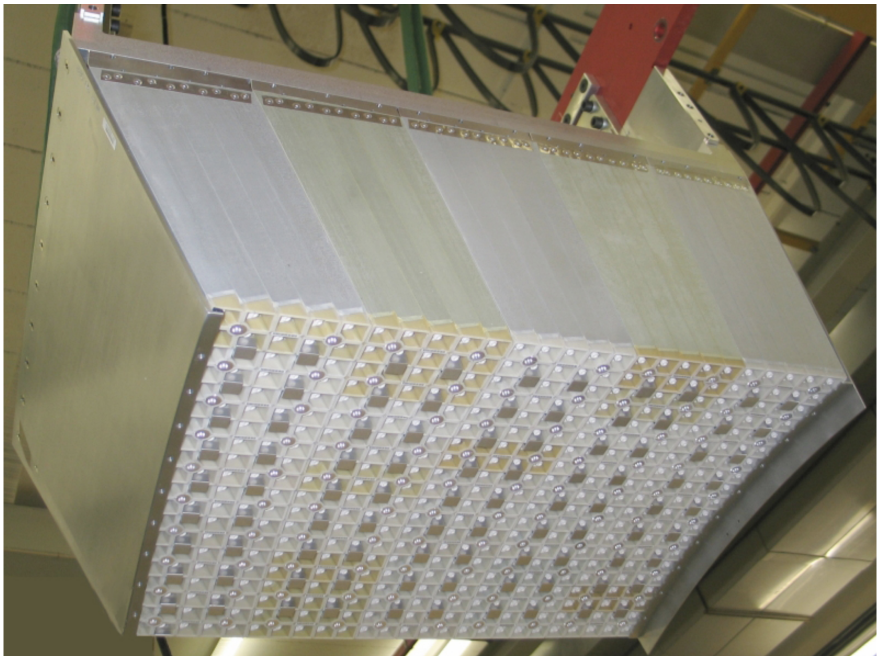

Figure 2.21: ECAL supermodule containing 1700 crystals [19].

In situ calibration with physics events is completed in three steps: local intercalibration, global intercalibration, and absolute calibration. The first establishes channel-to-channel connections and measures the individual e/γ energy resolution, the second works among the different sections of the calorimeter, which is necessary for reconstructing the mass of particles accurately, the third for the overall energy scale. In situ calibration can use $Z \rightarrow ee$ events. This has the advantages of allowing cross-calibration of different sets of crystals and cross-calibration of endcap and barrel components and also has the flexibility to run calibrations with or without information from the tracker[28].

Energy resolution effects are divided into a stochastic term with contributions from shower containment, preshower sampling term, and a photostatistics contribution. These are modeled with Monte Carlo and verified with test beam data. Additional resolution uncertainties include constant terms coming from calibration errors, the non-uniformity of crystals, and energy leakage, and a noise term that has contributions from the preamplifier, digitization, and pileup. The parameters shown in Table 2.4 were calculated for a (100 GeV) $H \rightarrow \gamma\gamma$ signal reconstructed in a 5 by 5 crystal array [28]. Figure 2.22 demonstrates the energy resolution of the ECAL.

	Barrel ($\|\eta\| = 0$)	Endcap ($\|\eta\| = 2$)
Stochastic term	$\frac{2.7\%}{\sqrt{E}}$	$\frac{5.7\%}{\sqrt{E}}$
Constant term	0.55%	0.55%
Noise (low luminosity)	155 MeV	770 MeV
Noise (high luminosity)	210 MeV	915 MeV

Table 2.4: Contributions to energy resolution in ECAL, summarized information from [28]. Low luminosity is defined to be $10^{33}\text{cm}^{-2}\text{s}^{-1}$ and high luminosity to be $10^{34}\text{cm}^{-2}\text{s}^{-1}$.

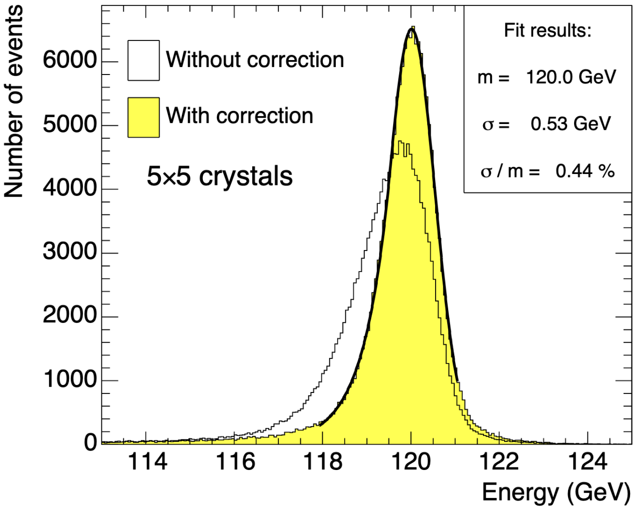

Figure 2.22: ECAL performance for 120 GeV electrons. The correction accounts for variations of the energy contained within the crystals [19].

2.8 Hadronic Calorimeter

Charged hadrons lose energy through ionization, and all hadrons passing through a medium will undergo strong interactions with its atomic nuclei. The nuclear interaction length λ_l is the mean distance between interactions of relativistic hadrons and sets the scale for hadronic calorimeter size, which is substantially larger than for electromagnetic calorimetry. Hadronic calorimetry is challenging due to a large number of different possible final states. Additionally, $\pi_0 \to \gamma\gamma$ contributes to an electromagnetic component. Furthermore, on average 30% of the incident energy is lost in nuclear excitations, neutrons, and neutrinos. Because of these effects, a common configuration for hadronic calorimetry is a sandwich of high density absorbers for the shower development with a thin layer of material where the energy deposition can be read out. In jets, roughly 60% of energy goes to charged particles, 30% to photons from $\pi_0 \rightarrow \gamma\gamma$, and 10% to neutral hadrons (neutrons and K_Ls) [2]. Additionally, the jet energy resolution is limited by the presence of a magnetic field, pile up, and jet fluctuations.

The HCAL of CMS is shown in Figure 2.3. The HCAL barrel (HB) extends from a radius of 1.77 m to 2.95 m and covers $|\eta| < 1.3$. It is split into two half barrels (labeled HB- and HB+) which are then split into 36 azimuthal wedges. The plastic scintillator is segmented in η and ϕ. The absorbers in this portion of the calorimeter are one layer of 40 mm steel plate, eight layers of 50.5 mm brass plates, six layers of 56.5 mm brass plates, and one 75 mm steel plate. The steel gives structural rigidity. The total absorber thickness of HB at its minimum is 5.82 λ_l, and it increases with polar angle to it is maximum of 10.6 λ_l at an $|\eta|$ value of 1.3. Because the particles reach HCAL after already passing through the ECAL, they have already traversed 1.1 λ_l, so small fraction of hadronic shower development can begin in the ECAL [19].

The scintillating material is 3.7 mm thick Kuraray SCSN81 plastic tiles. A wavelength-shifting fiber is used to collect the light from the plastic and transmit it to an optical connection which then goes to an optical decoding unit (ODU), which sends the light to a hybrid photodiode (HPD). The plastic tiles are organized into trays, which are stacked to form the wedges of HB. There is a layer 0 of HB that samples in between EB and HB, and a layer 16 that is thicker to prevent leakage. Each tray is scintillator material attached to a plastic substrate with wavelength shifting fibers to collect light. Stainless steel tubes containing radioactive Cs^{137} are used to calibrate the detector to within 2% and quartz fibers inject UV light in a layer of tiles to test performance [19].

The HCAL Endcap (HE) covers $1.3 < |\eta| < 3$. Both HE calorimeters have 20,916 tiles organized into 1368 trays. C26000 cartridge brass was chosen for this section of HCAL because it is not magnetic, provides many interaction lengths, is structurally sound, and inexpensive. The brass plates are 79 mm thick with 9 mm gaps for the scintillating material. The scintillators here are trapezoidal and made of 3.7 mm thick SCSN8 and

9mm thick Bicron BC408. The performance can be monitored using a UV light signal from a nitrogen laser. The absorber fills in the gaps between HB and HE. The total length of the calorimeter in the endcap region including ECAL is 10 λ_l [19].

The outer HCAL (HO) provides additional interaction lengths of material at a larger radius. The magnetic field of CMS is returned through an iron yoke that is segmented into five rings outside the vacuum tank of the solenoid. The HO is located within these rings centered at either z = 0 m, ± 3.82 m, or ±4.07 m from the interaction point. This increases the coverage to at least 11.8 λ_l except where the barrel and endcap meet. The rings are split into 12 sectors in ϕ, and contain one or two layers of Bicron BC408 scintillator, whose light is collected by wavelength shifting fibers. An HO module is shown in Figure 2.23. The Forward HCAL (HF) is a cylinder with an outer radius of 1.3 m with its front face 11.2 m from the interaction point and is divided in 18 wedges in ϕ. It covers $4.5 < |\eta| < 5$. It has quartz fibers that connect to photo multiplier tubes that are behind 40 cm of steel and borated polyethlene slabs to shield them from the high levels of radiation [19].

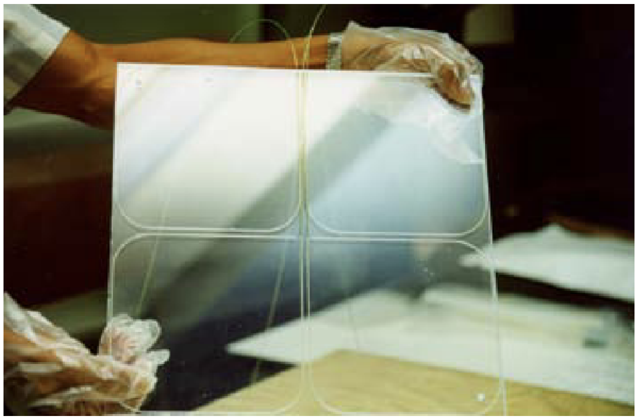

Figure 2.23: Outer HCAL module with fiber.

In HB, HE, and HO, scintillator light is converted by HPDs to electrical signals, while HF uses PMTs directly receiving input from quartz fibers. The Charge-Integrator and Encoder ASIC converts analog signals from the HPDs and PMTs to digital signals, which are transmitted to HCAL Trigger/Readout (HTR) boards. The HTR boards construct the trigger primitives that are used by central CMS trigger system to determine whether a level one trigger accept is called. The Channel Control ASIC controls the clock of the QIE (Charge Integrator and Encoder), which adjusts for differences in time-of-flight from the interaction point primary vertex z-position and the difference in optical pathlength. Figure 2.24 shows a pulse from the QIE and the resulting time resolution, with 68% of the pulse within a window of 25 ns, the frequency of LHC bunch crossings in CMS [19].

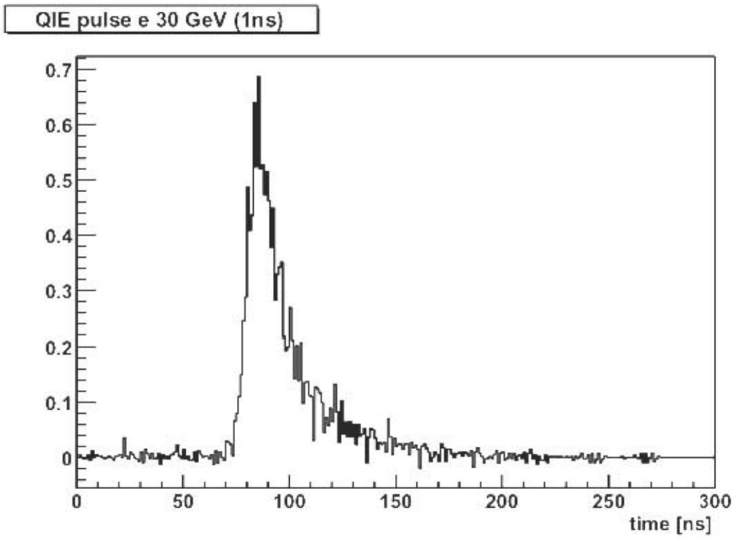

Figure 2.24: Pulse in HCAL [19].

2.9 Muon Detectors

The CMS detector has three different gas detector subsystems dedicated to identifying muons, determining muon momentum, and triggering on muons. There are drift tubes (DT) in the barrel region, resistive plate chambers (RPC) in both the barrel and endcap region, and the cathode strip chambers (CSC) in the endcap region. An overview of the muon system is displayed in Table 2.5.

2.9.1 Drift Tubes

The drift tubes (DTs) are in the barrel region of CMS, covering $|\eta| < 1.2$. The drift tube chambers are organized into four layers called stations. The three inner stations have 60 drift chambers that are paired such that one measures coordinates in the r-ϕ plane and one measures in the z-direction. The outer layer has 70 drift chambers that measure only

Muon subsystem	DT	CSC	RPC
$\lvert\eta\rvert$ coverage	0.0–1.2	0.9–2.4	0.0–1.9
Number of stations	4	4	4
Number of chambers	250	540	Barrel: 480 Endcap: 576
Number of layers/chamber	R-ϕ: 8; z: 4	6	2 in RB1 and RB2 1 elsewhere
Number of readout channels	172 000	Strips: 266 112 Anode channels: 210 816	Barrel: 68 136 Endcap: 55 296
Percentage of active channels	98.4%	99.0%	98.3%

Table 2.5: Summary of the properties of the muon systems of CMS for 2016 datataking [29].

in the r-ϕ plane. The inner layer is inside the magnet yoke, there are two layers embedded within the yoke, and there is one outside. Drift tubes are rectangular and stacked in four layers to form a superlayer, and 2 or 3 superlayers are combined to make one chamber. The individual drift tubes are staggered by half a tube with respect to the neighboring layers[19]. The layout is shown in Figure 2.25.

Drift tube cells are filled with a mixture of 85% Argon and 15% CO_2. As a muon passes through the gas, ionized particles move towards either the anode wire or cathode strip, which propagate the signal. Cathode wires are set to -1.2 kV, electrode strips set to 1.8 kV, and anode wires set to 3.6 kV. Each individual superlayer contributes to bunch crossing tagging with timing resolution of a few nanoseconds and track position and angle information. This timing and transverse momentum information is then used for first-level muon trigger. A schematic showing how a muon traverses a drift tube is shown in Figure 2.26 [19].

For Run 2, the DT electronics used an AMC13 board that receives timing data from TCDS and transmits detector data to central DAQ. A processor board called TM7 was developed to work with the TwinMux trigger and upgraded electronics with μROS (read out servers using μTCA creates) boards. The DT system uses 25 μROS boards, with each of them handling up to 72 DT channels. The total payload bandwidth is 4.8 Gbps for the

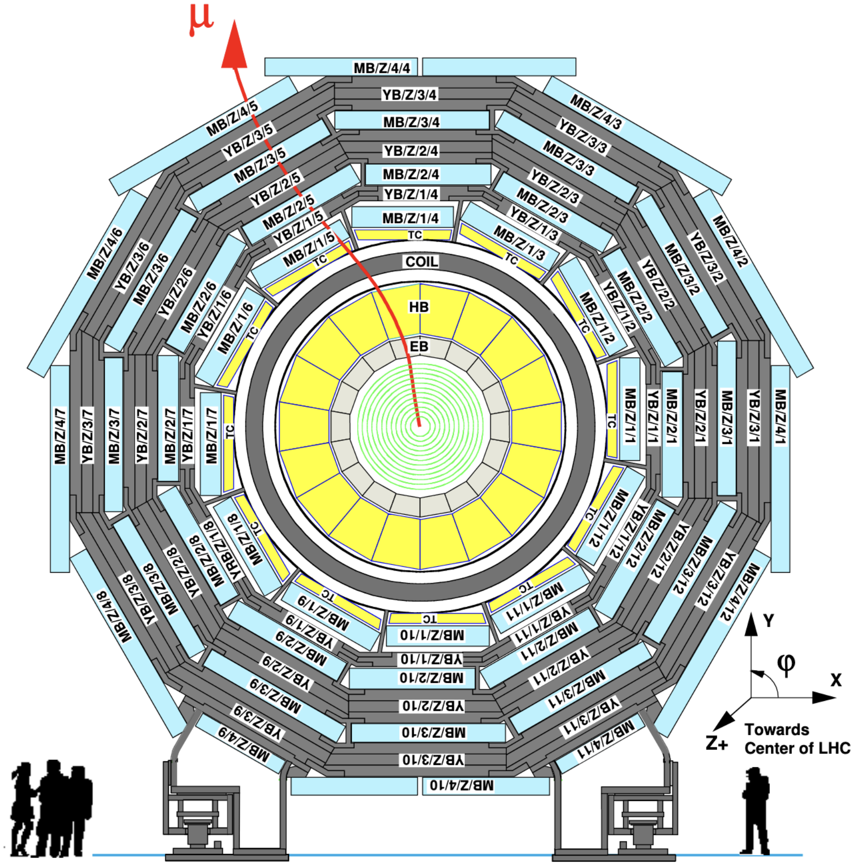

Figure 2.25: Drift tube geometry with the active elements shown in cyan. [19].

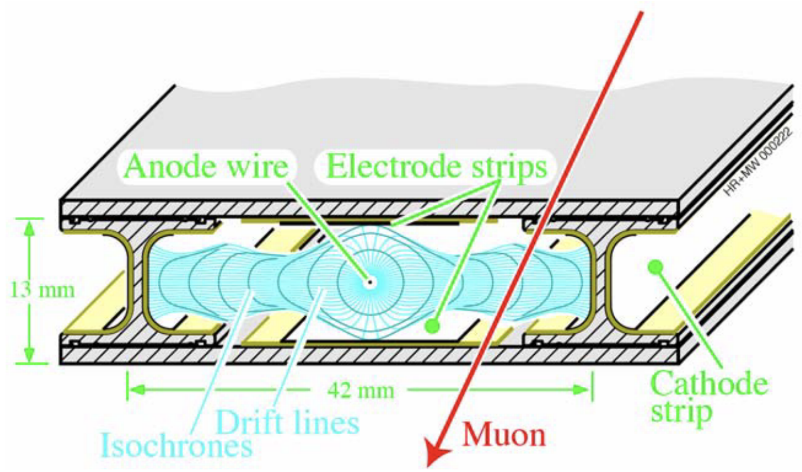

Figure 2.26: A drift tube [19].

central wheel and 9.6 Gbps for the other wheels at the step of AMC13 transmission [45].

2.9.2 Cathode Strip Chambers

In the endcaps, cathode strips chambers (CSCs) are used for muon measurement and muon triggering. CSCs are organized into 4 stations in each endcap. Cathode strips make measurements in the r-ϕ plane, while anode wires make measurements in η and time. CSCs are multiwire chambers with anode wires and cathode panels. In total there are 220,000 cathode strip read out channels and 180,000 anode wire read out channels. The chambers are trapezoidal and fit together to make disks in groups of 72 or 36. Figure 2.27 shows their arrangement when installed in CMS [19].

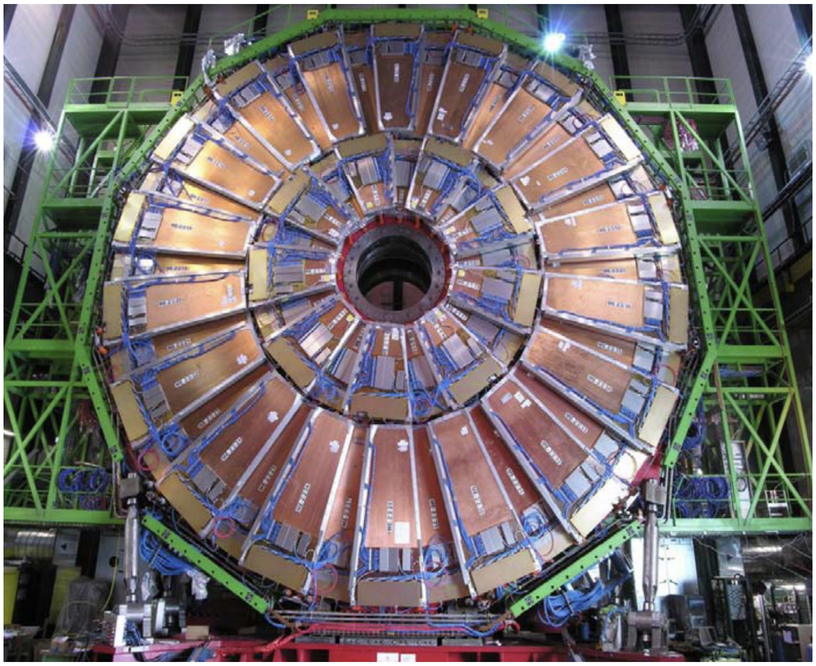

Figure 2.27: The ME2 station of CSCs installed in CMS[19].

The CSCs provide 2 mm resolution in r-ϕ for use in the first level trigger, and 150 μm during offline analysis. They also are excellent for bunch crossing tagging, correctly assigning the bunch crossing 99% of the time. Seven panels are stacked together and attached with bolts to each other to make a single chamber, which is then filled with a gas mixture of 40% Ar, 50% CO_2, and 10% CF_4. The high voltage is set between 2.9 and 3.5 kV. An FPGA board on each chamber stores output from the chamber and sends this information to the DAQ when an L1Accept is received. It also checks for patterns at each bunch crossing and transmits the patterns to the muon level-1 trigger electronics. Panels with gaps are stacked together. Some panels are FR4 (fiber glass and epoxy material) clad with copper and have cathode panels with FR4 cathode gap bars and some panels are anode panels with copper-clad FR4 anode bars with gold-plated tungsten wires wound around them. The design of the panels inside chambers is shown in Figure 2.28[19].

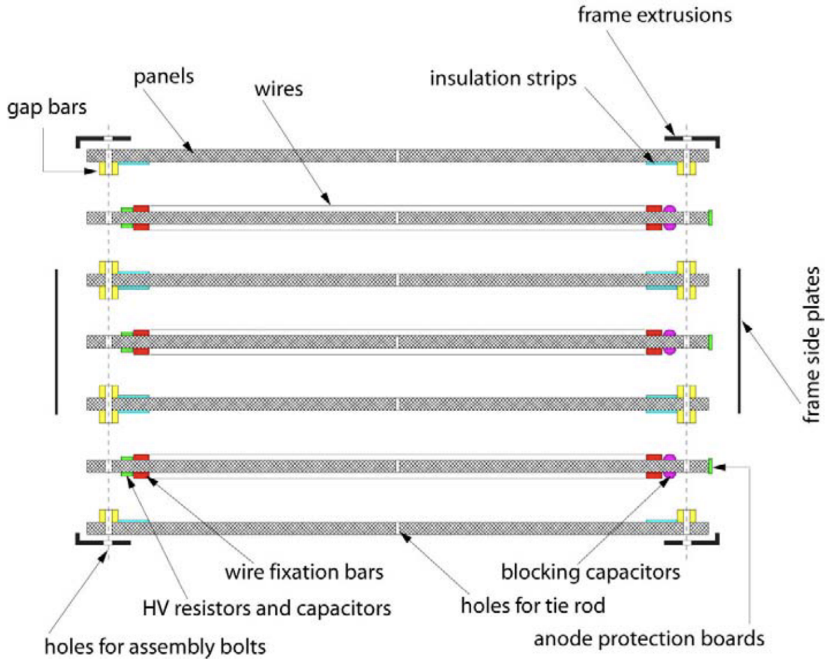

Figure 2.28: An exploded view of the inside of a CSC chamber with its seven layers of panels[19].

2.9.3 Resistive Plate Chambers

The resistive plate chambers (RPCs) are specialized to allow triggering on muons by quickly and accurately matching a muon to its bunch crossing. In the barrel, there are 6 layers of RPCs, with 2 layers in the inner 2 stations and 1 layer in the 2 outer stations. The barrel RPC stations are made of 480 rectangular chambers that are 245.5 cm long. There are 4 stations on both the plus and minus end of CMS. Additional chambers in the fourth station were added before Run 2 to improve performance [19, 29].

Each chamber has an positively-charged plate and a negatively-charged plate and is filled with a gas mixture through which muons pass and induce a signal. The RPCs operate with a closed loop circulation of a gas mixture of 96.2% $C_2H_2F_4$, 3.5% iC_4H_{10}, and 0.3% SF_6. The readout strips connect to Front-End Boards (FEB) that sent signals to Link Boards (LB), which synchronize the signal with the LHC clock. The signal is then transmitted to the trigger system [19].

The powering scheme consists of mainframes that control up to 16 branch controller boards and crates that contain high voltage and low voltage boards. In total there are 480 HV channels in the barrel and 216 HV channels in the endcap, which each can have an output voltage of up to 12 kV with a monitored current resolution of 0.1 μA. The LV system has 720 channels in the barrel and 432 in the endcap with an output voltage range or 1.5-8 V and a monitored current resolution of 10 mA.

2.10 Trigger and Data Acquisition

The peak instantaneous luminosity during Run 2 was $2.1 \times 10^{34}\mathrm{cm}^{-2}\mathrm{s}^{-1}$ with 25 ns spacing between collisions, corresponding to collisions in CMS at rate of 40 MHz and an average pileup of 55. The trigger of CMS has two steps, the Level 1 (L1) Trigger and the High Level Trigger (HLT). The L1 trigger is implemented in FPGAs, ASICs, and memory look up tables and cuts the 40MHz rate of collisions down to 100kHz. Figure 2.29 shows how this 100kHz is shared among triggers for different objects [21, 46].

The global trigger determines whether to issue an L1Accept, which causes all subdetectors read out an event's information to send it to the HLT. The global trigger takes input from the calorimeter and muon triggers before issuing an L1Accept, which is delivered by the Trigger Control System to individual subsystems that read out the informaiton relevant to the selected event.

Jets, event total transverse energy and missing transverse energy, and electron/photon candidates are reported by the Global Calorimeter Trigger. ECAL and HCAL have trigger towers, which are groups of 5×5 crystals in EB and the corresponding HB section behind them. A similar setup is used in the endcap region though the geometry is more complicated. The calorimeter trigger towers correspond to $\Delta\eta \times \Delta\phi$ regions of 0.087×0.087 in the barrel and 0.17×0.17 in the endcap. Calibrations are applied at the layer 1 trigger that account for affects like η dependent energy loss in the tracker before the calorime-

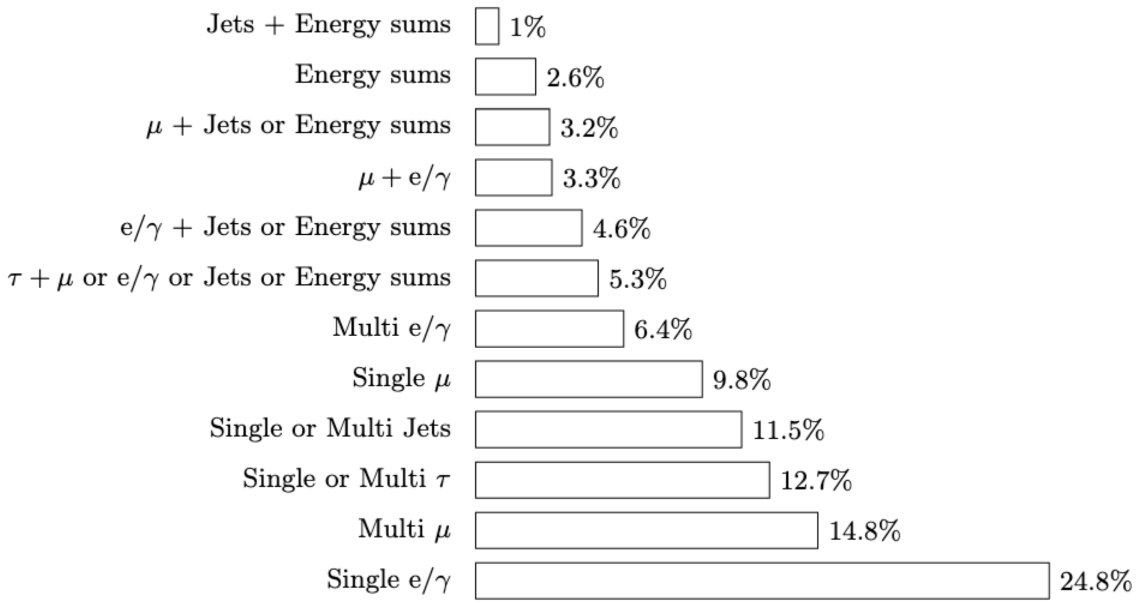

Figure 2.29: Relative fractions of triggers based on different objects [21].

ters. The layer 2 trigger receives the total calorimeter energy sum and the ratio of energy from ECAL to energy from HCAL. This information is then sent to a demultiplexing card (DeMux) that transmits the information to the global trigger [21].

DTs, CSCs, and RPCs all contribute to the L1 Trigger. Originally, the DT local trigger used hits to make track segments, the CSC local trigger used hits to build hit patterns and search for time coincidences, and the RPC local trigger provided bunch crossing identification and sent the best four barrel and best four endcap muons to the Global Muon Trigger. With the Level-1 trigger for Run 2, the global muon trigger uses information from all three subdetectors at once. The strategy is different based on pseudorapidity region: the Barrel Muon Track Finder uses inputs from DTs and RPCs, the Overlap Muon Track Finder uses all three types of chambers, and the Endcap Muon Track Finder uses input from CSCs and RPCs. Each of these track finders can send up to 36 muons to the μGMT that selects the 8 highest quality muons to be sent to the muon global trigger. Figure 2.30 shows the Level-1 Trigger system of CMS used in Run 2 [21].

The HLT is the second step of the CMS trigger system and takes the 100 kHz rate from the L1 Trigger and reduces it to about 1 kHz by running simplified reconstruction

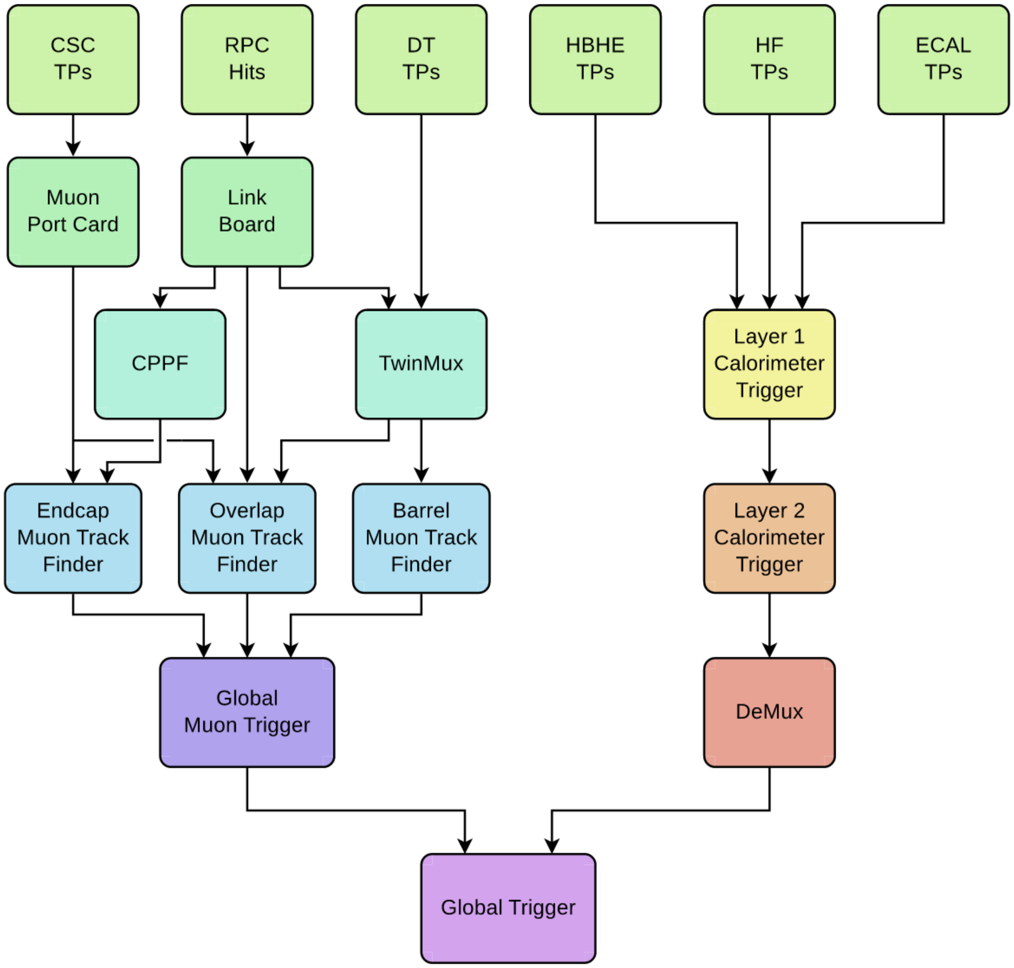

Figure 2.30: Flow of information within the Level 1 trigger. TP stands for Trigger Primitives and CPPF stands for concentration preprocessing and fan-out. The TwinMux combines DT trigger primitives and RPC hits from the same detector layer [21].

software on 32,000 CPU cores. Basic reconstruction of electrons, photons, tau decays, muons, and jets is performed at this step. These different HLT algorithms are called paths and can be updated or changed over the course of data taking. Some used during 2018 are listed in Table 2.6 [30].

2.11 Solenoidal Magnet

The CMS detector has a superconducting magnet that creates a field up to 3.8 T. A conductor made from NbTi makes up a 4 layer winding for the 220 metric ton cold mass that corresponds to only 3.9 X_0 long. The entire magnet is 12.5 m long and the cold bore

Description	Condition	Rate in a certified run at PU 50 ($\mathscr{L}$= 1.8×10^{34} Hz cm^{-2})
Isolated single muon	$p_T(\mu) > 24$ GeV	235 Hz
Isolated single electron	$p_T(e) > 32$ GeV	165 Hz
Non isolated single muon	$p_T(\mu) > 50$ GeV	46 Hz
Non isolated single electron	$p_T(e) > 115$ GeV	17 Hz
Isolated di-photon	$p_T(\gamma) > 30/22$ GeV, $M(\gamma\gamma) > 90$ GeV	40 Hz
Isolated di-tau	$p_T(\tau) > 35/35$ GeV, $\lvert\eta(\tau)\rvert < 2.1/2.1$	40 Hz
Isolated di-electron	$p_T(e) > 23/12$ GeV	25 Hz
Isolated di-muon	$p_T(\mu) > 17/8$ GeV, $M(\mu\mu) > 3.8$ GeV	28 Hz
Isolated electron-muon	$p_T(e) > 23(12)$ GeV, $p_T(\mu) > 8$ (23) GeV	7.5 (4) Hz
Single jet	$p_T(j) > 500$ GeV	11 Hz
Hadronic transverse energy	$H_T > 1050$ GeV	10 Hz
Missing transverse energy	PFMET> 120 GeV, PFMHT> 120 GeV	33 Hz
Hadronic $t\bar{t}$	H_T >380 GeV, $\geq$ 6 jets (p_T>32 GeV), 2 b-tagged jets	9 Hz
Boosted heavy jets	$p_T(j) > 400$ GeV, M(j)> 30 GeV	27 Hz
Isolated single photon	$p_T(\gamma) > 110$ GeV, $\lvert\eta(\gamma)\rvert < 1.479$	12 Hz
Non isolated single photon	$p_T(\gamma) > 200$ GeV	13 Hz
Triple muon	$p_T(\mu) > 5/3/3$ GeV, $M(\mu\mu) > 3.8$ GeV	9 Hz
isolated di-muon+electron	$p_T(\mu) > 4$ GeV, $p_T(e) > 9$ GeV	4.5 Hz
Displaced $J/\psi \to \mu\mu$	$p_T(\mu) > 4/4$ GeV, 2.9< $M(\mu\mu) < 3.3$ GeV + displaced vertex	33 Hz

Table 2.6: HLT paths used in 2018 datataking and their associated rates with instantaneous luminosity of 1.8×10^{34}cm^{-2}s^{-1} [30].

diameter is 6.3 m. Its flux is returned in an iron yoke that is 13 m long with a diameter of 14 m and with a total mass of 10,000 metric tons, spread among 6 endcap disks and 5 barrel wheels [19].

2.12 Particle Flow

Information from all the subdetectors must be synthesized to determine the identity of the particles that moved through the detector. Particle Flow is the name given to the event reconstruction technique to identify and reconstruct individual particles - electrons, muons, photons, charged hadrons, and netural hadrons. Figure 2.31 depicts the paths of various types of particles through the CMS detector.

Individual tracker hits are used to trace out the physical path taken by charged particles. To minimize fake tracks, tracks are first seeded with tight, high-quality requirements, and once those tracks are reconstructed, those hits are removed. The requirements are loosened and the process is repeated again in an iterative manner. The calorimeters, HCAL and ECAL, have deposits of energy that are called clusters. Cluster seeds above a threshold are grouped with adjacent cells to form topological clusters. A linking algo-

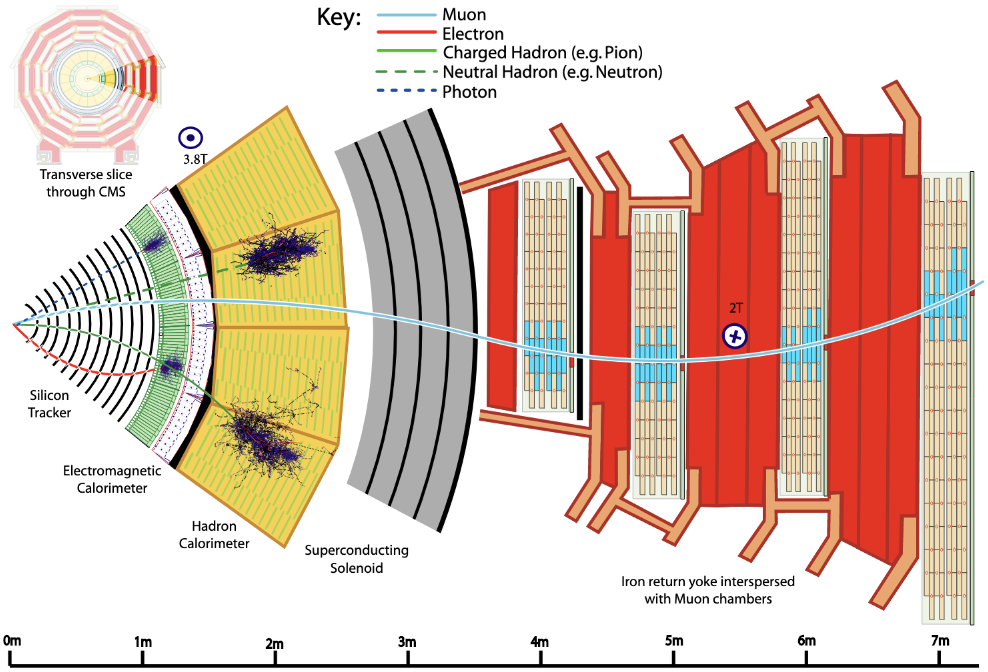

Figure 2.31: The paths of five different types of particles through CMS. Photons and neutral hadrons do not interact with the silicon tracker. Electrons and photons are stopped in the electromagnetic calorimeter and create a shower, and charged and neutral hadrons are stopped in the hadronic calorimeter. Muons are the only particle that traverse the muon detectors [19].

rithm connects data from tracker, the preshower, ECAL, and HCAL based on the distance between hits in the ϕ-η plane.

Global muons as determined by the muon detector subsystems are reconstructed as Particle Flow muons. The performance of muon identification efficiency from Z boson decays is shown in Figure 2.32. Electrons lose energy through bremsstrahlung and some ionization in the tracker before creating a shower in the ECAL. Tracker and calorimeter variables are used to classify Particle Flow electrons. Once a hit in tracker or energy deposit in the calorimeters is linked to a Particle Flow electron, they are removed from consideration for building other Particle Flow particles.

Charged hadrons make tracks in the tracker, move through the ECAL and shower in the HCAL. When tracks are linked with ECAL and HCAL clusters, if the calorimeter cluster energy is much larger than the charged particle momentum assuming it is a charged

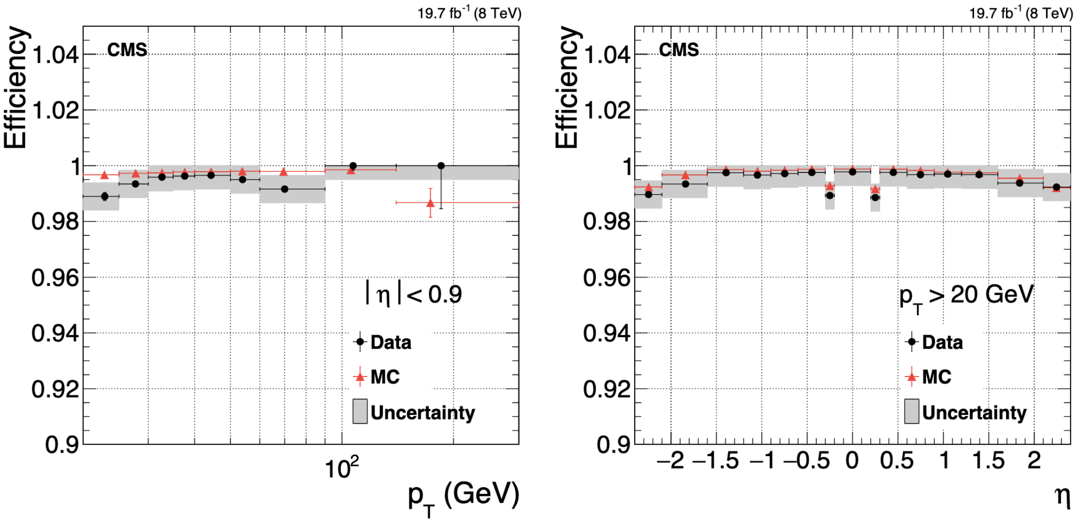

Figure 2.32: Muon identification efficiency as a function of p_T and η [22].

pion, the excess is classified as a Particle Flow photon. This is because a photon does not interact in the tracker and usually deposits all its energy in ECAL (unless pair production occurs). Energy excesses in HCAL create Particle Flow neutral hadrons. The comparison of jet energy composition measurements in observed and simulated events is shown in Figure 2.33 [47, 22].

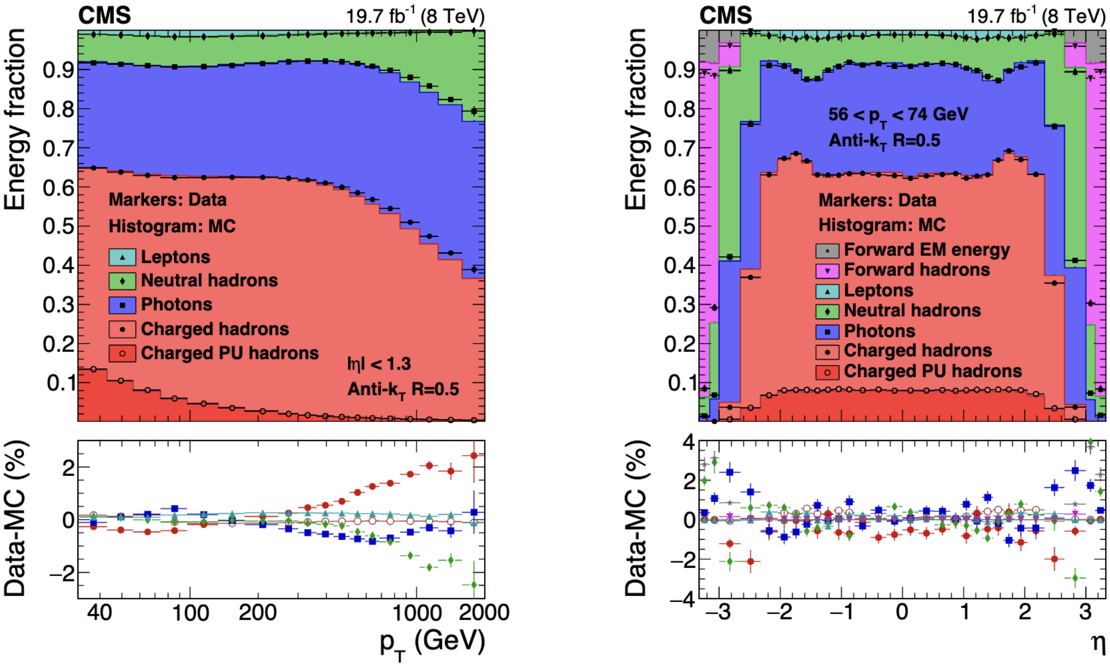

Figure 2.33: Jet energy fraction as a function of p_T and η [22].

Chapter 3

The CMS Pixel Detector

The pixel tracker was extracted from CMS at the end of Run 2 in January 2019 and was enclosed environmental control boxes in clean rooms to be kept cold and dry during Long Shutdown 2 before the beginning of Run 3. The extracted pixel tracker includes four layers of BPix, three endcap disks for each end of FPix, and the service cylinders that contain DCDC converters, cooling pipes, and portcards. The pixel tracker was refurbished with a new BPix layer 1 and hardware improvements. It was commissioned and calibrated in the clean room set up during Spring 2021 and then re-installed in CMS during Summer 2021. Further calibrations were performed until the beginning of Run 3 in Summer 2022. This chapter presents details about these steps of detector preparation and a study on radiation damage of BPix layer 1 modules.

3.1 Hardware Refurbishment

Hardware improvements were made to each half cylinder of FPix in the clean room including DCDC replacement, filterboard replacement, and cooling pipe reinforcement. Figure 3.1 shows a half cylinder of FPix undergoing this refurbishment and electronic racks in the pixel clean room that were used to run tests and calibrations. An important improvement for the performance of the pixel tracker was the upgrade of the DCDC converters. During Run 2, the DCDC converters incurred damage on a low-voltage clamping transistor after exposure to radiation. After this damage, the gate current of the circuit could lead to the DCDCs getting “stuck” and the under-voltage lock-out mechanism was disrupted, allowing the circuit to be powered at too low of a voltage. This caused DCDCs to fail during disable and enable cycles, creating an improper path for leakage current to drain and eventually leading to ROCs becoming nonfunctional. The new DCDC converters have the FEASTv2.3 chip, which replaced the problematic clamping transistors with an on-chip resistor that removes the leakage current path [48]. The new DCDCs are shown in Figure 3.2.

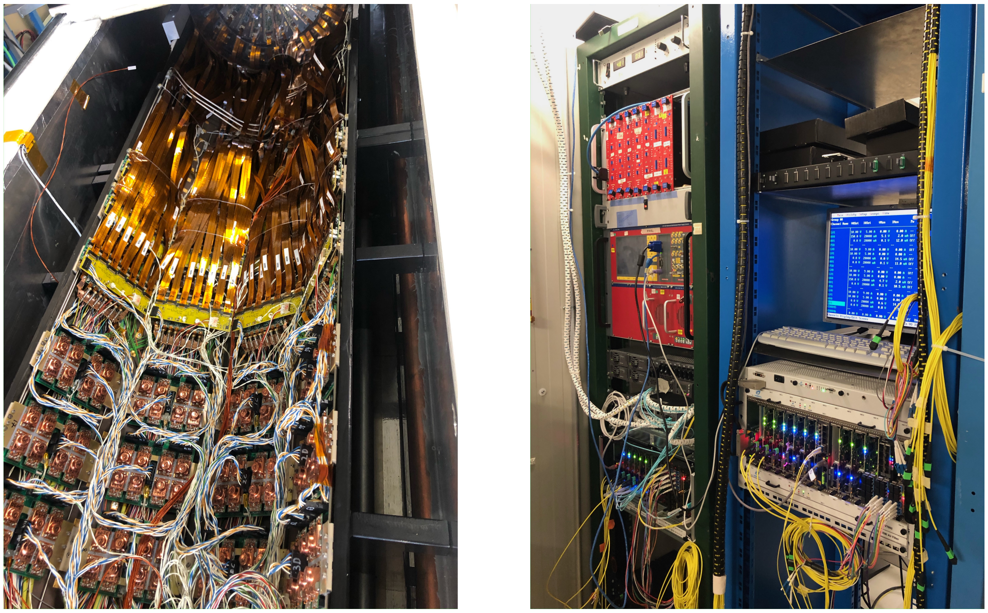

(a)

(b)

Figure 3.1: Left: A half cylinder of FPix. The modules are at the top of the photo, arranged in a half moon shape. The DCDC converters and services make up the rest of the half cylinder. Right: Backend electronics in the clean room used during the refurbishment and subsequent commissioning of the detector. Power supplies, pixel FEDs, pixel FECs, and TkFECs make up a test DAQ set up so the entire chain can be tested before installation.

The filterboards of FPix were switched to allow for more granularity in HV powering. This is especially important because without LV being applied to the detector, HV must be turned off. More granularity and matching between LV and HV lines allow a greater active detector fraction in the event of any issues with the LV or HV. The number of independent HV lines was increased from 2 to 4 for each power group. Additionally, the cooling pipes were reinforced to be more robust against breaking during movement

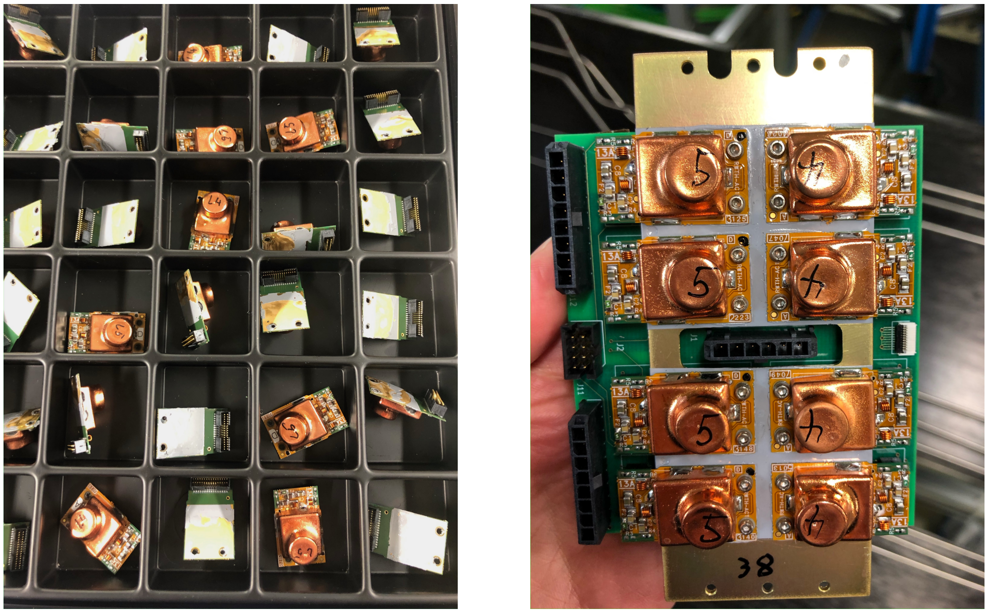

(a) (b)

Figure 3.2: Left: individual DCDCs that were already tested for the correct voltage output. Right: A group DCDCs attached with thermal tape to a cooling bridge, ready to be installed.

and installation of the detector with a rotating nut and custom fitting. A leak test was performed in the clean room on the cooling pipes.

The entire innermost layer of BPix was replaced with new modules. Besides the silicon being free from any radiation damage at the start of the run, the new BPix layer 1 has the following improvements:

- New ROC (PROC600v4): The new ROC decreases dynamic inefficiency and cross talk noise.
- New TBM (TMB10d): The new TBM has a reset option that allows powercycling modules in the “stuck” state during data-taking. There is also an additional delay setting that allows the timing settings of layers 1 and 2 to be set independently. The old design did not allow this due to layers 1 and 2 sharing the same portcard.
- New HDI design: There is more space between the HDI and the edge of the module, making it less susceptible to HV shorts.

3.2 Calibrations

After hardware replacements, the detector was commissioned in the clean room. Figure 3.3 shows a schematic with several components that underwent specific calibrations.

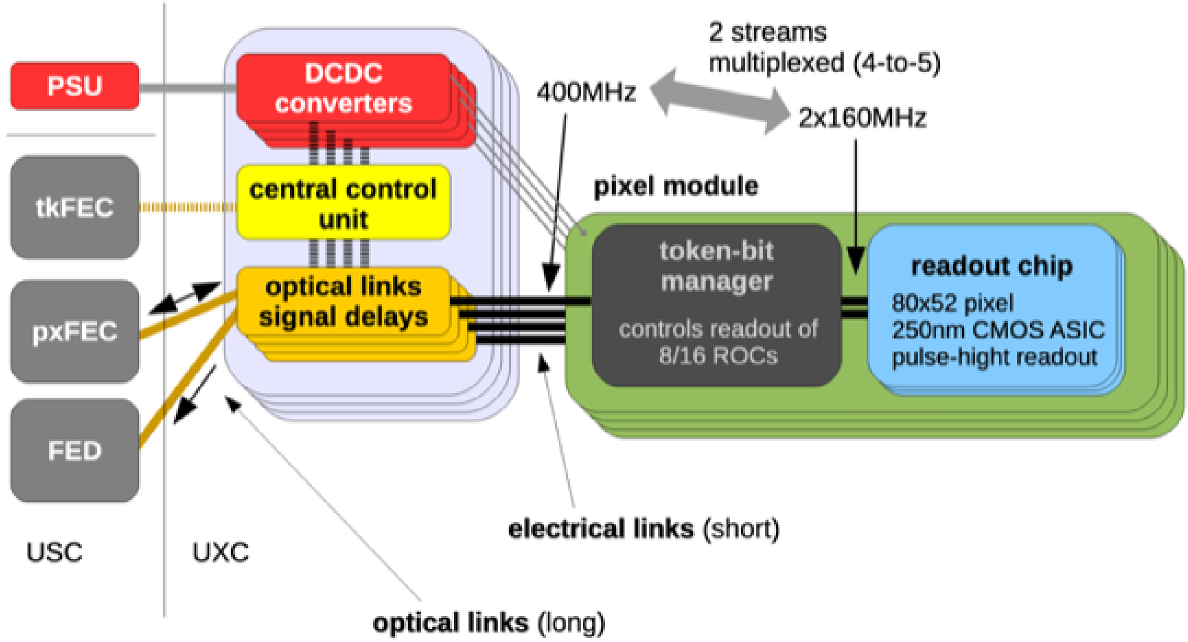

Figure 3.3: A schematic showing different components of the signal path of a hit in the pixel detector. If a pixel hit passes the ROC threshold and a L1Accept is issued, the readout of the measurement will be coordinated by the TBM. The data will be sent via electrical and optical links to FEDs that interface with CMS central DAQ. The power to the modules is provided by power supply units via DCDC converters [23].

First, the optical links were tested with a POH (Photo Opto Hybrid) laser bias scan. An example of the output of this calibration is shown in Figure 3.4. The delay settings of the TBMs were then calibrated. There are two data streams at 160 MHz coming to the TBM (one stream per four ROCs) which are then multiplexed and sent at 400 MHz at the output. These 160 MHz and 400 MHz settings must be in agreement, so a two dimensional calibration was done that changes both settings simultaneously, as shown in Figure 3.5.

An SCurve calibration measures the threshold values of ROCs. This calibration was run during commissioning in the clean room and is subsequently run about once per week during datataking to monitor performance. The plots in Figure 3.6 show the threshold

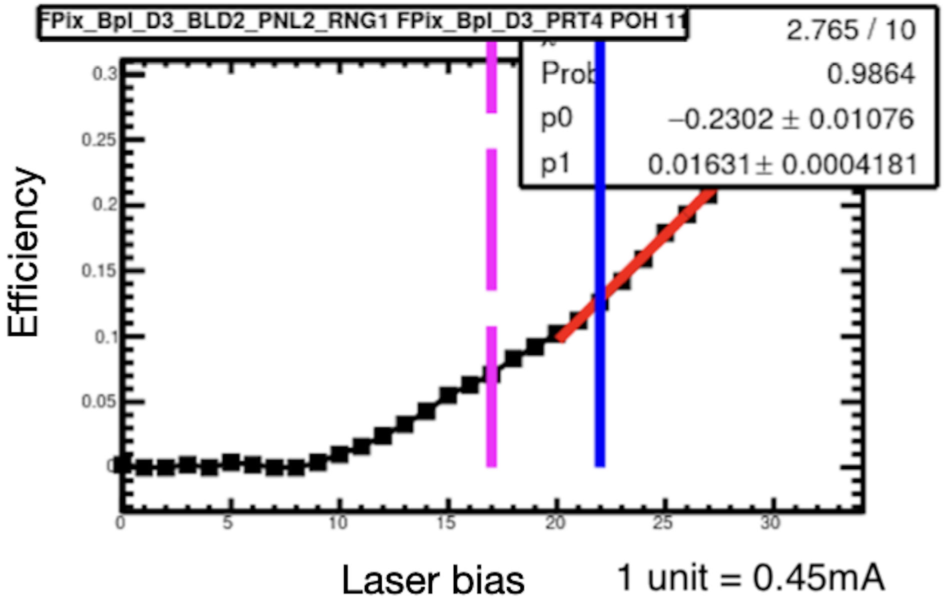

Figure 3.4: Output of a POH bias scan calibration. The pink dashed line shows the current setting and the blue line shows the proposed setting. It is best to have a POH bias setting where there is a constant slope, highlighted by the red line. A constant slope corresponds to a constant and clear difference in 0 and 1 in the optical signal.

measurement taken in November 2022 for BPix and FPix, respectively. The response of individual pixels to an injected charge was done with a PixelAlive calibration, which outputs a response map of individual pixels, as shown in Figure 3.7. A gain calibration measured the pixel amplifier response by injecting fixed units of charge, VCal, and measuring the corresponding pulse height in units of ADC.

3.3 Installation

After being refurbished and calibrated in the clean room, BPix and FPix were installed in their place in CMS. This was a delicate procedure over two weeks in late June and early July 2021. It first required the half cylinders to be lowered down the CMS shaft via crane, as pictured in Figure 3.8. BPix was installed one half at a time. FPix is split into quarters, so the inner and out quarters were aligned on the z plus end before a synchronized push was done to move them to their installed locations. The process was repeated with the other two quarters on the minus end [49]. Figure 3.9 shows half

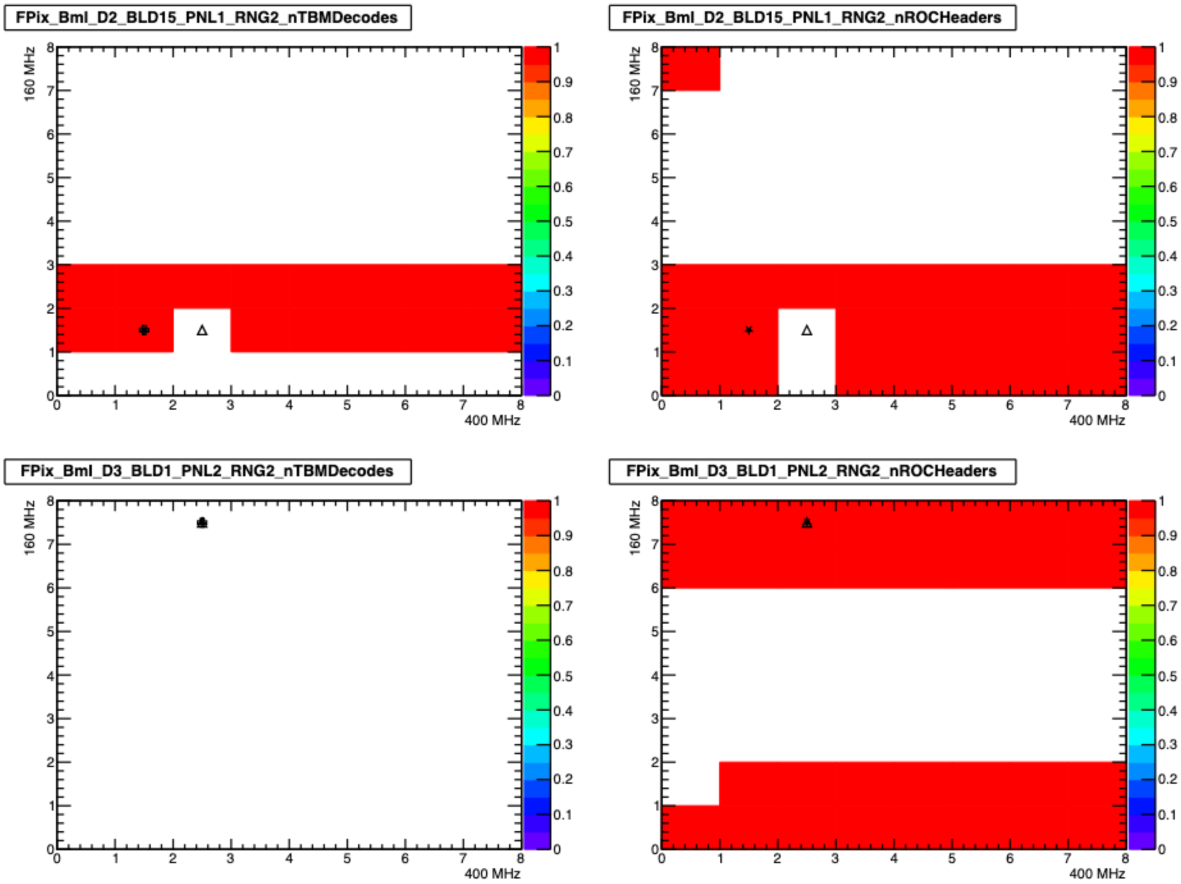

Figure 3.5: Calibration of TBM register settings for both the 160MHz and 400 MHz streams. The triangle denotes the current setting, the cross denotes the suggested setting, and the black star denotes the suggested setting from Pixel Online Software. The color scale is the efficiency for decoding the correct number of TBMs (left plots) and the correct number of ROCs (right plot). Note that in the top two plots, which come from module FPix BmI Disk 2, Panel 1, Ring 2, the current setting is in a space with no efficiency reading. This register can be reset to have full efficiency. This can be constrasted with the bottom two plots, corresponding to FPix BmI Disk 3 Blade 1, Panel 2, Ring 2, which has no proposed settings with any efficiency for the correct number of TBMs. This module is faulty and has been masked since the beginning of Run 3.

cylinders of FPix with a close up of the modules and a view of the service cylinder. Once the subdetector was put in its position, the cooling connections and power cables were connected at the pixel bore as seen in Figure 3.10.

3.4 Operations

When the LHC delivers stable beams, a stable beam report is completed with checks:

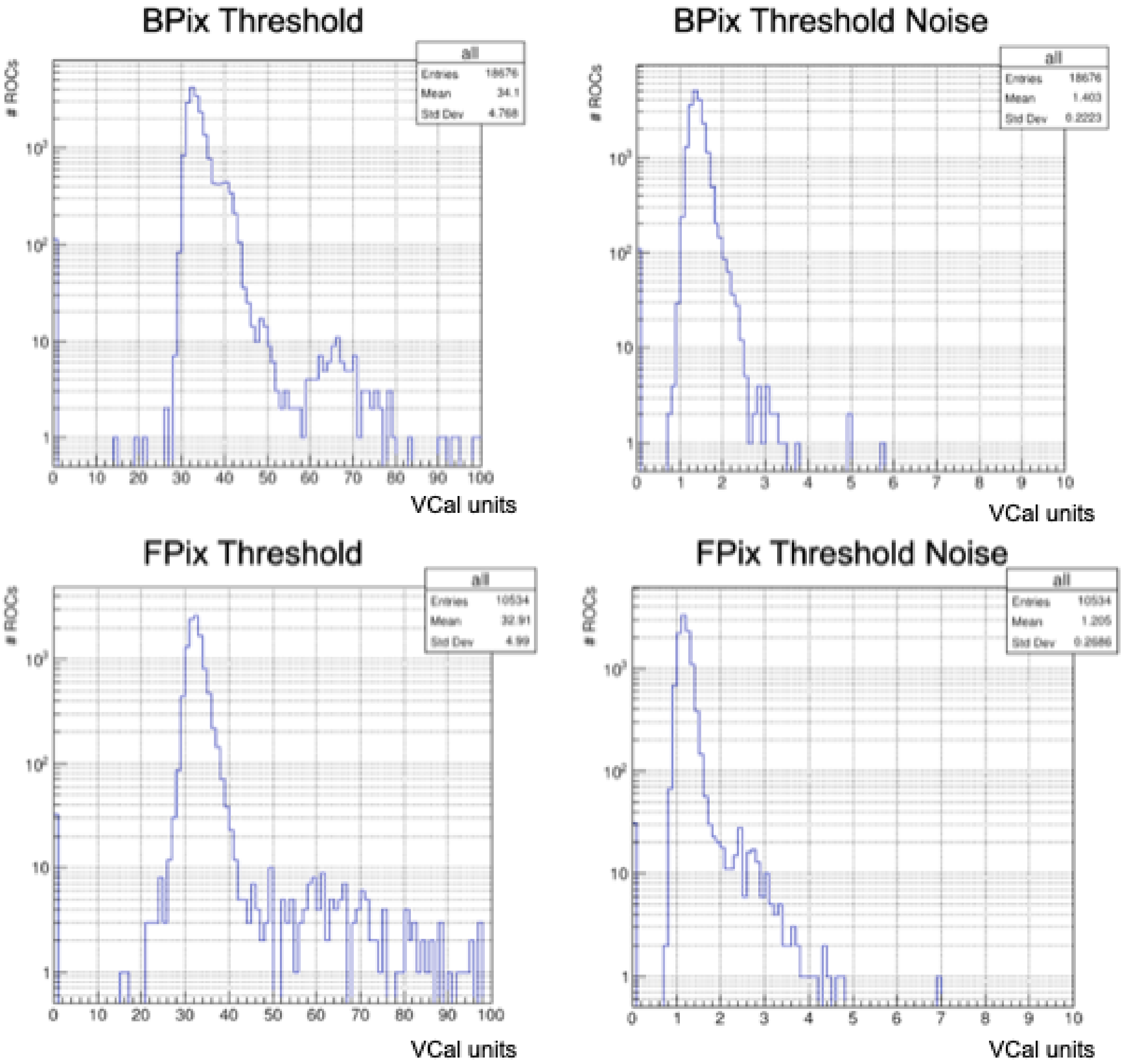

Figure 3.6: Threshold calibration of BPix and FPix. The VCal units are charge calibration units, each equal to 50 electron charge units. The expected value for the threshold is around 30 VCal units for FPix and layers 2,3, and 4 of BPix. Layer 1 of BPix has a higher threshold around 40 VCal units. The tail in the threshold plots corresponds to sensors with DCDC damage.

- Dectector Control System: Control power, LV, and HV are ON for the pixel tracker, and there are no alarms present.
- Data Acquistion: All pixel tracker FEDs are included in the run and successfully sending data to CMS central DAQ without causing unacceptably high deadtime.

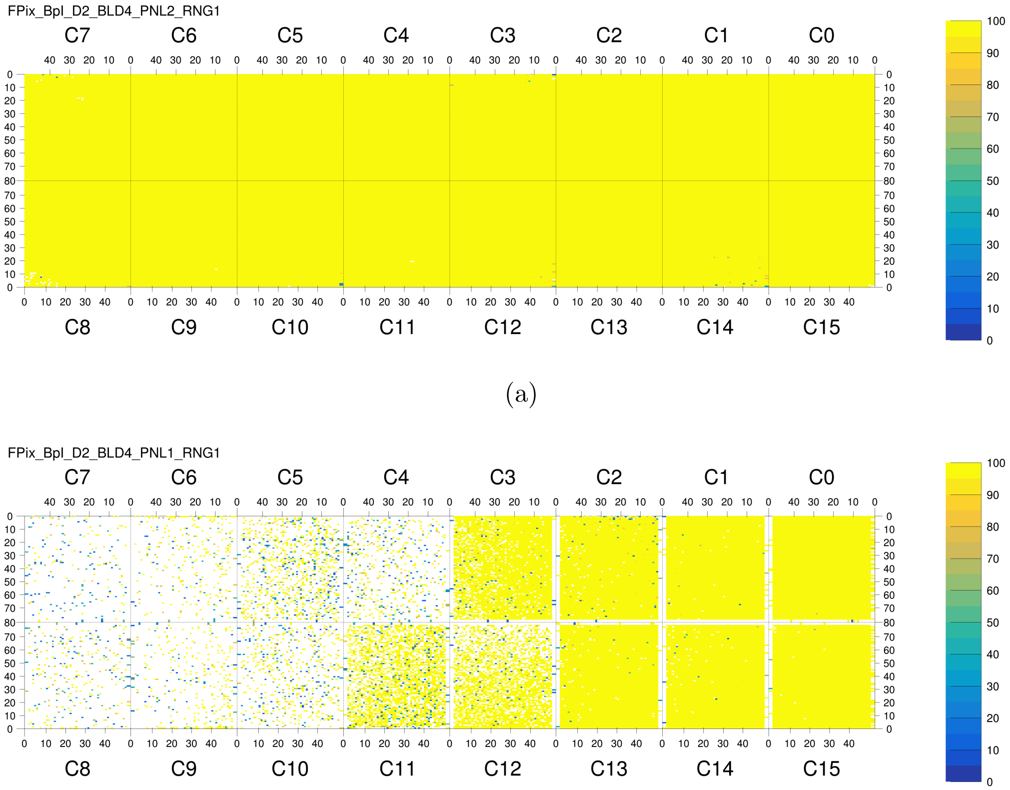

(a)

(b)

Figure 3.7: The PixelAlive calibration shows the response of individual pixels to injected charges. The top plot (a) shows a properly functioning module, and the bottom plot (b) shows a module that sustained DCDC damage.

- Data Quality Monitoring: Plots of occupancy and on-track cluster charge and size look as expected.

3.4.1 Bias voltage scan and settings

The settings of the pixel detector were optimized at the beginning of data taking. During the Pilot Beam Test of 2021, a timing scan was completed to find optimal settings. When stable beams at 900 GeV were delivered, a mini version of the timing scan (five different timing settings used for about four minutes per point) was performed. For stable beams at 13.6 TeV, the full timing scan (21 different timing settings used for about ten minutes per point) was done. Timing scans will be completed periodically throughout Run 3 to verify the settings are still appropriate, though they are not expected to shift.

The optimal bias voltage settings evolve over time, especially those for BPix layer 1,

(a) (b)

Figure 3.8: An FPix half cylinder protected in a cylinder transport unit and vibration isolation frame being lowered down the shaft of CMS.

and those scans are taken weekly. During the mini bias voltage scan, the voltages are changed simultaneously on six different modules, each representing their layer in BPix or disk in FPix. For FPix, the scan is performed by changing settings on the disks in different z-positions, but the bias setting during standard operation is set based on the rings at different radii. For stable beams at 13.6 TeV, the full high voltage bias scan with 15 bias settings tested for about four minutes each. In this case, entire layers of BPix and disks of FPix had their settings changed at once instead of only one representative module. The exact settings tested are listed in Table 3.1. Although the full version of the bias setting scans gives measurements more robust against anomalous behavior of single modules, they also cause the data delivered during the test to be unusable as physics data, so the mini scans are used when possible.

The analysis of these scans is completed by the Detector Performance Group. The settings at the beginning of Run 3 are listed in Table 3.2. Figure 3.11 shows a performance measurement as a function of bias voltage after 11 fb^{-1} of data was collected. Figure 3.12 demonstrates the need to keep the bias voltage setting updated.

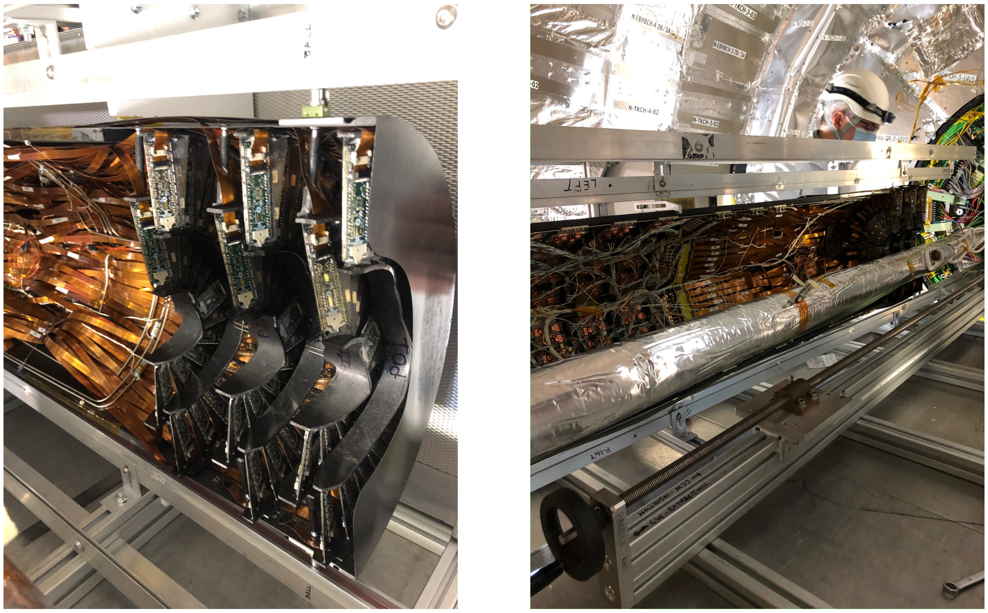

(a) (b)

Figure 3.9: Left: Modules are arranged in a half moon shape to form a half cylinder of FPix. Right: One of two service cylinders next to the beampipe before being aligned with the second half cylinder and then moved into the bore with a synchronized push.

BPix Layer/FPix Disk	Bias voltage settings (V)
Layer 1	5, 10, 15, 20, 25, 30, 35, 40 , 50 , 60 70, 80, 100, 125, 150
Layer 2	10, 20, 30, 40, 50, 60, 70, 80, 90, 100, 125, 150, 200, 250, 300
Layer 3	10, 20, 30, 40, 50, 60, 70, 80, 90, 100, 150, 200, 250, 300, 400
Layer 4	5, 10, 15, 20, 25, 30, 40, 50, 60, 80, 100, 150, 200, 250, 350
Disks 1, 2, 3	10, 20, 30, 40, 50, 60, 70, 80, 90, 100, 150, 200, 250, 300, 400

Table 3.1: The voltage points scanned for the first scan of Run 3. These points are adjusted over time as higher values are needed.

3.4.2 Powercycling during interfill periods

As particles bombard the pixel tracker during stable beams, a single event upset can occur in important registers in TBMs. When this happens, the corresponding module must be powercycled to restore function. However, this powercycling is not possible during stable beams. While the stable beams are still declared, the module is masked by the FED. Once the fill is over, the FED channel number is translated to CCU address and DCDC

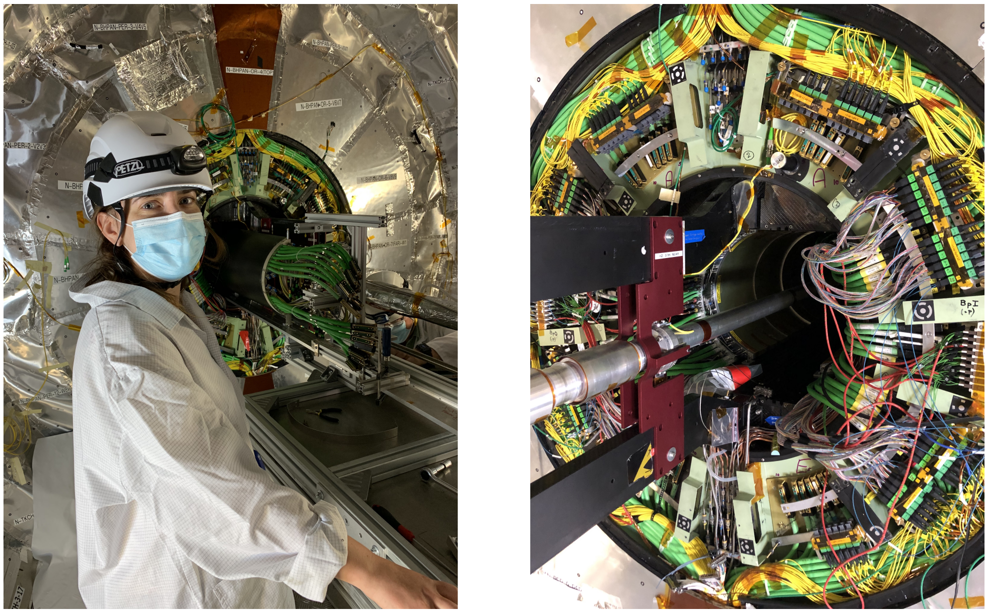

(a) (b)

Figure 3.10: Left: The author in front of the pixel bore during installation. Right: A view of the beampipe and cooling and powering connections at the PP0 patch panel.

Component	Bias voltage (V)
BPix layer 1	150
BPix layer 2	300
BPix layer 3	250
BPix layer 4	250
FPix ring 1	350
FPix ring 2	300

Table 3.2: HV bias settings for different layers and rings at the beginning of Run 3.

number, then the powercycling is done by executing CCU commands. Automating this process with a script greatly simplified the number of commands typed by hand by on-call shifters.

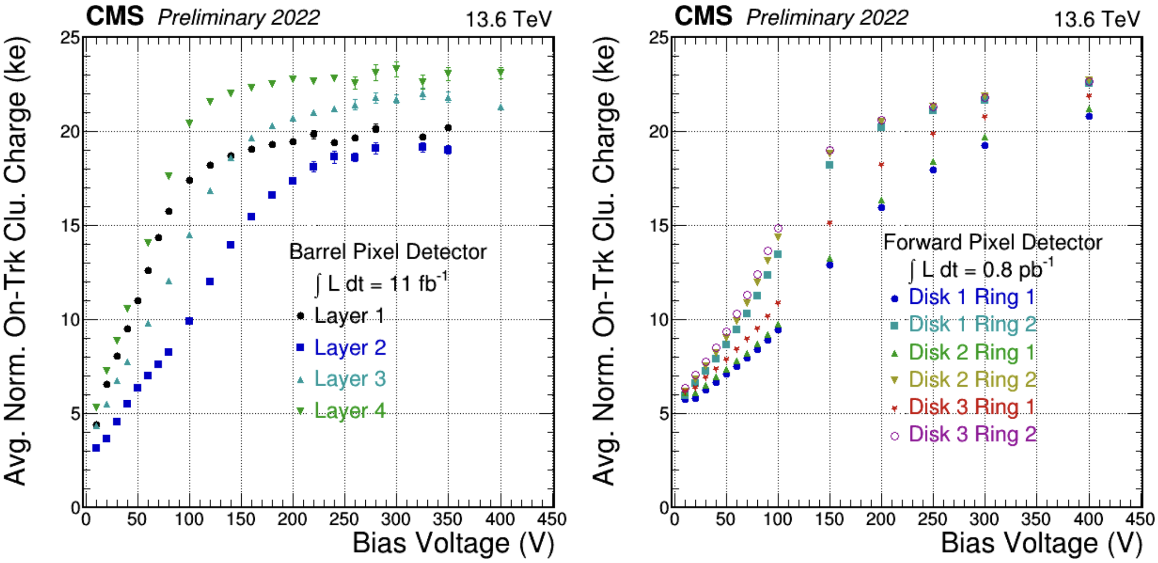

Figure 3.11: The average normalized on-track cluster charge for different layers of BPix and rings of FPix as a function of bias voltage. Note the new layer 1 of BPix performance is already lower than layers 3 and 4 which have been in use since 2017 [24].

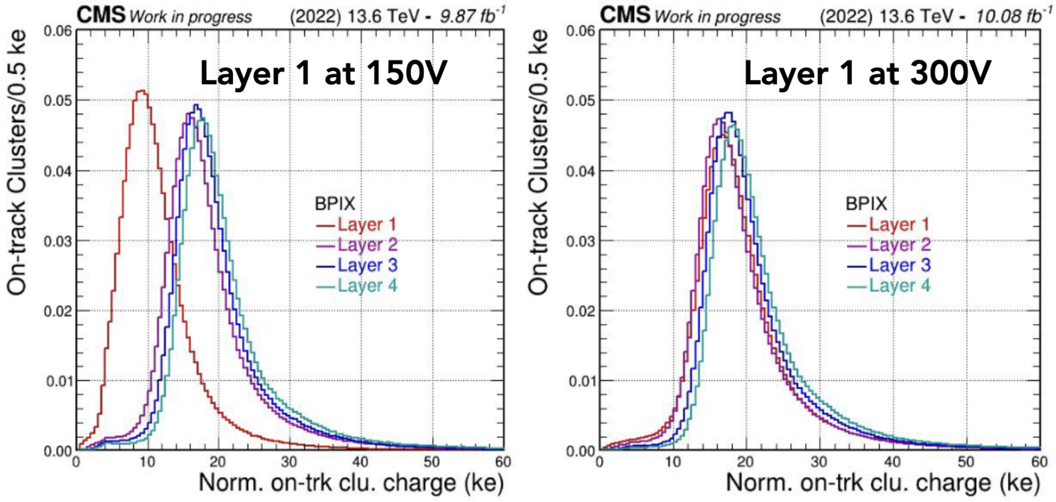

Figure 3.12: The bias voltage scan of layer 1 showed the bias voltage needed to be increased from 150 V to 300 V. Once the setting was updated, the performance of layer 1 improved as seen with the increase in normalized on-track cluster charge [24].

3.5 Safety of detector

There are multiple considerations for the safety of the detector. Especially as the LHC prepared for Run 3, there were scrubbing periods with the beam. Scrubbing refers to the process in which a high-energy beam is used to clean the beampipe of the LHC.

Historically, the pixel tracker has been turned off during these scrubbing periods to ensure any stray particles would not damage the detector. Scrubbing periods were often paired with machine development periods which required the pixel detector to be turned off anyway. However, the scrubbing periods leading up to Run 3 were interleaved with physics commissioning periods. Thus it had to be decided whether to complete many full power cycles of the detector, miss out on physics commissioning periods for CMS, or leave the detector as LV ON during scrubbing periods. The safety checks on the LHC beams during scrubbing are similar to those enforced before declaring stable beams, with the collimators left in place. The policy was changed to leave the detector in LV ON during scrubbing, and no damage to the detector occurred.

Once stable beams are declared, the pixel tracker and tracker strips should go to HV ON as soon as possible to collect physics data. This process is automated and happens according to the tracker semaphore. The tracker semaphore is maintained by the beam conditions and luminosity team. It has inputs from beam loss and beam background measurements that use a silicon pad detector and polycrystalline diamond and sapphire solid state sensors, which measure the number of MIPs/cm^{2}s. If over certain thresholds, it will prevent the pixel tracker and tracker strips from automatically turning HV ON. Additional checks were added to the core logic for Run 3, such as checking the number of active abort channels and doing a“sanity check” on the actual values for thresholds, given in ADC units.

3.6 Performance in Beginning of Run 3

Figure 3.13 shows the integrated luminosity of proton-proton collision data collected by CMS during 2022, the first year of Run 3. The CMS certified data had all detectors participating in the run and good performance from reconstructed physics objects. The active detector fraction of the pixel tracker is shown in Figure 3.14. This shows the number of modules that are included for data-taking in physics runs during stable beams. The residuals in the r-ϕ plane in Figure 3.15 show the position resolution performance of the pixel tracker which is crucial to the overall success of CMS tracking.

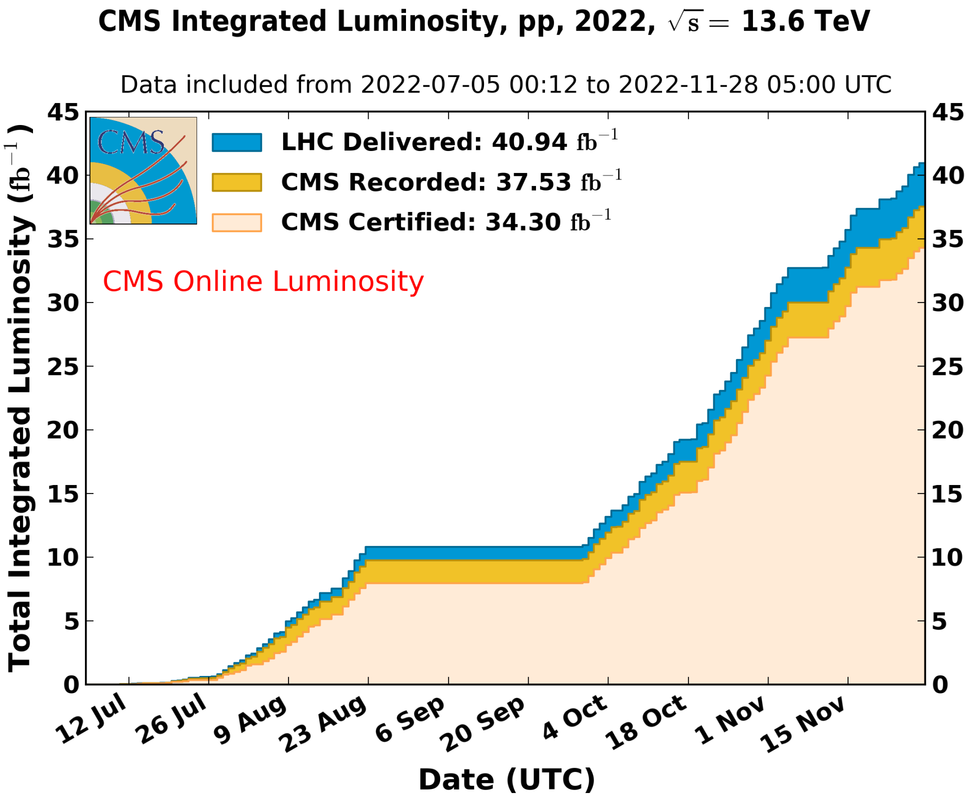

Figure 3.13: Integrated luminosity delivered by the LHC (azure), recorded by CMS (orange), and certified as good for physics analysis during stable beams (pale orange) [25].

3.7 Radiation Damage Investigation

The ATLAS experiment published measurements of radiation damage in their pixel detector and observed a greater z-dependence in the fluence-to-luminosity with calculations based on the Hamburg model and leakage current measurements as compared to simulation results (Pythia and FLUKA or Pythia and GEANT) [50]. The cabling scheme of the ATLAS pixel detector allows continuous readout of leakage currents during datataking periods separated by the z-position of their pixel modules.

For CMS, this continuous monitoring of leakage current as a function of z-position is not possible with the installed detector. The study of individual modules at different z-positions was done only after the pixel detector was extracted from CMS at the end of Run 2. Because BPix layer 1 was then replaced for Run 3, the old BPix layer 1 was available for studies. The z-dependence of radiation damage experienced by CMS pixel modules was investigated by measuring IV curves by performing bias scans and measuring

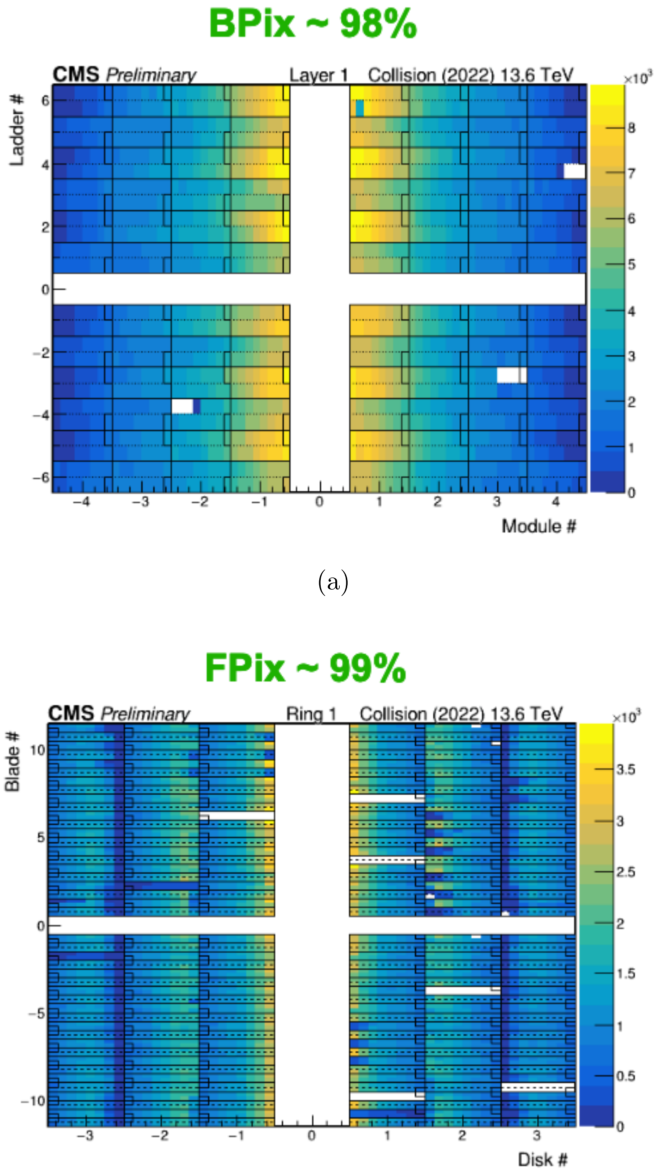

(a)

(b)

Figure 3.14: Occupancy plots of BPix layer 1 (top) and FPix ring 1 (bottom). The modules at smaller radii have higher occupancy, and the white rectangles show the modules that are masked during datataking [24].

the corresponding leakage currents. A test setup was prepared in the pixel clean room with a DAQ test board, the individual modules, a Keithley power supply, and a PC with some calibration software: psi46 and PXar. This allowed access to the cables connected to individual modules so individual IV curves could be measured for each. The half of

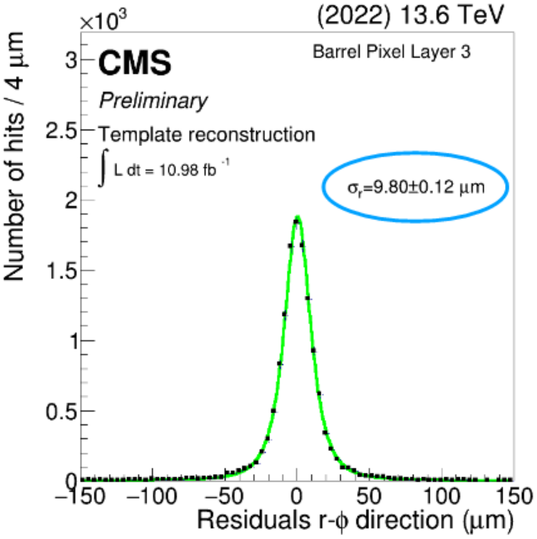

Figure 3.15: The resolution in the r-ϕ direction for BPix layer 3 and FPix disk 2. The performance is comparable to Run 2 performance [24].

BPix layer 1 used for this study is shown in Figure 3.16.

Figure 3.16: BPix layer 1 modules that were available to be tested in the clean room. In this picture they are sitting in the freezer.

Figure 3.17 is a representative plot of leakage current measurements at a 250V bias voltage as a function of z-position. There is not a clear trend of z-dependence for the radiation damage based on these measurements. The study was limited by the number of modules available to test. The complete measurements for the IV curves are shown in Figures 3.18, 3.19, and 3.20. These figures each have four different plots that correspond to the four different $|z|$-positions. Figure 3.18 shows the plus side and minus side in different colors, and Figure 3.19 shows sectors in ϕ in different colors. If there was perfect symmetry in z and ϕ, the effects of radiation damage would not be expected to have dependencies on these variables. However, in reality the pixel detector is not perfectly centered on the beam axis, so it could be possible to observe the effects of this asymmetry. Similarly, Figure 3.20 shows the inner and outer ladders in different colors. Although these are all layer 1 modules, there are some outer ladders at a radius of 3.056 cm and inner ladders at a radius of 2.856 cm. One may expect a difference in radiation damage due to the inner ladders being slightly closer to the beam axis. However, there is a such a large spread in the measurements for modules at the same z-positions that none of these smaller possible effects are observed.

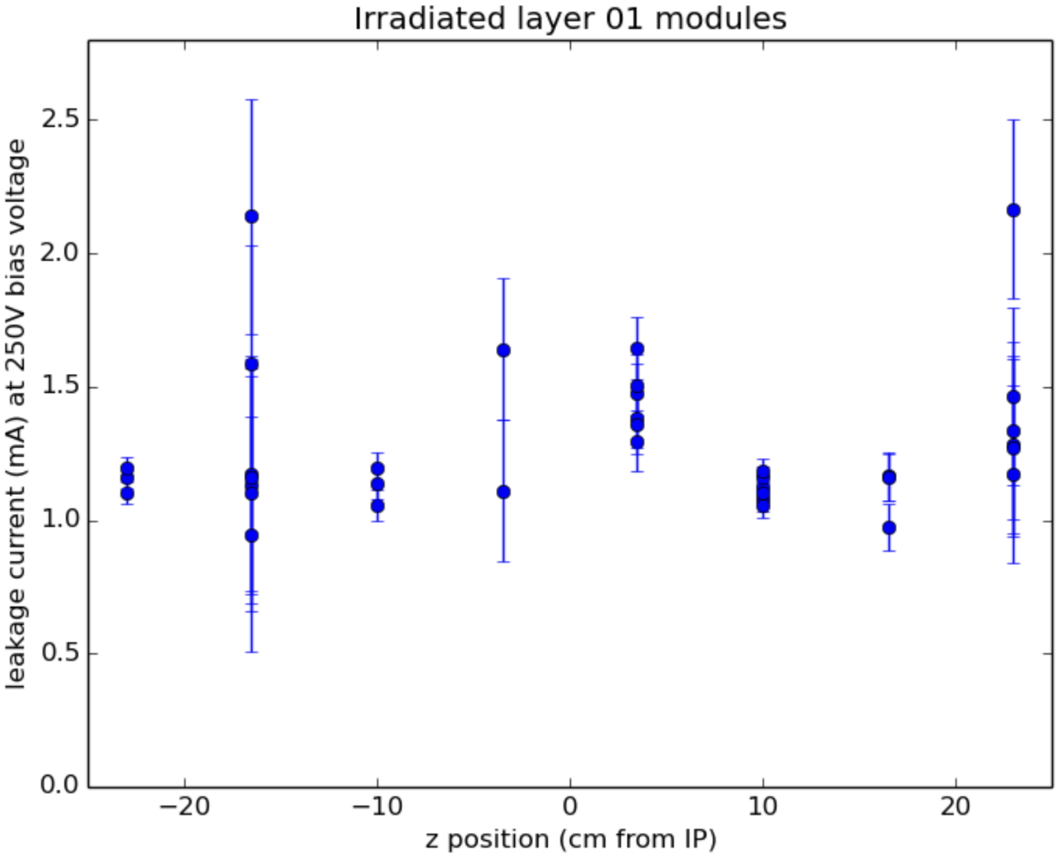

Figure 3.17: The leakage current at of different modules at 250 V as a function of z-position. There are different numbers of measurements at different z-positions because some modules had unstable connections or were not properly included in the connection mapping documentation. The error bars correspond to the root-mean-square deviation that depends on the number of data points for each z-position.

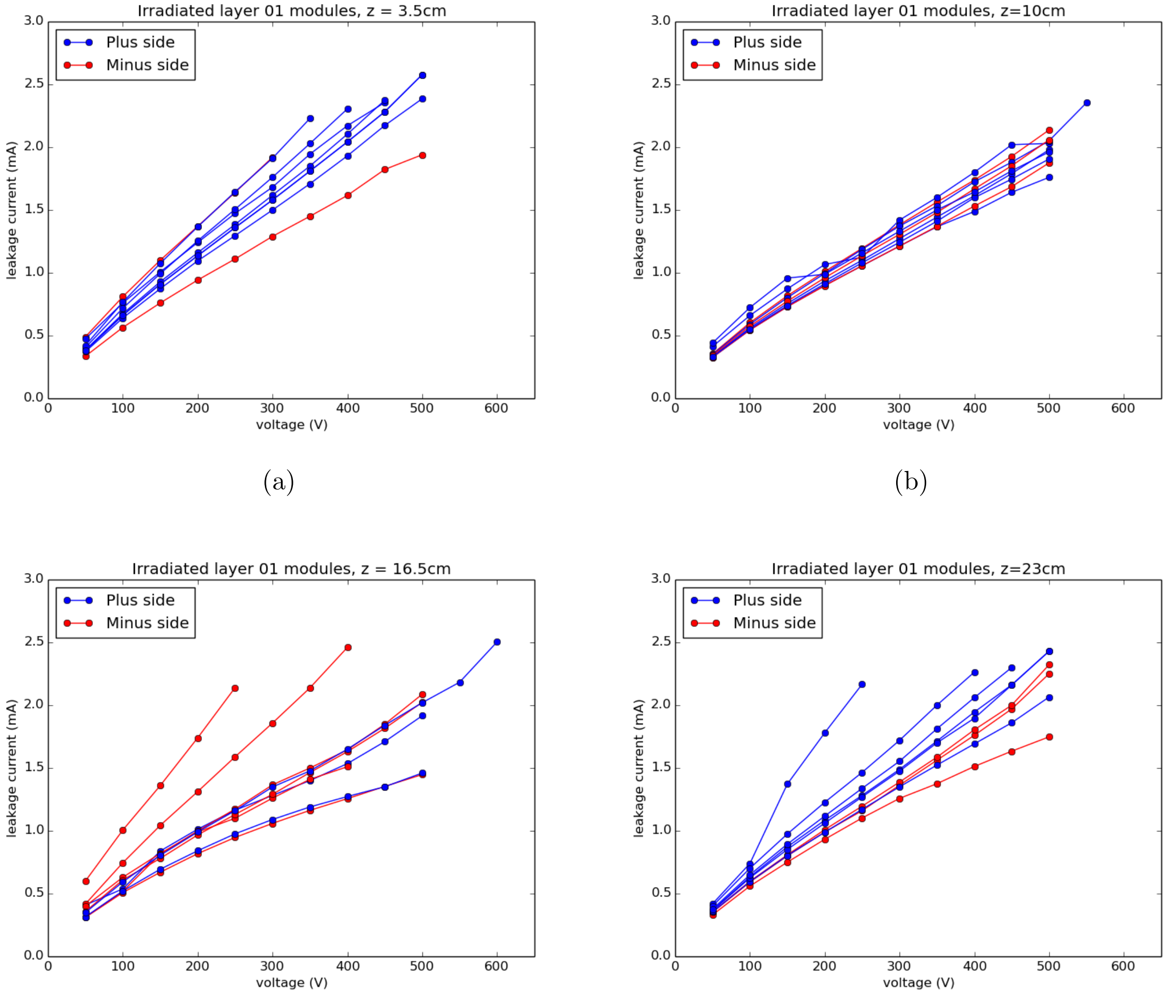

(a)

(b)

(c)

(d)

Figure 3.18: Leakage current as a function of bias voltage. Figure (a) shows the measurements for modules at z=3.5cm, Figure (b) with z=10 cm, Figure (c) with z=16.5 cm, and Figure (d) with z=23 cm. The blue curves show modules on the plus end of CMS and the red curves show modules from the minus end of CMS.

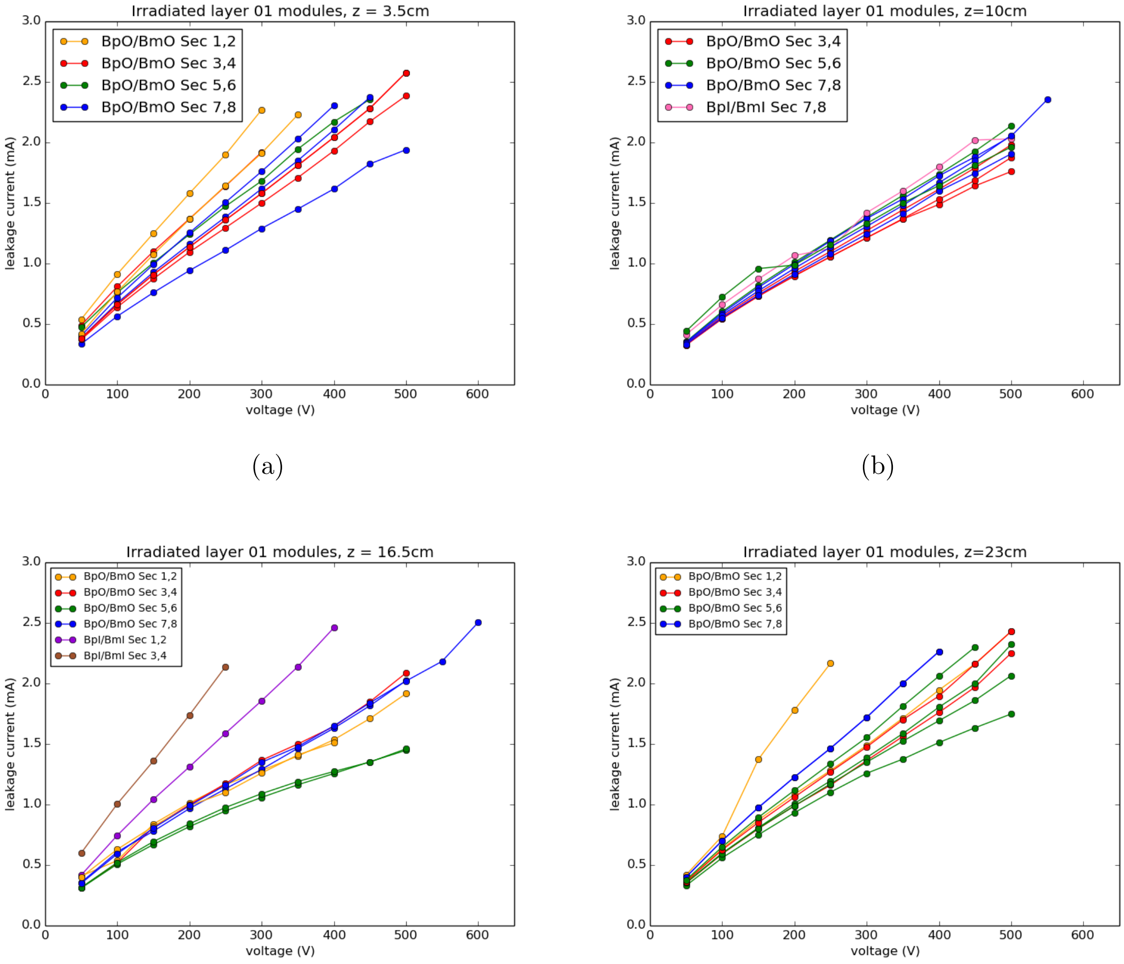

(a) (b)

(c) (d)

Figure 3.19: Leakage current as a function of bias voltage. Figure (a) shows the measurements for modules at z=3.5 cm, Figure (b) with z=10 cm, Figure (c) with z=16.5 cm, and Figure (d) with z=23 cm. The different colors correspond to different sectors, which are slices in the ϕ coordinate.

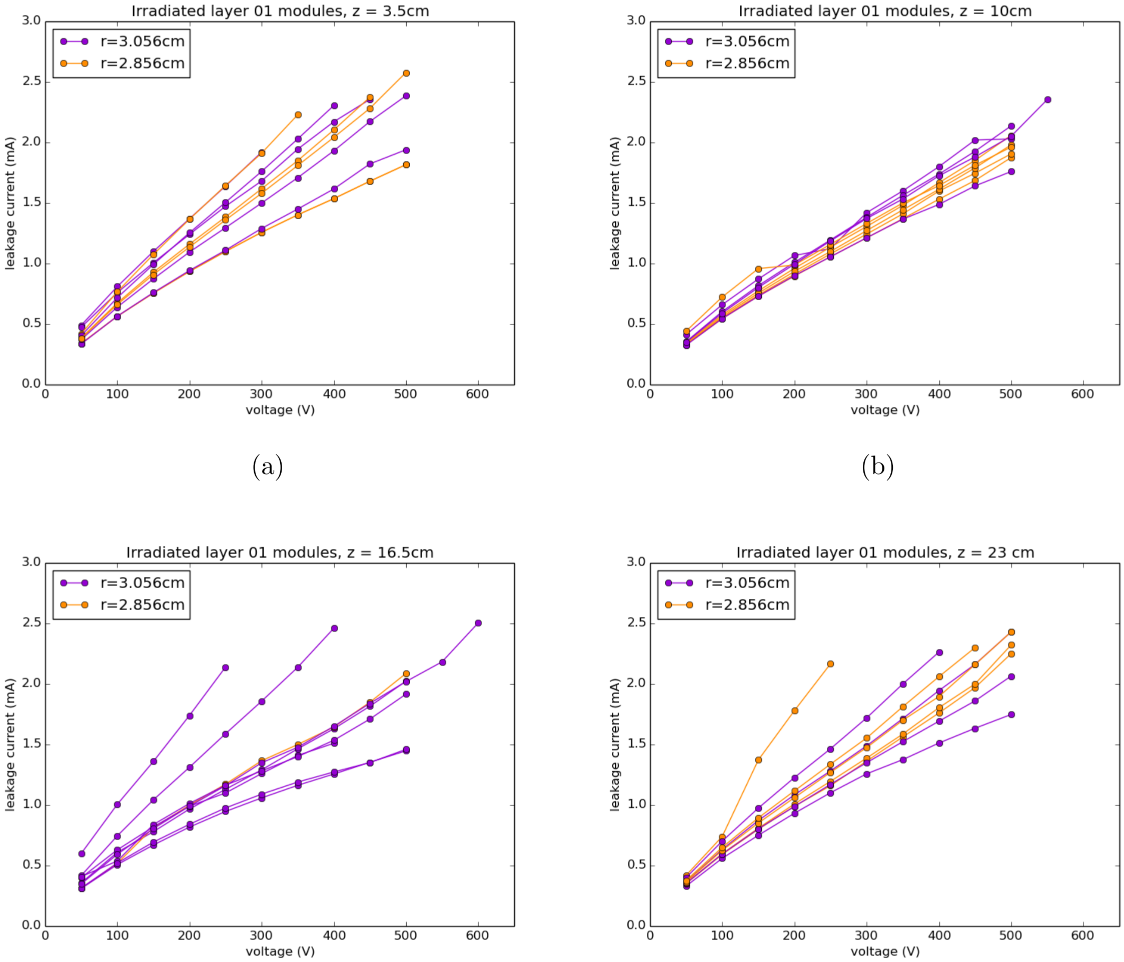
Irradiated layer 01 modules, z = 3.5cm

Irradiated layer 01 modules, z = 10cm

Irradiated layer 01 modules, z = 16.5cm

Irradiated layer 01 modules, z = 23 cm

(a)

(b)

(c)

(d)

Figure 3.20: Leakage current as a function of bias voltage. Figure (a) shows the measurements for modules at z= 3.5cm, Figure (b) with z=10 cm, Figure (c) with z=16.5 cm, and Figure (d) with z=23 cm. The orange curve show modules on the inner ladder and the purple curves show modules on the outer ladders, which leads to a difference in their radial positions.

Chapter 4

Search for a Light Pseudoscalar Higgs Boson with Run 2 Data

A search is performed for the decay of a 125 GeV or higher mass Higgs boson to a low mass pseudoscalar Higgs boson (a) through H $\rightarrow$ aa $\rightarrow$ $\mu\mu\tau\tau$. This chapter provides details about the datasets and Monte Carlo (MC) samples used and object definitions for electrons, muons, and taus. DeepDiTau, a machine learning application designed to identify pairs of overlapping hadronic tau decays that are reconstructed as jets, is presented. The strategy for event selection and background modeling for all channels is discussed, and the fitting procedure and expected limits are presented. In this document, plots labeled "CMS Preliminary" correspond to "CMS Work in Progress" or private plots.

4.1 Overview

The search for a light pseudoscalar Higgs boson is motivated by 2HDM+S and the NMMSM. Details on these models are presented in Section 1.3.2. To take advantage of the CMS detector's high efficiency of reconstructing muons and the large branching fraction to taus of the pseudoscalar Higgs boson, the channel investigated is H $\rightarrow$ aa $\rightarrow$ $\mu\mu\tau\tau$ as depicted in Figure 4.1. The Higgs boson masses range from 125 GeV, corresponding to the discovered particle, up to to 1000 GeV to include the search for heavier, exotic Higgs boson. Because the boosted topology with overlapping leptons is a result of the difference between m$_H$ and m$_a$, as the Higgs boson mass increases, the pseudoscalar Higgs boson mass range being probed also increases, as reflected in Table 4.1. The pseudoscalar Higgs boson masses in this search range from 4 to 50 GeV.

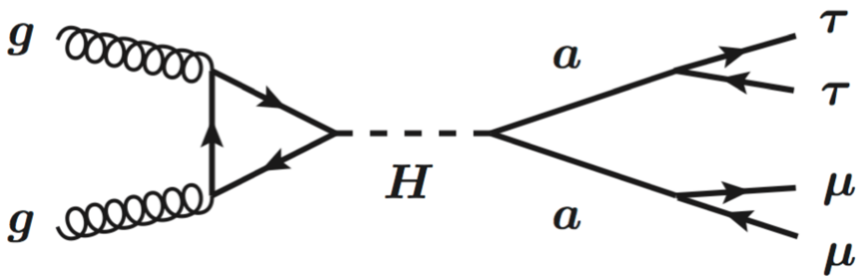

Figure 4.1: Gluon-gluon fusion production of a Higgs boson that decays to pseudoscalar Higgs bosons, which then decay to muons and taus.

m_H (GeV)	m_a (GeV)
125	4, 5, 6, 7, 8, 9, 10, 11, 12, 13, 14, 15, 16, 17, 18, 19, 20, 21
250	5, 10, 15, 20
500	5, 10, 15, 20, 25
750	10, 15, 20, 25, 30
1000	10, 20, 30, 40, 50

Table 4.1: Values of m_H with the corresponding m_a values for which there are signal samples. As m_H increases, the greatest value of m_a to which the search is sensitive also increases.

Due to the short lifetime (2.9x10^{-13} s) of taus, their decay products are what is measured by CMS. These decay products are often merged together due to the kinematic "boost" from the mass difference between the Higgs boson and pseudoscalar Higgs boson. Taus can decay several different ways, and the relative fractions of these final states are shown in Figure 4.2. Various hadronic decay channels are collectively referred to as τ_h.

In the case of both taus decaying hadronically, the largest background to the $\mu\mu\tau\tau$ signal is continuum and resonant production of muon pairs from the Drell-Yan process plus jets. Though CMS has software techniques tailored for the identification of a hadronic tau decay, they are not designed for the case where two of these decays overlap. To make feasible including the case of both taus decaying hadronically, machine learning techniques are developed to identify or “tag” the decay products of overlapping hadronic tau decays. In the case of one tau decaying hadronically and one decaying leptonically, a novel technique of “lepton cleaning” is applied, which involves removing a muon or electron from the group of particles to be reconstructed as a hadronic tau using standard CMS algorithms as shown in Figure 4.3. When both taus decay leptonically, standard selection criteria on lepton objects are applied. Using 2016 CMS detector data and only the $\tau_\mu\tau_h$ decay channel, the previous version of the analysis set the best limits on H → aa for most of the pseudoscalar Higgs boson mass range of $3 - 20$ GeV [8].

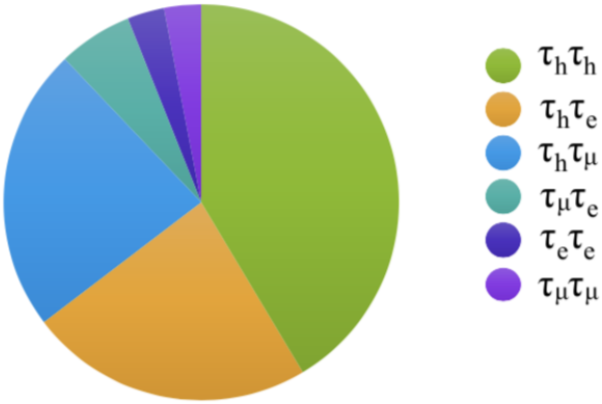

Figure 4.2: Relative rates of different tau decays. A hadronic tau decay is denoted by τ_h, $\tau \to \mu\nu_\tau\nu_\mu$ by τ_μ, and $\tau \to e\nu_\tau\nu_e$ by τ_e. Note the relative importance of the $\tau_h\tau_h$ case.

4.2 Datasets, trigger, and MC samples

This analysis uses data collected by the CMS experiment during 2016, 2017, and 2018 at $\sqrt{s} = 13$ TeV. The `SingleMu` primary datasets are used, which consist of events passing either the `HLT_IsoMu24` or the `HLT_IsoTkMu24` trigger, both of which require a single isolated muon with transverse momentum (p_T) greater than 24 GeV. For 2017 data, the `HLT_IsoMu27` and `HLT_IsoTkMu27` triggers that have a 27 GeV muon momentum requirement are also included. The names of the datasets along with the run ranges and integrated luminosity are shown in Table 4.2, which corresponds to a total integrated luminosity of 137 fb^{-1}.

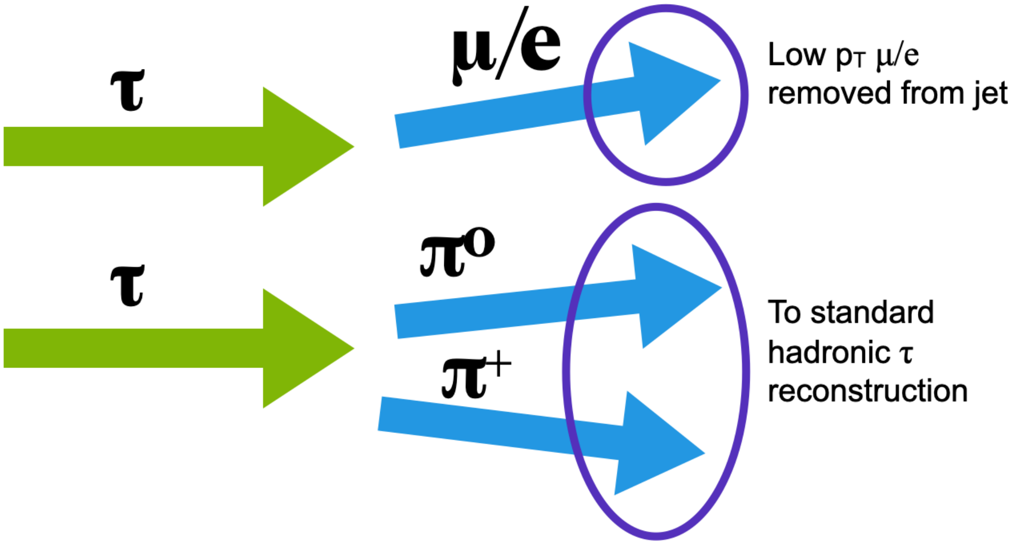

Figure 4.3: The lepton cleaning technique. One tau decays leptonically, either to an electron (e) or muon (μ) plus neutrinos. The lepton is removed from the hadronic decay products of the other tau (charged and neutral pions) that are sent to standard hadronic tau reconstruction. This technique is up to 40% more effective in reconstructing $\tau_\mu \tau_h$ [8].

The required background MC samples are from Drell-Yan, $t\bar{t}$, W plus jets, and diboson production (ZZ, WZ, ZZ). The samples used for 2016, 2017, and 2018 are summarized in Table 4.3. The signal MC samples are Ultra Legacy simulations of events with H → aa → $\mu\mu\tau\tau$ where the Higgs boson is produced from gluon-gluon fusion. The samples are listed in Table 4.4 [51].

4.3 Objects

The definitions for electrons, muons, and taus used in event selections are presented in this section. Standard electron and muon identification definitions are used, but the tau identification and reconstruction varies based on decay channel. Cuts may depend on relative isolation:

$$I_{\text{rel}} = \Big[\sum_{\text{charged}} p_T + \max\Big(0, \sum_{\text{neutral}} p_T + \sum_{\gamma} p_T - \frac{1}{2} \sum_{\text{charged,PU}} p_T \Big) \Big] / p_T \tag{4.1}$$

where the sums of the magnitudes of transverse momenta of charged hadrons, electrons, and muons ($\sum_{\text{charged}} p_T$) , neutral hadrons ($\sum_{\text{neutral}} p_T$), and photons ($\sum_\gamma p_T$) are from

Dataset	$\mathcal{L}$ (fb^{-1})
2016	35.92
/SingleMuon/Run2016B-ver2_HIPM_UL2016_MiniAODv2-v2/MINIAOD	
/SingleMuon/Run2016C-HIPM_UL2016_MiniAODv2-v2/MINIAOD	
/SingleMuon/Run2016D-HIPM_UL2016_MiniAODv2-v2/MINIAOD	
/SingleMuon/Run2016E-HIPM_UL2016_MiniAODv2-v2/MINIAOD	
/SingleMuon/Run2016F-HIPM_UL2016_MiniAODv2-v2/MINIAOD	
/SingleMuon/Run2016F-UL2016_MiniAODv2-v2/MINIAOD	
/SingleMuon/Run2016G-UL2016_MiniAODv2-v2/MINIAOD	
/SingleMuon/Run2016H-UL2016_MiniAODv2-v2/MINIAOD	
2017	41.53
/SingleMuon/Run2017B-UL2017_MiniAODv2-v1/MINIAOD	
/SingleMuon/Run2017C-UL2017_MiniAODv2-v1/MINIAOD	
/SingleMuon/Run2017D-UL2017_MiniAODv2-v1/MINIAOD	
/SingleMuon/Run2017E-UL2017_MiniAODv2-v1/MINIAOD	
/SingleMuon/Run2017F-UL2017_MiniAODv2-v1/MINIAOD	
2018	59.74
/SingleMuon/Run2018A-UL2018_MiniAODv2-v2/MINIAOD	
/SingleMuon/Run2018B-UL2018_MiniAODv2-v2/MINIAOD	
/SingleMuon/Run2018C-UL2018_MiniAODv2-v2/MINIAOD	
/SingleMuon/Run2018D-UL2018_MiniAODv2-v3/MINIAOD	

Table 4.2: Collision datasets and associated integrated luminosity

the primary vertex and the last sum in the equation ($\sum_{\text{charged,PU}} p_T$) is the contribution from other reconstructed vertices [26].

4.3.1 Electrons

The requirements for standard CMS electron categories `isLooseElectron` and `isTightElectron` are listed in Table 4.5 and Table 4.6 respectively. In this analysis,

Year	Physics processes	Dataset name	σ (pb)
2018	Z/γ^*	DYJetsToLL_M-50_TuneCP5_13TeV-madgraphMLM-pythia8/RunIISummer20UL18MiniAODv2-106X_upgrade2018_realistic_v16_L1v1-v2/MINIAODSIM	5398.0
	$t\bar{t}$	TTJets_TuneCP5_13TeV-amcatnloFXFX-pythia8/RunIISummer20UL18MiniAOD-106X_upgrade2018_realistic_v11_L1v1-v1/MINIAODSIM	750.5
	W-Jets	WJetsToLNu_TuneCP5_13TeV-madgraphMLM-pythia8/RunIISummer20UL18MiniAODv2-106X_upgrade2018_realistic_v16_L1v1-v1/MINIAODSIM	53870.0
	Di-Boson	WW_TuneCP5_13TeV-pythia8/RunIISummer20UL18MiniAODv2-106X_upgrade2018_realistic_v16_L1v1-v1/MINIAODSIM	75.95
	Di-Boson	WZ_TuneCP5_13TeV-pythia8/RunIISummer20UL18MiniAODv2-106X_upgrade2018_realistic_v16_L1v1-v1/MINIAODSIM	27.59
	Di-Boson $(\ell\nu)(\ell\ell)$	WZTo3LNu_TuneCP5_13TeV-amcatnloFXFX-pythia8/RunIISummer20UL18MiniAODv2-106X_upgrade2018_realistic_v16_L1v1-v2/MINIAODSIM	5.213
	Di-Boson	ZZ_TuneCP5_13TeV-pythia8/RunIISummer20UL18MiniAOD-106X_upgrade2018_realistic_v11_L1v1-v2/MINIAODSIM	12.17
	Di-Boson $(\ell\ell)(\ell\ell)$	ZZTo4L_TuneCP5_13TeV_powheg-pythia8/RunIISummer20UL18MiniAODv2-106X_upgrade2018_realistic_v16_L1v1-v2/MINIAODSIM	1.325
2017	Z/γ^*	DYJetsToLL_M-50_TuneCP5_13TeV-madgraphMLM-pythia8/RunIISummer20UL17MiniAODv2-106X_mc2017_realistic_v9-v2/MINIAODSIM	5398.0
	$t\bar{t}$	TTJets_TuneCP5_13TeV-amcatnloFXFX-pythia8/RunIISummer20UL17MiniAODv2-106X_mc2017_realistic_v9-v2/MINIAODSIM	750.5
	W-Jets	WJetsToLNu_TuneCP5_13TeV-madgraphMLM-pythia8/RunIISummer20UL17MiniAODv2-106X_mc2017_realistic_v9-v1/MINIAODSIM	53870.0
	Di-Boson	WW_TuneCP5_13TeV-pythia8/RunIISummer20UL17MiniAODv2-106X_mc2017_realistic_v9-v1/MINIAODSIM	75.95
	Di-Boson	WZ_TuneCP5_13TeV-pythia8/RunIISummer20UL17MiniAODv2-106X_mc2017_realistic_v9-v1/MINIAODSIM	27.59
	Di-Boson $(\ell\nu)(\ell\ell)$	WZTo3LNu_TuneCP5_13TeV-amcatnloFXFX-pythia8/RunIISummer20UL17MiniAODv2-106X_mc2017_realistic_v9-v2/MINIAODSIM	5.213
	Di-Boson	ZZ_TuneCP5_13TeV-pythia8/RunIISummer20UL17MiniAODv2-106X_mc2017_realistic_v9-v1/MINIAODSIM	12.17
	Di-Boson $(\ell\ell)(\ell\ell)$	ZZTo4L_TuneCP5_13TeV_powheg_pythia8/RunIISummer20UL17MiniAODv2-106X_mc2017_realistic_v9-v2/MINIAODSIM	1.325
2016	Z/γ^*	DYJetsToLL_M-50_TuneCP5_13TeV-amcatnloFXFX-pythia8/RunIISummer20UL16MiniAODAPVv2-106X_mcRun2_asymptotic_preVFP_v11-v1/MINIAODSIM	6404.0
		DYJetsToLL_M-50_TuneCP5_13TeV-amcatnloFXFX-pythia8/RunIISummer20UL16MiniAOD-106X_mcRun2_asymptotic_v13-v2/MINIAODSIM	6404.0
	$t\bar{t}$	TTJets_TuneCP5_13TeV-amcatnloFXFX-pythia8/RunIISummer20UL16MiniAODAPV-106X_mcRun2_asymptotic_preVFP_v8-v1/MINIAODSIM	750.5
		TTJets_TuneCP5_13TeV-amcatnloFXFX-pythia8/RunIISummer20UL16MiniAOD-106X_mcRun2_asymptotic_v13-v1/MINIAODSIM	831.7
	W-Jets	WJetsToLNu_TuneCP5_13TeV-amcatnloFXFX-pythia8/RunIISummer20UL16MiniAODAPV-106X_mcRun2_asymptotic_preVFP_v8-v1/MINIAODSIM	67350
		WJetsToLNu_TuneCP5_13TeV-madgraphMLM-pythia8/RunIISummer20UL16MiniAODv2-106X_mcRun2_asymptotic_v17-v1/MINIAODSIM	53870.0
	Di-Boson	WW_TuneCP5_13TeV-pythia8/RunIISummer20UL16MiniAODAPVv2-106X_mcRun2_asymptotic_preVFP_v11-v1/MINIAODSIM	75.95
		WW_TuneCP5_13TeV-pythia8/RunIISummer20UL16MiniAODv2-106X_mcRun2_asymptotic_v17-v1/MINIAODSIM	75.95
	Di-Boson	WZ_TuneCP5_13TeV-pythia8/RunIISummer20UL16MiniAODAPVv2-106X_mcRun2_asymptotic_preVFP_v11-v1/MINIAODSIM	27.59
		WZ_TuneCP5_13TeV-pythia8/RunIISummer20UL16MiniAOD-106X_mcRun2_asymptotic_v13-v2/MINIAODSIM	27.59
	Di-Boson $(\ell\nu)(\ell\ell)$	WZTo3LNu_TuneCP5_13TeV-amcatnloFXFX-pythia8/RunIISummer20UL16MiniAODAPV-106X_mcRun2_asymptotic_preVFP_v8-v3/MINIAODSIM	5.213
		WZTo3LNu_TuneCP5_13TeV-amcatnloFXFX-pythia8/RunIISummer20UL16MiniAODv2-106X_mcRun2_asymptotic_v17-v1/MINIAODSIM	5.213
	Di-Boson	ZZ_TuneCP5_13TeV-pythia8/RunIISummer20UL16MiniAODAPVv2-106X_mcRun2_asymptotic_preVFP_v11-v1/MINIAODSIM	12.17
		ZZ_TuneCP5_13TeV-pythia8/RunIISummer20UL16MiniAODv2-106X_mcRun2_asymptotic_v17-v1/MINIAODSIM	12.17
	Di-Boson $(\ell\ell)(\ell\ell)$	ZZTo4L_M-1toInf_TuneCP5_13TeV_powheg_pythia8/RunIISummer20UL16MiniAODAPVv2-106X_mcRun2_asymptotic_preVFP_v11-v1/MINIAODSIM	13.74
		ZZTo4L_M-1toInf_TuneCP5_13TeV_powheg_pythia8/RunIISummer20UL16MiniAODv2-106X_mcRun2_asymptotic_v17-v1/MINIAODSIM	13.74

Table 4.3: Background MC samples for 2016, 2017 and 2018.

electrons are required to pass the following criteria:

- $p_T > 7$ GeV
- $|\eta| < 2.5$
- `isLooseElectron`

For the $\mu\mu\tau_e\tau_h$ channel, the electron from the tau decay has no isolation requirement.

4.3.2 Muons

Standard CMS muon categories include:

Year	Physics processes	Dataset name	σ (pb)
2018	ggH	SUSYGluGluToHToAA_AToMuMu_AToTauTau_M-125_M-*_TuneCP5_13TeV_madgraph_pythia8/RunIISummer20UL18MiniAOD-106X_upgrade2018_realistic_v11_L1v1-v3/MINIAODSIM	48.58
		SUSYGluGluToHToAA_AToMuMu_AToTauTau_M-250_M-*_TuneCP5_13TeV_madgraph_pythia8/RunIISummer20UL18MiniAOD-106X_upgrade2018_realistic_v11_L1v1-v3/MINIAODSIM	10.2
		SUSYGluGluToHToAA_AToMuMu_AToTauTau_M-500_M-*_TuneCP5_13TeV_madgraph_pythia8/RunIISummer20UL18MiniAOD-106X_upgrade2018_realistic_v11_L1v1-v3/MINIAODSIM	1.7089
		SUSYGluGluToHToAA_AToMuMu_AToTauTau_M-750_M-*_TuneCP5_13TeV_madgraph_pythia8/RunIISummer20UL18MiniAOD-106X_upgrade2018_realistic_v11_L1v1-v3/MINIAODSIM	0.4969
		SUSYGluGluToHToAA_AToMuMu_AToTauTau_M-1000_M-*_TuneCP5_13TeV_madgraph_pythia8/RunIISummer20UL18MiniAOD-106X_upgrade2018_realistic_v11_L1v1-v3/MINIAODSIM	0.1845
2017	ggH	SUSYGluGluToHToAA_AToMuMu_AToTauTau_M-125_M-*_TuneCP5_13TeV_madgraph_pythia8/RunIISummer20UL17MiniAOD-106X_mc2017_realistic_v6-v3/MINIAODSIM	48.58
		SUSYGluGluToHToAA_AToMuMu_AToTauTau_M-250_M-*_TuneCP5_13TeV_madgraph_pythia8/RunIISummer20UL17MiniAOD-106X_mc2017_realistic_v6-v3/MINIAODSIM	10.2
		SUSYGluGluToHToAA_AToMuMu_AToTauTau_M-500_M-*_TuneCP5_13TeV_madgraph_pythia8/RunIISummer20UL17MiniAOD-106X_mc2017_realistic_v6-v3/MINIAODSIM	1.7089
		SUSYGluGluToHToAA_AToMuMu_AToTauTau_M-750_M-*_TuneCP5_13TeV_madgraph_pythia8/RunIISummer20UL17MiniAOD-106X_mc2017_realistic_v6-v3/MINIAODSIM	0.4969
		SUSYGluGluToHToAA_AToMuMu_AToTauTau_M-1000_M-*_TuneCP5_13TeV_madgraph_pythia8/RunIISummer20UL17MiniAOD-106X_mc2017_realistic_v6-v3/MINIAODSIM	0.1845
2016	ggH	SUSYGluGluToHToAA_AToMuMu_AToTauTau_M-125_M-*_TuneCP5_13TeV_madgraph_pythia8/RunIISummer20UL16MiniAOD*-106X_mcRun2_asymptotic_v13-v2/MINIAODSIM	48.58
		SUSYGluGluToHToAA_AToMuMu_AToTauTau_M-125_M-*_TuneCP5_13TeV_madgraph_pythia8/RunIISummer20UL16MiniAODAPV*-106X_mcRun2_asymptotic_preVFP_v8-v2/MINIAODSIM	48.58
		SUSYGluGluToHToAA_AToMuMu_AToTauTau_M-250_M-*_TuneCP5_13TeV_madgraph_pythia8/RunIISummer20UL16MiniAOD*-106X_mcRun2_asymptotic_v13-v2/MINIAODSIM	10.2
		SUSYGluGluToHToAA_AToMuMu_AToTauTau_M-250_M-*_TuneCP5_13TeV_madgraph_pythia8/RunIISummer20UL16MiniAODAPV*-106X_mcRun2_asymptotic_preVFP_v8-v2/MINIAODSIM	10.2
		SUSYGluGluToHToAA_AToMuMu_AToTauTau_M-500_M-*_TuneCP5_13TeV_madgraph_pythia8/RunIISummer20UL16MiniAOD*-106X_mcRun2_asymptotic_v13-v2/MINIAODSIM	1.7089
		SUSYGluGluToHToAA_AToMuMu_AToTauTau_M-500_M-*_TuneCP5_13TeV_madgraph_pythia8/RunIISummer20UL16MiniAODAPV*-106X_mcRun2_asymptotic_preVFP_v8-v2/MINIAODSIM	1.7089
		SUSYGluGluToHToAA_AToMuMu_AToTauTau_M-750_M-*_TuneCP5_13TeV_madgraph_pythia8/RunIISummer20UL16MiniAOD*-106X_mcRun2_asymptotic_v13-v2/MINIAODSIM	0.4969
		SUSYGluGluToHToAA_AToMuMu_AToTauTau_M-750_M-*_TuneCP5_13TeV_madgraph_pythia8/RunIISummer20UL16MiniAODAPV*-106X_mcRun2_asymptotic_preVFP_v8-v2/MINIAODSIM	0.4969
		SUSYGluGluToHToAA_AToMuMu_AToTauTau_M-1000_M-*_TuneCP5_13TeV_madgraph_pythia8/RunIISummer20UL16MiniAOD*-106X_mcRun2_asymptotic_v13-v2/MINIAODSIM	0.1845
		SUSYGluGluToHToAA_AToMuMu_AToTauTau_M-1000_M-*_TuneCP5_13TeV_madgraph_pythia8/RunIISummer20UL16MiniAODAPV*-106X_mcRun2_asymptotic_preVFP_v8-v2/MINIAODSIM	0.1845

Table 4.4: Signal MC samples for the 2016,2017 and 2018.

	barrel	endcap
full5x5$_{\sigma i\eta i\eta}$ <	0.0112	0.0425
abs(dEtaSeed) <	0.00377	0.00674
abs(dPhiIn) <	0.0884	0.169
H/E <	$0.05 + 1.16/E_{SC} + 0.0324\rho/E_{SC}$	$0.0441 + 2.54/E_{SC} + 0.183 * \rho/E_{SC}$
relIsoWithEA <	$0.112 + 0.506/p_T$	$0.108 + 0.963/p_T$
abs(1/E-1/p)<	0.913	0.111
expected missing inner hits ≤	1	1
pass conversion veto	yes	yes

Table 4.5: The requirements to be classified as a Loose Electron [31].

- `isPFMuon` refers to an object required to first be selected with inner tracks and calorimeter energy deposits with a ΔR < 0.3 with respect to the muon direction in the (η, ϕ) plane [22],

- `isTrackerMuon` refers to an object with tracker tracks $p_T > 0.5$ GeV, total momentum $p > 2.5$ GeV, and at least one muon segment, such a stub from DT or CSC hits, matching the tracker track

- `isGlobalMuon` refers to a track from the muon detectors matched to a tracker track

	barrel	endcap
full5x5$_{\sigma i\eta i\eta}$ <	0.0104	0.0353
abs(dEtaSeed) <	0.0025	0.00501
abs(dPhiIn) <	0.022	0.0236
H/E <	$0.026 + 1.15/E_{SC} + 0.0324\rho/E_{SC}$	$0.0188 + 2.06/E_{SC} + 0.183 * \rho/E_{SC}$
relIsoWithEA <	$0.0287 + 0.506/p_T$	$0.0445 + 0.963/p_T$
abs(1/E-1/p)<	0.159	0.0197
expected missing inner hits ≤	1	1
pass conversion veto	yes	yes

Table 4.6: The requirements to be classified as a Tight Electron [31].

- `isLooseMuon` is an object identified as a muon by Particle Flow (PFMuon) and is also a Tracker Muon or Global Muon [52].

In this analysis, muons are required to pass the following criteria:

- $p_T > 3$ GeV
- $|\eta| < 2.4$
- `isPFMuon AND (isTrackerMuon OR isGlobalMuon)`

Analysis regions defined in Section 4.5 depend partially on the isolation of the muon pair μ_1 and μ_2. For a muon to be considered isolated, it must pass an additional requirement:

- Relative isolation < 0.25

For the $\mu\mu\tau_\mu\tau_h$ channel, the muon from the tau decay (μ_3) has no isolation requirement.

4.3.3 Taus

Taus in the fully hadronic channel

When two taus are highly collimated and both decay hadronically, the daughter particles often overlap and it becomes less feasible to distinguish two separate τ_h objects. Standard CMS algorithms are designed to reconstruct single, isolate hadronic tau decays. For this channel, a neural net tagger was trained to identify the unique signature. This is detailed in Section 4.4.

Taus in the semi-leptonic channel

The hadronically decaying taus τ_h are reconstructed using a modified version of the Hadron-Plus-Strips (HPS) algorithm, since the $\tau_\mu\tau_h$ ($\tau_e\tau_h$) pair in the final state is highly collimated [53]. For the $\tau_\mu\tau_h$ ($\tau_e\tau_h$) pair, the muon from τ_μ (electron from τ_e) is found to end up frequently among the constituents of the jet seeded by the τ_h decay and therefore among the isolation constituents of the τ_h reconstructed with the HPS algorithm. The hadronic tau decays are reconstructed from the anti-k_T R = 0.4 PF jets using the HPS algorithm.

Before running HPS, jet constituents passing the `isLooseMuon` (`isLooseElectron`) criteria are removed in the $\mu\mu\tau_\mu\tau_h$ ($\mu\mu\tau_e\tau_h$) channel. In the majority of cases, only one soft muon (electron) is removed from a jet, but if more than one muon (electron) is removed, the highest p$_T$ removed muon (electron) is identified as the τ_μ (τ_e). This jet collection is then labeled as muon (electron) cleaned. A new jet (henceforth referred to as the cleaned jet after the removal of the muon (electron)) is then reconstructed from the remaining Particle Flow constituents. These cleaned jets are submitted to the HPS algorithm to be reconstructed as τ_h candidates.

This technique was originally developed in [26] and also applied for the $\tau_\mu\tau_h$ channel in [8]. The efficiency from the previous analysis is shown in Figure 4.4 and the updated efficiency for this analysis is shown in Figure 4.5. The modified version of HPS that includes lepton cleaning consistently performs better than the standard HPS algorithm. Figure 4.5 shows the efficiency for this selection calculated from MC for various Higgs boson mass points as a function of the pseudoscalar Higgs boson mass.

In the efficiency calculation, the denominator has the following selection:

Generator Level

- p$_T(\mu_1) > 26.0$ GeV and $|\eta|(\mu_1) < 2.5$
- p$_T(\mu_2) > 26.0$ GeV and $|\eta|(\mu_2) < 2.5$
- p$_T(\tau_\mu/\tau_e) > 3.0$ and $|\eta|(\tau_\mu/\tau_e) < 2.4$
- p$_T(\tau_h) > 10.0$ GeV and $|\eta|(\tau_h) < 2.4$

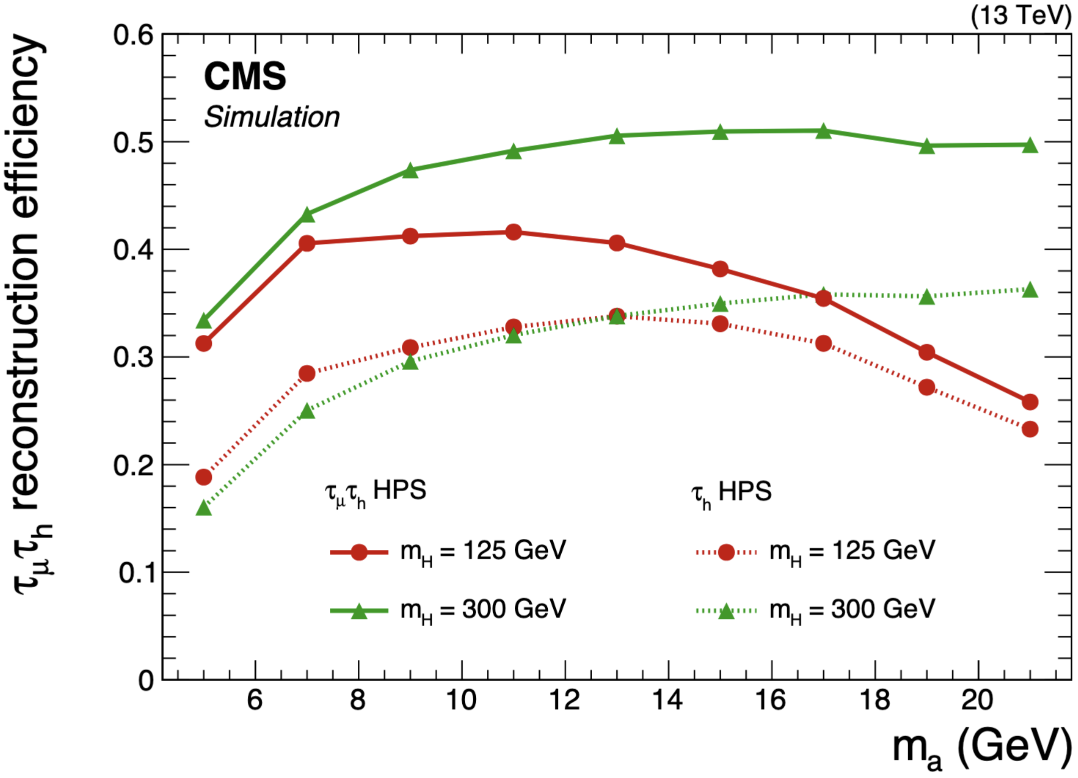

Figure 4.4: Comparison of efficiency of $\tau_\mu \tau_h$ reconstruction using the standard HPS (dashed lines) and using the lepton cleaning method (solid lines) [8].

Reconstruction Level

- $p_T(\mu_1) > 26.0$ GeV and $|\eta|(\mu_1) < 2.4$ and `isLooseMuon` and relative isolation < 0.25
- $p_T(\mu_2) > 3.0$ GeV and $|\eta|(\mu_2) < 2.4$ and `isLooseMuon` and relative isolation < 0.25
- $p_T(\tau_\mu/\tau_e) > 3.0$ GeV and $|\eta|(\tau_\mu)/\tau_e < 2.4$ and `isLooseMuon/isLooseElectron`
- $\Delta R(\mu_1, \tau_\mu/\tau_e) > 0.4$ and $\Delta R(\mu_2, \tau_\mu/\tau_e) > 0.4$

For an event to be included in the numerator of the efficiency calculation, the following additional selection must be met at the reconstruction level:

- $p_T(\tau_h) > 10.0(20.0)$ GeV and $|\eta|(\tau_h) < 2.3$ for muon (electron) cleaned HPS (standard HPS)
- $\Delta R(\mu_1, \tau_h) > 0.8$ and $\Delta R(\mu_2, \tau_h) > 0.8$ and $\Delta R(\tau_\mu, \tau_h) < 0.8$

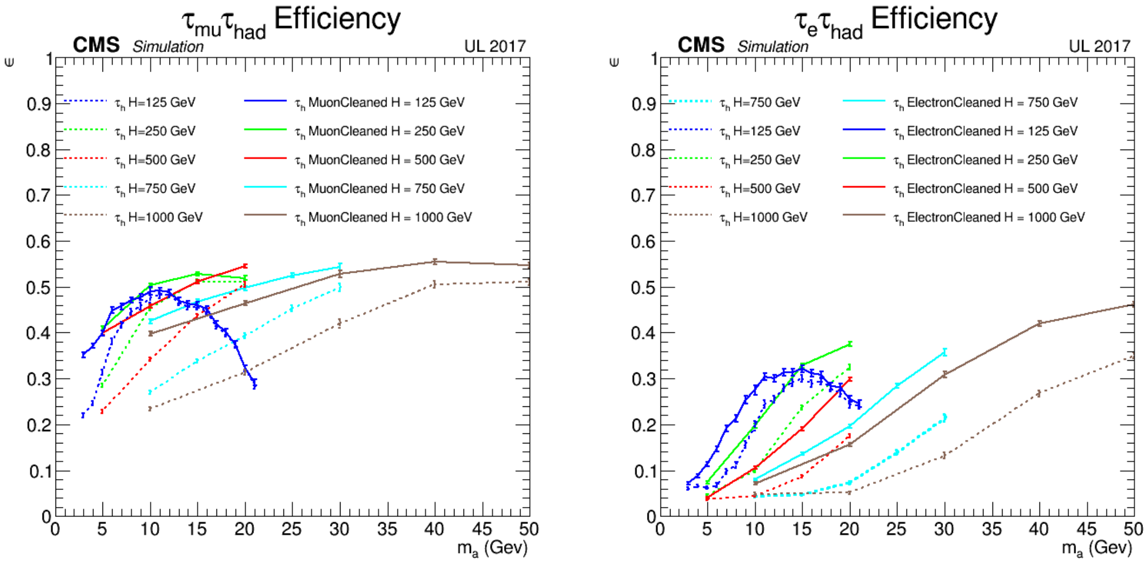

(a) (b)

Figure 4.5: The $\tau_\mu\tau_h$ (left) and $\tau_e\tau_h$ (right) reconstruction efficiency of the standard tau HPS (dashed line) compared to the μ-cleaned (left) and e-cleaned (right) HPS reconstruction (solid line) as a function of pseudoscalar Higgs boson mass for 2017 and for m_H = 125, 250, 500, 750 and 1000 GeV.

- τ_h passes decay mode finding
- τ_h passes the medium MVA discriminator working point `byMediumIsolationMVArun2017v2DBoldDMwLT2017`: standardized cut based on an MVA with inputs including charged and neutral hadron isolation sums, decay modes, transverse impact parameter of leading track and its significance, and distance between τ production and decay vertices and its significance [53]
- τ_h passes `againstElectronLooseMVA6` : standardized MVA cut value for discrimination against electrons
- τ_h passes `againstMuonTight3` : no hit present in CSC, DT, or RPC detectors in outermost muon stations within a cone size of $\Delta R = 0.3$ from the τ_h, and energy depositied in calorimeters associated through the PF algorithm to the leading charged hadron of the τ_h must be $> 20\%$ of its track momentum [54]

The hadronically decaying tau reconstructed from the muon (electron) cleaning algorithm described above must pass the following criteria:

- $p_T > 10$ GeV
- $|\eta| < 2.3$
- passes decay mode finding

Analysis regions defined in Section 4.5 also depend partially on whether the τ_h passes the MVA discriminator `byMediumIsolationMVArun2017v2DBoldDMwLT2017` [51].

4.4 DeepDiTau

Because this analysis has a boosted topology, the decay products from the taus are often overlapping and reconstructed as AK4 jets. DeepDiTau is a deep neural net tagger trained to classify AK4 jets into three categories. The output of DeepDiTau is a vector of three "scores" between 0 and 1 for each output node (light jet, b jet, or $\tau_h\tau_h$), which are normalized to sum to one for each AK4 jet. The three categories were selected because both light jets and b jets contribute to background, and preliminary studies showed the three category approach was more performant than a binary background vs. $\tau_h\tau_h$ classification. Additionally, separating charm jets into a category separate from light jets worsened the performance.

DeepDiTau was implemented using Keras, a python interface supporting the TensorFlow backend, and its trainings were run on GPUs provided by the Fermilab LPC cluster. DeepDiTau was trained over a sample of 3.2 million AK4 jets with light jets from QCD events, b jets from $t\bar{t}$ events, and $\tau_h\tau_h$ from signal events. The light jets and b jets are reweighted such that their p_T and η distributions match that of the sample of jets from $\tau_h\tau_h$. The weights are shown in Figure 4.6.

The input features to the tagger are variables from global jets (40 variables) and their constituent particles: charged hadrons (up to 10 objects, each with 18 variables), neutral hadrons (up to 10 objects, each with 5 variables), and photons (up to 4 objects, each

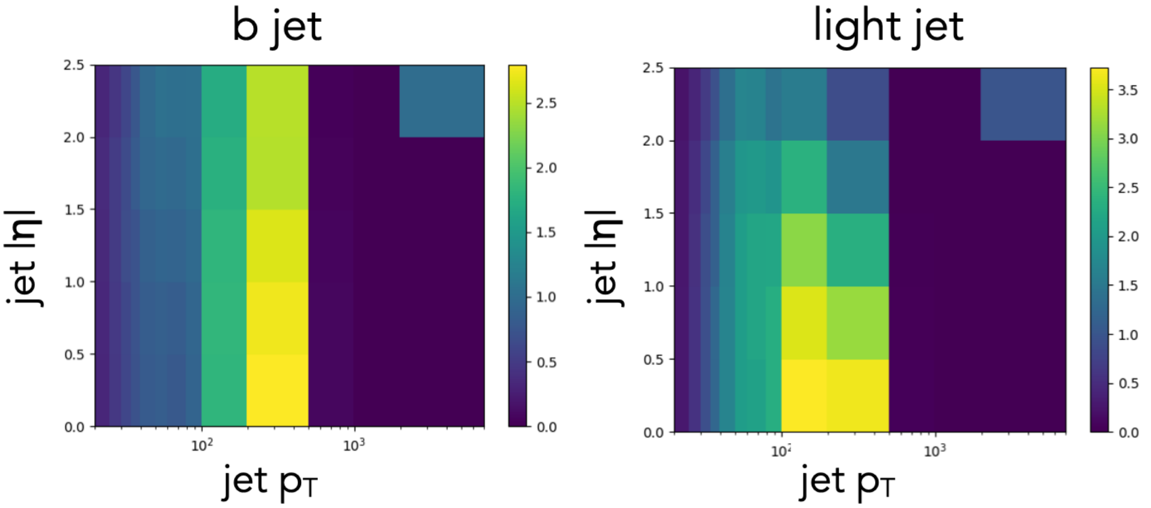

Figure 4.6: Samples of b jets and light jets are reweighted in ϕ and η to match the distribution of jets from signal samples and containing $\tau_h\tau_h$. The colors correspond to the weights that are applied.

with 6 variables). These variables are listed in Table 4.7. This list of input features was partially motivated by the list used by a jet flavor-tagging algorithm named DeepJet [55].

Before the training some signal masses ($m_H = 125$ GeV with $m_a = 6$ GeV, $m_H = 250$ GeV with $m_a = 15$ GeV, $m_H = 500$ GeV with $m_a = 20$ GeV, and $m_H = 1000$ GeV with $m_a = 20$ GeV), are removed from consideration, and these are used to verify the performance of the tagger later.

4.4.1 Network architecture

The distributions of each input variable are normalized to 0 with a standard deviation of 1, except the jet η and jet ϕ, which are linearized from 0 to 1, and the jet p_T that is log linearized. The jet Particle Flow constituents are transformed so that their features are relative to the jet axis. The length of input vectors must be consistent for this network, so jets with greater than the maximum number of particle flow candidates are truncated and jets with fewer than the minimum are zero padded.

The constituent Particle Flow objects of each jet are concatenated with the global jet input features and sent to a dense neural net. The width of the neural net is 256 and the depth is 8. The depth is the number of layers and the width is the number of nodes in each later. Batch normalization is implemented, which normalizes the inputs to each

Training inputs	
jet_pt	jet_pfDeepCSVJetTags_probbb
jet_eta	charged_hadron_eta
jet_phi	charged_hadron_phi
jet_mass	charged_hadron_charge
jet_jetCharge	charged_hadron_etaAtVtx
jet_chargedMultiplicity	charged_hadron_phiAtVtx
jet_neutralMultiplicity	charged_hadron_vx
jet_chargedHadronMultiplicity	charged_hadron_vy
jet_neutralHadronMultiplicity	charged_hadron_vz
jet_muonMultiplicity	charged_hadron_dxy
jet_electronMultiplicity	charged_hadron_dz
jet_photonMultiplicity	charged_hadron_isIsolatedChargedHadron
jet_chargedEmEnergy	charged_hadron_pixelLayersWithMeasurement
jet_neutralEmEnergy	charged_hadron_stripLayersWithMeasurement
jet_chargedHadronEnergy	charged_hadron_trackHighPurity
jet_neutralHadronEnergy	charged_hadron_puppiWeight
jet_muonEnergy	neutral_hadron_puppiWeightnoLep
jet_electronEnergy	neutral_hadron_eta
jet_photonEnergy	neutral_hadron_phi
jet_chargedEmEnergyFraction	neutral_hadron_puppiWeight
jet_neutralEmEnergyFraction	neutral_hadron_puppiWeightnoLep
jet_chargedHadronEnergyFraction	photon_eta
jet_neutralHadronEnergyFraction	photon_phi
jet_muonEnergyFraction	photon_puppiWeight
jet_electronEnergyFraction	photon_puppiWeightnoLep
jet_photonEnergyFraction	photon_isGoodEgamma
jet_pfDeepCSVJetTags_probb	jet_pfDeepCSVJetTags_probudsg
jet_pfDeepCSVJetTags_probc	

Table 4.7: Inputs for the training of DeepDiTau.

layer to have a mean of 0 and standard deviation of 1. The dropout rate is the fraction of nodes temporarily removed at each step during training, which prevents overfitting. The learning rate is the fraction of the distance toward the new input value that is traveled at each step, and momentum is the weight applied to the direction from the previous step. The learning rate and momentum can be thought of as balancing each other out - a high learning rate leads to a neural net that is more volatile, possibly making large changes at each step, and a high momentum steers the values on a smooth path whose direction does not change in large steps [56]. Hyperparameter values are shown in Table 4.8.

The neural net is trained through an iterative process where the weights connecting different nodes are adjusted. The cross entropy loss function is minimized to determine the best performing version of the net. The validation fraction of 0.1 corresponds to the fraction of jets removed from the training sample and used to check for possible overfitting. The loss and accuracy are monitored over the course of training on both the training sample and the validation sample as shown in Figure 4.7.

Hyperparameter	Value
Depth	8
Width	256
Momentum	0.6
Dropout rate	0.1
Learning rate	0.001

Table 4.8: Hyperparameters for DeepDiTau.

4.4.2 Performance

The overall performance is seen in the confusion matrix in Figure 4.8. The ROC curves are shown in Figure 4.9 and the working points are listed in Table 4.9. The ROC curves separated by p_T and η are shown in Figures 4.10 and 4.11. With the combination of score distributions in the top row and the DeepDiTau score vs. $\Delta R(\tau_h \tau_h)$ in the bottom row of Figure 4.12, it is clear the highly boosted events with a low $\Delta R(\tau_h \tau_h)$ value tend to score the highest in the case of $m_H = 125$ GeV and $m_a = 18$ GeV. At less boost and

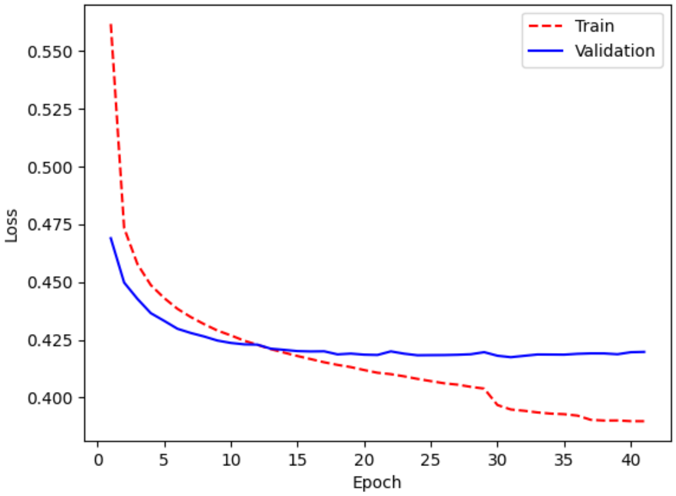

(a)

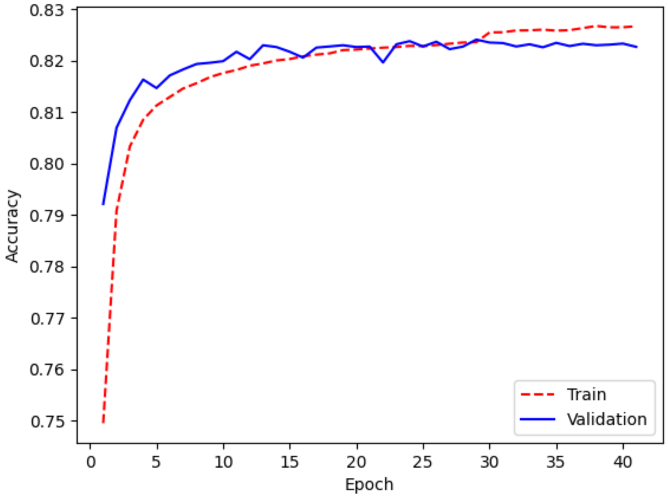

(b)

Figure 4.7: The cross entropy loss function and corresponding accuracy function for the training of DeepDiTau. Accuracy is defined as the sum of the true positives and true negatives divided by the total number of predictions.

higher $\Delta R(\tau_h \tau_h)$ values, it is more likely that not all the decay products from both taus will be contained with a jet of radius $R = 0.4$. This leads to those jets being assigned a slightly lower DeepDiTau score and also affects the jet mass. The jet mass distributions for different working points and different m_a values are shown in Figure 4.13. In the case of low m_a values, the jets may fully contain the tau decay products and even additional particles, reconstructing a mass that is equal to or greater than m_a. As m_a increases, so does $\Delta R(\tau_h \tau_h)$, so the jet mass may be less than m_a as it does not fully contain all the tau decay particles [51].

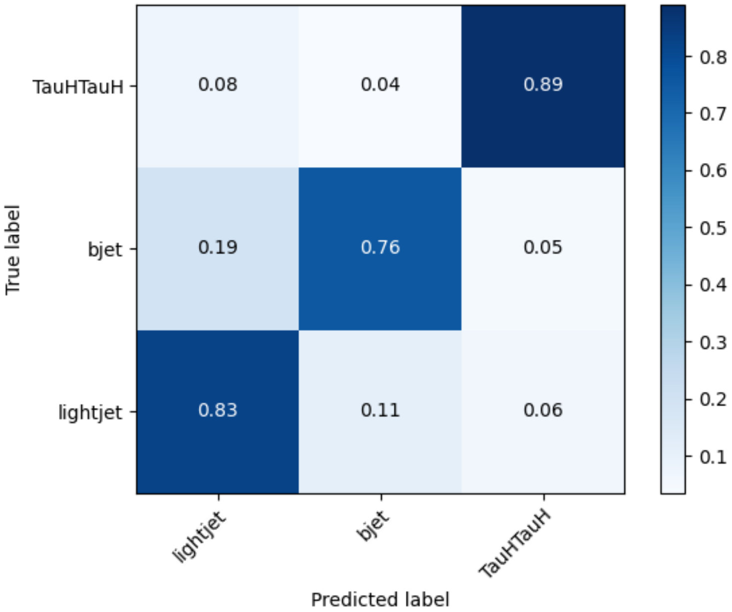

Figure 4.8: Confusion matrix of DeepDiTau.

	VVTight	VTight	Tight	Medium	Loose	VLoose	VVLoose	VVVLoose
True pos.	40%	50%	60%	70%	80%	90%	95%	98%
False pos.	0.1%	0.3%	0.6%	1.1%	2.4%	6.0%	10.9%	19.4%
Score	0.981	0.956	0.912	0.832	0.688	0.409	0.200	0.069

Table 4.9: Working points for DeepDiTau.

4.5 Event Selections and Analysis Region Definitions

For the events passing the `HLT_IsoMu24` / `HLT_IsoMu27` or the `HLT_IsoTkMu24` / `HLT_IsoTkMu27` trigger, further selections are applied to optimize for finding the signal process, H → aa → $\mu\mu\tau\tau$. All channels have common selections for the muons from the

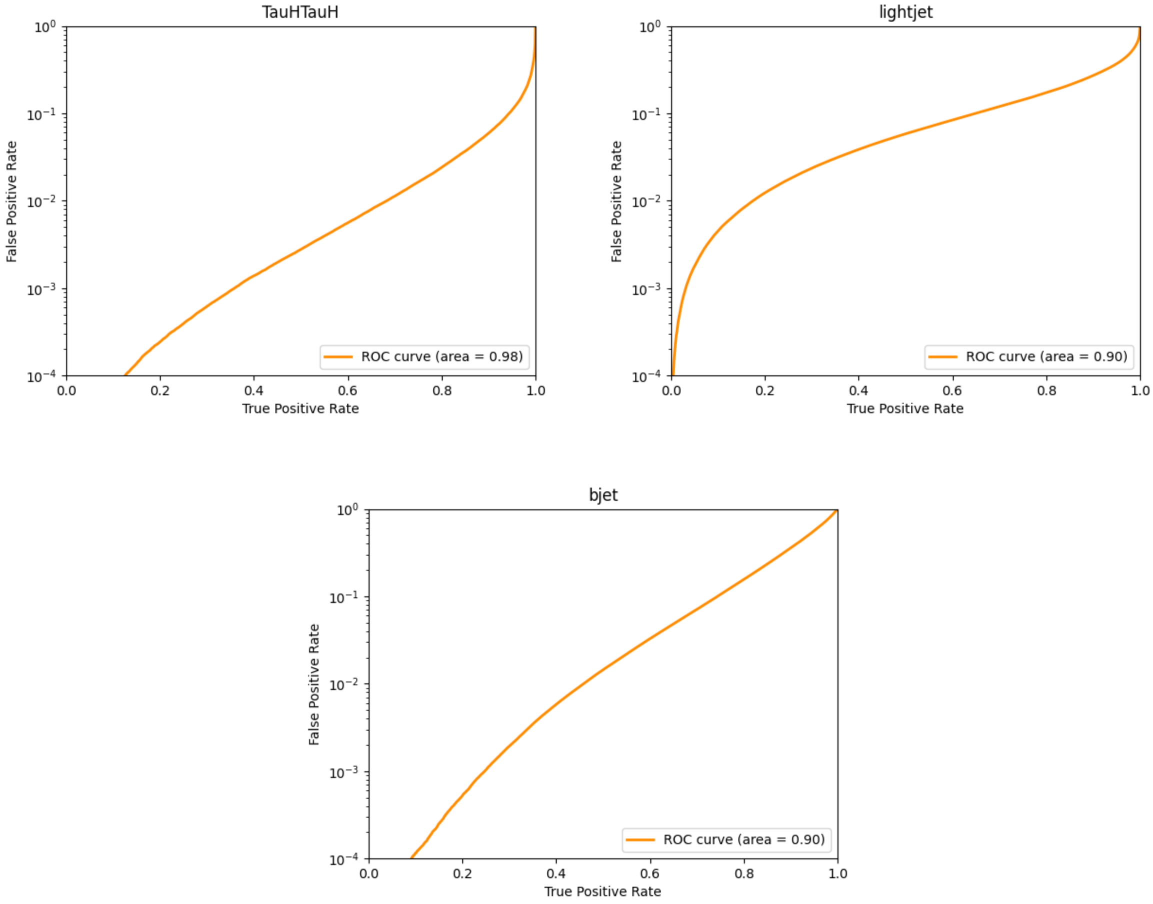

Figure 4.9: ROCs for $\tau_h\tau_h$, light jets, and b jets.

decay of the first pseudoscalar Higgs boson, denoted as μ_1 and μ_2. The selections are then tailored for individual channels based on tau decays from the second pseudoscalar Higgs boson. Cross cleaning refers to the ΔR requirements for the decay products of one pseudoscalar Higgs boson to be angularly separated from the decay products of the other pseudoscalar Higgs boson, which is expected for the boosted and "back-to-back" topology of this analysis.

4.5.1 All channels: $\mu_1\mu_2$

All channels of this analysis have one pseudoscalar Higgs boson decaying to two muons. The relevant selections are listed below.

Muons $\mu_1\mu_2$:

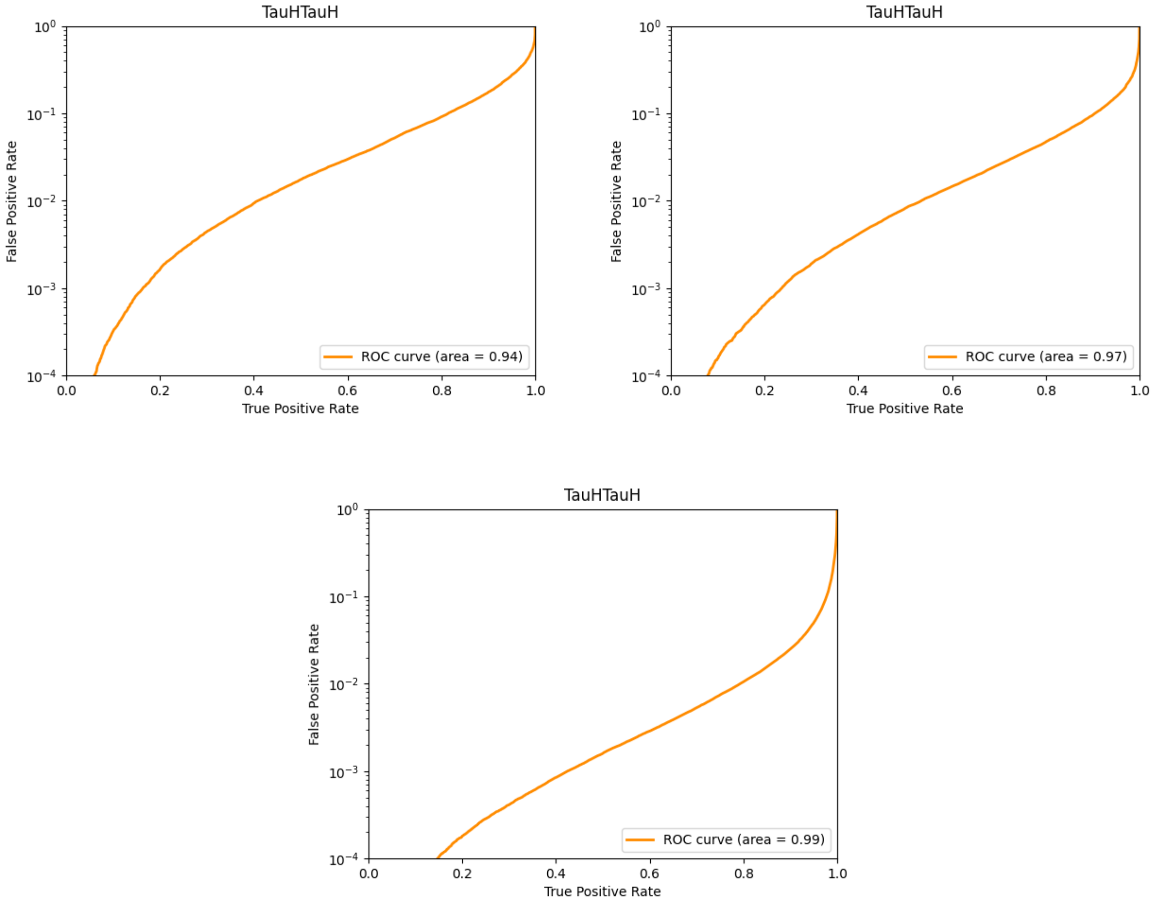

Figure 4.10: The performance of DeepDiTau in p_T ranges of $20-50GeV$, $50-100GeV$, $100-1000GeV$

- μ_1 and μ_2 are opposite sign
- Both muons pass `Loose muon ID`
- Leading isolated muon (μ_1) $p_T > 26$ GeV and matched to the trigger
- Subleading muon (μ_2) $p_T > 3$ GeV
- $2.5 < M(\mu_1, \mu_2) < 60$ GeV
- Smallest $\Delta\text{R}(\mu_1, \mu_2) < 1.0$
- Relative isolation $\mu_2 < 0.25$ in signal region and sideband, relative isolation $\mu_2 > 0.25$ in validation region and validation sideband

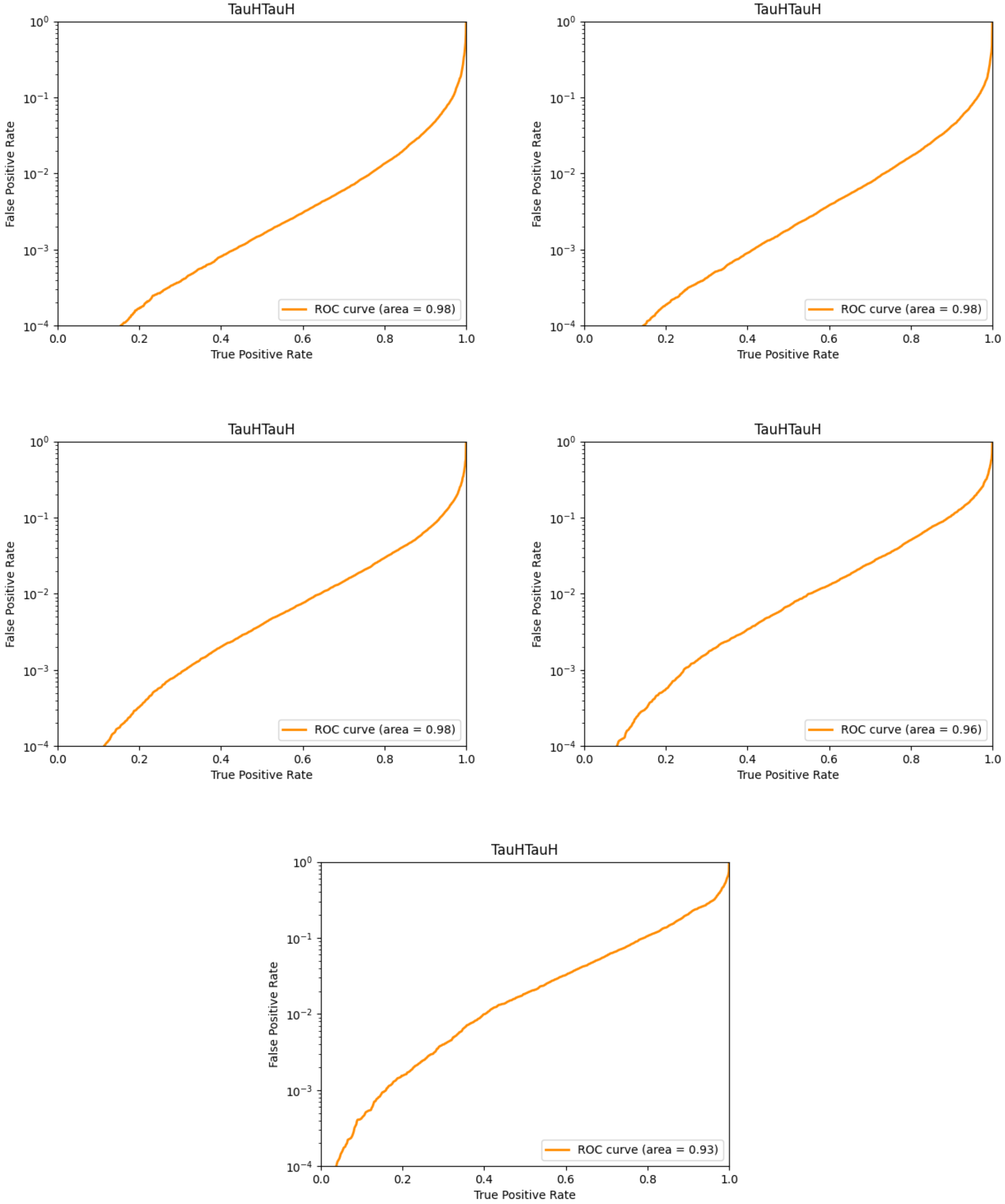

Figure 4.11: The performance of DeepDiTau in η ranges of $0-0.5$, $0.5-1.0$, $1.0-1.5$, $1.5-2.0$, $2.0-2.5$

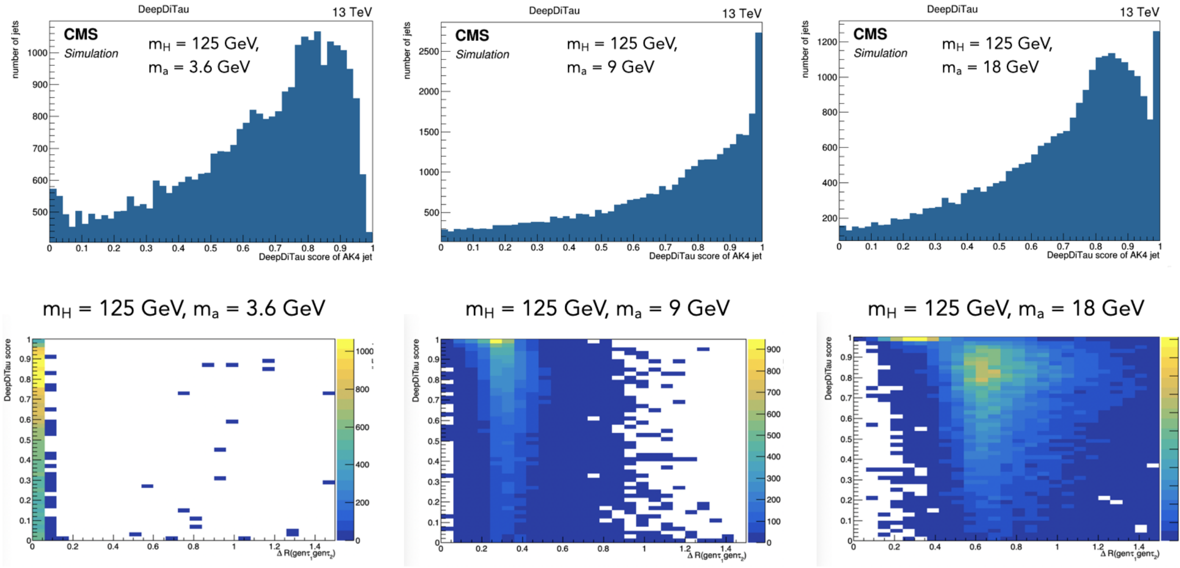

Figure 4.12: The top row of plots shows the score distribution for AK4 jets from signal MC samples ΔR matched to two τ_h objects. As the pseudoscalar Higgs boson mass increases, the shape of the distribution changes. Based on the bottom row of plots, one sees two distinct populations of jets in the less boosted topology, where jets from τ_h objects with a relatively low ΔR values cluster at DeepDiTau scores of 1, and jets from two τ_h objects with relatively high ΔR values cluster at somewhat lower DeepDiTau scores.

4.5.2 Fully hadronic decay channel: $\tau_h\tau_h$

Events are required to pass selections on $\mu_1\mu_2$ because of the two muons expected from the decay of one pseudoscalar Higgs boson. For this channel, the overlapping hadronic tau decays from the decay of the second pseudoscalar Higgs boson are selected by applying a cut on the DeepDiTau score on an AK4 jet. The detailed requirements are listed below:

AK4 jet from $\tau_h\tau_h$:

- Jet $p_T > 30$ GeV
- Jet passes `Tight jet ID` : standard CMS quality cut on jets that requires neutral hadron fraction of jet < 0.9, neutral electromagnetic fraction of jet < 0.9, charged electromagnetic fraction < 0.99, greater than 2 jet constituents, non-zero charged hadron fraction, non-zero charge multiplicity, and a neutral multiplicity based on $|\eta|$ value [57].
- Jet passes `bVeto Loose` : standard CMS quality cut meant to reject b-jets

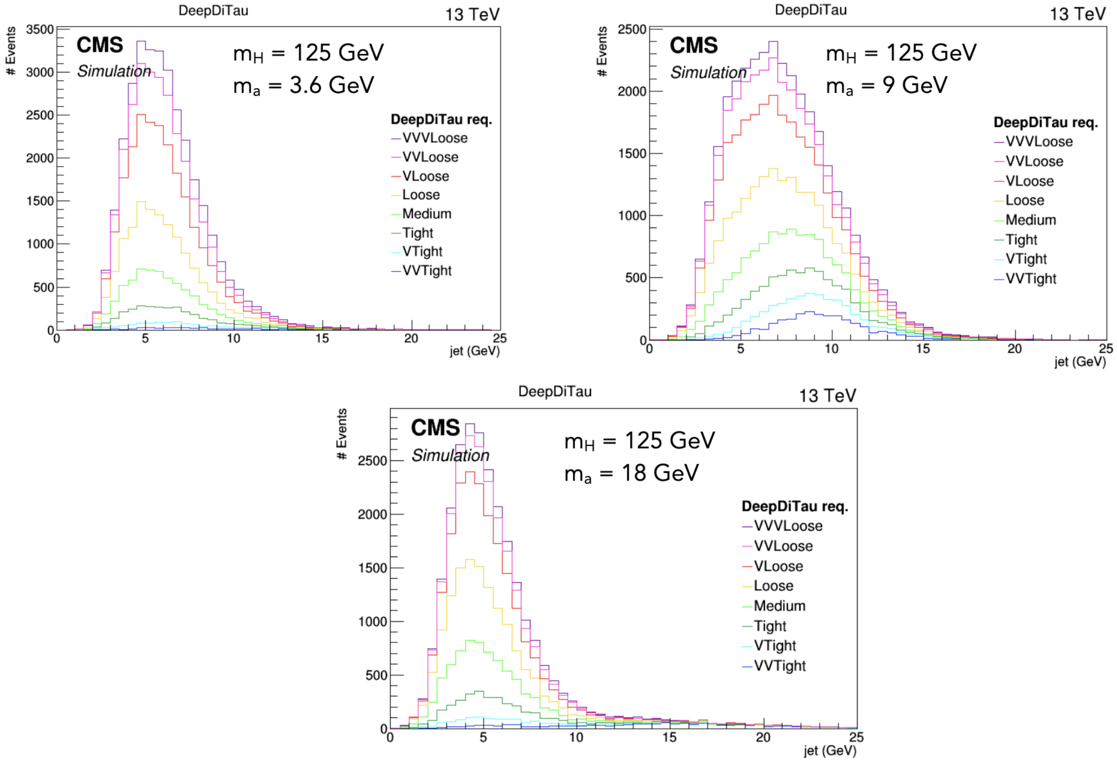

Figure 4.13: The mass of AK4 jets gen-matched to two τ_h objects. At low m_a, the jets corresponding to highly collimated τ_h decays may contain particles not associated with the decay of either τ_h, increasing the jet mass beyond m_a. At high m_a, the τ_h decays are less collimated and an AK4 jet may not contain all the associated decay products, leading to a jet mass less than m_a.

- Jet passes DeepDiTau medium (score > 0.832)

Cross-cleaning

- $\Delta R(\mu_1, \text{jet}) > 0.4$
- $\Delta R(\mu_2, \text{jet}) > 0.4$

In this channel, the signal region requires μ_2 to be isolated. The validation region and validation sideband are orthogonal to the signal region and sideband by requiring μ_2 to not be isolated. The sideband is then defined in the fully-hadronic channel based on whether an AK4 jet passes the `medium` DeepDiTau requirement, which is having a score above 0.832 on a scale from 0 to 1. A data driven fake-rate method is used to estimate background contributions in the signal region. The transfer factor is defined as the ratio of the contributions from background in the sideband and signal region as a function of p_T. It is derived in the control region and tested using the validation sideband and validation region. Figure 4.14 shows the analysis structure of this channel.

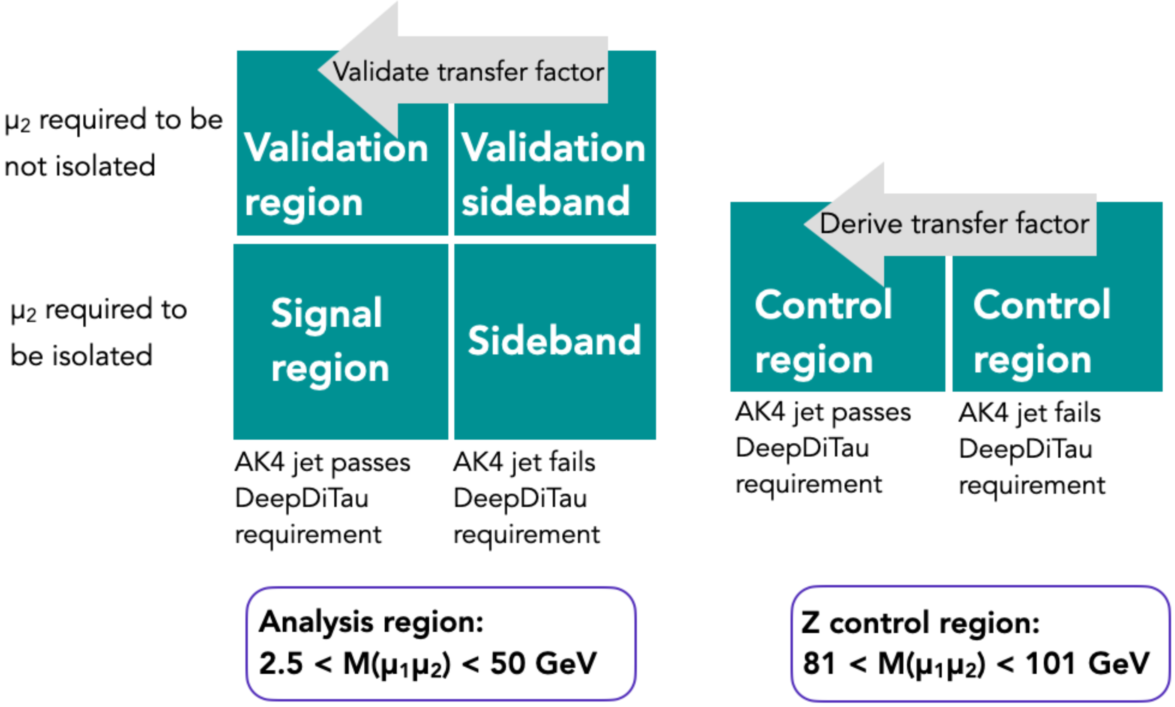

Figure 4.14: The structure of the analysis for $\tau_h\tau_h$ channel. Regions are defined based on μ_2 isolation and the presence of an AK4 jet with a DeepDiTau score over a certain threshold. The transfer factors are derived in the control region.

4.5.3 Semi-leptonic decay channels: $\tau_\mu\tau_h$ and $\tau_e\tau_h$

Events are required to pass selections on $\mu_1\mu_2$ because of the two muons expected from the decay of one pseudoscalar Higgs boson. For these channels, a third muon or electron is selected plus a hadronic tau that has undergone lepton cleaning. The detailed requirements are listed below:

$\mu\mu\tau_\mu\tau_h$: The μ from the decay of the τ_μ is labeled as μ_3.

- μ_3 and τ_h opposite sign
- μ_3 passes `Loose muon ID`
- $\mu_3(p_T) > 3$ GeV

- Muon cleaned τ_h $p_T > 10$ GeV
- Smallest ΔR$(\mu_3, \tau_h) < 0.8$
- Tau passes medium MVA tau ID in signal region and validation region, fails in sideband and validation sideband

Cross-cleaning

- ΔR$(\mu_1, \mu_3) > 0.4$
- ΔR$(\mu_2, \mu_3) > 0.4$
- ΔR$(\mu_1, \tau_h) > 0.8$
- ΔR$(\mu_2, \tau_h) > 0.8$

$\mu\mu\tau_e\tau_h$: The e is the electron from the decay of the τ_e.

- e and τ_h opposite sign
- Electron pass `Loose electron ID`
- Electron $p_T > 7$ GeV
- Electron cleaned τ_h $p_T > 10$ GeV
- Smallest ΔR(e, τ_h) < 0.8
- Tau passes medium MVA tau ID in signal region and validation region, fails in sideband and validation sideband

Cross-cleaning

- ΔR$(\mu_1, \mathrm{e}) > 0.4$
- ΔR$(\mu_2, \mathrm{e}) > 0.4$
- ΔR$(\mu_1, \tau_h) > 0.8$

- $\Delta\mathrm{R}(\mu_2, \tau_h) > 0.8$

In this channel, the signal region is defined by μ_2 passing an isolation requirement and the lepton-cleaned tau passing the MVATau discriminator. The sideband and validation sideband have a lepton-cleaned tau not passing the MVATau discriminator, and the validation region has a μ_2 that is not isolated. A schematic relating these regions is seen in Figure 4.15.

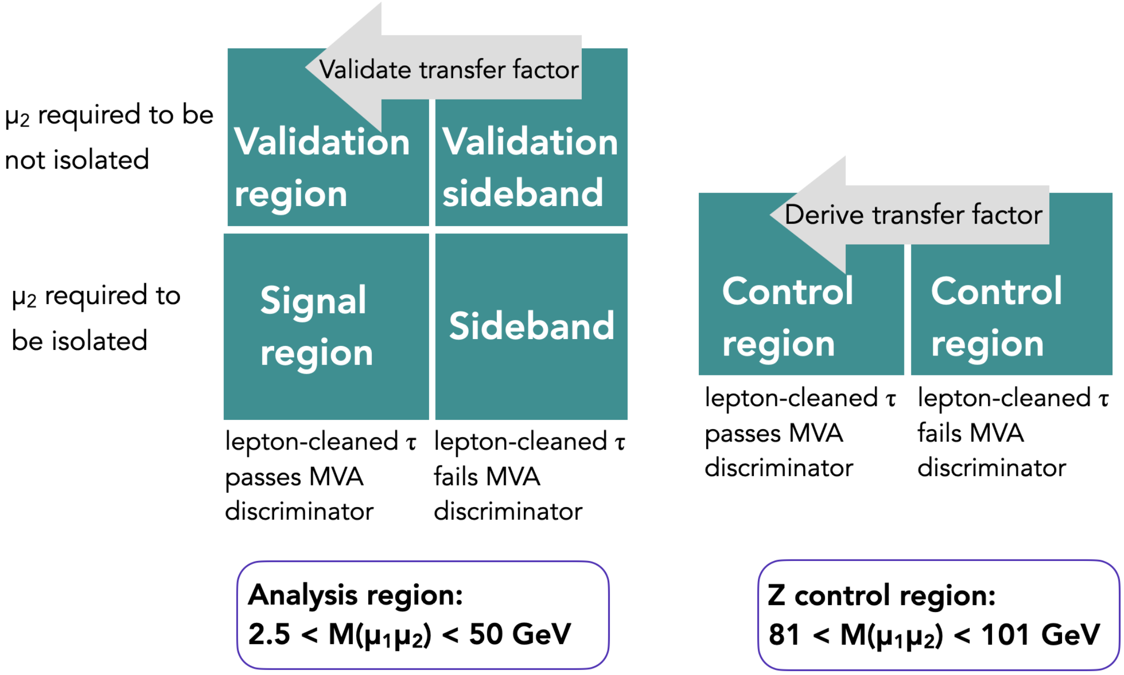

Figure 4.15: The structure of the analysis for $\tau_\mu\tau_h$ and $\tau_e\tau_h$ channels. Regions are defined based on μ_2 isolation and whether the lepton-cleaned τ passes the medium MVA tau ID. The transfer factors are derived in the control region.

4.5.4 Fully leptonic decay channels: $\tau_e\tau_\mu$ and $\tau_\mu\tau_\mu$

Events are required to pass selections on $\mu_1\mu_2$ because of the two muons expected from the decay of one pseudoscalar Higgs boson. For these channels, a third muon and electron or a third muon and fourth muon are selected.

$\boldsymbol{\mu_3}$**e**: The μ from the decay of the τ_μ is labeled as μ_3.

- e and μ_3 opposite sign

- Muon passes `Loose muon ID`
- Smallest $\Delta\mathrm{R}(\mu_3,\mathrm{e}) < 1.0$

Cross-cleaning

- $\Delta\mathrm{R}(\mu_1, \mathrm{e}) > 0.4$
- $\Delta\mathrm{R}(\mu_2, \mathrm{e}) > 0.4$
- $\Delta\mathrm{R}(\mu_1, \mu_3) > 0.4$
- $\Delta\mathrm{R}(\mu_2, \mu_3) > 0.4$

$\boldsymbol{\mu_3\mu_4}$: The μ objects from the decay of the $\tau_\mu\tau_\mu$ are labeled as μ_3 and μ_4.

- μ_3 and μ_4 opposite sign
- Both muons pass `Loose muon ID`
- Smallest $\Delta\mathrm{R}(\mu_3, \mu_4) < 1.0$

Cross-cleaning

- $\Delta\mathrm{R}(\mu_1, \mu_3) > 0.4$
- $\Delta\mathrm{R}(\mu_2, \mu_3) > 0.4$
- $\Delta\mathrm{R}(\mu_1, \mu_4) > 0.4$
- $\Delta\mathrm{R}(\mu_2, \mu_4) > 0.4$

For the case of both taus decaying leptonically, the analysis has a somewhat different structure. The signal region contains events where both leptons pass the isolation requirement, the `Loose muon ID` for muons or the `Tight electron ID` for electrons. There is a sideband region with both leptons failing the isolation requirement and a separate sideband region with one lepton failing the isolation requirement, as shown in Figure 4.16.

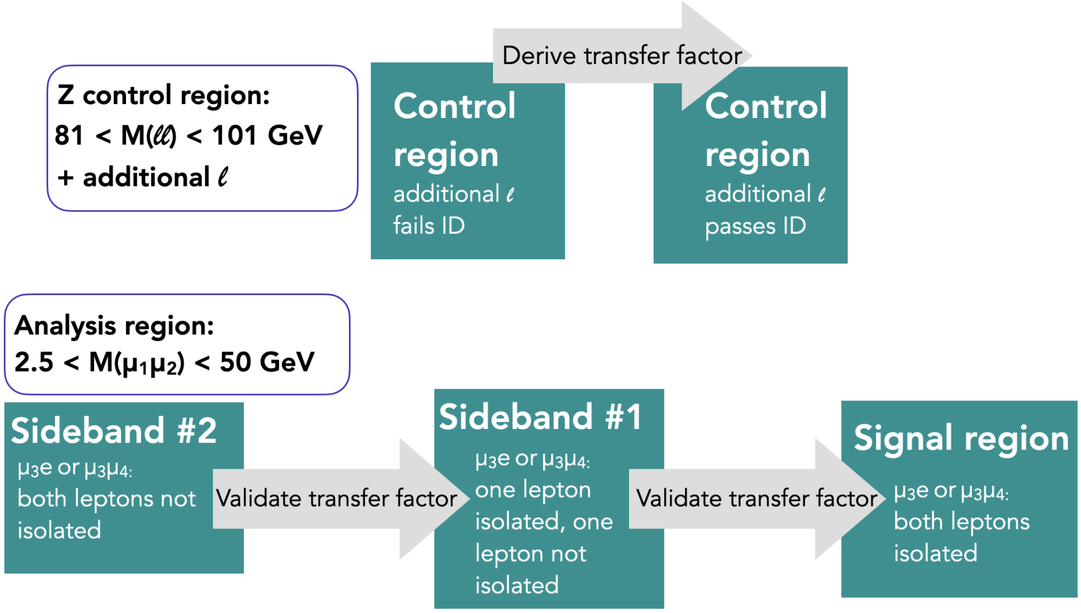

Figure 4.16: The structure of the analysis for $\tau_\mu\tau_e$ and $\tau_\mu\tau_\mu$ channels. Regions are defined based on how many leptons pass the isolation requirements. Here $\ell = e, \mu$. In Sideband 2, two leptons fail the isolation requirement. This region is also called 2P2F. In Sideband 1, one lepton fails the isolation requirement. This region is also called 3P1F. In the signal region, all four pass either the `Loose muon ID` or the `Tight electron ID`.

4.6 Background Estimation

4.6.1 Fully hadronic decay channel: $\tau_h\tau_h$

The main source of background in this channel is Drell-Yan dimuon production in association with at least one jet that fakes the a $\rightarrow \tau_h\tau_h$ decay. A Z+jet sample is obtained from the events passing the control region selections, which requires a dimuon pair with an invariant mass in the Z range. The fake rates are calculated in data with the residual contribution from diboson, $t\bar{t}$, and W+jets processes subtracted as estimated in simulation. The fake rates are calculated as a function of p_T (8-20 GeV, 20-30 GeV, 30-50 GeV, 50-80 GeV, 80-120 GeV, 120-170 GeV, 170-230 GeV, 230-300 GeV, 300-380 GeV, and >380 GeV). The fake rates are compared for different DeepDiTau working points applied to the leading jet. Figure 4.17 show these fake rates as a function of the leading jet p_T, which is be used as the transfer factor.

This fake rate method is validated in the two non-isolated muon regions: the sideband

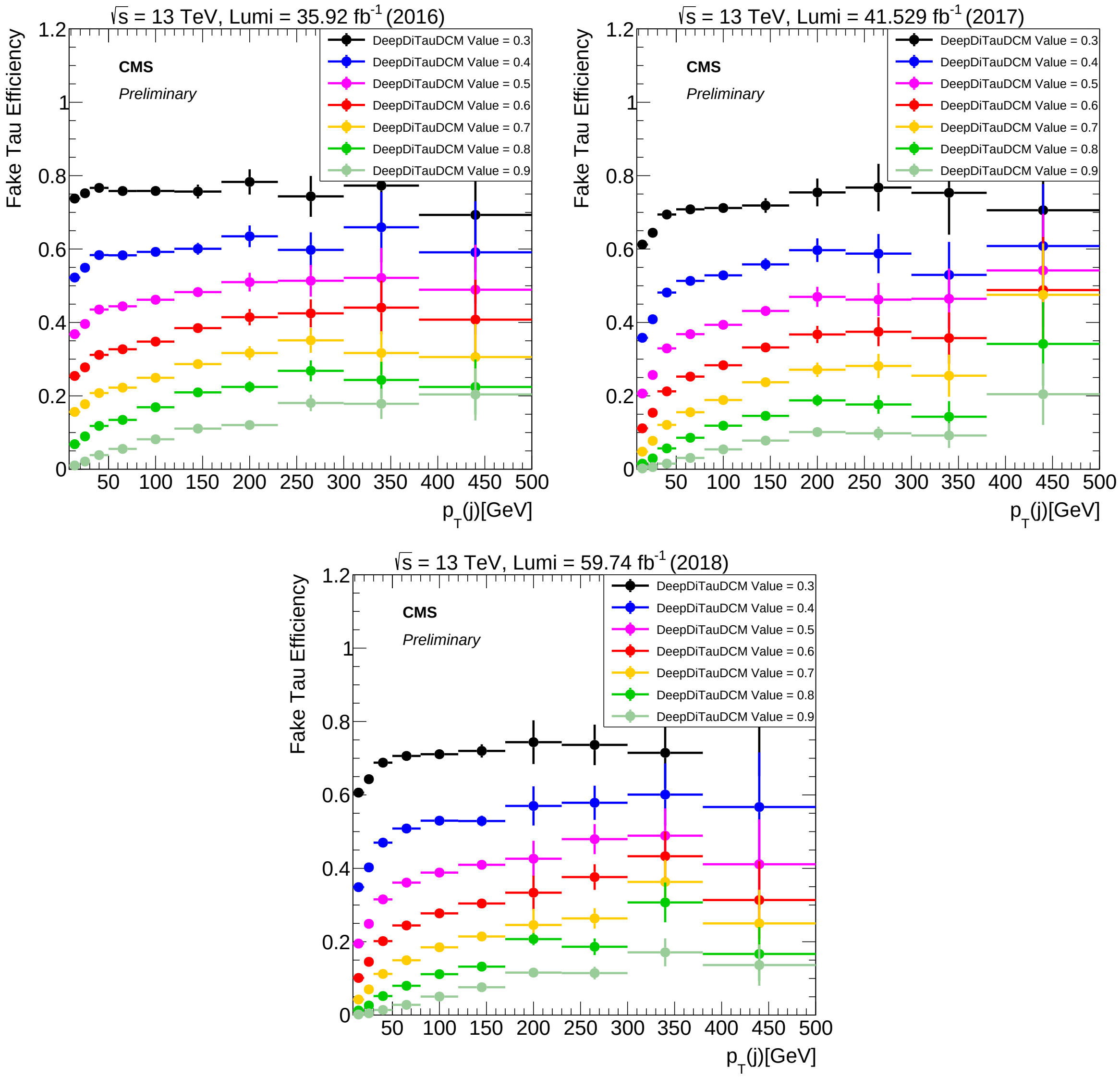

Figure 4.17: The fake rates used in estimating the signal region for the $\tau_h\tau_h$ pair, using 2016 (left), 2017 (middle), and 2018 (right) data. Events in the denominator have a jet that passes the very loose working point (0.2) of DeepDiTau. Events in the numerator have a jet passes the different working points of DeepDiTau.

region and validation sideband. The data in the validation region is compared to an estimate of validation region by applying the transfer factor to validation sideband data. Plots of this comparison are shown in Figures 4.18 and 4.19. The uncertainties on these plots include the statistical uncertainty from the sideband and the uncertainty on the fake rate values from the fake rate measurement control regions.

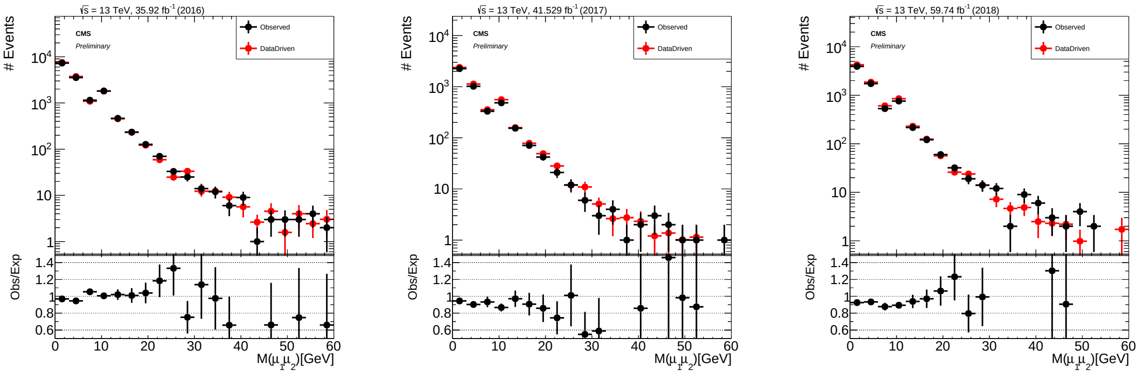

Figure 4.18: Comparisons of M($\mu_1\mu_2$) between the validation region and the estimation of the validation region from the validation sideband using the fake rate method in $\tau_h\tau_h$ channel, using 2016 (left), 2017 (middle), and 2018 (right) data.

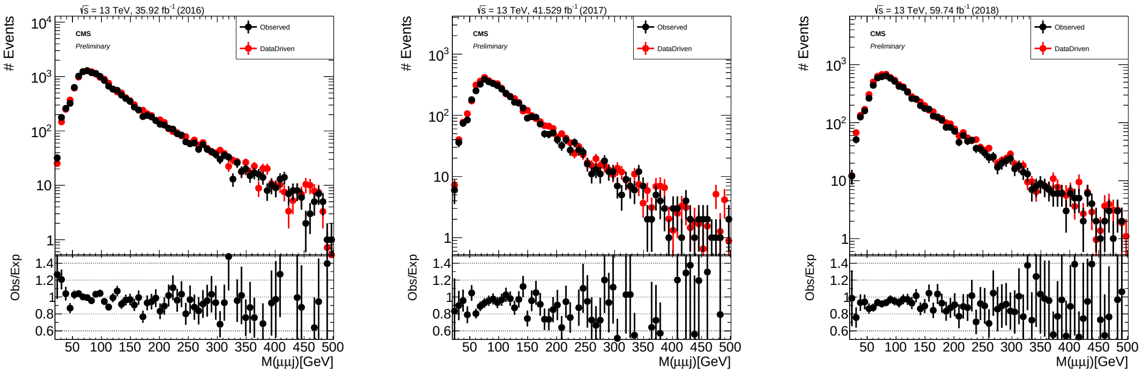

Figure 4.19: Comparison of M($\mu_1\mu_2$jet) between the validation region and the estimation of the validation region from the validation sideband using the fake rate method in $\tau_h\tau_h$ channel, using 2016 (left), 2017 (middle), and 2018 (right) data.

4.6.2 Semi-leptonic decay channels: $\tau_\mu\tau_h$ and $\tau_e\tau_h$

The main source of background in the semi-leptonic channels is Drell-Yan dimuon production in association with at least one jet that fakes the a → $\tau_\mu\tau_h$ or a → $\tau_e\tau_h$. This background modeling takes into account prominent known dimuon resonances with masses in the range being fit, 2.5 to 50 GeV [58]:

- ψ' : 3.69 GeV
- Υ(1S) : 9.46 GeV
- Υ(2S) : 10.02 GeV
- Υ(3S) : 10.36 GeV

In the reconstructed dimuon invariant mass $\mathrm{M}(\mu_1, \mu_2)$ distribution, the known resonance peaks are visible on top of the Drell-Yan continuum, such as in Figure 4.34c. In the visible 4-body mass $\mathrm{M}(\mu_1\mu_2\tau\tau)$ distribution, the dimuon + jet background appears as an exponentially falling distribution which rises around 40-60 GeV due to the transverse momentum thresholds of the reconstructed muons (and/or electrons) and one reconstructed τ_h. The signal is characterized by a narrow dimuon mass resonance from a pseudoscalar Higgs boson decay and a broader 4-body mass resonance from the Higgs boson decay.

The search strategy consists of fitting $\mathrm{M}(\mu_1\mu_2\tau\tau)$ versus $\mathrm{M}(\mu_1\mu_2)$ with analytical models for the signal and background shapes in each dimension. The background shape model includes the Drell-Yan continuum and the meson resonances mentioned above. Additionally, the J/ψ ($m_{\mathrm{J}/\psi} = 3.10$ GeV) resonance comes from the sideband, a data control region enriched in dimuon + jet events. Although the J/ψ resonance falls outside the kinematically allowed search window for a di-tau resonance, it is modeled in the fit to provide a better background description near the ψ'. Details of the fit are provided in Section 4.7. The remainder of this section describes the dimuon + jet sideband, the construction of jet$\rightarrow \tau\tau$ fake rates to be applied to the sideband region to obtain a prediction for the background shape, and the validation of the fake rate method.

Jet $\rightarrow \tau_\mu\tau_h$ / $\tau_e\tau_h$ fake rates

Using the analysis region definition in Figure 4.15, the sideband is used to predict the normalization of the background in signal region. The background events in the sideband are typically dimuon resonances with a jet and muon which are reconstructed as a $\tau_\mu\tau_h$

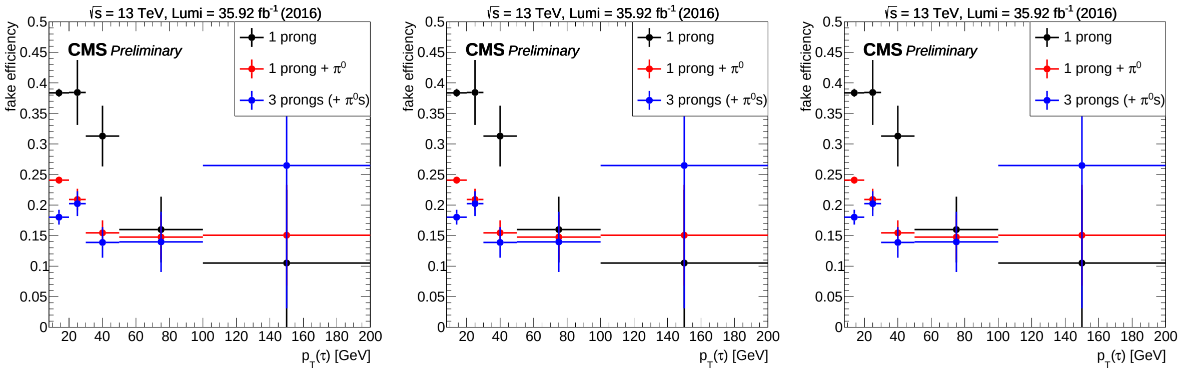

Figure 4.20: The tau fake rates used in estimating the signal region for a $\tau_\mu\tau_h$ pair, using 2016 (left), 2017 (middle), and 2018 (right) data. The denominator consists of "jets" selected as a muon cleaned tau from the HPS algorithm passing "decayModeFinding". The numerator is the "jets" that pass the medium MVA isolation. Rates are separated by decay mode: DM0 (one prong), DM1 (one prong + π^0), and DM10 (3 prongs + π^0s).

or $\tau_e\tau_h$ pair. Low-mass dimuon resonances listed at the beginning of this section are the primary source of background.

To estimate the fake rates of jets to ditau objects, a Z+jet sample is obtained from the events passing the control region selections. The fake rates are calculated in data with the residual contribution from diboson processes subtracted as estimated in simulation. The fake rates are calculated as a function of p_T (8-20 GeV, 20-30 GeV, 30-50 GeV, 50-100 GeV, and >100 GeV), and are applied as transfer factors. The fake rates are additionally divided by decay mode. Different hadronic tau decays are labeled with different decay modes as classified in Table 4.10. Figures 4.20 and 4.21 show these tau fake rates. The

DM label	Number of charged hadrons	Number of π^0
0	1	0
1	1	1
10	3	0

Table 4.10: Decay mode definitions for τ_h

statistics become poor at high p_T region.

The transfer factor method is applied to the sideband to estimate the background contamination in the signal region. A single event in the sideband contributes a weight

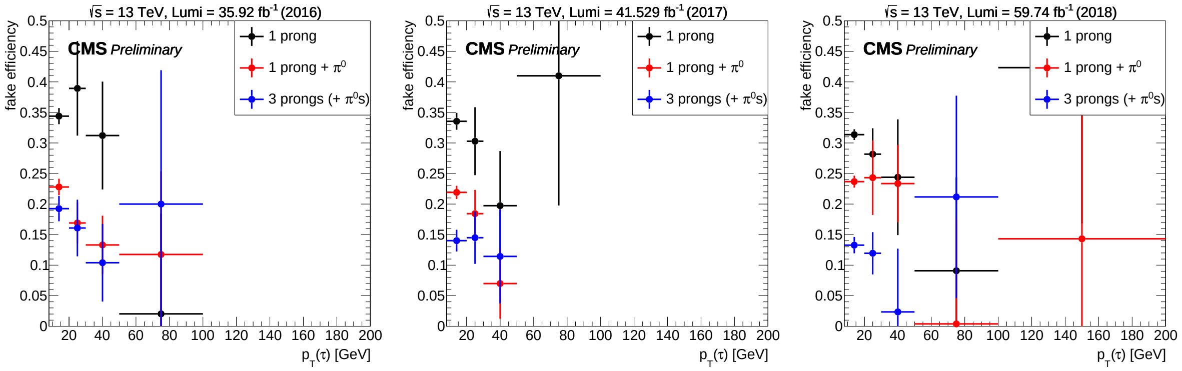

Figure 4.21: The tau fake rates used in estimating the signal region for a $\tau_e \tau_h$ pair, using 2016 (left), 2017 (middle), and 2018 (right) data. The denominator consists of "jets" selected as a electron cleaned tau from the HPS algorithm passing "decayModeFinding". The numerator is the "jets" that pass the medium MVA isolation. Rates are separated by decay mode: DM0 (one prong), DM1 (one prong + π^0), and DM10 (3 prongs + π^0s).

$$\frac{f}{1-f} \tag{4.2}$$

to the signal region where f is the fake efficiency for a jet to fake a tau. The total background contribution to the signal region is then

$$N_A^{exp} = \frac{f}{1-f} \cdot N_B, \tag{4.3}$$

where N_A^{exp} is the expected yield in a given bin of the signal region and N_B is the observed yield in a given bin of the sideband.

This fake rate method is validated in the two anti-isolated muon regions: the validation region and the validation sideband. The data in the validation region is compared to an estimate of validation region by applying the tau fake rate to the validation sideband data. Plots of this comparison are shown from Figure 4.22 to 4.25 for 2018 data. Appendix A contains the plots for 2016 and 2017 data. The uncertainties on these plots include the statistical uncertainty from the sideband and the uncertainty on the fake rate values from the fake rate measurement control regions.

With this validation, it is seen that there is some discrepancy between the expected background from the data driven method and the observed yields in the sideband region.

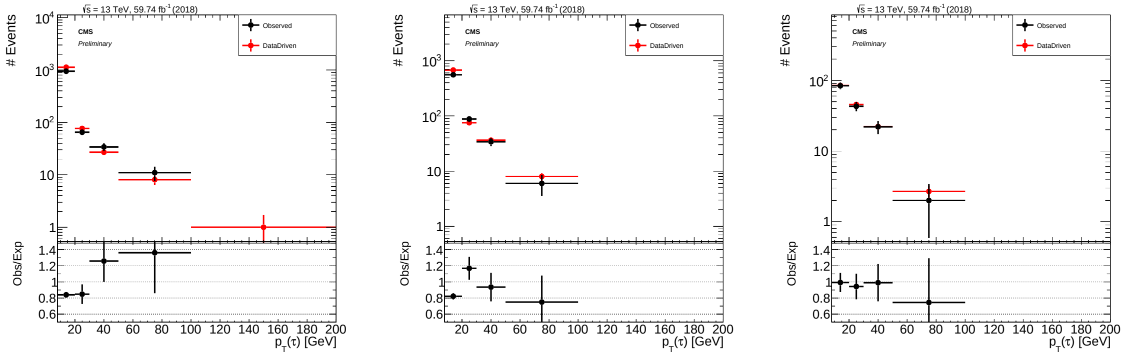

(a) DM0 (b) DM1 (c) DM10

Figure 4.22: Comparison of τ_h p_T spectra between the validation region and the estimation of the validation region from the validation sideband using the fake rate method in $\tau_\mu\tau_h$ channel using 2018 data. Different tau decay modes are shown separately.

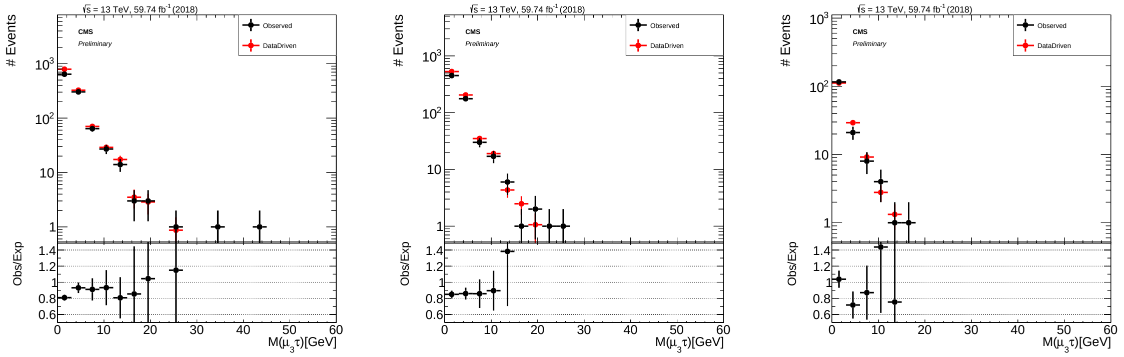

(a) DM0 (b) DM1 (c) DM10

Figure 4.23: Comparison of $\mathrm{M}(\mu_3, \tau_h)$ spectra between the validation region and the estimation of the validation region from the validation sideband using the fake rate method in $\tau_\mu\tau_h$ channel using 2018 data. Different tau decay modes are shown separately.

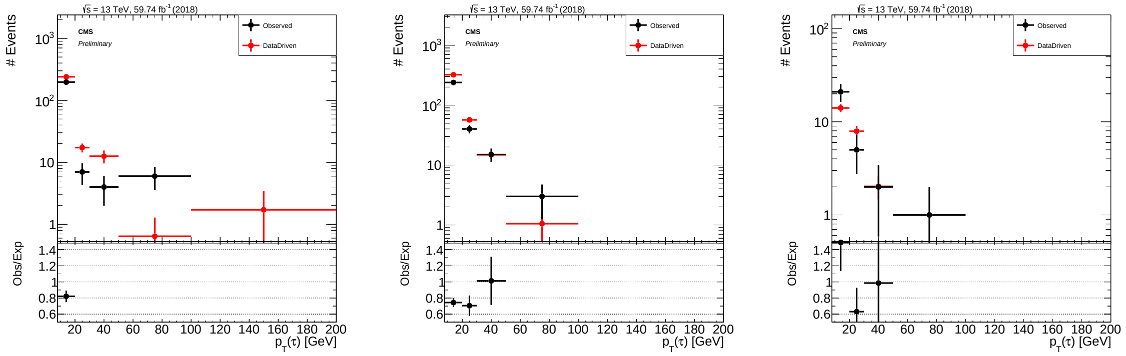

(a) DM0 (b) DM1 (c) DM10

Figure 4.24: Comparison of τ_h p_T spectra between the validation region and the estimation of the validation region from the validation sideband using the fake rate method in $\tau_e\tau_h$ channel using 2018 data. Different tau decay modes are shown separately.

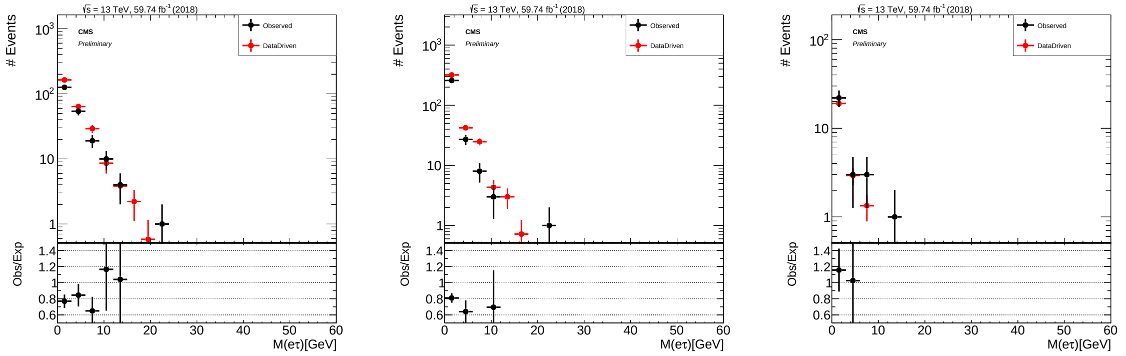

(a) DM0 (b) DM1 (c) DM10

Figure 4.25: Comparison of M(e,τ_h) between the validation region and the estimation of the validation region from the validation sideband using the fake rate method in $\tau_e\tau_h$ channel using 2018 data. Different tau decay modes are shown separately.

This discrepancy is larger than the statistical uncertainty shown in the figures. The discrepancy is accounted for with a 50% systematic uncertainty. Additionally, the above calculation makes the assumption the efficiency for a real tau or muon to enter the signal region is 1, but this is not the case. A simultaneous fit of the signal region and sideband is performed to account for signal contribution to the sideband.

4.6.3 Fully leptonic decay channels: $\tau_e\tau_\mu$ and $\tau_\mu\tau_\mu$

For the fully leptonic ditau decay channels, the background can be divided into irreducible and reducible parts. The irreducible background is ZZ decaying to four leptons. The reducible background originates from processes which contain one or more nonprompt leptons in the four lepton final state. The main sources of nonprompt leptons are non-isolated electrons and muons coming from decays of heavy flavor mesons, misreconstructed jets (usually originating from light flavor quarks), and electrons from γ conversions. In this discussion, any jet reconstructed as a lepton and any lepton originating from a heavy meson decay is a "fake lepton". Similarly, any electron originating from a photon conversion is considered a "fake electron".

To predict the number of fake leptons in our signal region, the probability of fake electrons and fake muons passing `Loose` selection criteria are measured in the control region and validated using the sideband regions. The rate of fake electrons f_e and fake muons f_μ are collectively referred to as fake rates. The fake rates as function of p_T are the transfer factors that are used to predict the background contribution in the signal region based on the sideband region after their performance is checked using the validation region and validation sideband.

In order to measure the fake rates f_e and f_μ, we select samples of $\mathrm{Z}(\ell\ell)+e$ and $\mathrm{Z}(\ell\ell)+\mu$ events. These events are required to have two same flavor and opposite charge leptons with $p_T > 26/20$ GeV passing the tight selection criteria and which form the Z candidate. In addition, there is exactly one lepton passing the loose selection criteria to be used as the probe lepton for the fake ratio measurement.

The fake ratios are evaluated using the requirement $|M_{inv}(\ell_1, \ell_2) - M_Z| < 10$ GeV to reduce the contribution from photon (asymmetric) conversions populating low masses.

The fake ratios are measured in bins of the transverse momentum of the loose lepton in the barrel and endcap regions. The electron and muon fake rates are measured within $|M_{inv}(\ell_1,\ell_2)-M_Z| < 10$ GeV and $E_{\mathrm{T}}^{\mathrm{miss}} < 20$ GeV separately for the 2016, 2017, and 2018 data. Figures 4.26 and 4.27 show the comparison of data-driven jet faking muon/electron efficiency as a function of muon/electron p_T with different muon isolation or electron ID requirements.

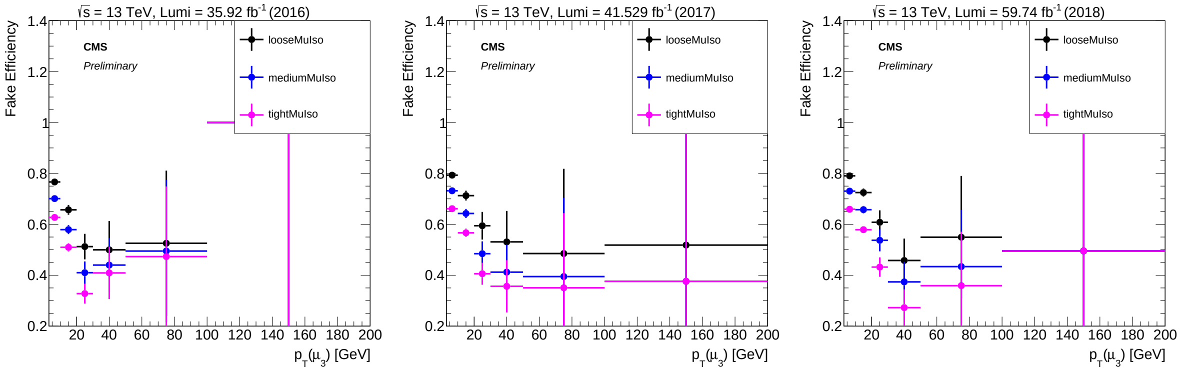

Figure 4.26: Fake rates as a function of the probe p_T for muons which satisfy the loose selection criteria, measured in a $Z(\ell\ell)+\ell$ sample in the 2016 (left), 2017 (middle), 2018 (right) data at 13 TeV. Comparison of data with tight requirement $|M_{inv}(\mu_1,\mu_2)-M_Z| <$ 10 GeV, and an additional μ_3 with different isolation requirements.

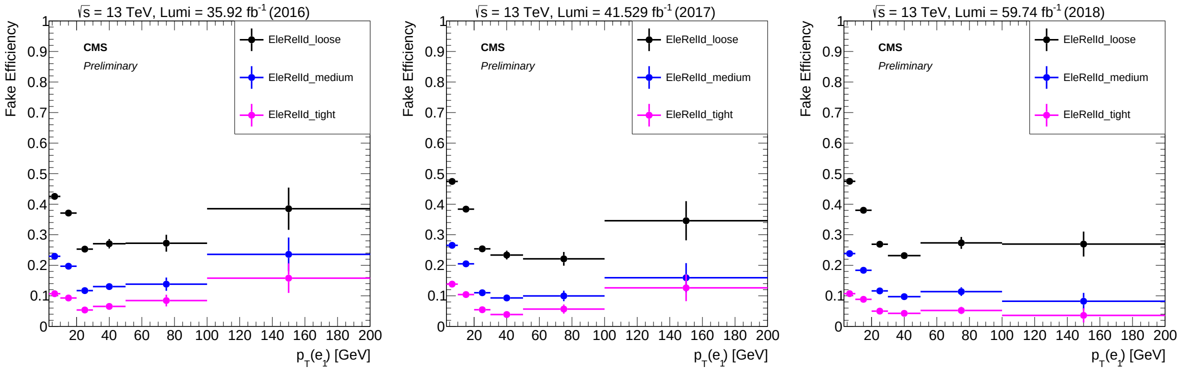

Figure 4.27: Fake rates as a function of the probe p_T for electrons which satisfy the loose selection criteria, measured in a $Z(\ell\ell)+\ell$ sample in the 2016 (left), 2017 (middle), 2018 (right) data at 13 TeV. Comparison of data with tight requirement $|M_{inv}(\mu_1,\mu_2)-M_Z| <$ 10 GeV, and an additional electron with different electron IDs.

As discussed in Section 4.5.4 with Figure 4.16, selections on the leptons sort the events into regions. In the signal region, both leptons (either μ_3 and e or μ_3 and μ_4) are be isolated. In Sideband 1, three leptons pass the standard requirements and one fails. This is referred to as “3 Prompt + 1 Fail” (3P+1F) sample. In Sideband 2, two leptons pass the standard requirements and two fail. This is referred to as “2 Prompt + 2 Fail” (2P+2F) sample.

Background events are expected to come from QCD multi-jet, Z+γ^*, and Drell-Yan. The 2P+2F region also has WZ events, and the proportions of the different events in the 3P + 1F and 2P + 2F are different. These events are used to estimate the reducible background in the signal region. The invariant mass distribution of events selected in the 2P+2F control sample is shown in Figures 4.28 and 4.29 for the $\tau_\mu\tau_e$ channel. The analogous plots for the $\tau_\mu\tau_\mu$ channel are given in Appendix B in Figures B.1 and B.2.

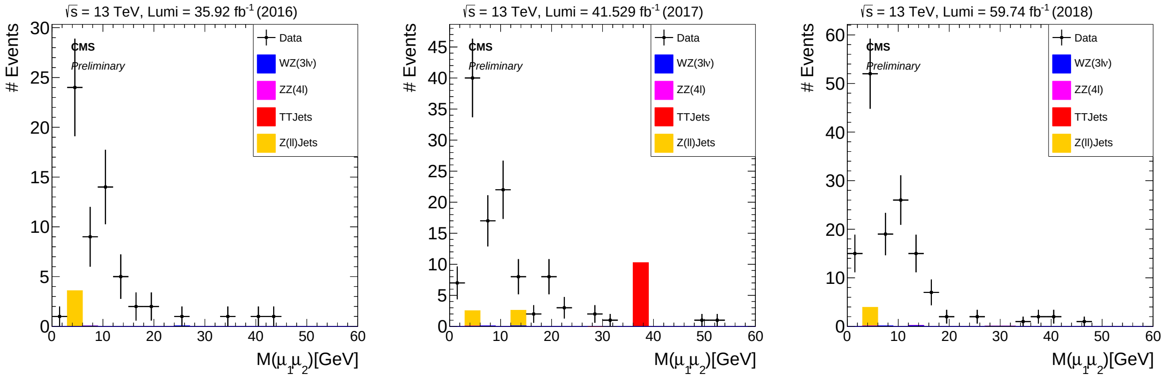

Figure 4.28: Dimuon invariant mass distribution of the events selected in the 2P+2F control sample in the $\tau_\mu\tau_e$ channel with the dataset of era: 2016 (left), 2017 (middle) and 2018 (right).

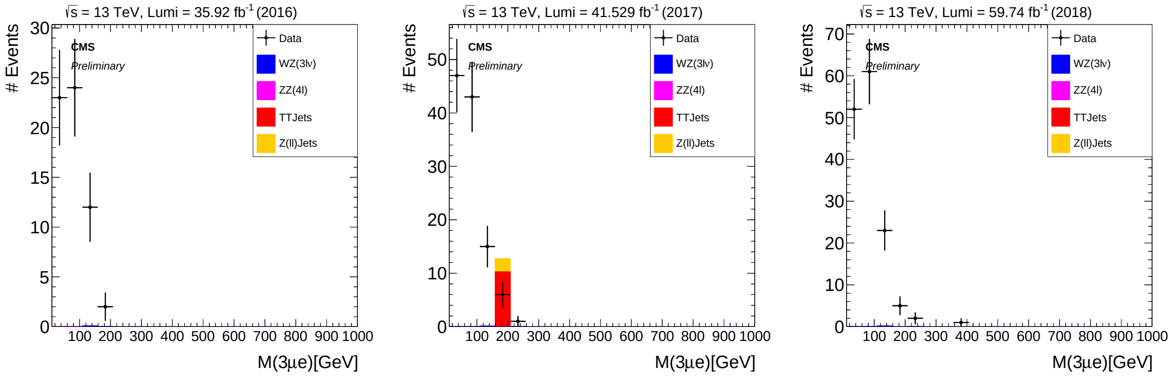

Figure 4.29: Four lepton visible mass distribution of the events selected in the 2P+2F control sample in the $\tau_\mu\tau_e$ channel with the dataset of era: 2016 (left), 2017 (middle) and 2018 (right).

The expected number of reducible background events in the 3P+1F region, $N_{\mathrm{3P1F}}^{\mathrm{bkg}}$, can be computed from the number of events observed in the 2P+2F control region, N_{2P2F}, by weighting each event in the region with the factor $(\frac{f_i}{1-f_i}+\frac{f_j}{1-f_j})$, where f_i and f_j correspond to the fake ratios of the two loose leptons:

$$N_{\mathrm{3P1F}}^{\mathrm{bkg}} = \sum(\frac{f_i}{1-f_i}+\frac{f_j}{1-f_j})N_{\mathrm{2P2F}} \tag{4.4}$$

Figures 4.30 and 4.31 show the invariant mass distributions of the events selected in the 3P+1F control sample, together with the expected reducible background estimated from Equation 4.4, stacked on the distribution of WZ and of irreducible background (ZZ, $Z\gamma* \to 4\ell$) taken from the simulation for the $\tau_\mu\tau_e$ channel. The analogous plots for the $\tau_\mu\tau_\mu$ channel are in the Appendix B in Figures B.4, and B.3.

If the same backgrounds were present in both the 2P+2F and the 3P+1F samples, the difference between the two would only come from the (small) WZ and Zγ* contributions. Large differences arise because the fake rates used in Equation 4.4 do not properly account for the background composition of the 2P+2F control sample. In particular, the difference seen in the $3\tau_\mu\tau_e$ channel between the observed 3P+1F distribution and the expectation from 2P+2F that is concentrated at low masses, is due to photon conversions, where a photon converts to a scattered photon and recoiling electron. This is confirmed explicitly by the simulation.

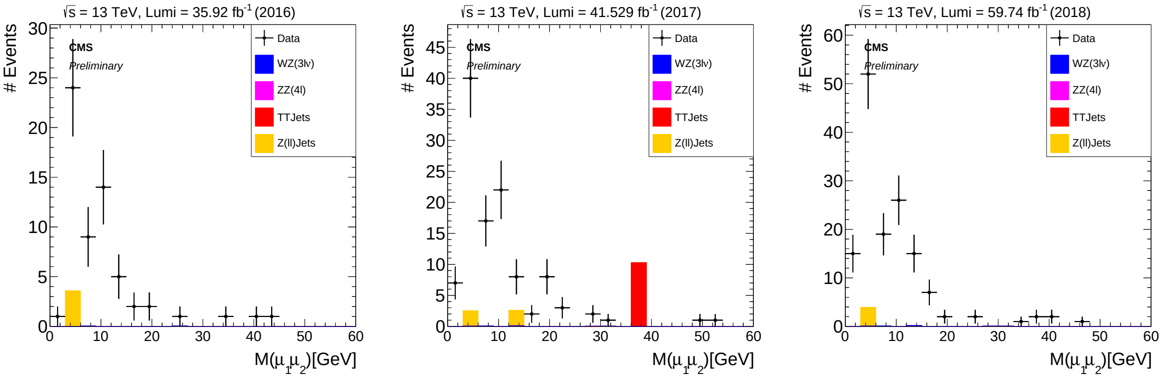

Figure 4.30: Dimuon invariant mass distribution of the events selected in the 3P+1F control sample in the $\tau_\mu\tau_e$ channel with the dataset of era: 2016 (left), 2017 (middle) and 2018 (right).

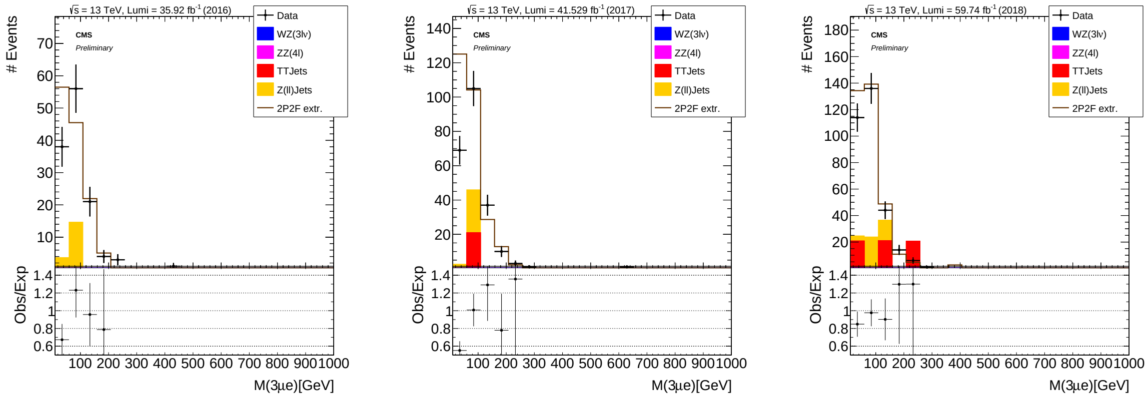

Figure 4.31: Four-lepton visible mass distribution of the events selected in the 3P+1F control sample in the $\tau_\mu\tau_e$ channel with the dataset of era: 2016 (left), 2017 (middle) and 2018 (right).

The difference between the 3P+1F observation and the prediction from 2P+2F to recover the missing contribution from conversions - and more generally, in principle, to “correct” for the fact that the fake rates do not properly account for the background composition of the 2P+2F sample. More precisely, the expected reducible background in the signal region is given by the sum of two terms :

- a “2P2F component” obtained from the number of events observed in the 2P+2F control region, N_{2P2F}, by weighting each event in that region with the factor $\frac{f_i}{1-f_i}\frac{f_j}{1-f_j}$, where f_i and f_j correspond to the fake ratios of the two loose leptons;
- a “3P1F component” obtained from the difference between the number of observed events in the 3P+1F control region, N_{3P1F}, and the expected contribution from the 2P+2F region and ZZ processes in the signal region, $N^{\mathrm{ZZ}}_{\mathrm{3P1F}} + N^{\mathrm{bkg}}_{\mathrm{3P1F}}$. The $N^{\mathrm{bkg}}_{\mathrm{3P1F}}$ is given by Eq. 4.4 and $N^{\mathrm{ZZ}}_{\mathrm{3P1F}}$ is the contribution from ZZ (from simulation). The difference $N_{\mathrm{3P1F}} - N^{\mathrm{bkg}}_{\mathrm{3P1F}} - N^{\mathrm{ZZ}}_{\mathrm{3P1F}}$, which may be negative, is obtained for each (p_T, η) bin of the “F” lepton, and is weighted by $\frac{f_i}{1-f_i}$, where f_i denotes the fake rate of this lepton. This “3P1F component” accounts for the contribution of reducible background processes with only one fake lepton (like WZ events), and for the contribution of other processes (e.g. photon conversions) that are not properly estimated by the 2P2F component, because of the fake rates used.

Therefore, the full expression for the prediction can be symbolically written as:

$$N_{\mathrm{SR}}^{bkg} = \sum \frac{f_i}{(1-f_i)}(N_{\mathrm{3P1F}} - N_{\mathrm{3P1F}}^{\mathrm{bkg}} - N_{\mathrm{3P1F}}^{\mathrm{ZZ}}) + \sum \frac{f_i}{(1-f_i)}\frac{f_j}{(1-f_j)}N_{\mathrm{2P2F}} \tag{4.5}$$

The previous equation is equivalent to the following:

$$N_{\mathrm{SR}}^{bkg} = (1 - \frac{N_{3P1F}^{ZZ}}{N_{3P1F}}) \sum_{j}^{N_{3P1F}} \frac{f_a^j}{1-f_a^j} - \sum_{i}^{N_{2P2F}} \frac{f_3^i}{1-f_3^i}\frac{f_4^i}{1-f_4^i} \tag{4.6}$$

The invariant mass distribution of the predicted events obtained from the combination of the results in the 2P+2F and 3P+1F control samples are shown in Figures 4.32 and 4.33 for the $\tau_\mu\tau_e$ channel. The analogous plots for the $\tau_\mu\tau_\mu$ channel are in the Appendix B in Figures B.5 and B.6. In general, the predicted background extrapolated in the signal region is dominated by the jets faking leptons, while the irreducible background ZZ from simulation is negligible [51].

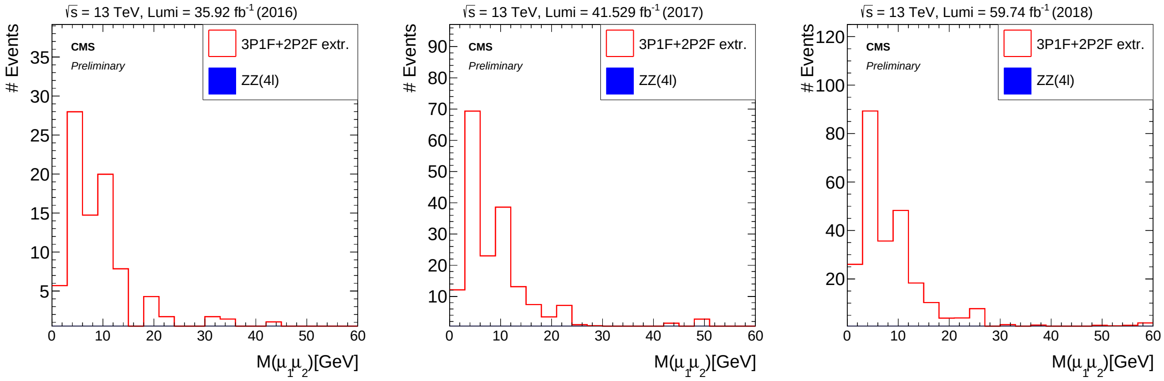

Figure 4.32: Dimuon invariant mass distribution of the events extrapolated in the signal region in the $\tau_\mu\tau_e$ channel with the dataset of era: 2016 (left), 2017 (middle) and 2018 (right).

4.7 Background and Signal Fitting

In this analysis, a parametric fit is used to extract either a signal significance or an upper limit on the signal confidence level. Previous studies found the most performant model is a 2-dimensional fit of the dimuon invariant mass and 4-body visible M($\mu\mu\tau\tau$) mass for all the decay channels [8]. In this section, control region refers to the region used to constrain fits on the relative normalizations of the J/ψ and Υ resonances.

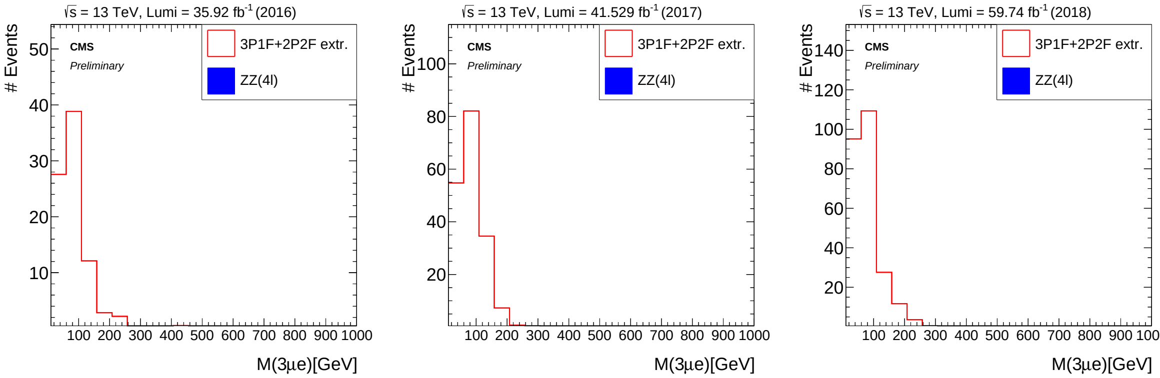

Figure 4.33: Four-lepton visible mass distribution of the events extrapolated in the signal region in the $\tau_\mu \tau_e$ channel with the dataset of era: 2016 (left), 2017 (middle) and 2018 (right).

For the dimuon invariant mass fit, a Voigtian probability density function (PDF) is used to fit the signal. The parameters of the Voigtians for each of the generated signal samples are fit by linear, quadratic, or cubic polynomials. The polynomials are then used to extrapolate between signal mass points. The background is modeled by sum of 2 exponentials for the continuum plus three Voigtians for the three Υ resonances and two Voigtians for the two J/ψ resonances.

For the 4-body visible mass fit, a double-sided Gaussian shape is used to fit the signal. Similar to the dimuon invariant mass fit, the parameters of the double-sided Gaussian for each of the generated signal samples are then fit by linear, quadratic, or cubic polynomials for extrapolating between signal mass points. The background is modeled by the multiplication of an error function and an exponential or sum of 2 exponentials, depending on the channel.

Due to technical difficulty of fitting different background shapes at once, the fits are further split into 3 regions of dimuon invariant mass: a low mass region with $\mathrm{m}(\mu_1\mu_2) < 8.5$ GeV, a region around the Υ resonances with $8.5 < \mathrm{m}(\mu_1\mu_2) < 11.5$ GeV, and a high mass region with $\mathrm{m}(\mu_1\mu_2) > 11.5$ GeV [51].

4.7.1 Background modeling

The fitting strategy is to simultaneously fit the signal region, sideband, and control regions. In initial fits, the signal region datasets are predicted by the fake rate methods described in Section 4.6. The initial fit for the control region is shown in Fig. 4.34. The initial fits for the background predictions in the signal region for the $\tau_h\tau_h$, $\tau_\mu\tau_h$, and $\tau_\mu\tau_e$ channels are shown in Figures 4.35, 4.36, 4.37 respectively. The fits for the $\tau_e\tau_h$ and $\tau_\mu\tau_\mu$ channels are in Appendix C in Figures C.1 and C.2. In these fits, the parameters for the mean, sigma, width, and relative normalizations of the J/ψ and Υ resonances are fixed to the values from the initial control region fit. The fits are done for each of the 2016, 2017, and 2018 datasets separately. Only the 2018 signal region results are shown here as an example.

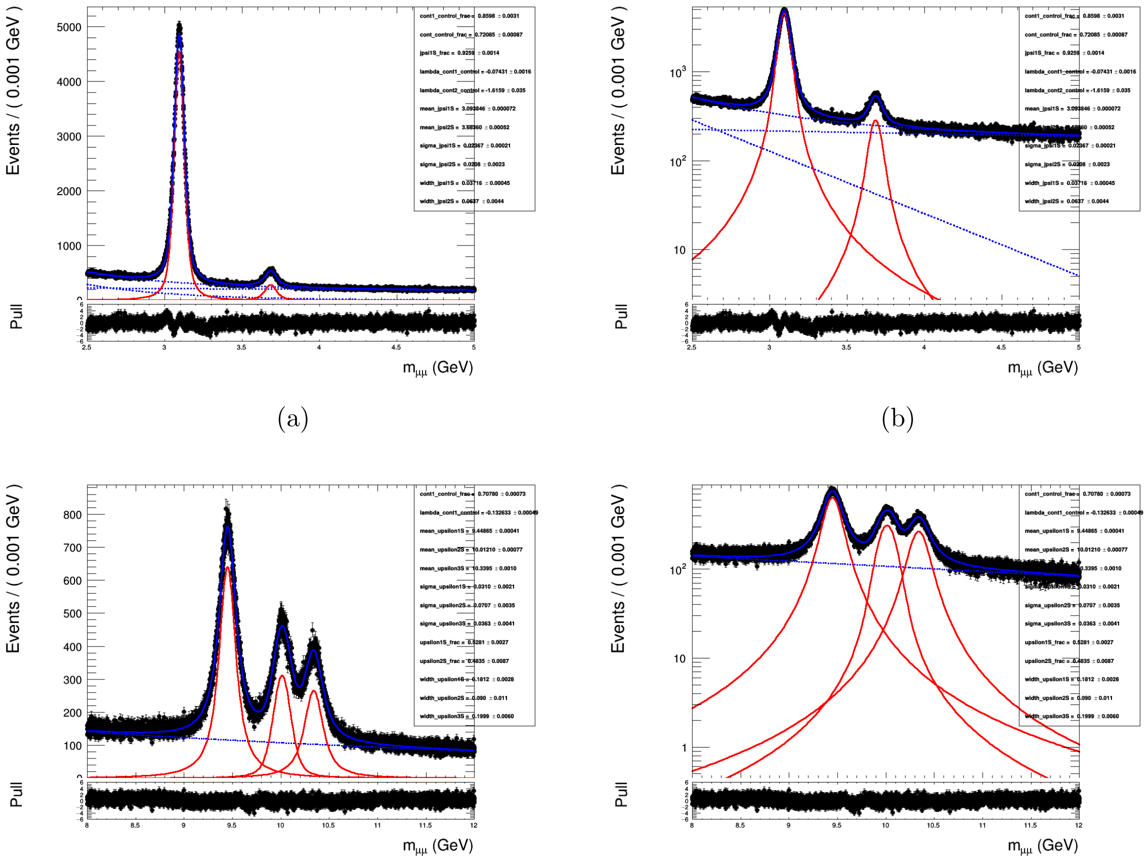

(a) (b)

(c) (d)

Figure 4.34: Initial fits of the $m(\mu_1, \mu_2)$ distributions for the control region in linear (left) and log (right) scales.

The results of the initial fits are then used to construct the final fitting models used in the Higgs Combine tool [59, 60]. Table 4.11 summarizes the background model parameters

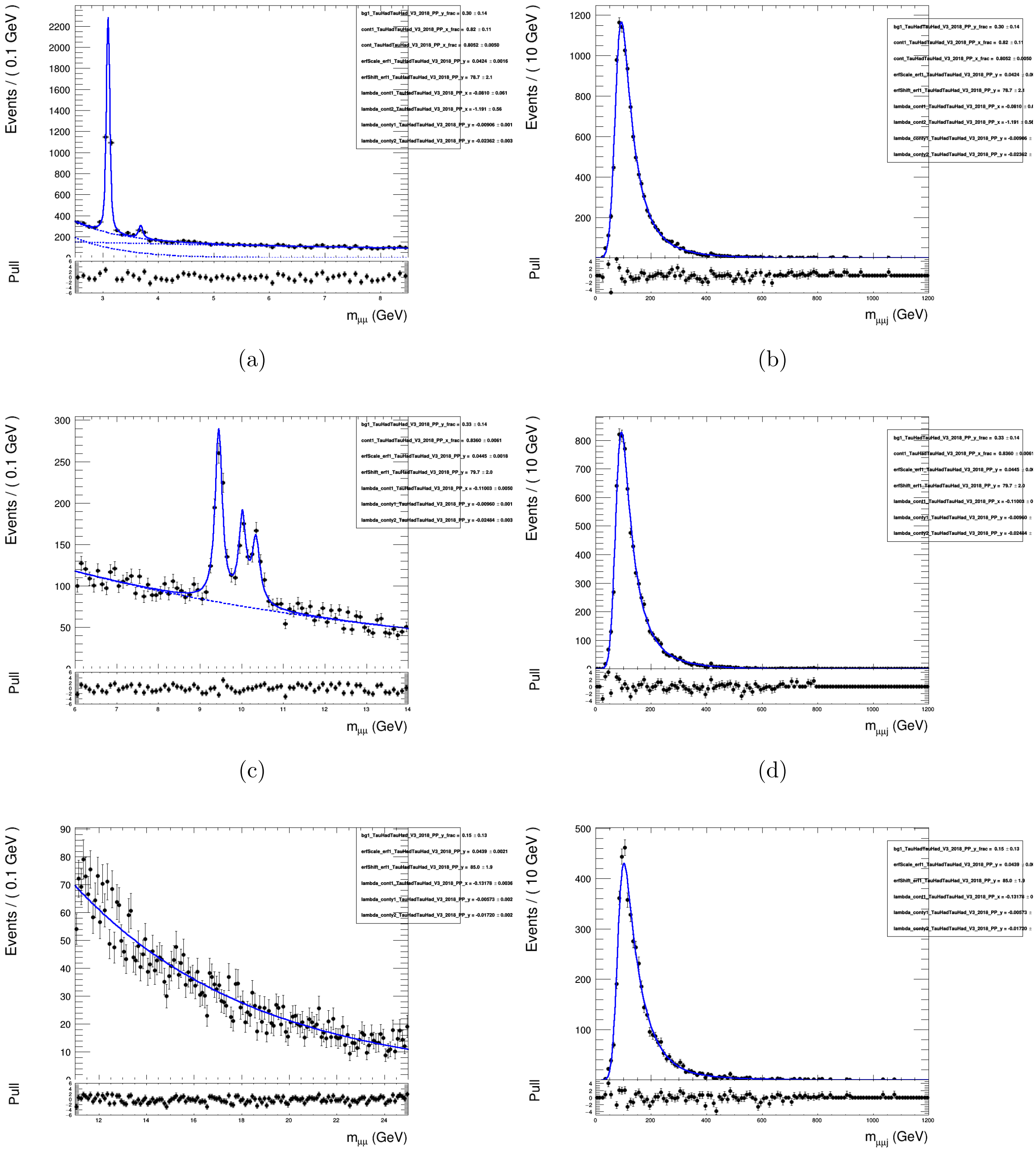

(a) (b)

(c) (d)

(e) (f)

Figure 4.35: Initial fits of the dimuon (left) and 4-body (right) visible mass distributions from the 2018 dataset in the signal region for the $\tau_h \tau_h$ channel.

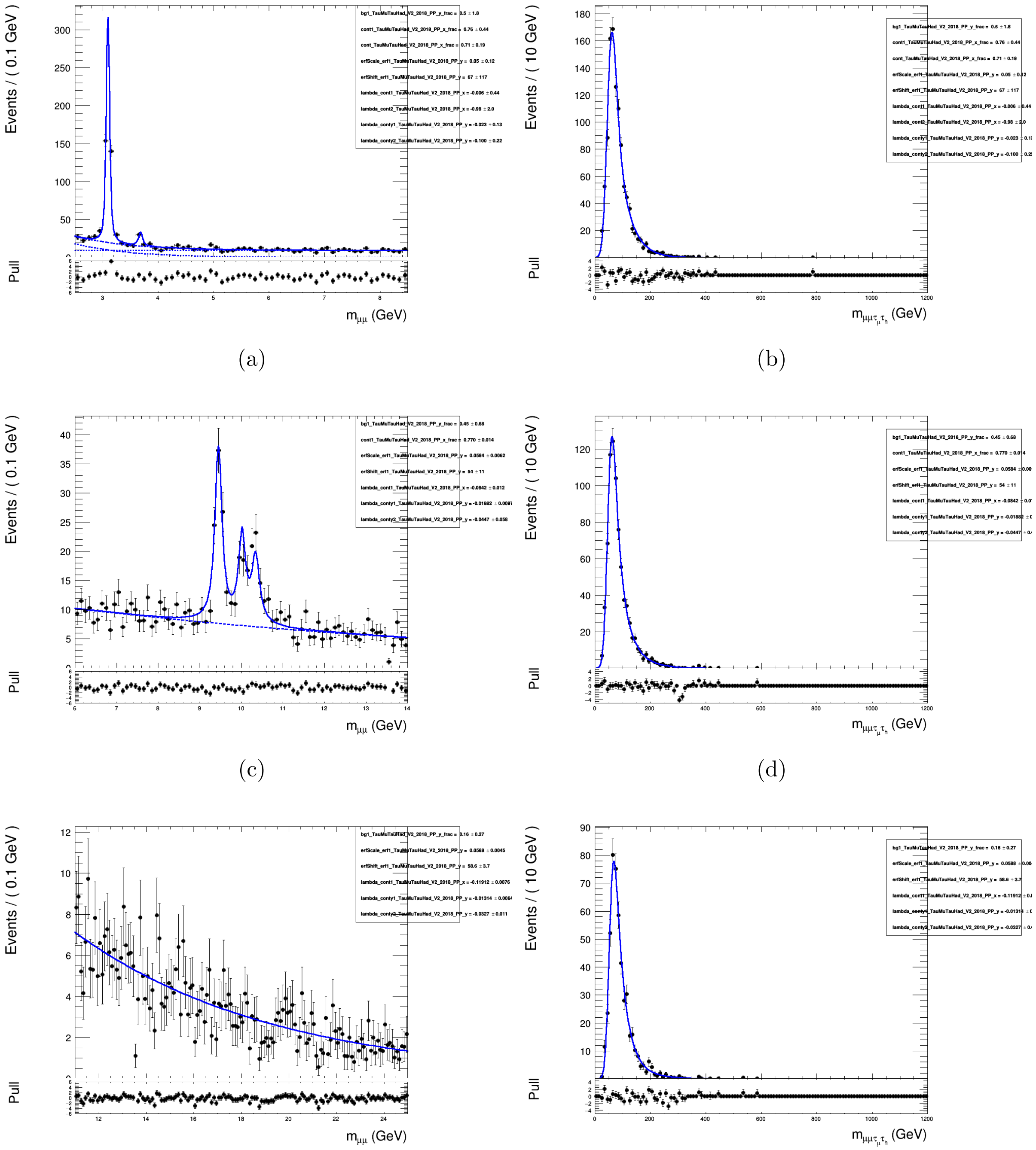

(a) (b)

(c) (d)

(e) (f)

Figure 4.36: Initial fits of the dimuon (left) and 4-body (right) visible mass distributions from the 2018 dataset in the signal region for the $\tau_\mu\tau_h$ channel.

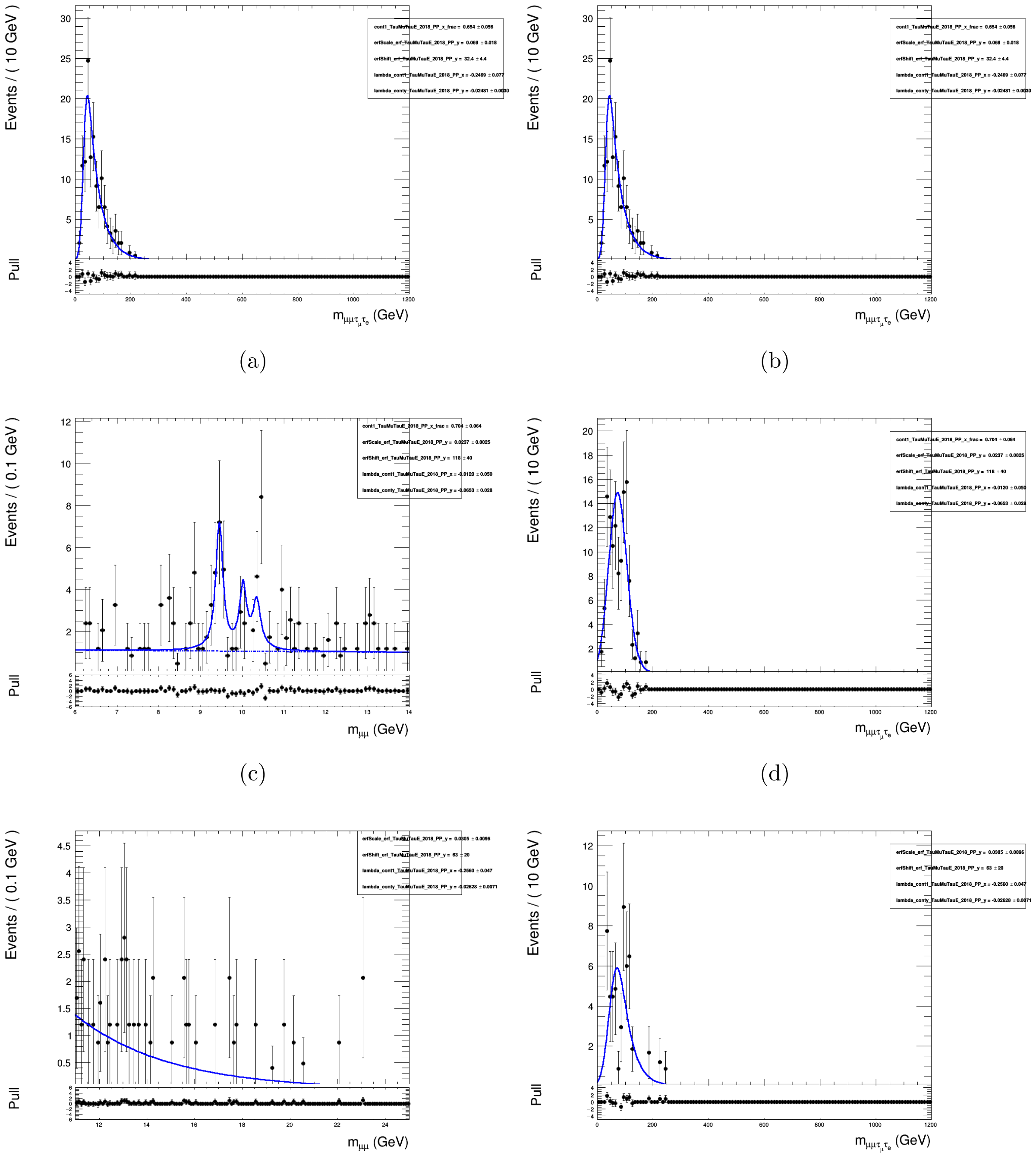

(a) (b)

(c) (d)

(e) (f)

Figure 4.37: Initial fits of the dimuon (left) and 4-body (right) visible mass distributions from the 2018 dataset in the signal region for the $\tau_\mu \tau_e$ channel.

and their relations among the three fit regions in the analysis. The construction of the final fitting models are described as follows:

1. Construct the control region PDF of 5 resonances over a double exponential continuum
2. Construct the sideband and signal region PDFs (dimuon invariant and 4-body visible ($\mu\mu\tau\tau$) masses as described above)
3. Set the parameters for the mean, sigma, width, and relative normalizations of the J/ψ and Υ resonances freely floating and shared between all three regions
4. Set the remaining parameters freely floating in sideband and control region
5. For each of the remaining parameters, derive a tight-to-loose ratio by dividing the fitted values in the signal and sideband regions from the initial fits
6. Set the parameters in the signal region as the tight-to-loose ratios times the corresponding parameters in the sideband region

Based on the discrepancies in the validation regions, a systematic uncertainty is assigned to the transfer factor. To do this, we first create a fake up and a fake down predicted signal region datasets by varying the fake rate by 20%–50% depending on channel, tau decay mode, and tau p_T. The above fitting procedure is rerun on the fake up and down datasets to obtain the up and down systematics for the transfer factors.

Category	Parameters	Signal region	Sideband	Control region
M($\mu\mu$) resonances	μ, σ, Γ	Constrained (three regions)		
M($\mu\mu$) continuum	λ^i	Transfer factor	Free	Free
M($\mu\mu\tau\tau$)	Erf_a, Erf_b, λ^{i}	Transfer factor	Free	
Normalizations	$N_{\Psi 2S}/N_{J/\Psi}$	Transfer factor	Constrained (two regions)	
	$N_{\Upsilon 2S}/N_{\Upsilon 1S}$	Transfer factor	Constrained (two regions)	
	$N_{\Upsilon 3S}/N_{\Upsilon 1S}$	Transfer factor	Constrained (two regions)	
	$N_{\Upsilon 1S}/N_{J/\Psi}$	Transfer factor	Free	Free
	$N_{J/\Psi}/N_{\mathrm{continuum}}$	Transfer factor	Free	Free

Table 4.11: Background model parameters and their relations among the three fit regions in the analysis. The background model includes the five meson resonances modeled using a Voigt function over an exponential continuum. The 4-body background model includes an error function multiplied with the sum of two exponential distributions. Three types of fit region relations are used: (a) constrained, in which the parameters are the same in the indicated regions, (top middle) free, in which the parameter is not related to those in any other region, and (c) related via the transfer factors, in which the indicated parameter in the signal region is constrained to the corresponding parameter in the sideband via a linear transformation [8].

4.7.2 Signal modeling

The signal model interpolations are built from signal fits at each generated pseudoscalar Higgs boson mass. For a given mass point, the signal is fit to the PDF described at the beginning of this section. The modeling of 5, 10, and 20 GeV pseudoscalar Higgs boson for the $\tau_h\tau_h$, $\tau_\mu\tau_h$, and $\tau_\mu\tau_e$ channels in the signal region from the 2018 MC are shown in Figures 4.38, 4.39, and 4.40. The fits for the $\tau_e\tau_h$ and $\tau_\mu\tau_\mu$ channels are in Appendix C in Figures C.3 and C.4. The fitted mean, sigma, width, and integral of the signal models as a function of the pseudoscalar mass for the $\tau_\mu\tau_h$ channel from the 2018 MC in the signal and sideband regions are shown in Figure 4.41 and Figure 4.42, respectively.

4.8 Systematic Uncertainties

The systematic uncertainties fall into two categories, normalization and shape. Normalization uncertainties affect all analysis bins equally while shape uncertainties cause a change in the spectrum.

The uncertainty on the background estimation includes multiple components. First, the statistical uncertainties of the fake efficiencies calculated in the Drell–Yan plus fake control region are propagated to the signal region. These were shown in Section 4.6. Secondly, the parameters of the meson resonance distributions (means, widths, and sigmas) are constrained via a simultaneous fit to the control region. Finally, the background meson resonance relative yields of ψ' and Υ(2S) and Υ(3S) from J/ψ and Υ are estimated from the sideband and propagated to the expected yields in the signal region. A deviation from the expectation is observed in the validation region and validation sideband distributions according to the robustness checks.

The yields of the Υ(2S) and Υ(3S) are given an uncertainty of 5% and 10%, respectively, while the yield of ψ' is given a 20% uncertainty. For the ranges where no meson resonance presents, a fake lepton uncertainty (a fake τ_h in the semi-hadronic decay channel or a fake $\tau_h\tau_h$ in the fully hadronic decay channel) is estimated according to the robustness checks and is propagated into the shape of the expected yields in the signal region. Similarly, fake lepton uncertainties in the fully leptonic decay channels are estimated according

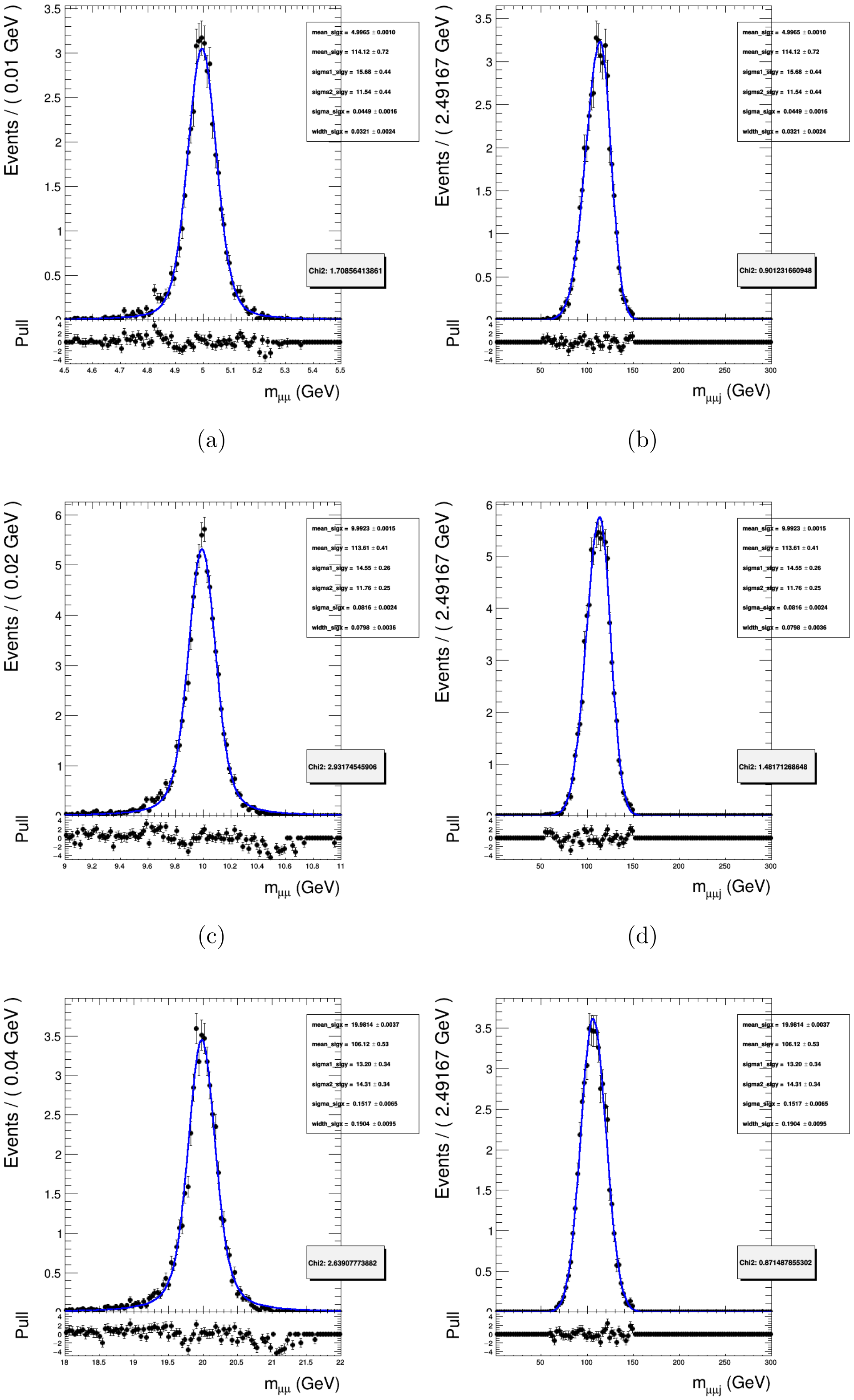

(a)

(b)

(c)

(d)

(e)

(f)

Figure 4.38: Modelling of the dimuon (left) and 4-body (right) visible mass distributions in the signal region for pseudoscalar masses of 5 (top), 10 (middle), and 20 (bottom) GeV for the $\tau_h\tau_h$ channel.

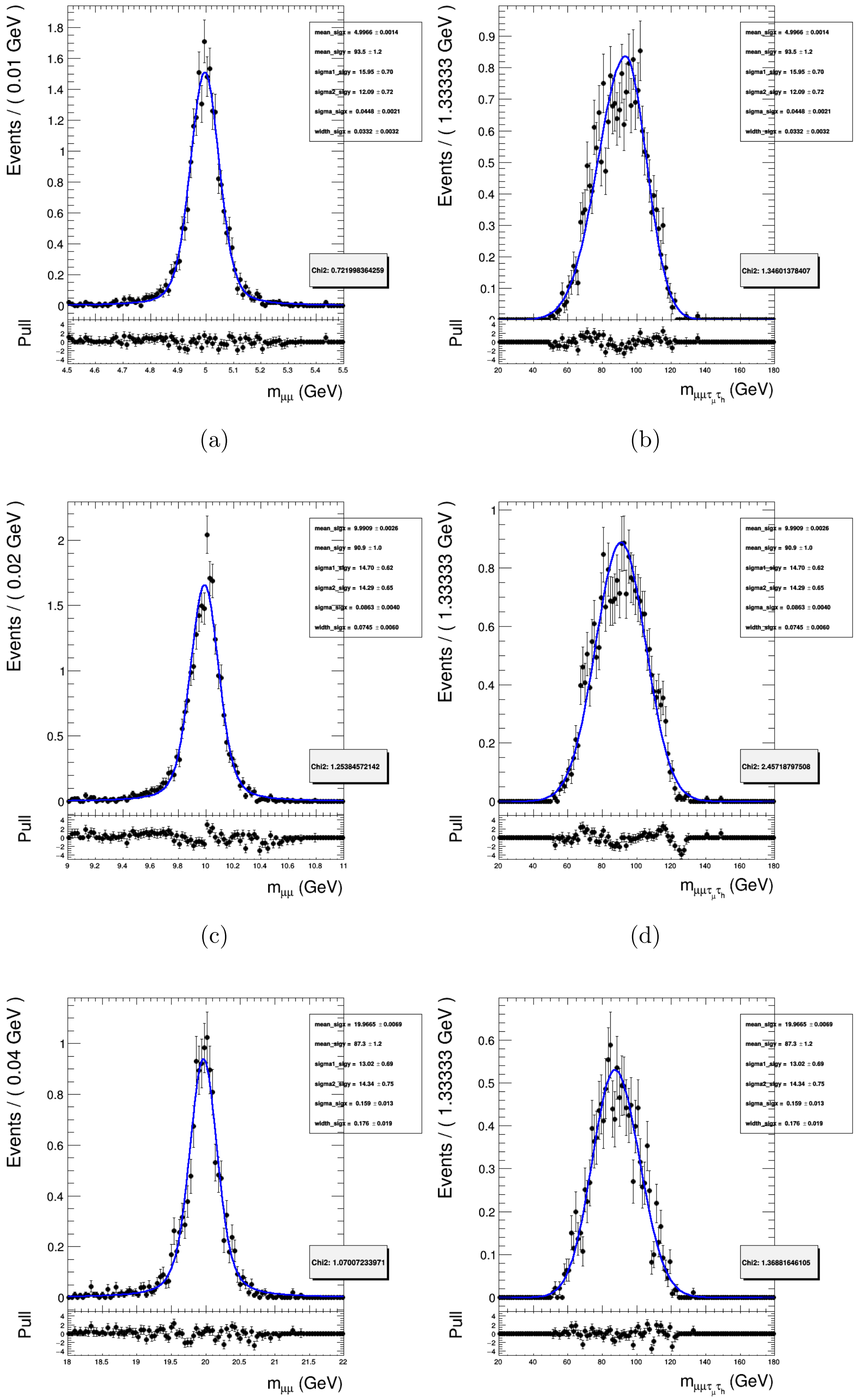

(a) (b)

(c) (d)

(e) (f)

Figure 4.39: Modelling of the dimuon (left) and 4-body (right) visible mass distributions in the signal region for pseudoscalar masses of 5 (top), 10 (middle), and 20 (bottom) GeV for the $\tau_\mu\tau_h$ channel.

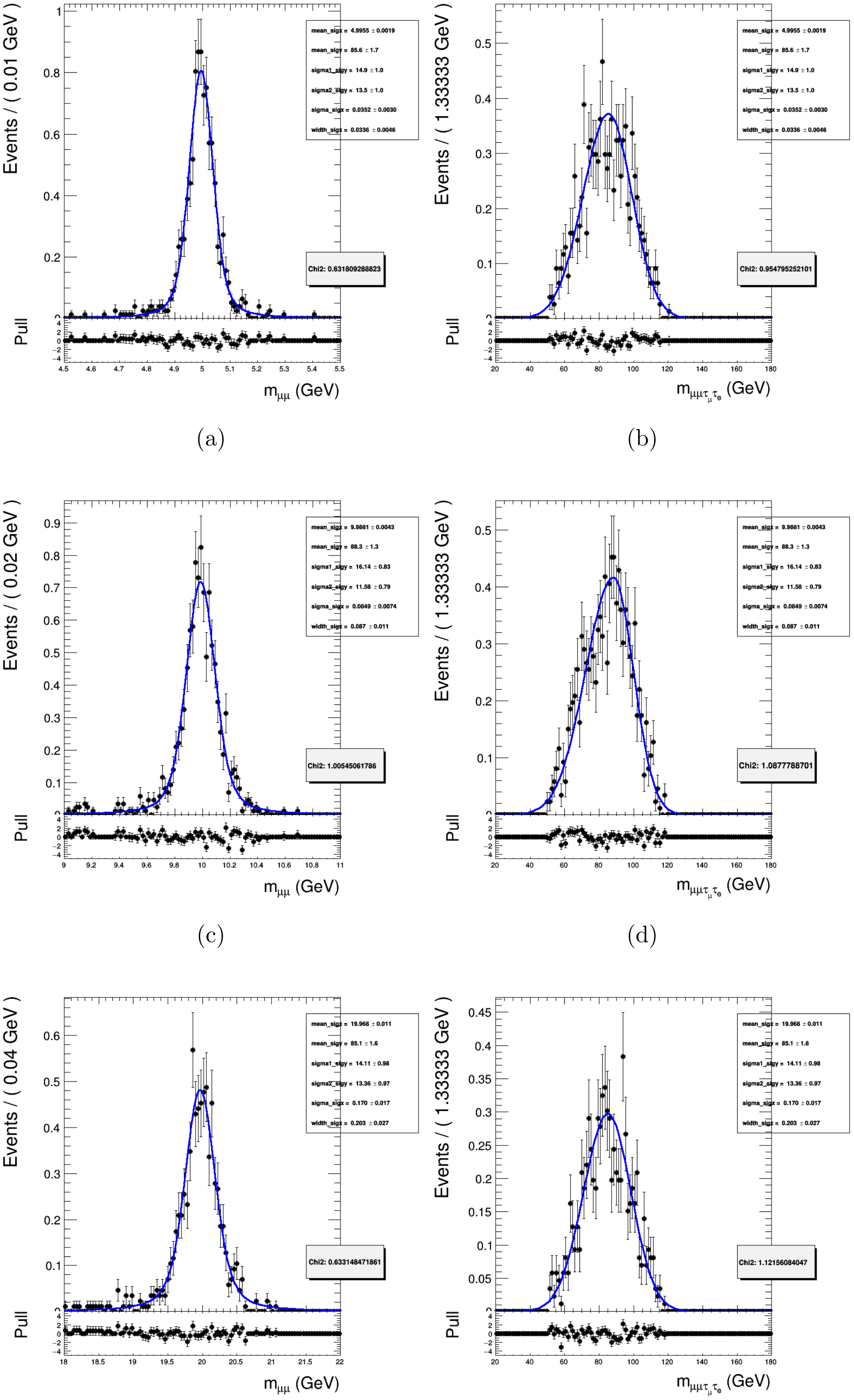

(a) (b)

(c) (d)

(e) (f)

Figure 4.40: Modelling of the dimuon mass distribution in the signal region for pseudoscalar masses of 5 (left), 10 (middle), and 20 (right) GeV for the $\tau_\mu\tau_e$ channel.

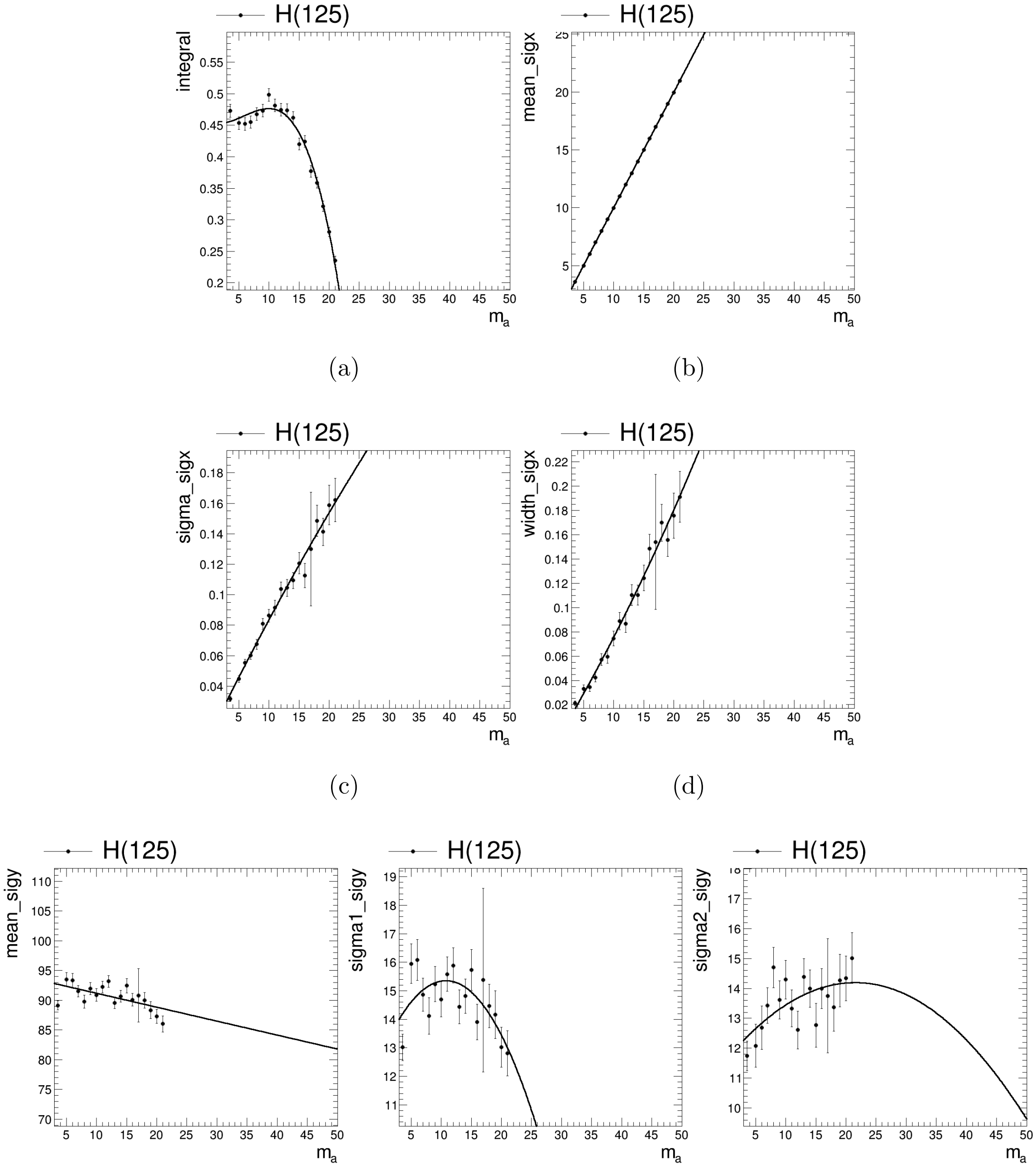

(a) (b)

(c) (d)

(e) (f) (g)

Figure 4.41: Fitted parameters from the 2018 signal MC as a function of pseudoscalar mass in signal region for the $\tau_\mu \tau_h$ channel. From top-left to bottom-right, parameters shown are integral, dimuon mean, dimuon sigma, dimuon width, 4-body mean, 4-body sigma below mean, and 4-body sigma above mean.

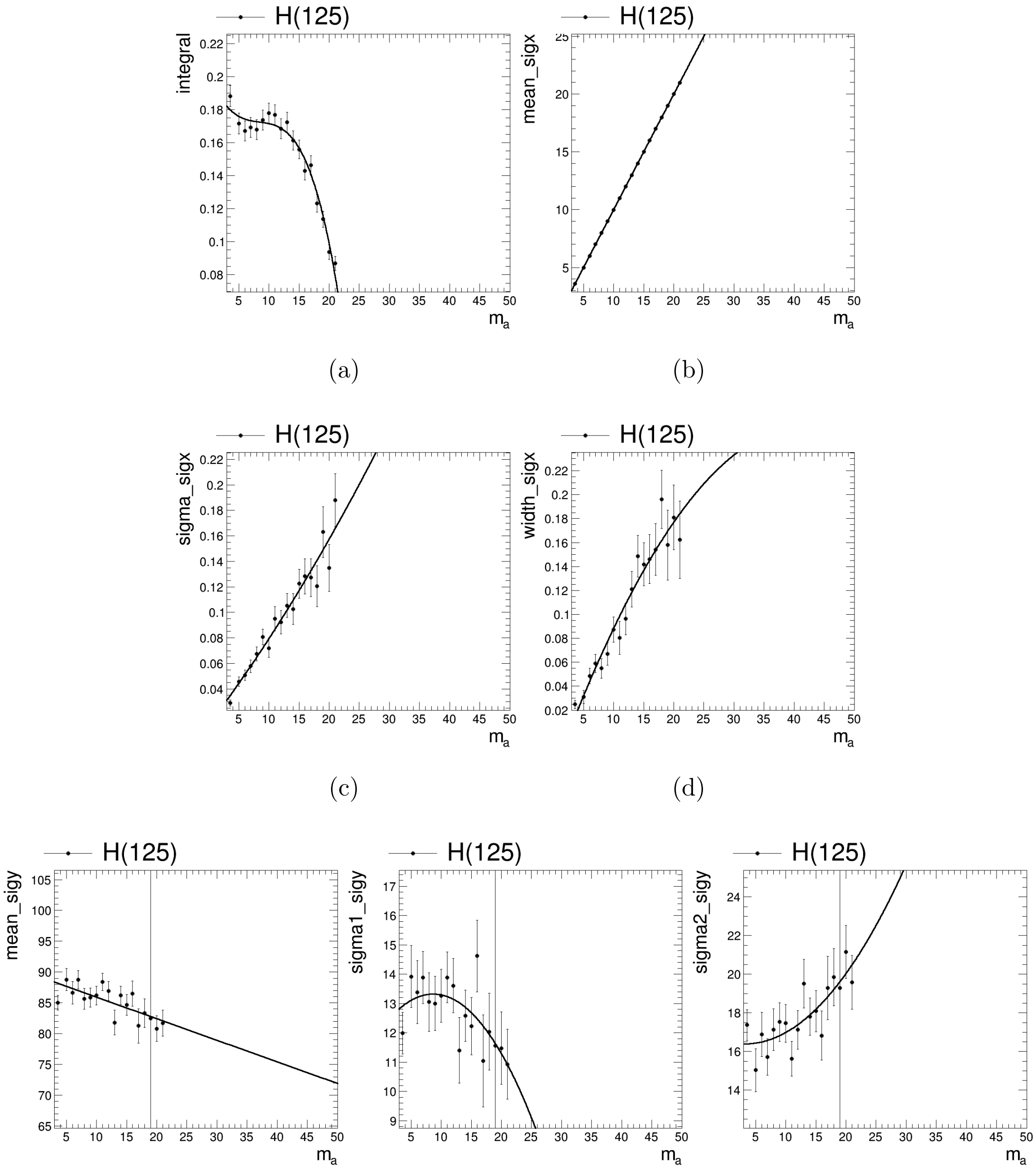

(a) (b)

(c) (d)

(e) (f) (g)

Figure 4.42: Fitted parameters from the 2018 signal MC as a function of pseudoscalar mass in sideband region for the $\tau_\mu\tau_h$ channel. From top-left to bottom-right, parameters shown are integral, dimuon mean, dimuon sigma, dimuon width, 4-body mean, 4-body sigma below mean, and 4-body sigma above mean.

to the discrepancy between the observed distributions and the extrapolated data distributions in the 3P1F region. These uncertainties are propagated into the extrapolated data in the signal region.

For the combined asymptotic expected limit settings in Section 4.9, the theory uncertainties are correlated among all years and channels. All the experimental uncertainties are independent among all years and channels. The systematic uncertainties are shown in Table 4.12.

Uncertainty source	Combine type	Uncertainty
Trigger efficiency	normalization	0.5%
Minbias cross section	shape	5%
Luminosity	normalization	2.3%
Muon identification	normalization	1%
Muon isolation	normalization	0.5%
Tau identification	shape	5-18%
Fake lepton uncertainty	shape	20%
b veto	shape	1-3%
Muon energy scale, p_T <100 GeV	shape	0.2%
Muon energy scale, $p_T \geq 100$ GeV	shape	5%
Electron energy scale	shape	1%
Tau energy scale	shape	1.2-3%
Jet energy scale	shape	2-5%
Meson resonance yields	normalization	5-20%
Factorization and Renormalization	shape	1% ($0.5 \leq \mu_R/\mu_F \leq 2$)
Acceptance correction	normalization	0.5%
Higgs PDF+α	normalization	3-4% (From YR4)

Table 4.12: The sources of systematic uncertainties and whether they affect the shape or normalization.

4.9 Expected Limits

The expected limits presented in this dissertation are determined using the modified frequentist approach [61, 62] with the LHC test statistic. Significance and expected exclusions are calculated using the Higgs Combine tool [59] and the `AsymptoticLimits` method. This method uses the asymptotic approximation [60] the LHC test-statistic to speed up the calculation. Systematic uncertainties are represented as nuisance parameters assuming a log-normal PDF in the likelihood fit for uncertainties in the expected yields and a Gaussian PDF of uncertainties in the signal and background model parameters. At the moment, only the major systematic uncertainties (transfer factor and tau ID scale factor) are included. In the combination, each year's data are treated as an independent bin in the datacard [51].

Expected limits on $\sigma_H \mathcal{B}(\mathrm{H} \rightarrow \mathrm{aa} \rightarrow \mu\mu\tau\tau)/\sigma_{SM}$ for a Higgs boson mass of $m_H = 125$ GeV for each year and each of the $\tau_h\tau_h$, $\tau_\mu\tau_h$, $\tau_e\tau_h$, $\tau_\mu\tau_e$, and $\tau_\mu\tau_\mu$ channels are presented in Figures 4.43, 4.44, 4.45, 4.46, and 4.47, respectively. Expected limits on $\sigma_H \mathcal{B}(\mathrm{H} \rightarrow \mathrm{aa} \rightarrow \mu\mu\tau\tau)/\sigma_{SM}$ for each of the 2016, 2017, and 2018 datasets with all channels combined are presented in Fig. 4.48. Expected limits on $\sigma_H \mathcal{B}(\mathrm{H} \rightarrow \mathrm{aa} \rightarrow \mu\mu\tau\tau)/\sigma_{SM}$ for each individual channel and for the full Run 2 datasets combined are presented in Fig. 4.49. The $\tau_\mu\tau_\mu$, $\tau_\mu\tau_e$ and $\tau_\mu\tau_h$ channels have strong performance with limits on $\sigma_H \mathcal{B}(\mathrm{H} \rightarrow \mathrm{aa} \rightarrow \mu\mu\tau\tau)/\sigma_{SM}$ mostly below 0.2×10^{-3} across the pseudoscalar Higgs boson mass range (except around the Υ mass range). There is similar performance in the $\tau_h\tau_h$ channel with improvement at higher pseudoscalar Higgs boson masses, and the $\tau_e\tau_h$ contributes at higher pseudoscalar Higgs boson masses. The overall combination of all channels gives expected limits near values around 0.1×10^{-3} over most of the pseudoscalar mass range. This is an improvement of the 2016 analysis searching for a light pseudoscalar Higgs boson in the $\mathrm{H} \rightarrow \mathrm{aa} \rightarrow \mu\mu\tau_h\tau_\mu$ channel, which had expected limits consistently above 0.2×10^{-3} $\sigma_H \mathcal{B}(\mathrm{H} \rightarrow \mathrm{aa} \rightarrow \mu\mu\tau\tau)/\sigma_{SM}$ [8].

The full Run 2 combined asymptotic limits for heavy Higgs bosons are shown in Figures 4.50, 4.51, 4.52, and 4.53. The $\tau_\mu\tau_e$, $\tau_\mu\tau_h$, and $\tau_h\tau_h$ show significant sensitivity on the cross section constraint. The $\tau_\mu\tau_\mu$ channel does not have comparable sensitivity to these channels. The $\tau_e\tau_h$ channel shows increased sensitivity at high pseudoscalar mass region.

These limits are expected to improve the current limits set by previous CMS searches. The plots presented in this dissertation will be superseded by published results that include observed limits or evidence of observation of a light pseudoscalar Higgs boson. The results will be interpreted in the context of 2 Higgs doublet plus singlet models.

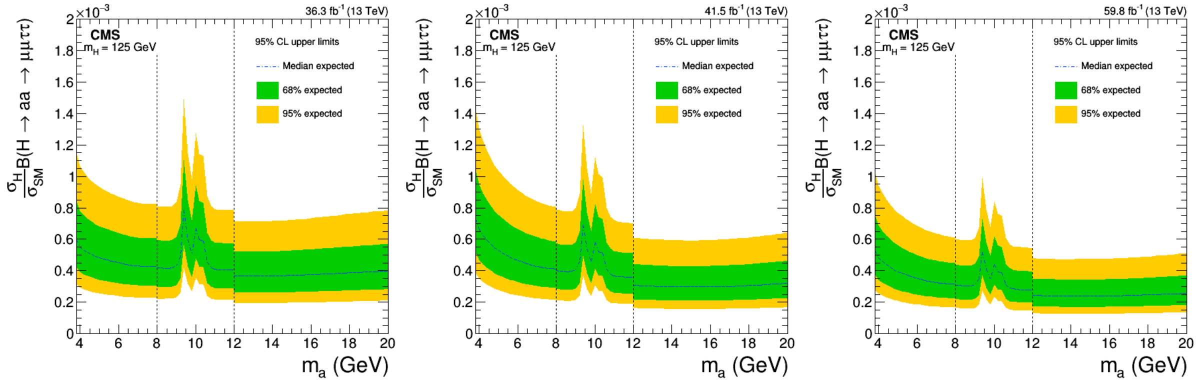

(a) (b) (c)

Figure 4.43: Expected limits on $\sigma_H\mathcal{B}(\mathrm{H} \rightarrow \mathrm{aa} \rightarrow \mu\mu\tau\tau)/\sigma_{SM}$ for the $\tau_h\tau_h$ channel of the 2016 (left), 2017 (middle), and 2018 (right) datasets.

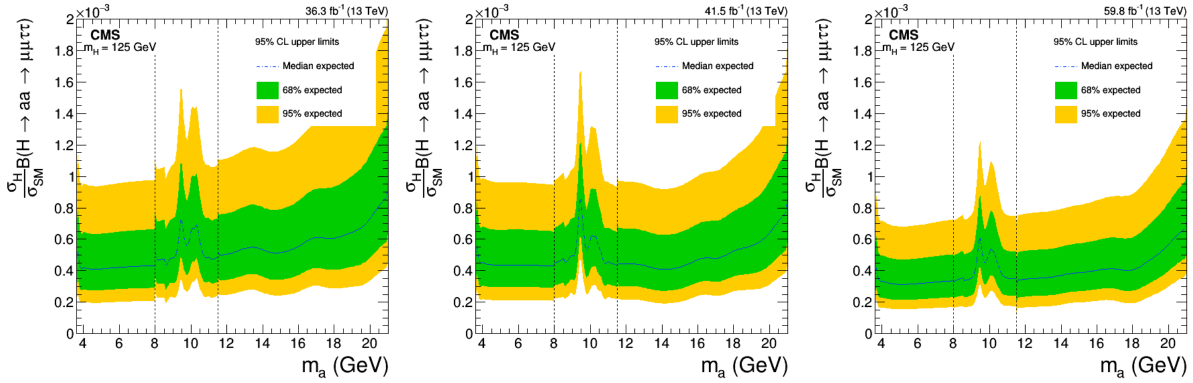

(a) (b) (c)

Figure 4.44: Expected limits on $\sigma_H\mathcal{B}(\mathrm{H} \rightarrow \mathrm{aa} \rightarrow \mu\mu\tau\tau)/\sigma_{SM}$ for the $\tau_\mu\tau_h$ channel of the 2016 (left), 2017 (middle), and 2018 (right) datasets.

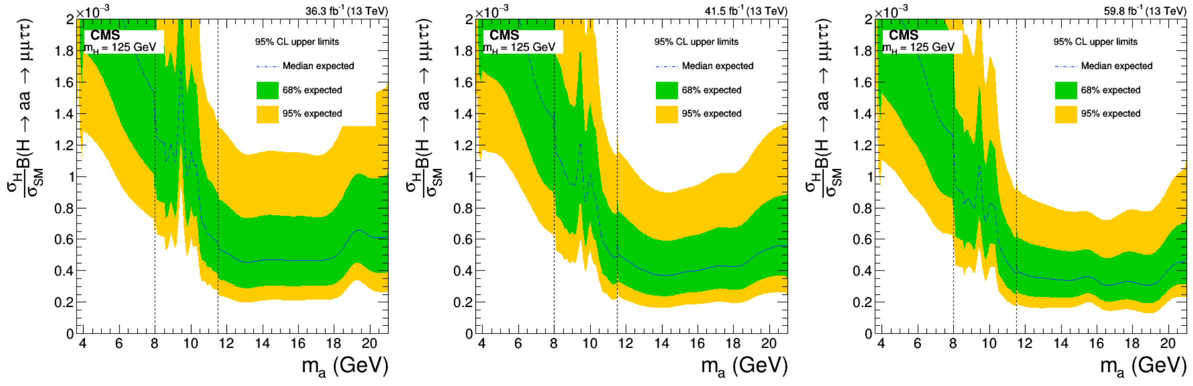

(a) (b) (c)

Figure 4.45: Expected limits on $\sigma_H\mathcal{B}(\mathrm{H} \to \mathrm{aa} \to \mu\mu\tau\tau)/\sigma_{SM}$ for the $\tau_e\tau_h$ channel of the 2016 (left), 2017 (middle), and 2018 (right) datasets.

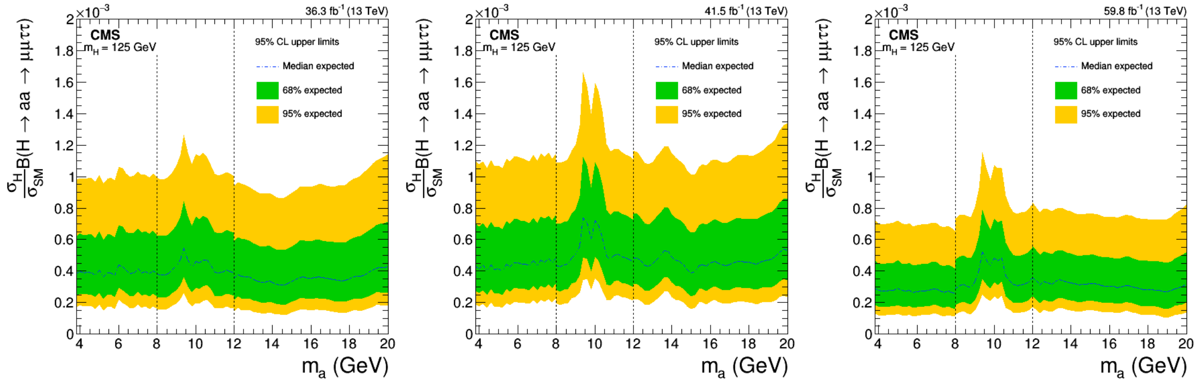

(a) (b) (c)

Figure 4.46: Expected limits on $\sigma_H\mathcal{B}(\mathrm{H} \to \mathrm{aa} \to \mu\mu\tau\tau)/\sigma_{SM}$ for the $\tau_\mu\tau_e$ channel of the 2016 (left), 2017 (middle), and 2018 (right) datasets.

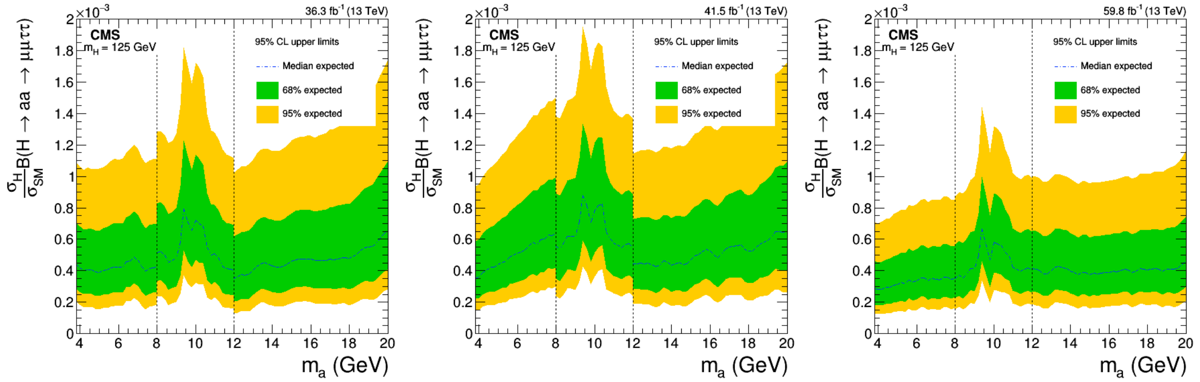

(a) (b) (c)

Figure 4.47: Expected limits on $\sigma_H\mathcal{B}(\mathrm{H} \to \mathrm{aa} \to \mu\mu\tau\tau)/\sigma_{SM}$ for the $\tau_\mu\tau_\mu$ channel of the 2016 (left), 2017 (middle), and 2018 (right) datasets.

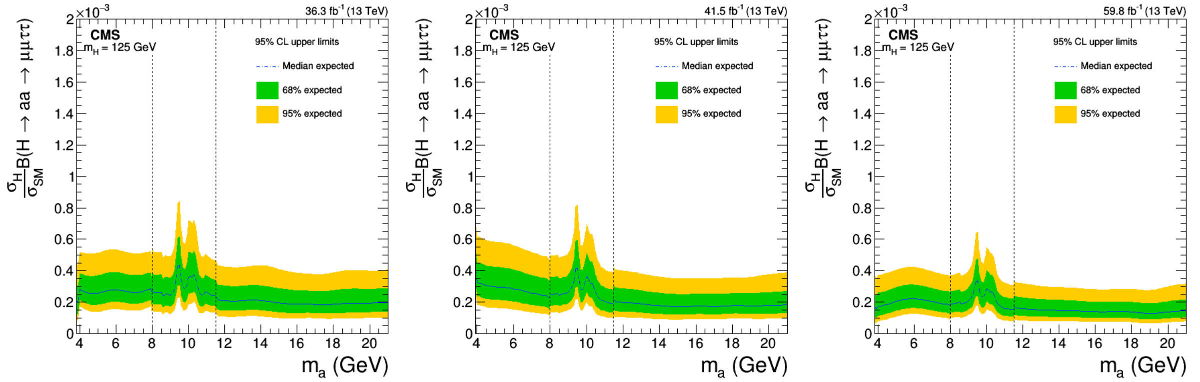

(a) (b) (c)

Figure 4.48: Expected limits on $\sigma_H\mathcal{B}(\mathrm{H} \to \mathrm{aa} \to \mu\mu\tau\tau)/\sigma_{SM}$ for all channels combined of the 2016 (left), 2017 (middle), and 2018 (right) datasets.

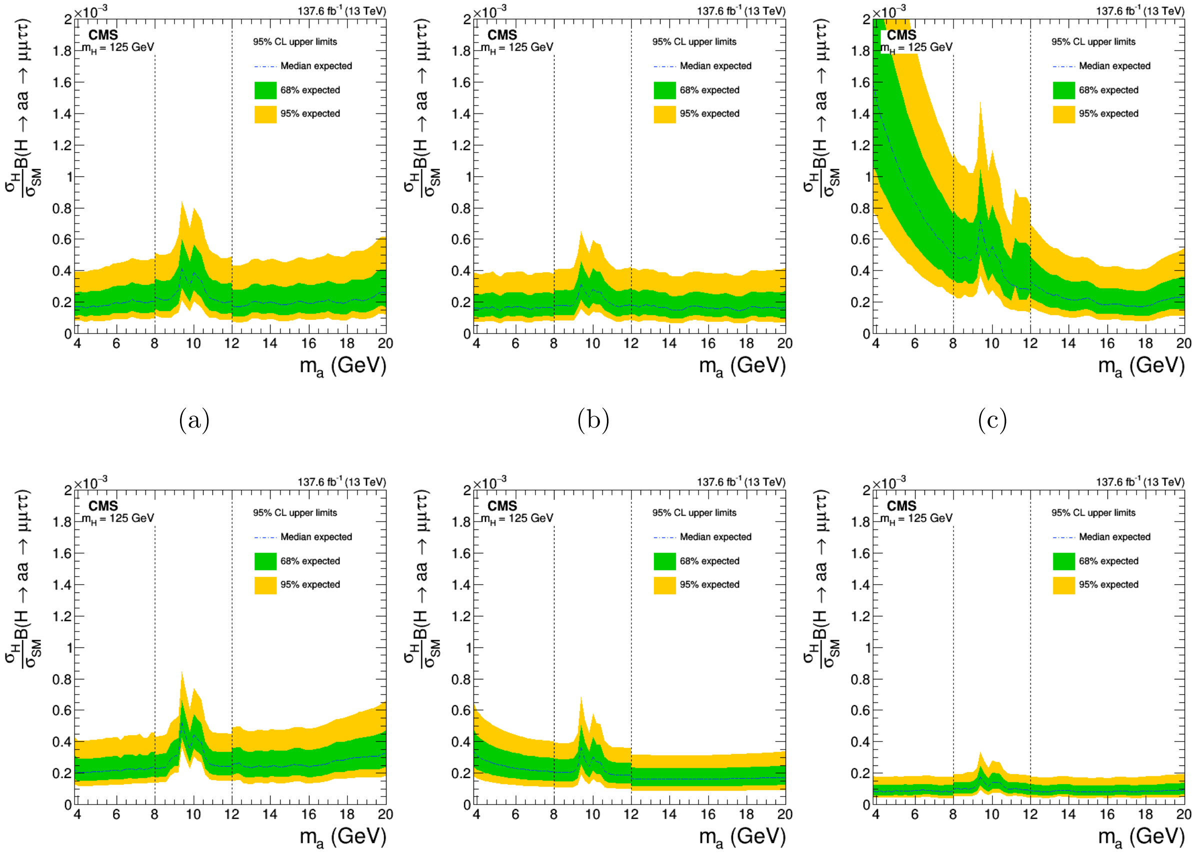

(a) (b) (c)

(d) (e) (f)

Figure 4.49: Expected limits on $\sigma_H \mathcal{B}(\mathrm{H} \rightarrow \mathrm{aa} \rightarrow \mu\mu\tau\tau)/\sigma_{SM}$ for the full Run 2 dataset $\tau_\mu\tau_\mu$ (top left), $\tau_\mu\tau_e$ (top middle), $\tau_e\tau_h$ (top right), $\tau_\mu\tau_h$ (bottom left), $\tau_h\tau_h$ (bottom middle), and combined (bottom right) channels for a Higgs boson with $m_H = 125$ GeV.

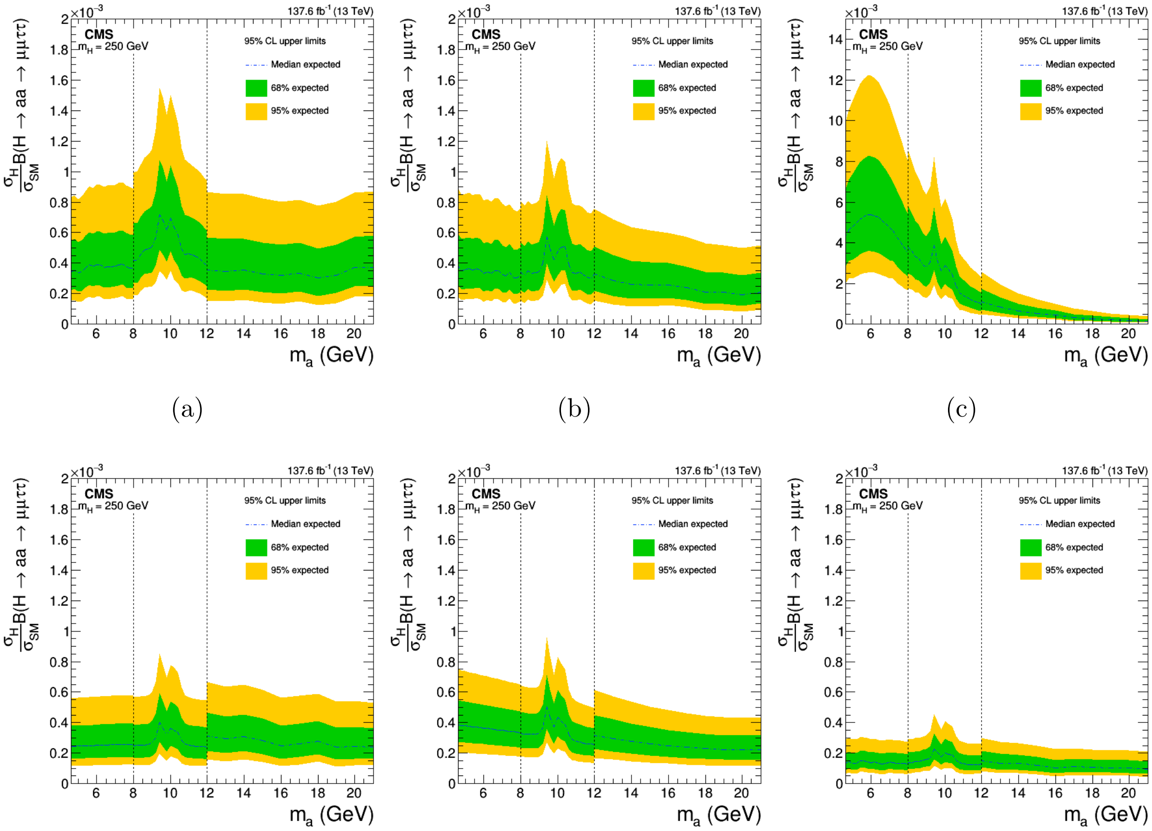

(a) (b) (c)

(d) (e) (f)

Figure 4.50: Expected limits on $\sigma_H \mathcal{B}(\mathrm{H} \rightarrow \mathrm{aa} \rightarrow \mu\mu\tau\tau)/\sigma_{SM}$ for the full Run 2 dataset $\tau_\mu\tau_\mu$ (top left), $\tau_\mu\tau_e$ (top middle), $\tau_e\tau_h$ (top right), $\tau_\mu\tau_h$ (bottom left), $\tau_h\tau_h$ (bottom middle), and combined (bottom right) channels for a heavy Higgs boson with $m_H = 250$ GeV.

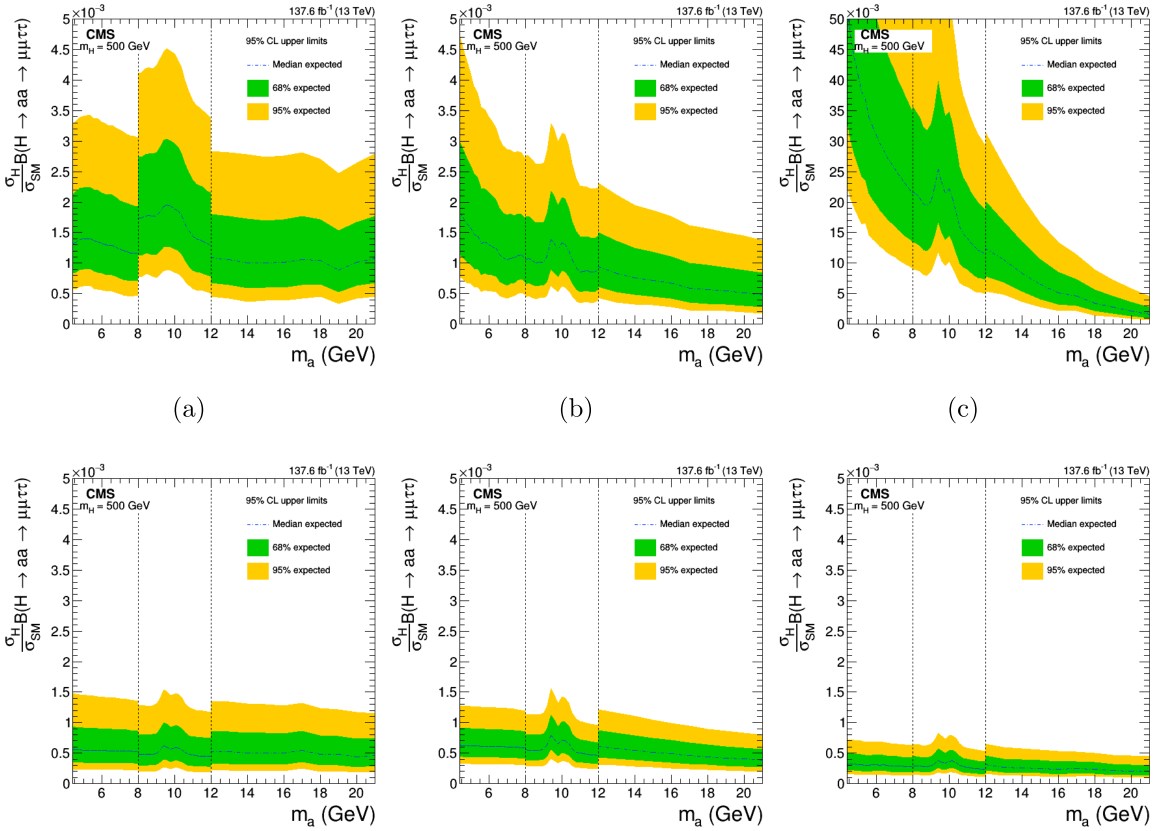

(a) (b) (c)

(d) (e) (f)

Figure 4.51: Expected limits on $\sigma_H \mathcal{B}(\mathrm{H} \rightarrow \mathrm{aa} \rightarrow \mu\mu\tau\tau)/\sigma_{SM}$ for the full Run 2 dataset $\tau_\mu\tau_\mu$ (top left), $\tau_\mu\tau_e$ (top middle), $\tau_e\tau_h$ (top right), $\tau_\mu\tau_h$ (bottom left), $\tau_h\tau_h$ (bottom middle), and combined (bottom right) channels for a heavy Higgs boson with $m_H = 500$ GeV.

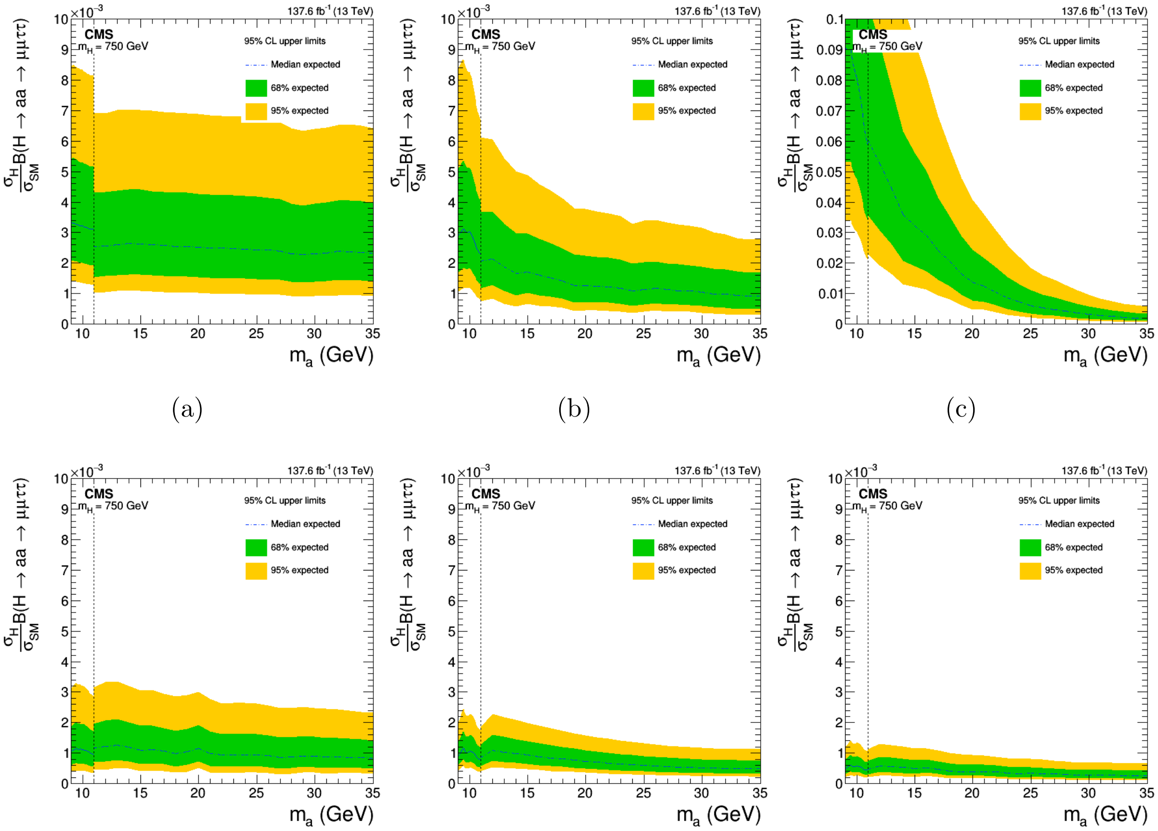

(a) (b) (c)

(d) (e) (f)

Figure 4.52: Expected limits on $\sigma_H \mathcal{B}(\mathrm{H} \rightarrow \mathrm{aa} \rightarrow \mu\mu\tau\tau)/\sigma_{SM}$ for the full Run 2 dataset $\tau_\mu\tau_\mu$ (a), $\tau_\mu\tau_e$ (b), $\tau_e\tau_h$ (c), $\tau_\mu\tau_h$ (d), $\tau_h\tau_h$ (e), and combined (f) channels for a heavy Higgs boson with $m_H = 750$ GeV.

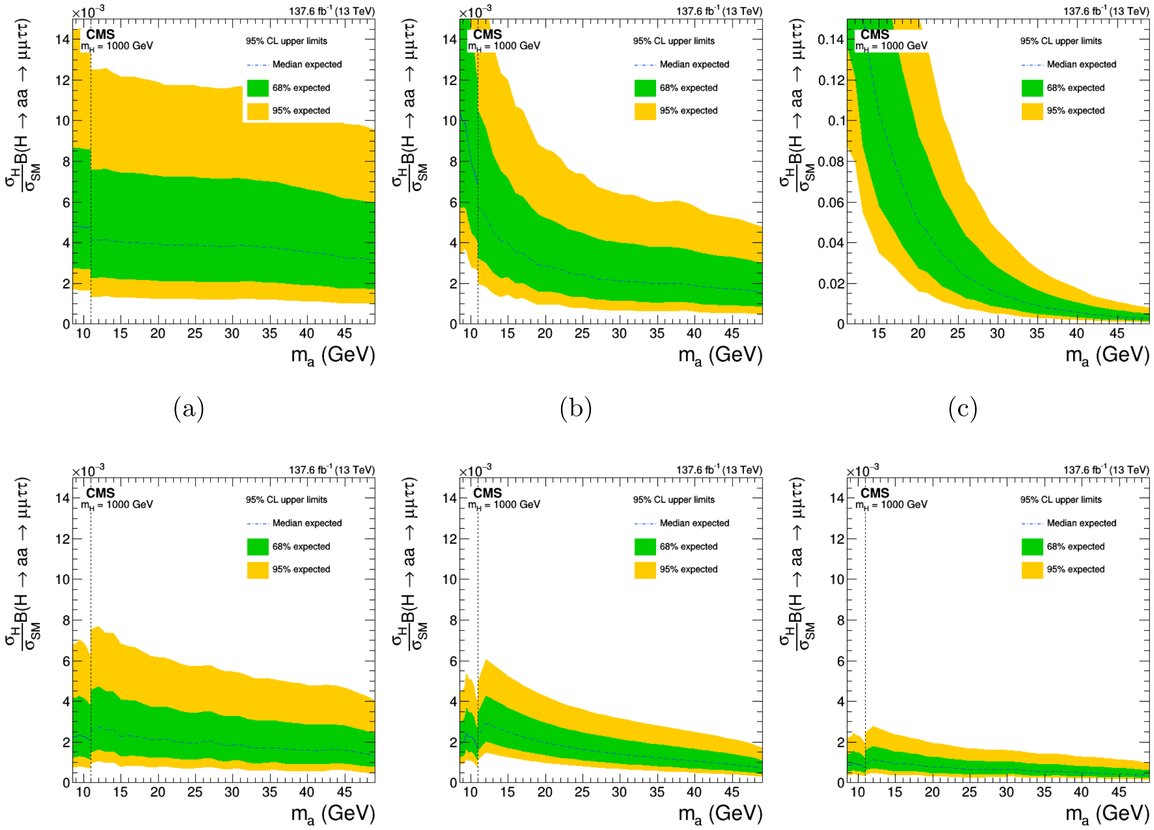

(a) (b) (c)

(d) (e) (f)

Figure 4.53: Expected limits on $\sigma_H \mathcal{B}(\text{H} \rightarrow \text{aa} \rightarrow \mu\mu\tau\tau)/\sigma_{SM}$ for the full Run 2 dataset $\tau_\mu\tau_\mu$ (top left), $\tau_\mu\tau_e$ (top middle), $\tau_e\tau_h$ (top right), $\tau_\mu\tau_h$ (bottom left), $\tau_h\tau_h$ (bottom middle), and combined (bottom right) channels for a heavy Higgs boson with $m_H = 1000$ GeV.

Chapter 5

Conclusions

A search for a pseudoscalar Higgs boson in the H→ aa → $\mu\mu\tau\tau$ decay channel using the full Run 2 dataset collected by the CMS detector at the LHC was performed. Due to the boosted topology, this search uses novel techniques in both the semi-leptonic case of tau decays and in the case of the both taus decaying hadronically. DeepDiTau is neural net tagger designed to identify overlapping hadronic tau decays reconstructed as jets and is used for the first time in an analysis. The expected limits for $\sigma_H\mathcal{B}(H \to \mathrm{aa} \to \mu\mu\tau\tau)/\sigma_{SM}$ are forecasted to exceed the previous results.

The CMS pixel tracker was refurbished and re-installed in CMS for a successful start of datataking in Run 3. Modules from the innermost layer of BPix were tested for radiation damage and no clear evidence of z-dependence was found.

The ongoing Run 3 of the LHC is scheduled to end in 2025. The LHC will then be upgraded to the High Luminosity LHC, which can can achieve instantaneous luminosities a factor of 5 to 7.5 times greater than the current LHC. Over the period of 2026-2028, detectors including CMS will undergo major upgrades to ensure smooth datataking for Run 4 and Run 5, which are expected to deliver at least $3000\mathrm{fb}^{-1}$ of integrated luminosity [63].

References

[1] H. Murayama and K. Riesselmann, “DOE Explains the Standard Model of Particle Physics.” `https://www.energy.gov/science/doe-explainsthe-standard-model-particle-physics`.

[2] M. Thomson, *Modern particle physics*, Cambridge University Press, New York (2013), 10.1017/CBO9781139525367.

[3] *Precision electroweak measurements on the Z resonance*, *Physics Reports* **427** (2006) 257.

[4] V.A. Bednyakov, N.D. Giokaris and A.V. Bednyakov, *On the Higgs mass generation mechanism in the Standard Model*, *Physics of Particles and Nuclei* **39** (2008) 13.

[5] CMS collaboration, *Observation of a new boson at a mass of 125 GeV with the CMS experiment at the LHC*, *Physics Letters B* **716** (2012) 30.

[6] S.P. Martin, *A Supersymmetry Primer*, in *Perspectives on Supersymmetry*, pp. 1–98, World Scientific (1998), DOI.

[7] CMS collaboration, *Combined measurements of Higgs boson couplings in proton–proton collisions at* $\sqrt{s} = 13$ *TeV*, *The European Physical Journal C* **79** (2019) .

[8] CMS collaboration, *Search for a light pseudoscalar Higgs boson in the boosted* $\mu\mu\tau\tau$ *final state in proton-proton collisions at* $\sqrt{s}$ *= 13 TeV*, *Journal of High Energy Physics* **2020** (2020) .

[9] E. Lopienska, “The CERN accelerator complex, layout in 2022. Complexe des accélérateurs du CERN en janvier 2022.” `https://cds.cern.ch/record/2800984`, 2022.

[10] L.R. Evans and P. Bryant, *LHC Machine*, *JINST* **3** (2008) S08001.

[11] CMS collaboration, *A New Boson with a Mass of 125 GeV Observed with the CMS Experiment at the Large Hadron Collider*, *Science* **338** (2012) 1569.

[12] Neutelings, Izaak, “CMS coordinate system – TikZ.net.” `https://tikz.net/axis3d_cms/`, 2022.

[13] P.D. Group, *Passage of Particles Through Matter*, 2021.

[14] F. Hartmann, *Evolution of Silicon Sensor Technology in Particle Physics*, vol. 275 of *Springer Tracts in Modern Physics*, Springer (2017), 10.1007/978-3-319-64436-3.

[15] CMS Tracker Group collaboration, *The CMS Phase-1 Pixel Detector Upgrade*, *JINST* **16** (2021) P02027 [`2012.14304`].

[16] CMS collaboration, *CMS Technical Design Report for the Pixel Detector Upgrade*, Tech. Rep. CERN-LHCC-2012-016, CMS-TDR-011 (September, 2012), DOI.

[17] CMS collaboration, *The DAQ and control system for the CMS Phase-1 pixel detector upgrade*, *JINST* **14** (2019) P10017.

[18] M. Brice, "First half of CMS inner tracker barrel." `https://cds.cern.ch/record/995912`, 2006.

[19] CMS collaboration, *The CMS Experiment at the CERN LHC*, *JINST* **3** (2008) S08004.

[20] S.R. Chowdhury, *Status of the CMS Silicon Strip Tracker*, 2022.

[21] CMS collaboration, *Performance of the CMS level-1 trigger in proton-proton collisions at $\sqrt{s} = 13$ TeV*, *Journal of Instrumentation* **15** (2020) P10017.

[22] A.S. et. al., *Particle-flow reconstruction and global event description with the CMS detector*, *Journal of Instrumentation* **12** (2017) P10003.

[23] B. Vormwald, *DAQ Workshop: Introduction to Pixel DAQ*, .

[24] G. Negro, "CMS Inner Tracker Status and Performance." `https://cds.cern.ch/record/2846684`, 2022.

[25] CMS collaboration, "Public CMS Data Quality Information." `https://twiki.cern.ch/twiki/bin/view/CMSPublic/DataQuality#2022_up_to_the_latest_certified`, 2022.

[26] CMS collaboration, *Search for light bosons in decays of the 125 GeV Higgs boson in proton-proton collisions at $\sqrt{s} = 8\,TeV$*, *Journal of High Energy Physics* **2017** (2017) .

[27] M. Maniatis, *The Next-to-Minimal Supersymmetric Extension of the Standard Model Reviewed*, *International Journal of Modern Physics A* **25** (2010) 3505.

[28] CMS collaboration, *The CMS electromagnetic calorimeter project: Technical Design Report*, Tech. Rep. CERN-LHCC-97-033 ; CMS-TDR-4, Geneva (1997).

[29] CMS collaboration, *Performance of the CMS muon detector and muon reconstruction with proton-proton collisions at $\sqrt{s}$ = 13 TeV*, *Journal of Instrumentation* **13** (2018) P06015.

[30] CMS collaboration, *CMS High Level Trigger performance at 13 TeV*, *PoS* **ICHEP2018** (2019) 226.

[31] CMS EGamma POG, "Electron Cut Based ID for 94X samples." `https://twiki.cern.ch/twiki/bin/viewauth/CMS/CutBasedElectronIdentificationRun2`.

[32] M.E. Peskin and D.V. Schroeder, *An Introduction to Quantum Field Theory*, Westview Press (1995).

[33] F. Halzen and A. Martin, *Quarks and Leptons: An Introductory Course in Modern Particle Physics*, John Wiley and Sons, Inc., New York, USA (1984).

[34] L. Di Lella and C. Rubbia, *The Discovery of the W and Z Particles*, *Adv. Ser. Direct. High Energy Phys.* **23** (2015) 137.

[35] A. Djouadi, *The anatomy of electroweak symmetry breaking*, *Physics Reports* **457** (2008) 1.

[36] ATLAS collaboration, *Observation of a new particle in the search for the Standard Model Higgs boson with the ATLAS detector at the LHC*, *Physics Letters B* **716** (2012) 1.

[37] Y.F. et. al., *Evidence for Oscillation of Atmospheric Neutrinos*, *Physical Review Letters* **81** (1998) 1562.

[38] I.J. Aitchison, "Supersymmetry and the MSSM: An Elementary introduction." `https://arxiv.org/pdf/hep-ph/0505105.pdf`, 2005.

[39] G. Branco, P. Ferreira, L. Lavoura, M. Rebelo, M. Sher and J.P. Silva, *Theory and phenomenology of two-Higgs-doublet models*, *Physics Reports* **516** (2012) 1.

[40] D. Curtin, R. Essig, S. Gori, P. Jaiswal, A. Katz, T. Liu et al., *Exotic decays of the 125 GeV Higgs boson*, *Physical Review D* **90** (2014) .

[41] CMS collaboration, *Search for a Light Pseudoscalar Higgs Boson in the Dimuon Decay Channel in pp Collisions at $\sqrt{s} = 7$ TeV*, *Phys. Rev. Lett.* **109** (2012) 121801 [`1206.6326`].

[42] M. Moll, "An introduction to Silicon Detectors with focus on applications at Hadron Colliders." `https://indico.in2p3.fr/event/17763/contributions/66813/attachments/50770/64925/2018-10-29-Paris-SIMDET-Silicon_Sensors.pdf`, 2018.

[43] E. Butz, "Operation and Performance of the CMS Outer Tracker." `https://pos.sissa.it/309/013/pdf`, September, 2017.

[44] CMS collaboration, *CMS Physics: Technical Design Report Volume 1: Detector Performance and Software*, Tech. Rep. CERN-LHCC-2006-001, CMS-TDR-8-1 (2006).

[45] CMS collaboration, *CMS Drift Tubes Readout Phase 1 Upgrade*, *PoS* **TWEPP2018** (2019) 039.

[46] CMS collaboration, *CMS Technical Design Report for the Level-1 Trigger Upgrade*, Tech. Rep. CERN-LHCC-2013-011, CMS-TDR-12 (2013).

[47] CMS collaboration, *Particle-Flow Event Reconstruction in CMS and Performance for Jets, Taus, and MET*, Tech. Rep. CMS-PAS-PFT-09-001, CERN (2009).

[48] F. Faccio, *The lonely perpetrator in the DCDC FEAST2 case - how an individual transistor threatened the operations of the CMS pixel detector*, 2019.

[49] Maxwell Chertok, John Conway, David Pellett, John Thomson, Ricardo Vasquez Sierra, Rachel Yohay, Greg Derylo, *CMS Forward Pixel Installation Procedure*, December, 2014.

[50] ATLAS collaboration, *Modelling radiation damage to pixel sensors in the ATLAS detector*, *Journal of Instrumentation* **14** (2019) P06012.

[51] CMS collaboration, *Search for a light pseudoscalar Higgs boson in the boosted dimuon-ditau final state in proton-proton collisions at* $\sqrt{s} = 13$ *TeV using the full CMS Run II data*, Tech. Rep. CMS-AN-20-018 (2023).

[52] CMS collaboration, *Performance of CMS muon reconstruction in pp collision events at*$\sqrt{s} = 7$ *TeV*, *Journal of Instrumentation* **7** (2012) P10002.

[53] CMS collaboration, *Reconstruction and identification of tau lepton decays to hadrons and tau neutrino at CMS*, *Journal of Instrumentation* **11** (2016) P01019.

[54] CMS collaboration, *Performance of reconstruction and identification of tau leptons decays to hadrons tau neutrino in pp collisions at* $\sqrt{s}$ *= 13 TeV*, *Journal of Instrumentation* **13** (2018) P10005.

[55] CMS collaboration, *Jet flavour classification using DeepJet*, *Journal of Instrumentation* **15** (2020) P12012.

[56] N. Qian, *On the Momentum Term in Gradient Descent Learning Algorithms*, *Neural Networks* **12** (1999) 145–151.

[57] CMS collaboration, *Jet algorithms performance in 13 TeV data*, Tech. Rep. CMS-PAS-JME-16-003, CERN, Geneva (2017).

[58] Particle Data Group collaboration, *Review of particle physics*, *Phys. Rev. D* **98** (2018) 030001.

[59] CMS collaboration, "CMS Higgs Analysis Combined Limit GitHub page." `http://cms-analysis.github.io/HiggsAnalysis-CombinedLimit/`.

[60] G. Cowan, K. Cranmer, E. Gross and O. Vitells, *Asymptotic formulae for likelihood-based tests of new physics*, *The European Physical Journal C* **71** (2011) [`1007.1727`].

[61] T. Junk, *Confidence level computation for combining searches with small statistics*, *Nucl. Instrum. Meth. A* **434** (1999) 435 [`hep-ex/9902006`].

[62] A.L. Read, *Presentation of search results: The CL(s) technique*, *J. Phys. G* **28** (2002) 2693.

[63] CERN, “What is HiLumi? HL-LHC project website..” `https://hilumilhc.web.cern.ch`.

Appendix A

Background estimation for semi-leptonic decay channels

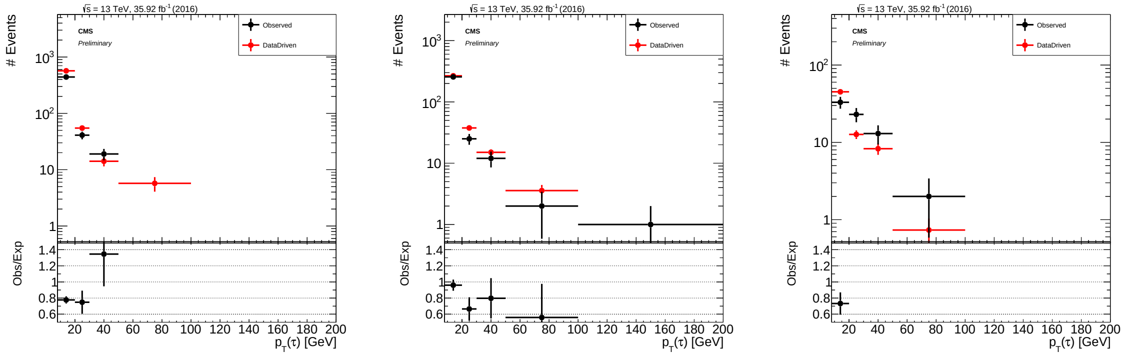

(a) DM0 (b) DM1 (c) DM10

Figure A.1: Kinematic comparisons between the validation region and the estimation of the validation region from the validation sideband using the fake rate method in $\tau_\mu \tau_{had}$ channel, using 2016 data. Additionally, total events are split by decay mode.

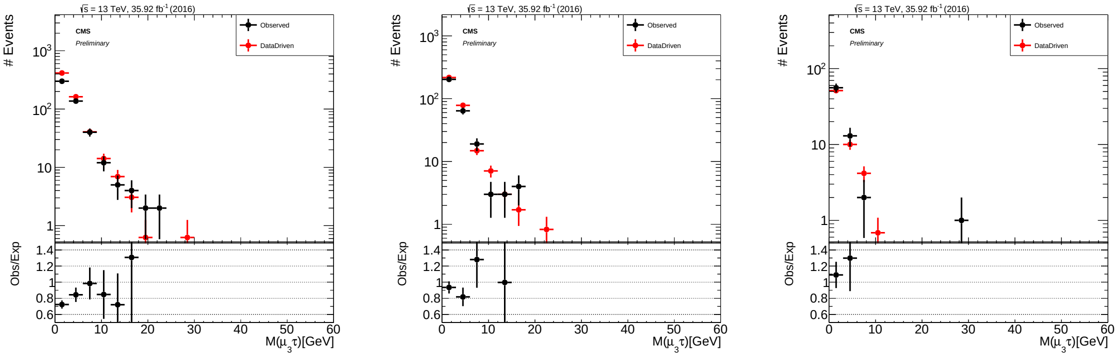

(a) DM0 (b) DM1 (c) DM10

Figure A.2: Kinematic comparisons between the validation region and the estimation of the validation region from the validation sideband using the fake rate method in $\tau_\mu \tau_{had}$ channel, using 2016 data. Additionally, total events are split by decay mode.

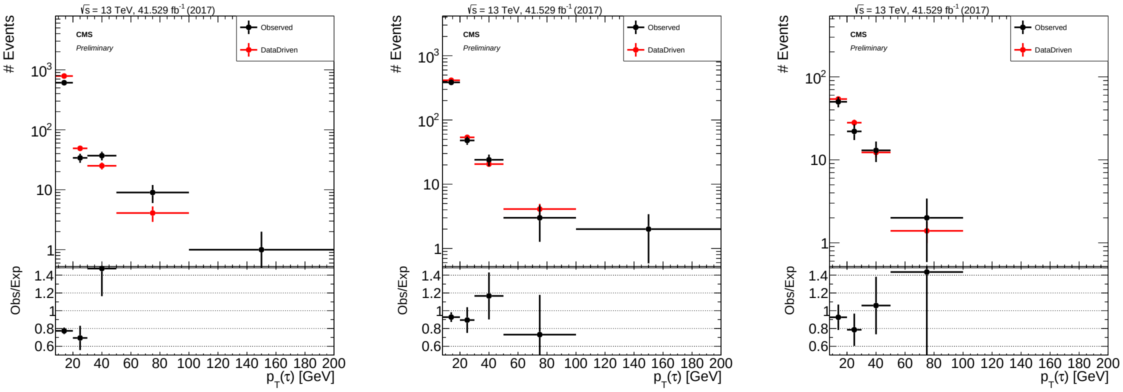

(a) DM0 (b) DM1 (c) DM10

Figure A.3: Kinematic comparisons between the validation region and the estimation of the validation region from the validation sideband using the fake rate method in $\tau_\mu \tau_{had}$ channel, using 2017 data. Additionally, total events are split by decay mode.

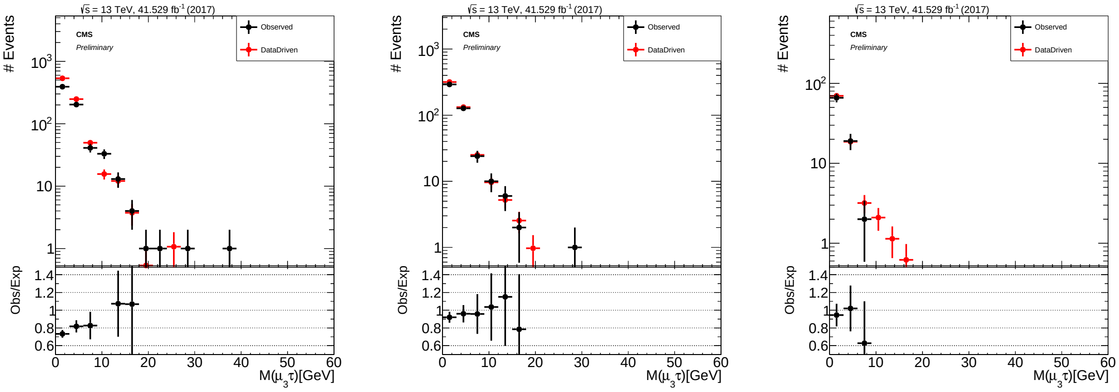

(a) DM0 (b) DM1 (c) DM10

Figure A.4: Kinematic comparisons between the validation region and the estimation of the validation region from the validation sideband using the fake rate method in $\tau_\mu\tau_{had}$ channel, using 2017 data. Additionally, total events are split by decay mode.

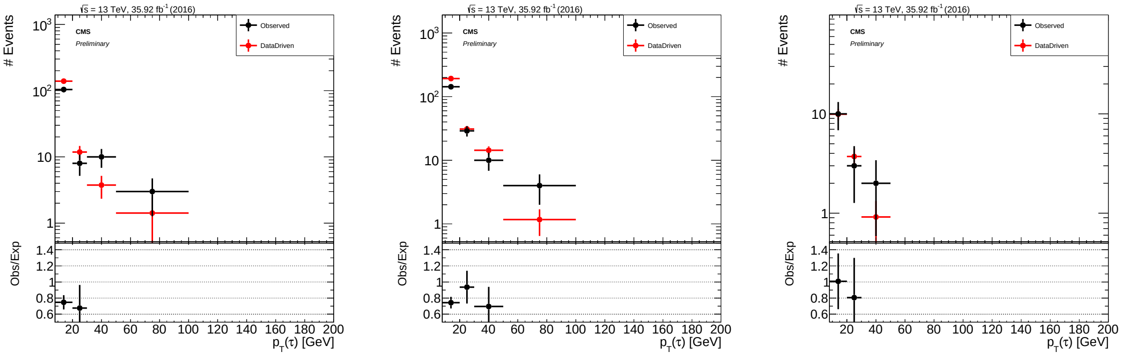

(a) DM0 (b) DM1 (c) DM10

Figure A.5: Kinematic comparisons between the validation region and the estimation of the validation region from the validation sideband using the fake rate method in $\tau_e\tau_{had}$ channel, using 2016 data. Additionally, total events are split by decay mode.

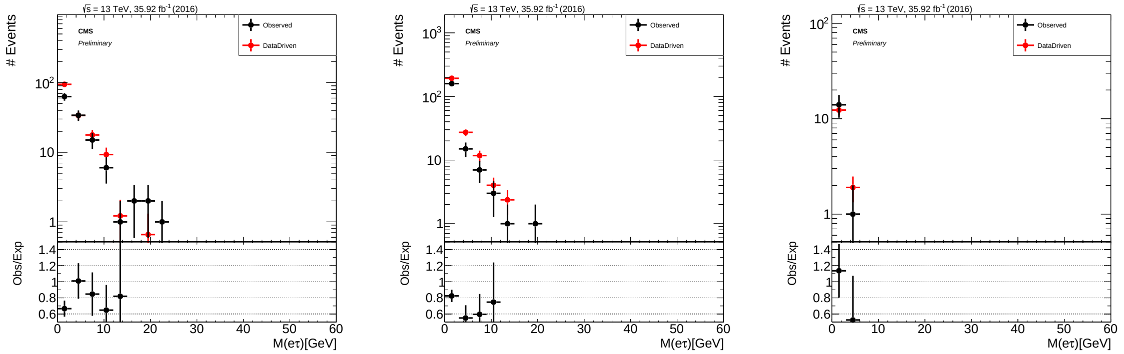

(a) DM0 (b) DM1 (c) DM10

Figure A.6: Kinematic comparisons between the validation region and the estimation of the validation region from the validation sideband using the fake rate method in $\tau_e\tau_{had}$ channel, using 2016 data. Additionally, total events are split by decay mode.

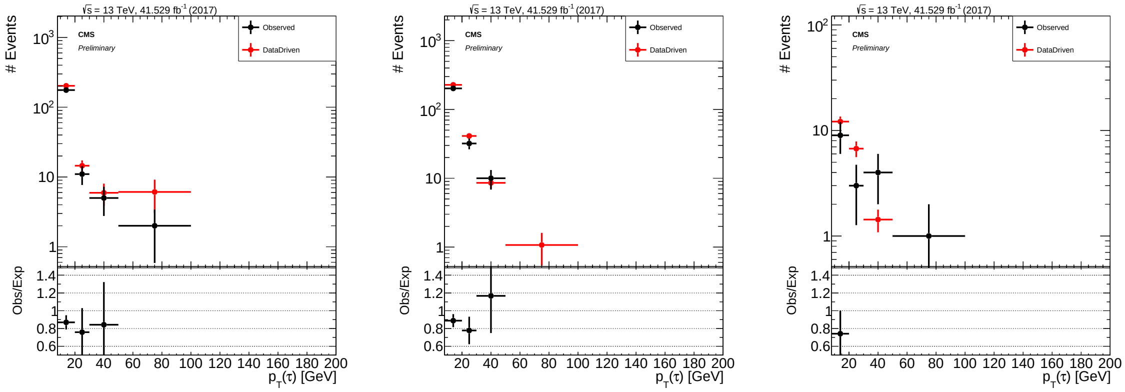

(a) DM0 (b) DM1 (c) DM10

Figure A.7: Kinematic comparisons between the validation region and the estimation of the validation region from the validation sideband using the fake rate method in $\tau_e\tau_{had}$ channel, using 2017 data. Additionally, total events are split by decay mode.

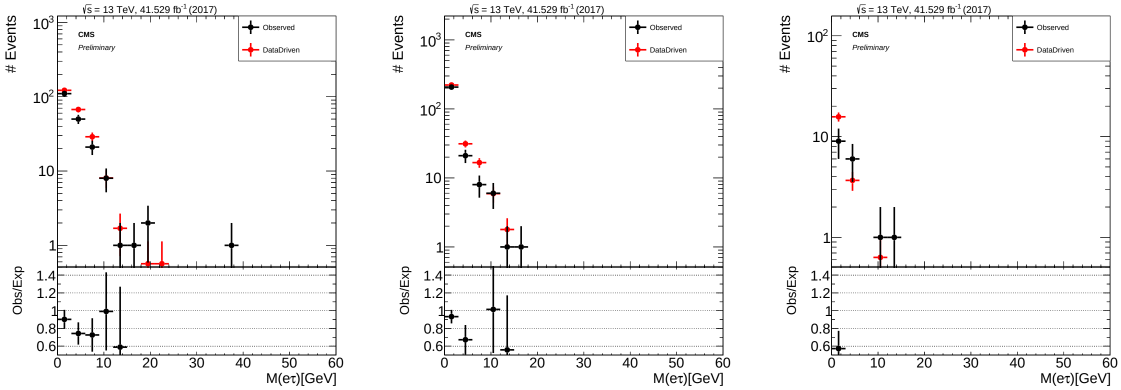

(a) DM0 (b) DM1 (c) DM10

Figure A.8: Kinematic comparisons between the validation region and the estimation of the validation region from the validation sideband using the fake rate method in $\tau_e\tau_{had}$ channel, using 2017 data. Additionally, total events are split by decay mode.

Appendix B

Background estimation for fully-leptonic channels

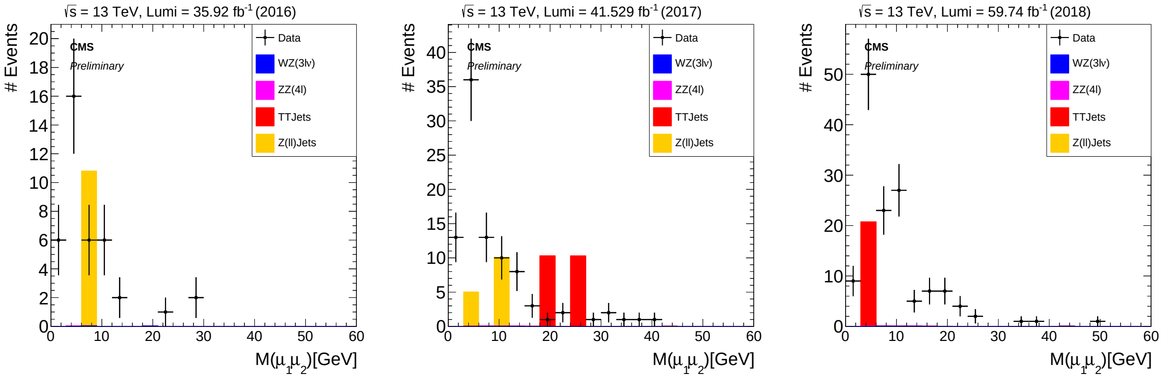

Figure B.1: Dimuon invariant mass distribution of the events selected in the 2P+2F control sample in the $\tau_\mu\tau_\mu$ channel with the dataset of era: 2016 (left), 2017 (middle) and 2018 (right).

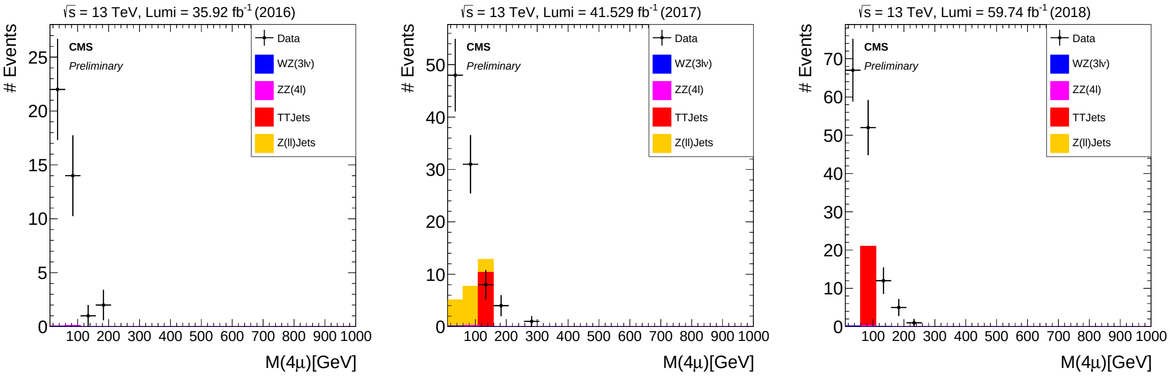

Figure B.2: Four lepton visible mass distribution of the events selected in the 2P+2F control sample in the $\tau_\mu\tau_\mu$ channel with the dataset of era: 2016 (left), 2017 (middle) and 2018 (right).

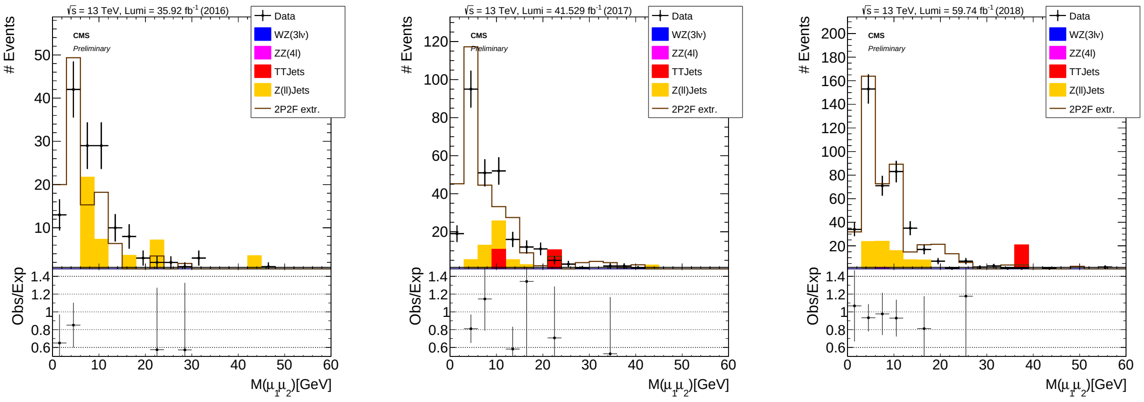

Figure B.3: Dimuon invariant mass distribution of the events selected in the 3P+1F control sample in the $\tau_\mu\tau_\mu$ channel with the dataset of era: 2016 (left), 2017 (middle) and 2018 (right).

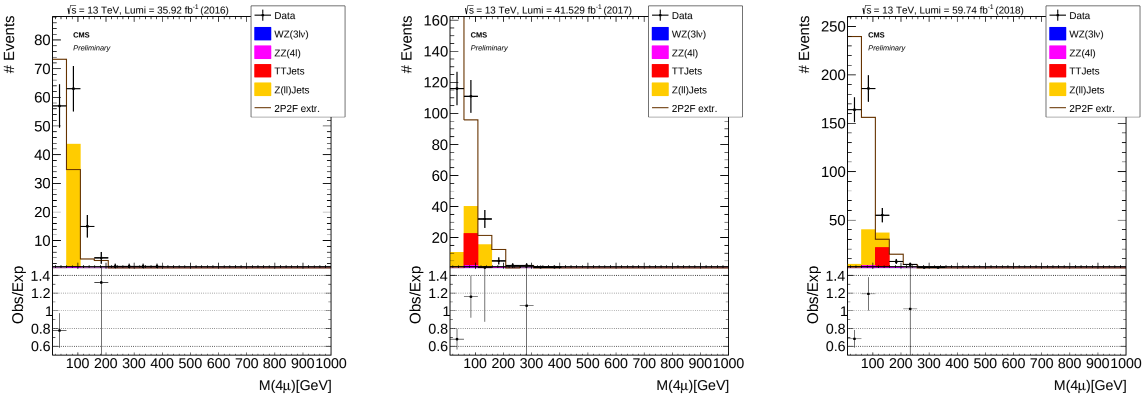

Figure B.4: Four-lepton visible mass distribution of the events selected in the 3P+1F control sample in the $\tau_\mu\tau_\mu$ channel with the dataset of era: 2016 (left), 2017 (middle) and 2018 (right).

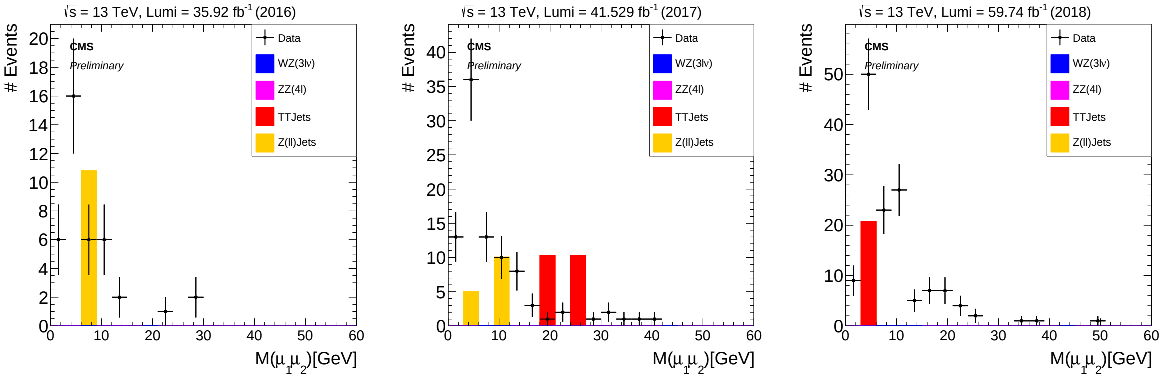

Figure B.5: Dimuon invariant mass distribution of the events extrapolated in the signal region in the $\tau_\mu\tau_\mu$ channel with the dataset of era: 2016 (left), 2017 (middle) and 2018 (right).

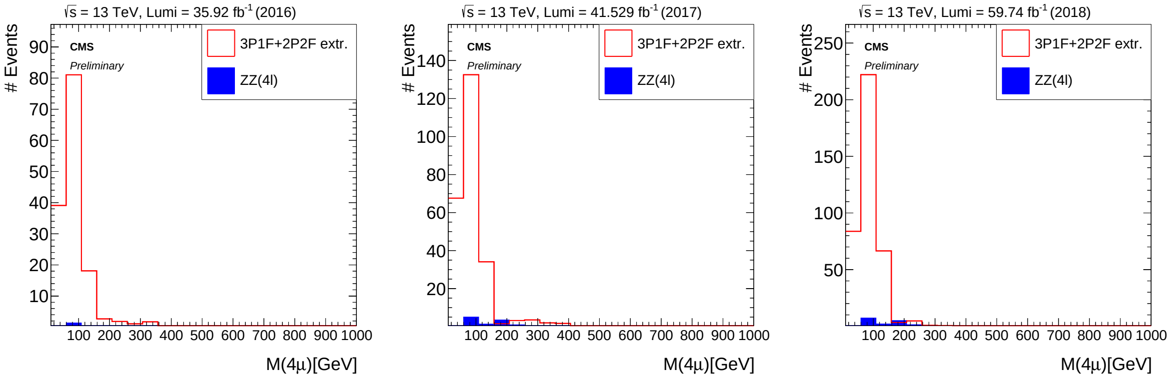

Figure B.6: Four-lepton visible mass distribution of the events extrapolated in the signal region in the $\tau_\mu\tau_\mu$ channel with the dataset of era: 2016 (left), 2017 (middle) and 2018 (right).

Appendix C

Additional fits

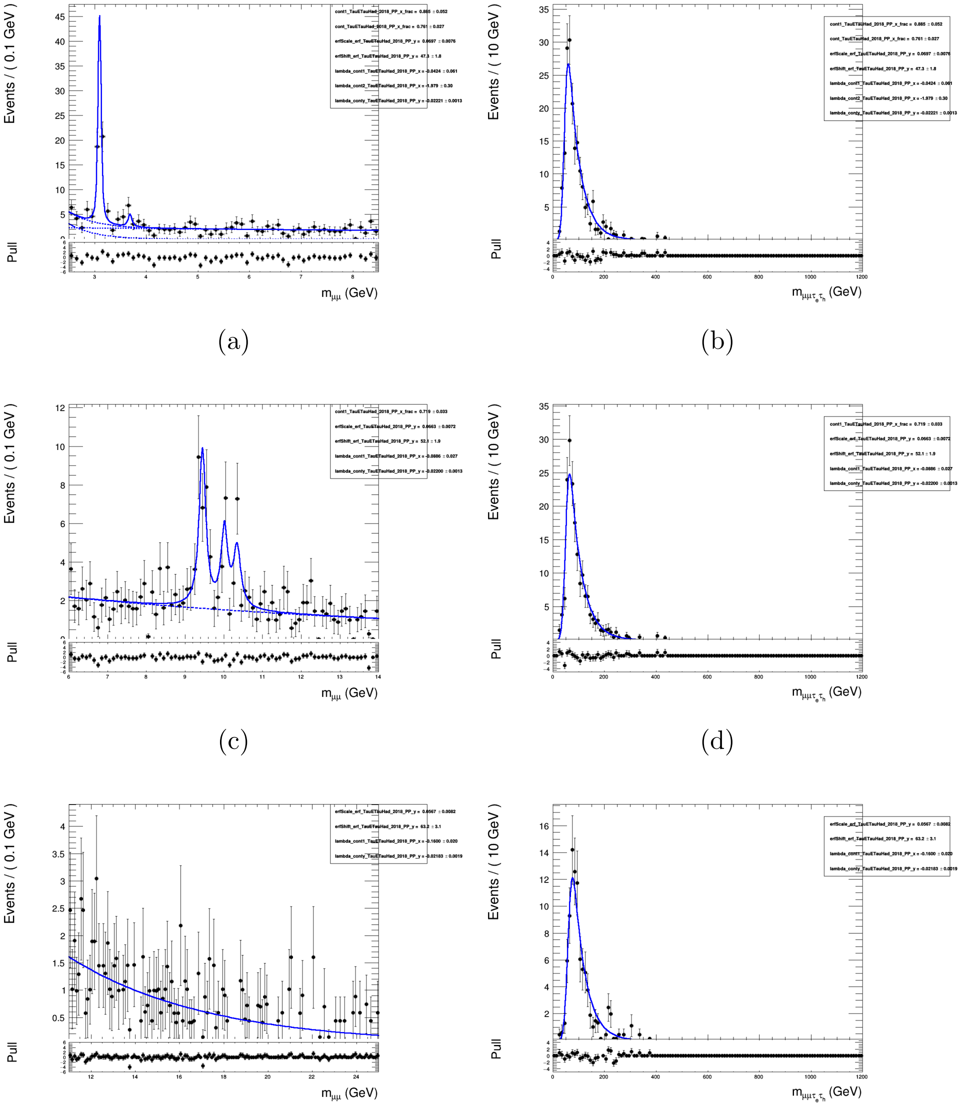

(a) (b)

(c) (d)

(e) (f)

Figure C.1: Initial fits of the dimuon (left) and 4-body (right) visible mass distributions from the 2018 dataset in the signal region for the $\tau_e\tau_{had}$ channel.

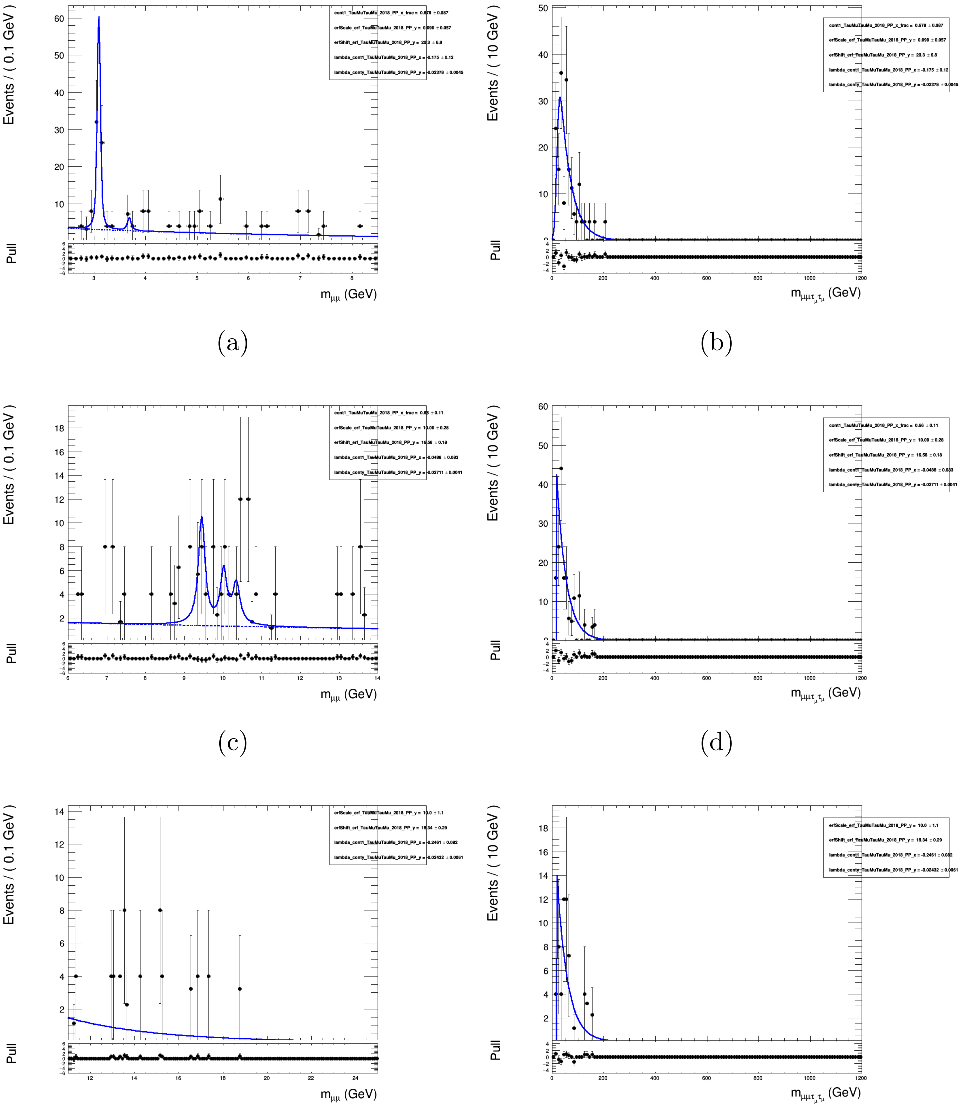

(a) (b)

(c) (d)

(e) (f)

Figure C.2: Initial fits of the dimuon (left) and 4-body (right) visible mass distributions from the 2018 dataset in the signal region for the $\tau_\mu\tau_\mu$ channel.

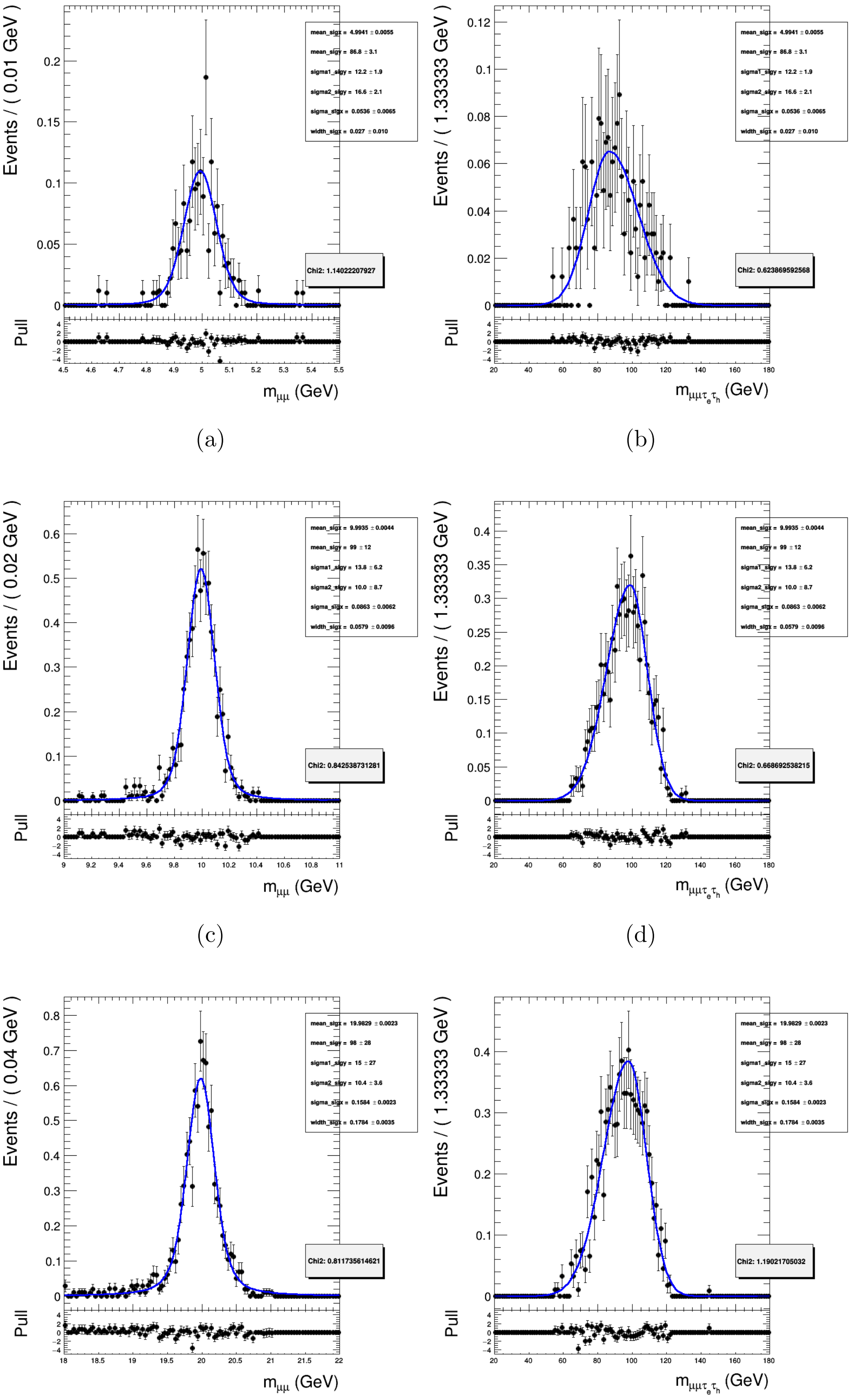

(a) (b)

(c) (d)

(e) (f)

Figure C.3: Modelling of the dimuon (left) and 4-body (right) visible mass distributions in the signal region for pseudoscalar masses of 5 (top), 10 (middle), and 20 (bottom) GeV for the $\tau_e\tau_{had}$ channel.

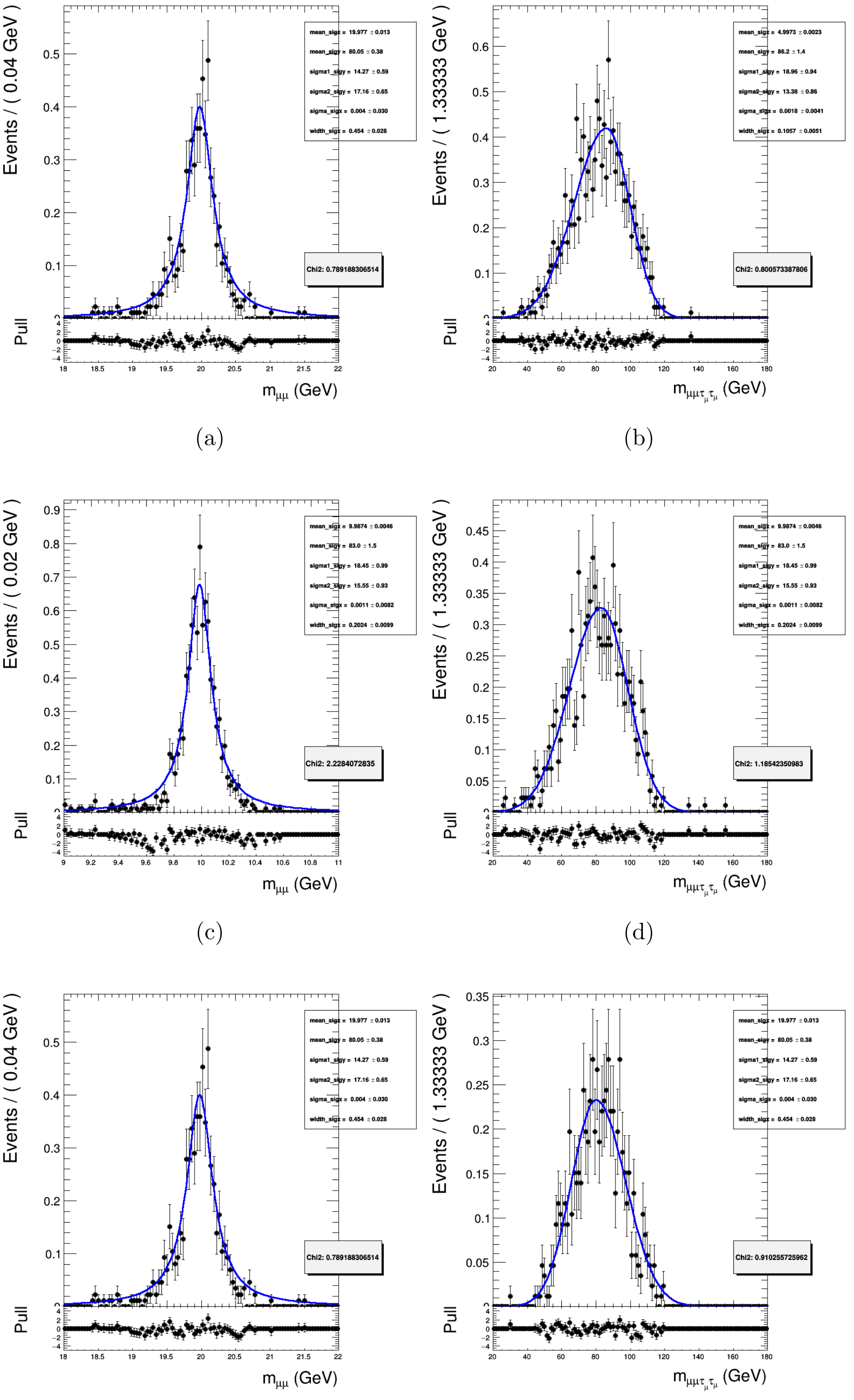

(a) (b)

(c) (d)

(e) (f)

Figure C.4: Modelling of the dimuon mass distribution in the signal region for pseudoscalar masses of 5 (left), 10 (middle), and 20 (right) GeV for the $\tau_\mu\tau_\mu$ channel.